

# Pd And Cu Monometallic And Single Atom Alloy Catalysts For The Hydrogenation Of Biomass Based Chemicals

Mohammed Johirul Islam

Doctor of Philosophy

ASTON UNIVERSITY  
Energy and Bioproducts Research Institute

March 2021

©Mohammed Johirul Islam, 2021

Mohammed Johirul Islam asserts his moral right to be identified as the author of this thesis

This copy of the thesis has been supplied on condition that anyone who consults it is understood to recognise that its copyright belongs to its author and that no quotation from the thesis and no information derived from it may be published without appropriate permission or acknowledgement

Aston University

Pd And Cu Monometallic And Single Atom Alloy Catalysts For The  
Hydrogenation Of Biomass Based Chemicals

Mohammed Johirul Islam

Doctor of Philosophy

2021

### Thesis Summary

The liquid-phase selective hydrogenation of bio-based platform molecules like furfural was studied with non-toxic Cu-based heterogeneous catalysts. The initial materials were synthesised via wet impregnation using various copper precursors (nitrate, acetate, and sulfate) at two different loadings. High Cu loading (5 wt%) led to the formation of well-defined nanoparticles, while lower loading (1 wt%) generated highly dispersed atomic and dimeric Cu species on the non-porous nano-Al<sub>2</sub>O<sub>3</sub> support. Copper sulfate derived catalysts severely reduced the selectivity of furfuryl alcohol from 94.6% to 0.8% and promoted acetalisation reactions instead. On the contrary, sulfur-free copper acetate derived catalysts were found optimal for catalysing this reaction.

The research then focused on enhancing colloiddally synthesised Cu catalysts by incorporating trace-amounts of Pd atoms via galvanic replacement. These materials were referred as single atom alloy catalysts (SAA), as EXAFS confirmed they were atomically dispersed Pd atoms on Cu nanoparticles. These SAA catalysts improved the furfural conversion to furfuryl alcohol compared to the monometallic catalysts, as they presented the advantages of Cu (high selectivity) and Pd (superior activity) monometallic catalysts, without the drawbacks (copper's low activity and palladium's poor selectivity). As a result, SAA proved to be optimal green/atom efficient catalysts.

Finally, the synthesised materials were tested for the hydrogenation of crotonaldehyde. Crotonaldehyde was chosen as it lacked the directing group present in furfural (furan ring), so the catalysts can be examined when the C = O hydrogenation is not specifically preferred. The SAA catalysts improved the normalised catalytic activity by nineteen-fold when compared to the Pd<sub>100</sub> benchmark catalyst, while maintaining the reactive pathway of the Cu nanoparticle host. In essence, the presence of Pd "fast-forwarded" the extent of the reaction. For the wet impregnation monometallic Cu materials, the acetate precursor catalysts (1 and 5 wt%) showed superior activity, while the 5 wt% sulfur-based was the worst.

## Acknowledgements

To begin with, I would like to thank my amazing supervisory team, Dr Georgios Kyriakou, Dr Marta Granollers Mesa and Dr Amin Osatiashtiani for their help over the past three years. I would also like to extend a huge thanks to Dr Georgios Kyriakou, without his and Dr Martin Taylor's supervision and guidance during my bachelor's research on gold nanoparticles, as I probably would not have been on this PhD journey. Also, without Dr Kyriakou's own finesse and style of supervision and expertise, this PhD project would not have been remotely possible. I would also like to express my deepest gratitude to Dr Marta Granollers Mesa for picking up the mantle and spearheading the supervisory team of mine and many others, with her unwavering support. My thanks also go to Dr Amin Osatiashtiani, whose supervision and guidance with the experiments was also vital.

There are many people who I have met and guided me along the way, from current and past EBRI and CEAC colleagues. I am sure it would be impossible to name everyone, but my sincerest thanks go out to all of you. Next, I would like to thank Drs Amin Osatiashtiani, Jinesh C. Manayil, Mark A. Isaacs and Christopher M. A. Parlett for their help with the collection of TEM and XPS measurements. I would like to acknowledge the Diamond Light Source and the UK Catalysis Hub for provision of beamtime (proposal numbers: SP19850-1, SP19850-5 and SP19850-6) and especially, Dr Nitya Ramanan and Dr June Callison for their help with both the *ex-situ* and pseudo *in-situ* XAFS experiments. Also, acknowledge the Energy Research Accelerator (ERA) for the funding of equipment used in this work and their doctoral training program. Finally, my special thanks go to the past and present PhD students/post-docs at EBRI: Tom, Filipe, Regina, Jorge, Joe, Chris, Costanza, Jinesh, and Iram.

Last but not least, I would like to thank my incredible parents and my brothers who have encouraged me throughout my life and studies.

## Publications

Some of the work presented in this thesis has been published in peer reviewed journals, as listed below:

1. **M. J. Islam**, M. Granollers Mesa, A. Osatiashtiani, M. J. Taylor, J. C. Manayil, C. M. A. Parlett, M. A. Isaacs and G. Kyriakou, The effect of metal precursor on copper phase dispersion and nanoparticle formation for the catalytic transformations of furfural, *Appl. Catal. B*, 2020, **273**, 119062.
2. M. J. Taylor, S. K. Beaumont, **M. J. Islam**, S. Tsatsos, C. A. M. Parlett, M. A. Isaacs and G. Kyriakou, Atom efficient PtCu bimetallic catalysts and ultra dilute alloys for the selective hydrogenation of furfural, *Appl. Catal. B*, 2021, **284**, 119737.
3. **M. J. Islam**, M. Granollers Mesa, A. Osatiashtiani, J. C. Manayil, M. A. Isaacs, M. J. Taylor and G. Kyriakou, PdCu single atom alloys for the hydrogenation of furfural, *Appl. Catal. B*, **Under review**.

## Poster Presentations

1. Title: The effect of Cu in PtCu bimetallic particles for the selective transformation of furfural  
 Authors: Martin J. Taylor, Mohammed J. Islam, Thomas Bryant, Christopher Parlett, Mark Isaacs, Karen Wilson, Adam Lee and Georgios Kyriakou.  
 Conference: UK Catalysis Conference 2018  
 Location: Loughborough University, Loughborough, United Kingdom  
 Date: 3<sup>rd</sup> – 5<sup>th</sup> January 2018
2. Title: The effect of different Cu precursors in the synthesis of Cu monometallic particles for the selective transformation of furfural  
 Authors: Mohammed J. Islam, M. J. Taylor, Amin Osatiashtiani and Georgios Kyriakou  
 Conference: EAS PGRS conference 2018  
 Location: Aston University, Birmingham, United Kingdom  
 Date: 19<sup>th</sup> April 2018
3. Title: The effect copper phase dispersion and nanoparticle formation altered by metal precursor selection for the catalytic hydrogenation of furfural  
 Authors: Mohammed J. Islam, Marta Granollers Mesa, Amin Osatiashtiani, Martin J. Taylor, Jinesh C. Manayil, Christopher M. A. Parlett, Mark A. Isaacs, and Georgios Kyriakou  
 Conference: UK Catalysis Conference 2021  
 Location: Virtual  
 Date: 6<sup>th</sup> – 8<sup>th</sup> January 2021

M. J. Islam, PhD Thesis, Aston University, 2021

## Table of Contents

Thesis Summary .....	2
Acknowledgements .....	3
Publications .....	4
Poster Presentations.....	4
Table of Contents .....	5
List of Abbreviations.....	9
List of Tables .....	11
List of Figures .....	14
Chapter 1 Introduction.....	20
Introduction .....	21
1.1 Catalysis .....	21
1.2 The use of precious metals in industry .....	24
1.3 Adsorption of species .....	26
1.3.1 Hydrogen dissociation.....	27
1.4 Hydrogenation of unsaturated aldehydes .....	28
1.5 Furfural valorisation .....	29
1.6 Crotonaldehyde hydrogenation .....	32
1.7 Single-atom heterogeneous catalysts.....	33
1.8 Deactivation of supported metal catalysts.....	38
1.8.1 Sulfur Poisoning.....	38
1.8.2 Thermal sintering .....	38
1.8.3 Carbon deposition (coking).....	39
1.9 Thesis Aims.....	40
1.10 References .....	41
Chapter 2 Experimental .....	54
2.1 Material synthesis.....	55

2.1.1 Wet impregnation Cu catalyst synthesis .....	55
2.1.2 Colloidal Cu nanoparticle catalyst synthesis.....	55
2.1.3 High loading SAA PdCu catalyst synthesis .....	56
2.1.4 Low loading SAA PdCu catalyst synthesis.....	57
2.1.5 Colloidal Pd nanoparticle catalyst synthesis .....	58
2.2 Material Characterisation .....	59
2.2.1 Powder X-ray diffraction (XRD) .....	59
2.2.2 X-ray photoelectron spectroscopy (XPS) and x-ray excited Auger electron spectroscopy (XAES).....	63
2.2.3 X-ray absorption spectroscopy (XAS).....	68
2.2.4 Inductively coupled plasma optical emission spectroscopy (ICP-OES).....	70
2.2.5 Scanning transmission electron microscopy (STEM).....	72
2.2.6 N <sub>2</sub> Porosimetry .....	74
2.2.7 H <sub>2</sub> -Temperature Programmed Reduction (H <sub>2</sub> -TPR) .....	76
2.2.8 Thermal Gravimetric Analysis with Mass Spectrometry (TGA-MS).....	76
2.3 Catalytic testing .....	77
2.3.1 Hydrogenation of furfural using monometallic Cu catalysts .....	77
2.3.2 Hydrogenation of furfural using single atom alloy catalysts .....	79
2.3.3 Hydrogenation of crotonaldehyde.....	80
2.3.4 Recyclability tests .....	80
2.3.5 Calculations for the catalytic experiments .....	81
2.4 References .....	83
Chapter 3 The effect of metal precursor on copper phase dispersion and nanoparticle formation for the catalytic transformations of furfural. ....	86
3.1 Introduction .....	87
3.2 Characterisation of Cu-based catalysts.....	89
3.2.1 Elemental and Surface Area Analysis.....	89
3.2.2 Powder X-Ray Diffraction (PXRD).....	92

3.2.3 Scanning Transmission Electron Microscopy (STEM) .....	96
3.2.4 X-ray Photoelectron Spectroscopy (XPS) and X-ray excited Auger Electron Spectroscopy (XAES).....	99
3.2.5 X-ray Absorption Spectroscopy (XAS) .....	104
3.3 Catalytic testing .....	108
3.4 Conclusions .....	120
3.5 References .....	121
Chapter 4 PdCu single atom alloys for the selective hydrogenation of furfural .....	129
4.1 Introduction .....	131
4.2 Characterisation of alumina supported catalysts .....	133
4.2.1 PdCu SAA catalysts 12 wt%.....	133
4.2.2 PdCu SAA catalysts 1 wt%.....	145
4.3 Catalytic testing .....	161
4.3.1 PdCu SAA catalysts 12 wt%.....	161
4.3.2 PdCu SAA catalysts 1 wt%.....	162
4.3.3 Spent catalyst characterisation and recycling experiments .....	168
4.4 Conclusions .....	170
4.5 References .....	171
Chapter 5 Single atom alloy and monometallic catalysts for the hydrogenation of crotonaldehyde .....	180
5.1 Introduction .....	181
5.2 Catalytic testing .....	184
5.2.1 Optimisation of the hydrogenation of crotonaldehyde.....	184
5.2.2 PdCu SAA catalysts .....	187
5.2.3 Cu/Al <sub>2</sub> O <sub>3</sub> wet impregnation catalysts.....	198
5.2.4 Catalyst performance against literature.....	201
5.3 Conclusions .....	203
5.4 References .....	204

Chapter 6 Conclusions and Future work.....	210
6.1 Conclusions .....	211
6.1.1 Effect of metal precursors on nanoparticle morphology for the copper catalysed transformation of furfural .....	211
6.1.2 PdCu single atom alloys for the hydrogenation of furfural.....	212
6.1.3 Single-atom alloy and monometallic catalysts for the hydrogenation of crotonaldehyde ....	212
6.2 Future work .....	213
6.3 References .....	215
Chapter 7 Appendices.....	216
7.1 Figures.....	217
7.2 References .....	219

## List of Abbreviations

$\alpha'$ : Modified Auger Parameter

AES: Auger electron spectroscopy

DFT: Density functional theory

EtOH: Ethanol

EXAFS: Extended x-ray absorption fine structure

FCC: Face centered cubic

FFA: Furfuryl alcohol

FDMA: 2-Furaldehyde dimethyl acetal

FID: Flame ionisation detector

FWHM: Full width at half maxima

GC: Gas chromatography

GR: Galvanic replacement

HCP: Hexagonal close packed

ICP-OES: Inductively coupled plasma optical emission spectroscopy

IMFP: Inelastic mean free path

LCF: Linear combination fitting

LH: Langmuir-Hinshelwood

LT-STM: Low temperature scanning tunneling microscopy

MeOH: Methanol

MS: Mass spectrometry

PMMA: Poly(methyl methacrylate)

PSD: Position sensitive detector

PXRD: Powder x-ray diffraction

RPM: Revolutions per minute

SAA: Single atom alloys

SAC: Single atom catalysts

SSA: Specific surface area

STEM: Scanning transmission electron microscopy

THFA: Tetrahydrofurfuryl alcohol

TOF: Turnover frequency

TCD: Thermal conductivity detector

TPR: Temperature programmed reduction

UHV: Ultra-high vacuum

WPPM: Whole powder pattern modelling

XAES: X-ray excited Auger spectroscopy

XAFS: X-ray absorption fine structure

XANES: X-ray absorption near edge structure

XAS: X-ray absorption spectroscopy

XPS: X-ray photoelectron spectroscopy

XRD: X-ray diffraction

## List of Tables

Table 1.5.1 Batch liquid-phase hydrogenation of furfural to furfuryl alcohol (FFA) over non-Cr bimetallic catalysts.....	32
Table 3.2.1. Bulk elemental analysis and surface area measurements. Catalysts synthesised using copper nitrate, copper acetate and copper sulfate pentahydrate were denoted (N), (A) and (S), respectively.....	90
Table 3.2.2 Tabulated crystallite sizes, particle sizes, lattice parameters and bond lengths. Catalysts synthesised using copper nitrate, copper acetate and copper sulfate pentahydrate were denoted (N), (A) and (S), respectively. ....	93
Table 3.2.3. Summarised binding energies for Cu 2p <sub>3/2</sub> , kinetic energies for the Auger Cu L <sub>3</sub> VV transitions, modified Auger parameters for copper catalysts and change in relaxation energy compared to bulk Cu for catalysts and reference materials.....	101
Table 3.2.4 Calculated particle size and dispersion from XPS for the six monometallic catalysts in both their calcined and reduced ( <i>ex-situ</i> ) state.....	102
Table 3.2.5 Cu K edge energies and XANES linear combination fitting.....	104
Table 3.2.6 EXAFS model fitting of reduced <i>ex-situ</i> Cu/Al <sub>2</sub> O <sub>3</sub> catalysts, Cu and CuO reference foil/powder.....	107
Table 3.3.1 Bulk elemental analysis, surface area measurements, Cu crystallite, Cu particle size analysis and EXAFS determined structure. Catalysts synthesised using copper nitrate, copper acetate and copper sulfate pentahydrate were denoted (N), (A) and (S), respectively. ....	108
Table 3.3.2 Summary of blanks and bare support catalytic data for the hydrogenation of furfural. Reaction conditions: 7 h, 50 °C, 1.5 bar and 10 bar of H <sub>2</sub> , 600 RPM, and 30 mg of catalyst. ....	109
Table 3.3.3. Summary of catalytic data for the hydrogenation of furfural using copper catalysts. Reaction conditions: 7 h, 50 °C, 1.5 bar and 10 bar of H <sub>2</sub> , 600 RPM, and 30 mg of catalyst. ....	110
Table 3.3.4 Summary of catalytic data for the acetalization of furfural using sulfate and sulfate-free catalysts. Reaction conditions: 7 h, 50 °C, 1.5 bar, 600 RPM, and 30 mg of catalyst.....	115
Table 3.3.5 Turnover frequencies for the hydrogenation of furfural using copper catalysts. Reaction conditions: 7 h, 50 °C, 1.5 bar and 10 bar of H <sub>2</sub> , 600 RPM, and 30 mg of catalyst. ....	118
Table 3.3.6 Furfural hydrogenation over recycled catalysts. Reaction conditions: 4 h, 50 °C, 10 bar of H <sub>2</sub> and 600 RPM.....	119
Table 4.2.1 Bulk elemental analysis, for the 12 wt% PdCu catalysts determined by ICP-OES...	133

Table 4.2.2 Crystallite size and lattice parameters for the 12 wt% PdCu catalysts .....	136
Table 4.2.3 Summarised binding energies for the Pd 3d <sub>5/2</sub> and Cu 2p <sub>3/2</sub> , kinetic energies for the Auger Cu L <sub>3</sub> VV transitions, surface composition, modified Auger parameters for copper catalysts and change in relaxation energy compared to bulk Cu for the <i>ex-situ</i> reduced 12 wt% catalysts and reference materials.....	139
Table 4.2.4 EXAFS model fitting of the re-oxidised PdCu/Al <sub>2</sub> O <sub>3</sub> catalyst, Pd and Cu reference foils. ....	143
Table 4.2.5 Bulk elemental analysis of the 1 wt% catalysts determined by ICP-OES.....	145
Table 4.2.6 Summary of lattice parameters determined from XRD (WPPM) for the 1% catalysts after being reduced <i>ex-situ</i> at 300 °C for 0.5 h under flowing H <sub>2</sub> . For reference data the following JCPDS cards were used 40836, 05-068, 29-0063 and 46-1215 for Cu, Pd, γ- Al <sub>2</sub> O <sub>3</sub> and δ- Al <sub>2</sub> O <sub>3</sub> ...	149
Table 4.2.7 Pd/Cu crystallite and particle size analysis for the 1 wt% catalysts after being reduced <i>ex-situ</i> at 300 °C for 0.5 h under flowing H <sub>2</sub> .....	152
Table 4.2.8 Summarised binding energies for Pd 3d <sub>5/2</sub> and Cu 2p <sub>3/2</sub> , kinetic energies for the Auger Cu L <sub>3</sub> VV transitions, surface composition, modified Auger parameters for copper catalysts and change in relaxation energy compared to bulk Cu for the <i>ex-situ</i> reduced catalysts and reference materials. ....	154
Table 4.2.9 Pd K edge energies for Pd foil and PdCu catalysts in their reduced and re-oxidised states. ....	157
Table 4.2.10 EXAFS model fitting of the re-oxidised and reduced PdCu/Al <sub>2</sub> O <sub>3</sub> catalysts, Pd and Cu reference foils. ....	158
Table 4.3.1 Summary of the characterisation data for the 12 wt% Cu/Al <sub>2</sub> O <sub>3</sub> and PdCu/Al <sub>2</sub> O <sub>3</sub> catalysts. ....	161
Table 4.3.2 Summary of the characterisation data for the 1 wt% Al <sub>2</sub> O <sub>3</sub> supported catalysts.....	162
Table 4.3.3 Summary of the catalytic data for the hydrogenation of furfural using Pd/Cu catalysts. Reaction conditions: 7 h, 50 °C, 1.5 bar, 600 RPM, and 30 mg of catalyst. ....	163
Table 4.3.4 Summarised energies for the Cu 2p <sub>3/2</sub> and the Auger Cu L <sub>3</sub> VV transitions, surface composition, modified Auger parameters and XPS calculated dispersion for the fresh and spent catalysts. ....	168
Table 4.3.5 Furfural hydrogenation over the recycled catalysts. Reaction conditions: 7 h, 50 °C, 1.5 bar of H <sub>2</sub> and 600 RPM. ....	169

Table 5.2.1 Summary of the catalytic hydrogenation of crotonaldehyde using monometallic Cu and Pd Al <sub>2</sub> O <sub>3</sub> supported catalysts. Reaction conditions: 7 h, 50 °C, 1.5 bar, 600 RPM, and 30mg or 10 mg of catalyst.....	184
Table 5.2.2 Summary of the catalytic hydrogenation of crotonaldehyde using monometallic Cu and Pd Al <sub>2</sub> O <sub>3</sub> supported catalysts. Reaction conditions: 7 h, 50 °C, 1.5 or 10 bar, 600 RPM, and 10 mg of catalyst.....	187
Table 5.2.3 Summary of the characterisation data for the 1 wt% Al <sub>2</sub> O <sub>3</sub> supported catalysts.....	188
Table 5.2.4 Summary of blanks and bare support catalytic data for the hydrogenation of crotonaldehyde. Reaction conditions: 7 h, 50 °C, 1.5 bar, 600 RPM, and 10 mg of catalyst.....	189
Table 5.2.5 Summary of the catalytic data for the hydrogenation of crotonaldehyde using Pd/Cu catalysts. Reaction conditions: 7 h, 50 °C, 1.5 bar, 600 RPM, and 10 mg of catalyst.....	189
Table 5.2.6 Summary of the catalytic data for the hydrogenation of crotyl alcohol using monometallic Pd/Cu catalysts. Reaction conditions: 7 h, 50 °C, 1.5 bar, 600 RPM, and 10 mg of catalyst.....	192
Table 5.2.7 Summarised energies for the Cu 2p <sub>3/2</sub> and the Auger Cu L <sub>3</sub> VV transitions, surface composition, modified Auger parameters and XPS calculated dispersion for the unused and spent catalysts. ....	196
Table 5.2.8 Crotonaldehyde hydrogenation over the recycled catalysts. Reaction conditions: 7 h, 50 °C, 1.5 bar, 600 RPM, and 10 mg of catalyst. ....	197
Table 5.2.9 Bulk elemental analysis, surface area measurements, Cu crystallite, Cu particle size analysis and EXAFS determined structure. Catalysts synthesised using copper nitrate, copper acetate and copper sulfate pentahydrate were denoted (N), (A) and (S), respectively. ....	198
Table 5.2.10 Summary of the catalytic data for the hydrogenation of crotonaldehyde using Cu/Al <sub>2</sub> O <sub>3</sub> catalysts derived from different metal precursors. Reaction conditions: 7 h, 50 °C, 1.5 bar, 600 RPM, and 10 mg of catalyst.....	199

## List of Figures

Fig. 1.1.1 A general exothermic energy profile of the reaction $X + Y \rightarrow Z$ indicating the effect of a catalyst. The catalyst proposes an alternative reaction pathway (given in red) where the rate-determining step has a smaller $E_a$ . The relative thermodynamic stabilities are unchanged [7].	22
Fig. 1.1.2 Schematic representation of a well-known catalytic reaction, the oxidation of carbon monoxide over noble metal catalysts: $CO + \frac{1}{2} O_2 \rightarrow CO_2$ . Redrawn from reference [8].	23
Fig. 1.2.1 Relative abundance of elements in the Earth's upper crust [13].	25
Fig. 1.3.1 Schematic representation of the adsorbing molecule and-surface interactions via physisorption based on the Lennard-Jones potential energy diagram [15].	26
Fig. 1.3.2 Schematic representation of the hydrogen-surface interactions via activated (red dashed line) and non-activated chemisorption (green dotted) routes based on the Lennard-Jones potential energy diagram [15].	27
Fig. 1.4.1 Possible hydrogenation pathways for $\alpha$ , $\beta$ -unsaturated carbonyls	28
Fig. 1.5.1 Reaction scheme for upgrading furfural.	30
Fig. 1.5.2 Schematic 3-dimensional structure of monometallic nanoparticles with their corresponding alloyed nanoparticle.	31
Fig. 1.6.1 Reaction scheme for the hydrogenation of crotonaldehyde.	33
Fig. 1.7.1 Plot of Cu atom dispersion against nanoparticle size. Dispersion was determined assuming the nanoparticles are spherical. The number of Cu atoms on the surface was determined using the area a Cu atom occupies ( $6.80 \text{ \AA}^2$ ) and the surface area of the nanoparticle. The number of atoms below the surface of the nanoparticle was determined by working out the volume of the nanoparticle without the surface atoms. Knowing the radius of the nanoparticle $R_t$ , one can then determine the radius of the bulk $R_b$ , by removing the contribution due to the surface atoms ( $R_b = R_t - \text{atomic diameter Cu atom}$ ). The volume of the bulk is then determined using the volume of a sphere. The number of atoms inside the nanoparticles is then calculated by dividing the volume of the bulk with the volume of a Cu unit cell and since each Cu unit cell contains 4 atoms the number of atoms under the surface of the nanoparticle is known. Dispersion finally calculated by [number of surface atoms divided by (surface atoms + atoms under the surface)] times by 100.	34
Fig. 1.7.2 Publications mentioning “single-atom catalysts” and “single-atom alloys” registered by Web of Science.	35
Fig. 1.7.3 Schematic diagram of $H_2$ dissociation and spillover from isolated Pt atoms onto the Cu surface.	37

Fig. 2.2.1 Bragg diffraction from a cubic crystal lattice [5].	59
Fig. 2.2.2 (a) Schematic of a basic x-ray tube and (b) electron transitions in an atom, which produce the characteristic $K_{\alpha 1}$ , $K_{\alpha 2}$ and $K_{\beta}$ x-rays after core-hole creation.	61
Fig. 2.2.3 Schematic illustration of photo-ionisation of a core electron and the subsequent decay of the core-hole via an Auger transition. $E_{kin}$ = Kinetic energy of photoelectron/Auger electron, $E_B$ = electron binding energy, $\Phi$ = work function and $E_K$ , $E_{L2}$ , $E_{L3}$ represent the binding energy of electrons in the K, $L_2$ and $L_3$ orbitals, respectively.	64
Fig. 2.2.4 Gas-tight cell for air-sensitive samples for XAS experiments.	69
Fig. 2.2.5 Typical ICP-OES schematic showing the process of the sample solution reaching the plasma torch.	70
Fig. 2.2.6 Schematic diagram of the operating principle of scanning transmission electron microscopy. Modified from referenced [24].	73
Fig. 2.3.1 Schematic diagram of the H.E.L. Digicat reactor system	78
Fig. 3.2.1 Isotherm for Cu/Al <sub>2</sub> O <sub>3</sub> catalysts as well as the bare support.	91
Fig. 3.2.2 XRD patterns of (a) reduced and (b) calcined Cu/Al <sub>2</sub> O <sub>3</sub> catalysts synthesised from their respective copper nitrate (N), copper acetate (A) and copper sulfate (S) precursors at loadings of 5 wt% and 1 wt%.	93
Fig. 3.2.3 <i>In-situ</i> XRD diffractograms of (a) 5 wt% Cu/Al <sub>2</sub> O <sub>3</sub> (A), (b) 5 wt% Cu/Al <sub>2</sub> O <sub>3</sub> (S) catalysts and (c) the change in volume-weighted Cu crystallite size in a reductive atmosphere (20% H <sub>2</sub> /80% He gas flow) between 25-700 °C.	95
Fig. 3.2.4 Bright and Dark field STEM images and interplanar spacing measurement of (a) 5 wt% Cu/Al <sub>2</sub> O <sub>3</sub> (A), (b) lattice spacing of 5 wt% Cu/Al <sub>2</sub> O <sub>3</sub> , area of measurement indicated by a yellow line. (c) 5 wt% Cu/Al <sub>2</sub> O <sub>3</sub> (A, low magnification), (d) 5.0 wt% Cu/Al <sub>2</sub> O <sub>3</sub> (N) and (e) 5.0 wt% Cu/Al <sub>2</sub> O <sub>3</sub> (S).	98
Fig. 3.2.5 Copper size distribution for 5 wt% Cu/Al <sub>2</sub> O <sub>3</sub> catalysts after reduction. STEM (histogram) and WPPM result (lognormal distributions).	98
Fig. 3.2.6 High resolution stacked XPS and XAES spectra of the (a) Cu 2p and (b) Cu L <sub>3</sub> VV for the six Cu/Al <sub>2</sub> O <sub>3</sub> catalysts after calcination and reduction at 500 °C and 300 °C respectively. Reference spectra of the Cu, CuO and Cu <sub>2</sub> O [35] are also presented.	100
Fig. 3.2.7 High resolution stacked XPS of the (a) S 2p and (b) N 1s for the six Cu/Al <sub>2</sub> O <sub>3</sub> catalysts after calcination and reduction at 500 °C and 300 °C respectively. Reference spectra of the CuSO <sub>4</sub> and Al <sub>2</sub> (SO <sub>4</sub> ) <sub>3</sub> are also presented.	103

Fig. 3.2.8 Normalised Cu-K edge XANES spectra of six Cu/Al <sub>2</sub> O <sub>3</sub> catalysts (reduced <i>ex-situ</i> ) and reference standards. ....	104
Fig. 3.2.9 EXAFS spectra in (a) k-space (k-weight = 3) and (b) R-space (k-weight = 3) for the <i>ex-situ</i> reduced Cu/Al <sub>2</sub> O <sub>3</sub> catalysts along with Cu and CuO reference foil/powder. A k range of 3.0 – 12.8 Å was used to Fourier transform and analyse the data. ....	106
Fig. 3.3.1 Reaction scheme for upgrading furfural [50]. ....	109
Fig. 3.3.2 The reaction profiles of furfural conversion and furfuryl alcohol selectivity. Reaction conditions: 50 °C, (a) 1.5 bar and (b) 10 bar of H <sub>2</sub> , 600 RPM, 30 mg of catalyst and using supported 1 wt% Cu/Al <sub>2</sub> O <sub>3</sub> catalysts. Solid and dashed lines represent the conversion and selectivity to furfuryl alcohol, respectively. ....	112
Fig. 3.3.3 The reaction profiles of furfural conversion and furfuryl alcohol selectivity. Reaction conditions: 7 h, 50 °C, (a) 1.5 bar and (b) 10 bar of H <sub>2</sub> , 600 RPM, 30 mg of catalyst and using supported 5 wt% Cu/Al <sub>2</sub> O <sub>3</sub> catalysts. Solid and dashed lines represent the conversion and selectivity to furfuryl alcohol, respectively. ....	113
Fig. 3.3.4 Acetalisation of furfural with methanol [15]. ....	114
Fig. 3.3.5 Acetalization of furfural with metal sulfate catalyst. The reaction profiles of furfural conversion and 2-furaldehyde dimethyl acetal (FDMA) selectivity. Reaction conditions: 50 °C, 1.5 bar of H <sub>2</sub> , 600 RPM, 30 mg of catalyst and using CuSO <sub>4</sub> , Al <sub>2</sub> (SO <sub>4</sub> ) <sub>3</sub> and 5 wt% Cu/Al <sub>2</sub> O <sub>3</sub> catalysts at varying states of reduction. ....	116
Fig. 3.3.6 Normalised initial rates of furfural consumption per gram of Cu after the induction period across the (a) 1.0 wt% and (b) 5.0 wt% Cu/Al <sub>2</sub> O <sub>3</sub> catalysts at differing hydrogen pressures. ....	117
Fig. 4.2.1 BET isotherm for the bare Al <sub>2</sub> O <sub>3</sub> support. ....	134
Fig. 4.2.2 XRD diffractograms of reduced <i>ex-situ</i> 12 wt% PdCu species supported on Al <sub>2</sub> O <sub>3</sub> catalysts and the bare support. ....	136
Fig. 4.2.3 High-resolution stacked XPS and XAES spectra of the (a) Cu 2p, (b) Cu L <sub>3</sub> VV and (c) Pd 3d regions for the 12 wt% PdCu catalysts synthesised using different methods after being reduced <i>ex-situ</i> at 300 °C for 0.5 h under flowing H <sub>2</sub> . ....	138
Fig. 4.2.4 XPS derived dispersions for the 12 wt% PdCu catalysts synthesised using different methods after being reduced <i>ex-situ</i> at 300 °C for 0.5 h under flowing H <sub>2</sub> . ....	141
Fig. 4.2.5 Survey XPS spectrum of the <i>ex-situ</i> reduced Pd <sub>1</sub> Cu <sub>98</sub> (12% M3) catalyst with an insert of the Cl 2s and 2p region. ....	142

- Fig. 4.2.6 EXAFS spectra in k-space (k-weight = 3) and (b) R-space (k-weight = 3) for the Pd<sub>1</sub>Cu<sub>158</sub>/Al<sub>2</sub>O<sub>3</sub> catalyst (reduced *ex-situ*) along with Pd and Cu reference foils. Dashed-lined rectangles indicate k ranges over which the data were then Fourier transformed and analysed..... 144
- Fig. 4.2.7 TGA-MS data of the 1 wt% colloiddally capped Cu/Al<sub>2</sub>O<sub>3</sub> catalyst under flowing N<sub>2</sub> with a heating rate of 10 °C min<sup>-1</sup>. ..... 146
- Fig. 4.2.8 H<sub>2</sub> Temperature programmed reduction of Cu, PdCu and Pd catalysts. Gas composition was 5% H<sub>2</sub>/ 95% N<sub>2</sub> v/v at 40 ml/min with a heating rate of approximately 6 °C min<sup>-1</sup>..... 147
- Fig. 4.2.9 XRD diffractograms of the reduced *ex-situ* Pd, Cu and PdCu species supported on Al<sub>2</sub>O<sub>3</sub> catalysts and the bare support. .... 149
- Fig. 4.2.10 SAED images of the reduced *ex-situ* (a) Pd<sub>1</sub>Cu<sub>234</sub> and (b) Pd<sub>100</sub> catalysts supported on Al<sub>2</sub>O<sub>3</sub> after being reduced *ex-situ* at 300 °C for 0.5 h under flowing H<sub>2</sub>..... 150
- Fig. 4.2.11 STEM/TEM images and particle distributions of (a) Cu<sub>100</sub>/Al<sub>2</sub>O<sub>3</sub>, (b) Pd<sub>1</sub>Cu<sub>234</sub> /Al<sub>2</sub>O<sub>3</sub>, (c) Pd<sub>1</sub>Cu<sub>216</sub> /Al<sub>2</sub>O<sub>3</sub>, (d) Pd<sub>1</sub>Cu<sub>53</sub>/Al<sub>2</sub>O<sub>3</sub>, (e) Pd<sub>100</sub>/Al<sub>2</sub>O<sub>3</sub>, and (f) lognormal STEM/TEM size distributions for the catalysts reduced *ex-situ* at 300 °C for 0.5 h under flowing H<sub>2</sub>. ..... 152
- Fig. 4.2.12 High-resolution stacked XPS and XAES spectra of the (a) Cu 2p, (b) Cu L<sub>3</sub>VV and (c) Pd 3d regions for the 1 wt% PdCu catalysts after being reduced *ex-situ* at 300 °C for 0.5 h under flowing H<sub>2</sub>. ..... 153
- Fig. 4.2.13 XPS derived dispersions for the 1 wt% Cu/PdCu/Pd catalysts after being reduced *ex-situ* at 300 °C for 0.5 h under flowing H<sub>2</sub>..... 156
- Fig. 4.2.14 Normalised Pd K edge XANES of the PdCu catalysts in their re-oxidised and reduced state. .... 157
- Fig. 4.2.15 (a) Pseudo *in-situ* EXAFS spectra in k-space (k-weight = 3) and (b) R-space (k-weight = 3) for PdCu/Al<sub>2</sub>O<sub>3</sub> catalysts (reduced *ex-situ* and placed in a gas-tight cell via a glovebox to prevent oxidation) along with Pd and Cu reference foils. Dashed-lined rectangles indicate k ranges over which the data were then Fourier transformed and analysed. .... 160
- Fig. 4.2.16 (a) EXAFS spectra in k-space (k-weight = 3) and (b) R-space (k-weight = 3) for PdCu/Al<sub>2</sub>O<sub>3</sub> catalysts (reduced *ex-situ*) along with Pd and Cu reference foils. Dashed-lined rectangles indicate k ranges over which the data were then Fourier transformed and analysed..... 160
- Fig. 4.3.1 Initial rate of the furfural consumption normalised to Cu and Pd content for 12 wt% PdCu catalyst using different GR methods. The initial rate was determined after the induction period for the Cu-based catalysts. Reaction conditions: 7 h, 50 °C, 1.5 bar of H<sub>2</sub>, 600 RPM, 30 mg of catalyst.... 162

- Fig. 4.3.2 The reaction profiles of (a) furfural conversion, selectivity and (b) carbon balance. Reaction conditions: 7 h, 50 °C, 1.5 bar of H<sub>2</sub>, 600 RPM, 30 mg of catalyst. Solid lines, dashed, and dotted lines represent conversion, selectivity, and carbon balance, respectively. .... 164
- Fig. 4.3.3 (a) Initial rate of the furfural consumption normalised to Cu and Pd content. The initial rate was determined after the induction period for the Cu-based catalysts. (b) Furfuryl alcohol production over time normalised to the majority nanoparticle metal. Reaction conditions: 7 h, 50 °C, 1.5 bar of H<sub>2</sub>, 600 RPM, 30 mg of catalyst..... 165
- Fig. 4.3.4 Turnover frequency of both Cu and Pd surface atoms for the catalysts determined from the XPS calculated dispersion. Reaction conditions: 7 h, 50 °C, 1.5 bar of H<sub>2</sub>, 600 RPM, 30 mg of catalyst..... 166
- Fig. 4.3.5 Furfuryl alcohol/metal mole ratio per hour or called productivity of catalysts from this work and various catalysts found in the literature under low to moderate conditions (<140 °C and <20 bar). Square bracketed Roman numerals [i], [ii], [iii], [iv], [v], [vi], [vii], [viii], [ix], [x], [xi], [xii], [xiii], [xiv] and [xv] represent references [68], [69], [1], [6], [67], [4], [3], [70], [71], [2], [66], [72], [73], [74] and [48], respectively. Log<sub>10</sub> scale is used for the furfuryl alcohol/metal ratio per hour z axis and the colour of the spheres represents which metal is used for the calculation. Pd, Pt, Ru, Ni and Cu represent sphere colours dark grey, red, blue, green, and orange, respectively..... 167
- Fig. 4.3.6 High-resolution stacked XPS and XAES spectra of the (a) Cu 2p and (b) Cu L<sub>3</sub>VV regions for the fresh and spent Pd<sub>1</sub>Cu<sub>216</sub> catalyst. .... 169
- Fig. 5.2.1 Percentage yields of the products formed against time for the monometallic (a) Cu<sub>100</sub> and (b) Pd<sub>100</sub> Al<sub>2</sub>O<sub>3</sub> supported catalysts. Reaction conditions: 7 h, 50 °C, 1.5 bar, 600 RPM, and 30mg or 10 mg of catalyst..... 185
- Fig. 5.2.2 Percentage yields of the products formed against time for the monometallic (a) Cu<sub>100</sub> and (b) Pd<sub>100</sub> Al<sub>2</sub>O<sub>3</sub> supported catalysts. Reaction conditions: 7 h, 50 °C, 1.5 bar or 10 bar, 600 RPM, and 10 mg of catalyst..... 187
- Fig. 5.2.3 Reaction scheme for the transformation of crotonaldehyde..... 188
- Fig. 5.2.4 The reaction profiles of (a) crotonaldehyde conversion and (b) yield of major products across monometallic and bimetallic catalysts. Reaction conditions: 7 h, 50 °C, 1.5 bar, 600 RPM, and 10 mg of catalyst..... 190
- Fig. 5.2.5 (a) Yield of butanal vs conversion and (b) yield of butanol vs yield of butanal reaction graphs. Reaction conditions: 7 h, 50 °C, 1.5 bar, 600 RPM, and 10 mg of catalyst..... 191

Fig. 5.2.6 The reaction profiles of (a) crotyl alcohol conversion and (b) product selectivity across the monometallic catalysts. Reaction conditions: 7 h, 50 °C, 1.5 bar, 600 RPM, and 10 mg of catalyst. ....	193
Fig. 5.2.7 Initial rate of the crotonaldehyde consumption normalised to Cu and Pd content. The initial rate was determined after the induction period for the Cu-based catalysts. Reaction conditions: 7 h, 50 °C, 1.5 bar, 600 RPM, and 10 mg of catalyst. ....	194
Fig. 5.2.8 Turnover frequency of both Cu and Pd surface atoms for the catalysts determined from the XPS calculated dispersion. Reaction conditions: 7 h, 50 °C, 1.5 bar, 600 RPM, and 10 mg of catalyst. ....	195
Fig. 5.2.9 High-resolution stacked XPS and XAES spectra of the (a) Cu 2p and (b) Cu L <sub>3</sub> VV regions for the unused and spent Pd <sub>1</sub> Cu <sub>216</sub> catalyst. ....	196
Fig. 5.2.10 The reaction profiles of (a) crotonaldehyde conversion and (b) yield of major products across the 1 wt% and 5 wt% Cu/Al <sub>2</sub> O <sub>3</sub> wet impregnation catalysts. Reaction conditions: 7 h, 50 °C, 1.5 bar, 600 RPM, and 10 mg of catalyst. ....	200
Fig. 5.2.11 (a) Normalised initial rates of crotonaldehyde consumption per gram of Cu and TOF (b) Normalised initial rates of butanal consumption after the induction period across the 1 wt% and 5 wt% Cu/Al <sub>2</sub> O <sub>3</sub> catalysts. ....	201
Fig. 5.2.12 TOF* (h <sup>-1</sup> ) of catalysts from this work and various catalysts found in the literature under low to moderate conditions (<150 °C and <20 bar). TOF* calculation took in consideration both metal atoms on the surface and in the bulk. Reference represented by the square bracketed Roman numerals [i]=[39], [ii]=[40], [iii]=[20], [iv]=[18], [v]=[26], [vi]=[17], [vii]=[16], [viii]=[41], [ix]=[11], [x]=[42], [xi]=[43], [xii]=[44], [xiii]=[24], [xiv]=[45], [xv]=[46] and [xvi]=[47]. Log <sub>10</sub> scale is used for the TOF*(h <sup>-1</sup> ) z-axis and the colour of the spheres represents which metal is used for the calculation. Pd, Pt, Ir, Ag, Ni, Cu, Ru, Rh, Au and Co represent sphere colours dark grey, blue, red, purple, green, orange, greenish-yellow, yellow, cyan, and brown, respectively. ....	202
Fig. 6.1.1 Schematic representation of the Cu nanostructures observed as the Cu precursor and loading are altered. ....	211
Fig. 7.1.1 MS spectrum 2-furaldehyde dimethyl acetal [1]. ....	217
Fig. 7.1.2 Actual and computed [2-4] MS spectra of crotonaldehyde dimethyl acetal. ....	218

# Chapter 1 Introduction

## Introduction

The global population growth and diminishing energy security requires new technological advancements to fulfil the ever-increasing demand for fuels and chemicals. The future market is searching for reduced reliance on fossil resources due to political and environmental issues prompted by carbon dioxide emissions and the ensuing global warming [1, 2]. To solve, or at least to delay the effects of our current unsustainable energy consumption, various forms of renewable resources have been explored to develop sustainable processes. A renewable non-fossil carbon fuel being investigated is biomass, as it is being considered an ideal alternative to fossil resources due to it being abundant and environmentally friendly [3]. In recent years, much interest has been spent on producing biochemical and biofuels from non-edible lignocellulosic biomass, which is ample in agriculture waste streams and residues [4]. The usage of lignocellulosic biomass circumvents the food against fuel argument and can significantly reduce carbon dioxide emissions.

### 1.1 Catalysis

Catalysis plays a central role in our society. Most of the fuels and chemicals produced in industry have been in contact in one way or another with a catalyst. Such materials play a significant role in green chemistry and are essential in controlling environmental pollution, with selective catalytic routes replacing stoichiometric processes that generate chemical waste problems. One obvious example that is used in everyday life is the three-way automotive catalyst, which converts the severe pollutants from internal combustion engines into nitrogen, carbon dioxide and water. These catalysts can be comprised of Rh/Pt and CeO<sub>2</sub>. If waste gasses were left untreated, large amounts of cancer-causing smog would be formed, which would affect the general populace [5].

Fundamentally, a catalyst is a substance that accelerates a reaction but does not undergo irreversible chemical change itself [6]. This ‘substance’ can range from being an enzyme found in living tissue to inorganic metallic nanoparticles, and accelerates the reaction by lowering the activation energy ( $E_a$ ) required for it to commence, and therefore offering an alternate route for the reaction to proceed at lower energy. Fig. 1.1.1 describes this premise of the reducing on  $E_a$ , where the multiple peaks indicate

different steps of the reaction e.g. reactant adsorption. For example, as catalysts enable a more energy-efficient reaction path, they enable to work at lower temperatures and pressures than without a catalyst. In addition, most reactions do not just produce one single product, which would be preferred, so catalysts' secondary job is to direct the reaction to produce the preferred product or product of interest. This increases the efficiency and selectivity of the process, while reduces costs derived from waste production and/or implementation of complex separation and purification steps downstream.

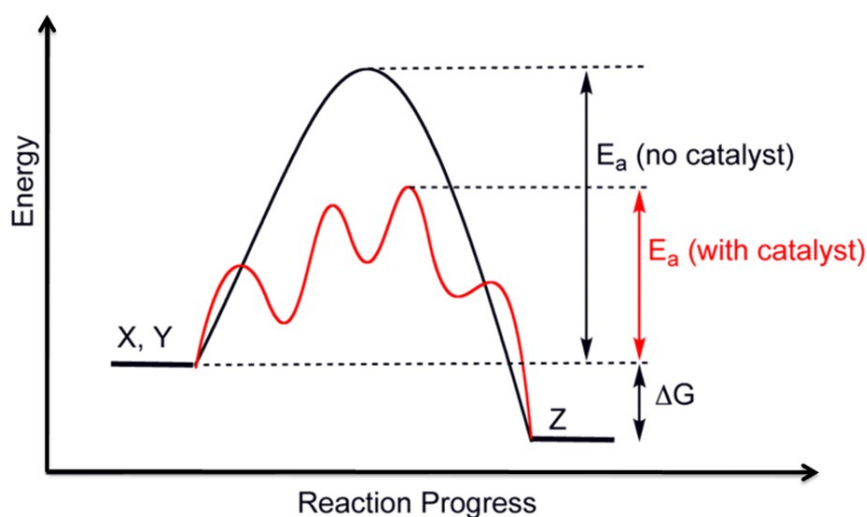


*Fig. 1.1.1 A general exothermic energy profile of the reaction  $X + Y \rightarrow Z$  indicating the effect of a catalyst. The catalyst proposes an alternative reaction pathway (given in red) where the rate-determining step has a smaller  $E_a$ . The relative thermodynamic stabilities are unchanged [7].*

Catalysts are typically broken down into two categories of homogeneous and heterogeneous catalysts (example shown in Fig. 1.1.2). The homogeneous catalyst is defined as existing in the same physical state as the reactants, with all molecules being generally in the liquid or gaseous phase. As both the reactant and the catalyst are in the same phase, there is greater interaction between the two species. This makes the catalyst very atom efficient, so the catalysts have a very high effective concentration, which allows for milder conditions and high selectivity [6]. The greater interactions arise from reactants directly interacting with the metal complexes and selectivity from modifiable ligands complexes which

promotes specific reaction pathways. Examples of such substances include organometallic complexes and enzymes [6]. The main disadvantage of such catalysts is the difficulty in separating and recovering the catalyst from the product, requiring demanding synthetic and purification protocols that affect the overall efficiency.

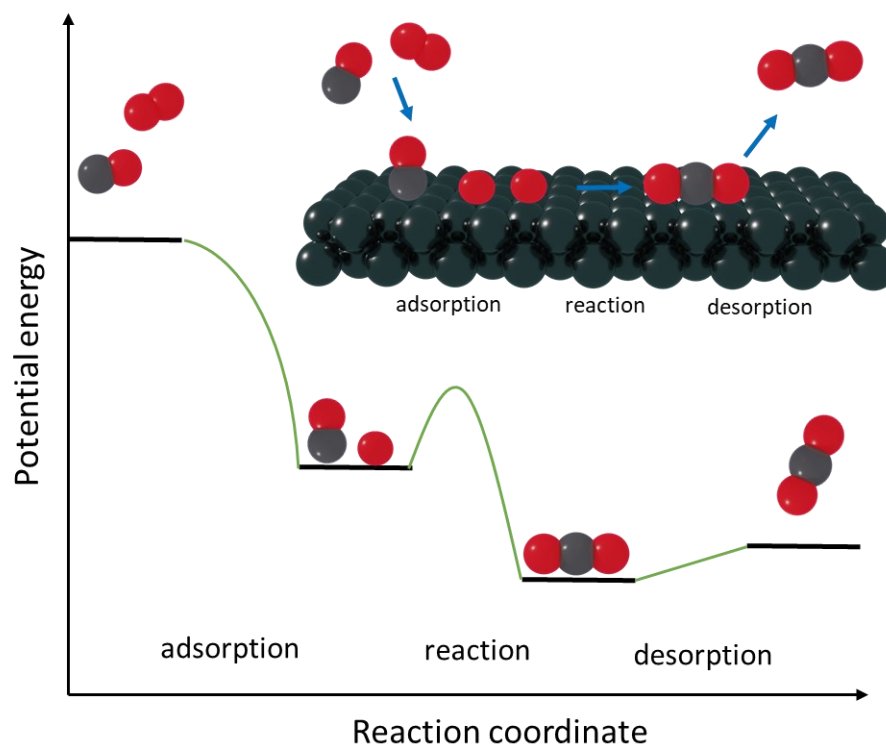


Fig. 1.1.2 Schematic representation of a well-known catalytic reaction, the oxidation of carbon monoxide over noble metal catalysts:  $\text{CO} + \frac{1}{2} \text{O}_2 \rightarrow \text{CO}_2$ . Redrawn from reference [8].

[9]

However, heterogeneous catalysts can be facily synthesised, and easily recovered once the reaction is complete by filtration, centrifugation or magnetism [10]. At industrial level, heterogeneous catalysts are also used in reactors as a packed bed or fluidised bed , so reactants enter and leave converted, while the catalyst remains inside until it is deactivated. This reduces even further the expenditure in separation and recovery steps.

Heterogeneous catalysts typically consist of catalytically active species in solid bulk form, or deposited and dispersed on a high-surface-area supporting material, which can vary in surface area from 200 to 1500  $\text{m}^2 \text{g}^{-1}$  [11]. Alternatively, nanosized catalysts can also be used unsupported or even

deposited themselves on non-porous nanophase supports, but this results in surface areas of 1 to  $50 \text{ m}^2 \text{ g}^{-1}$  [12]. Surface area is an important factor in catalysis, as the larger the surface area the larger the interface of contact between the solid-phase catalyst and the fluid-phase reactants. However, non-porous nano-crystalline supports may be preferred in some instances, as the active phase on the external surface of the support is always exposed and accessible during the reaction. On the contrary, porous materials with relatively larger surface area for reaction are not always fully accessible, as pore blockage or sterical effects may inhibit the access to the internal surface area of the support. Finally, the advantages of nanosized catalyst particles are that their reactivity differs vastly compared to their bulk state counterparts, which are due to various factors such as electronic and quantum size effects [13]. E.g., from discrete energy levels to a continuum in bulk materials. This can result in a very different atom efficiency, and selectivity compared to the catalyst in bulk form.

Due to their high reusability and simple synthesis, heterogeneous catalysts are seen as the greener and more environmentally-friendly choice, though heterogenized homogeneous catalysts have similar advantages. One of the problems of heterogeneous catalysts compared to their homogeneous counterparts is that they sometimes lack the selectivity factor. This is because catalytic reactions usually occur on the surface sites of the catalyst, and in a real catalyst, such sites are not equal, as the catalytic surface is not uniform [14]. Thus, specific sites may stabilise/destabilise some chemical intermediates while other sites may not.

## **1.2 The use of precious metals in industry**

Precious metals [15] and rare earth elements (REEs) [16] take a significant role in catalytic systems for energy conversion and chemical transformations. The integral role of metals and REEs as catalysts include applications such as petroleum refining, fuel cells, automotive catalytic converters and productions of fine chemicals, pharmaceuticals and agrochemicals [17]. Precious metals such as palladium are not only vital to the green chemical industry; they are also used in automotive catalytic converters. REEs are also used in wind turbines, where approximately 2 tonnes of neodymium is required to make a single turbine [18]. However, REE extraction is one of the most environmentally



### 1.3 Adsorption of species

Adsorption of reactants on the catalytic surface is crucial for the reactions to proceed for heterogeneous catalysts. Adsorption can occur in two modes: physisorption and chemisorption. Physisorption, or also called physical adsorption, is a reversible process where the electronic structure of an atom or molecules is slightly distorted upon adsorption [22]. It also refers to the weakest adsorbate-substrate interaction due to van der Waals forces, with typical binding energies of 10-100 meV [22]. From the Lennard-Jones diagram (Fig. 1.3.1) one can see that a shallow well is formed where the attractive forces are dominant and where the van der Waals forces are the strongest. When the adsorbing molecule is moved closer, the potential energy of the interaction is increased as the repulsive forces become dominant due to the overlap of the electron clouds of the surface and the molecule.

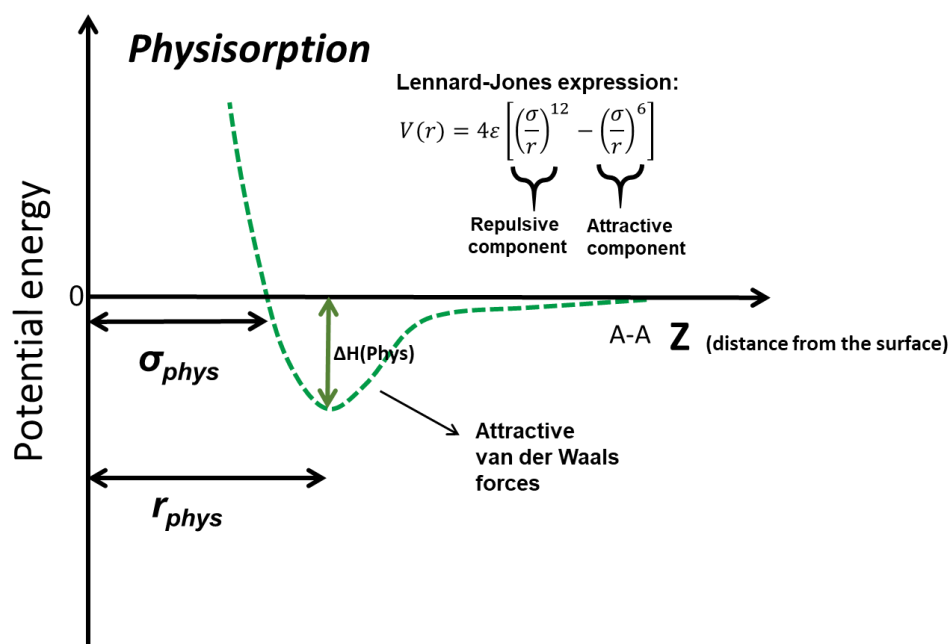


Fig. 1.3.1 Schematic representation of the adsorbing molecule and-surface interactions via physisorption based on the Lennard-Jones potential energy diagram [23], where  $r$  is the distance between the two interacting particles,  $\epsilon$  is the depth potential of the potential well and  $\sigma$  is the distance at which the particle-particle potential energy  $V$  is zero.

Chemisorption or chemical adsorption occurs when an adsorbate forms strong chemical bonds with the substrate atoms. These bonds can either be covalent or ionic, and typical binding energies are in the order of 1-10 eV [22]. This interaction changes the adsorbate's chemical state and, in the case of

chemisorption of molecules, it can occur associatively or dissociatively. Dissociative adsorption occurs when a molecule such as a diatomic is split, and the individual atoms adsorb onto the surface. Associative adsorption can also occur where during the molecule stays intact during adsorption. Chemisorption can also be activated and non-activated (Fig. 1.3.2), and in the activated process the molecule must overcome an energy barrier (requiring energy) before the molecule can adsorb onto the surface, whereas, in a non-activated process, the molecules must overcome a negligible barrier to transfer from a non-activated physisorption interaction to a chemisorption interaction.

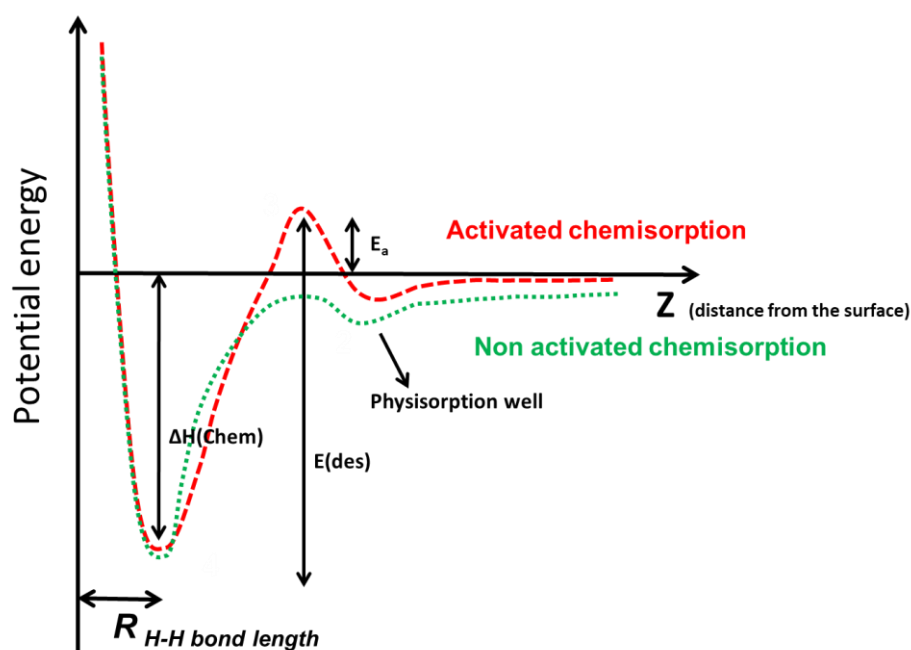


Fig. 1.3.2 Schematic representation of the hydrogen-surface interactions via activated (red dashed line) and non-activated chemisorption (green dotted) routes based on the Lennard-Jones potential energy diagram [23].

### 1.3.1 Hydrogen dissociation

The dissociation of diatomic hydrogen onto the surface is essential for hydrogenation reactions. On low-index surfaces for metals such as Cu [24], Ni [25] and Fe [26], the hydrogen chemisorption is energetically activated (Fig. 1.3.2), and activation energy,  $E_a$ , must be applied to the molecule for the dissociation to take place. So, the dissociation probabilities are relatively small compared to systems with negligible activation energy.

However, on transition metals such as Pd, W and high-index plane Ni and Pt, the dissociative chemisorption is nearly spontaneous (non-activated chemisorption shown in Fig. 1.3.2) with high sticking dissociation probabilities [27]. Nakanishi *et al.* reports that the changes in the activation energy is dependent on whether the hydrogen 1s electrons are repelled by a specific metallic surface [28]. High-index surfaces for Cu have also shown a 0.1 eV difference in the dissociation of hydrogen against low-index terrace sites [24]. However, the process is still activated, unlike Ni and Pt surfaces. Surfaces such as copper and iron cannot dissociate hydrogen at room temperature. This can be overcome by high temperatures, high hydrogen pressures to “force” hydrogen onto the surface, [29] or by addition of a second metal such as a Cu<sub>3</sub>Pt system, where it is shown to be just as active as pure Pt sites [30].

#### 1.4 Hydrogenation of unsaturated aldehydes

Many fine chemicals, especially those used in the flavouring, fragrances [31], and pharmaceutical industry [32, 33] are synthesised by the selective hydrogenation of unsaturated carbonyl intermediates. The hydrogenation of  $\alpha$ ,  $\beta$ -unsaturated carbonyls (Fig. 1.4.1) to their saturated counterparts is relatively easy, as the hydrogenation of the C = C bond is thermodynamically favourable; thus, much effort has been directed at reducing the carbonyl group [33, 34]. However, it is reported that if the hydrogenation of the unsaturated ketones is attempted, saturated ketones will be likely formed [33].

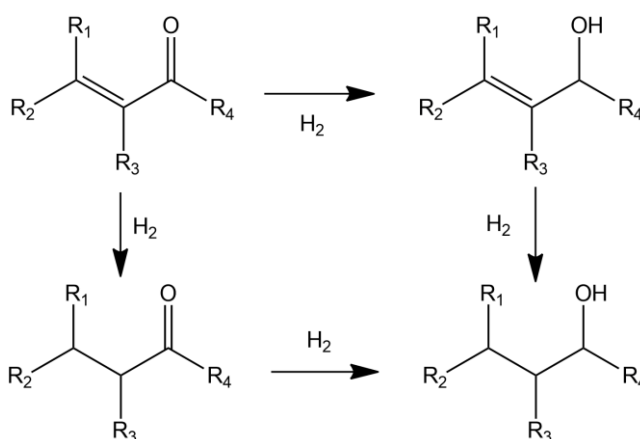


Fig. 1.4.1 Possible hydrogenation pathways for  $\alpha$ ,  $\beta$ -unsaturated carbonyls

Selective hydrogenations have in the past been achieved with stoichiometric quantities of reducing agents such as metal hydrides [35].  $\text{LiAlH}_4$  has been utilised for the selective reduction of cinnamaldehyde to cinnamic alcohol at 99% selectivity [36]. However, these methods are only viable for small scale production of high-priced chemicals, as the reagents are costly [33]. Thus, subsequent research efforts have been focussed on homogeneous and heterogeneous catalysts, with the latter studied more intensively. Thus, the pioneering work on the hydrogenation of molecules like vanillin by Adams *et al.* [37] on Pt and Pd black catalysts in the 1920s paved the way for the current state-of-the art heterogeneous catalysts.

### 1.5 Furfural valorisation

Furfural is considered one of the top 30 biomass-derived platform by the U.S. Department of Energy by numerous factors such as the raw material, processing cost, market potential and technical complexity. Furfural,  $\alpha$ ,  $\beta$ -unsaturated carbonyl is primarily synthesised by the hydrolysis and dehydration of xylan, which exists in ample quantities in hemicellulose; which was first industrialised in 1921 by the Quaker Oat Company [38].

The majority of furfural consumption (62%) is used to synthesise furfuryl alcohol [39] (Fig. 1.5.1). Furfuryl alcohol is industrially produced by the selective hydrogenation of furfural in both liquid and gas phase using Cu-based catalysts, with Cu-Cr being the most dominantly used catalyst [40-42]. However, the problem with using chromate catalysts is that it causes severe environmental problems due to its high toxicity and requires harsh reaction conditions to function commercially. Consequently, many chromium-free catalysts have been researched for furfural hydrogenation for both gas and liquid phase reactions.

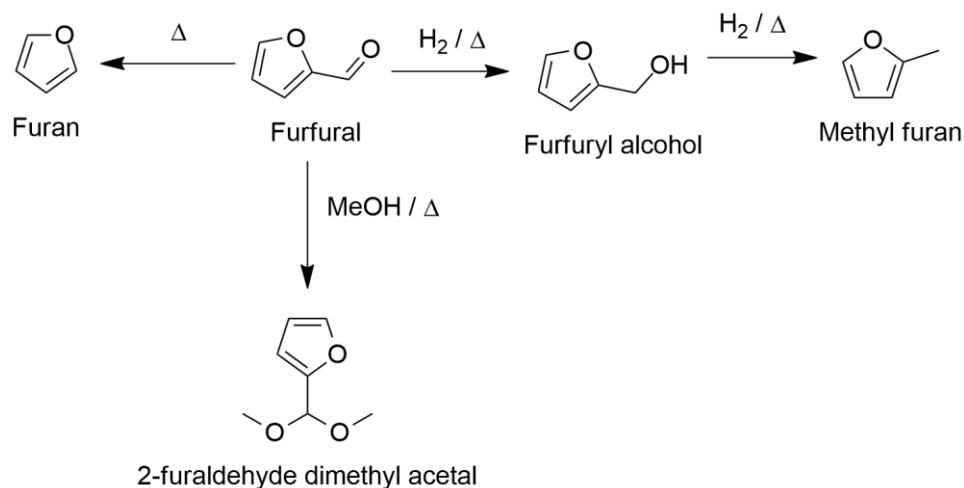


*Fig. 1.5.1 Reaction scheme for upgrading furfural.*

There has been extensive research on numerous more environmentally friendly metallic active sites (Cu, Pt, Pd, Ru, Rh, Co, Zn and Ni) that have been discussed both theoretically and experimentally in both liquid and gas-phase reactions. The advantages of using Pt over commonly used and researched metallic elements such as Cu, Co and Ni [43-48] are that Pt sites offer higher selectivity towards furfuryl alcohol, while functioning at significantly lower reaction conditions [12]. The reaction conditions involved are milder temperatures and pressures, which are both costly factors in large-scale commercial operations. Elements such as platinum can readily dissociatively adsorb diatomic hydrogen [28], which is, unfortunately, the rate-limiting step for hydrogenation reactions using solely copper catalysts. Alternatives to platinum such as palladium have been mainly used in hydrogenation reactions, in both heterogeneous and homogeneous catalysis, and often thought of as the industry standard for such reactions [49]. Unfortunately, it has been reported that Pd has certain selectivity towards one of the side products, methyl furan; but still can perform the catalysis at milder conditions than Cu [3, 50, 51]. Base metal Ni catalysts have lower activity but similar selectivity to Pd [52] with the selectivity shifting towards decarbonylation pathways at high temperatures [45]. Both Pt and Pd are precious metals and active towards the production of furfuryl alcohol, However, crafting catalysts solely on such elements are not sustainable in terms of cost. Therefore, engineering materials with low precious metal content are of critical importance.

Recent progress in the transformation of furfural into furfuryl alcohol (FFA) using heterogeneous catalysts is summarised in Table 1.5.1 and illustrated catalytically active nanoparticles in Fig. 1.5.2. Table 1.5.1 also shows that many bimetallic chromium-free heterogeneous catalysts have been explored to find an efficient environment-friendly alternative to chromium-based catalysts.

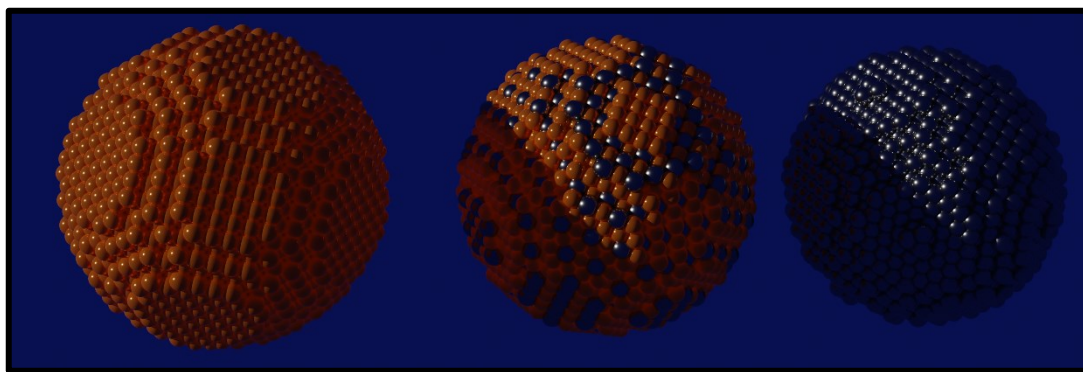


Fig. 1.5.2 Schematic 3-dimensional structure of monometallic nanoparticles with their corresponding alloyed nanoparticle (left to right).

For example, Merlo *et al.* investigated Pt-Sn bimetallic catalysts for the formation of furfuryl alcohol [53]. They reported a 96.2% selectivity and 100% conversion in 8 hours. The study, also optimised the Pt and Sn composition to Sn/Pt = 0.3. A comparison of the catalytic activities of Sn and Ge as the second metal for Pt-based bimetallic catalysts was also investigated by Merlo *et al.* [54]. It was observed that the subsequent conversion of Pt/SiO<sub>2</sub>, PtGe(0.2)/SiO<sub>2</sub> and PtSn(0.2)/ SiO<sub>2</sub> were 46%, 42% and 99%, respectively. Increasing the concentration of Ge to PtGe (0.6) was found to increase the catalytic activity to 74%. These datasets demonstrated the importance of the right composition of metals to exploit the advantages of using bimetallic catalysts.

Table 1.5.1 Batch liquid-phase hydrogenation of furfural to furfuryl alcohol (FFA) over non-Cr bimetallic catalysts.

Catalyst	Solvent	H <sub>2</sub> pressure (Bar)	T (°C)	Time (h)	Conversion (%)	FFA selectivity (%)	FFA yield (%)	Ref.
<i>Pd-Cu/Al<sub>2</sub>O<sub>3</sub></i>	H <sub>2</sub> O	20	90	6	94	56	-	[55]
<i>Pd-Cu/MgO</i>	H <sub>2</sub> O	8	130	1.5	98.5	93	-	[56]
<i>Pd-Cu/C</i>	H <sub>2</sub> O	6	120	0.42	100	91.2	-	[56]
<i>Pd-Ir/SiO<sub>2</sub></i>	H <sub>2</sub> O	80	27	1	61	67	-	[57]
<i>Pt-Co/C</i>	2-Propanol	10	50	5	90	-	90	[58]
<i>Pt-Ge/SiO<sub>2</sub></i>	2-Propanol	10	100	8	42	-	-	[54]
<i>Pt-Sn/SiO<sub>2</sub></i>	2-Propanol	10	100	8	100	96.2	-	[53]
<i>Pt-Sn/TiO<sub>2</sub>-ZrO<sub>2</sub></i>	Ethanol	50	130	8	98.3	47.8	-	[59]
<i>Pt-Re/TiO<sub>2</sub>-ZrO<sub>2</sub></i>	Ethanol	50	130	8	100	95.7	-	[59]
<i>Pt-In/TiO<sub>2</sub>-ZrO<sub>2</sub></i>	Ethanol	50	130	8	73.3	74.9	-	[59]
<i>Pt-Cu/γ-Al<sub>2</sub>O<sub>3</sub></i>	Methanol	20	150	12	100	100	-	[60]
<i>Pt<sub>38</sub>-Cu<sub>62</sub>/γ-Al<sub>2</sub>O<sub>3</sub></i>	Methanol	1.5	50	7	47.6	90.8	-	[61]
<i>Pt<sub>38</sub>-Cu<sub>62</sub>/γ-Al<sub>2</sub>O<sub>3</sub></i>	Methanol	10	50	7	90.9	97.9	-	[61]
<i>Pt<sub>38</sub>-Cu<sub>62</sub>/γ-Al<sub>2</sub>O<sub>3</sub></i>	Methanol	20	50	7	90	98.1	-	[61]
<i>Cu-Pt</i>	2-Propanol	69	250	1.5	16.4	86.8	-	[52]
<i>Cu-Fe oxides</i>	Octane	90	220	4	99.4	-	51.1	[62]
<i>Cu-Co/SBA-15</i>	2-Propanol	20	170	4	99	80	-	[63]
<i>Cu-Co/C</i>	Ethanol	30	140	-	99	97.3	-	[48]
<i>Cu-Ni/MgO</i>	Ethanol	40	150	3	54	99	-	[47]
<i>Cu-Ni/MgAlO</i>	Ethanol	40	150	3	99	80	-	[47]
<i>Cu-Ni/SiO<sub>2</sub></i>	2-Propanol	60	110	-	100	94	-	[64]
<i>CuNiMgAl oxides</i>	Ethanol	10	220	2	84.8	89.4	-	[65]
<i>Ni-Mo-B/Al<sub>2</sub>O<sub>3</sub></i>	Methanol	50	80	3	91.5	95.5	-	[66]
<i>Ni-Fe-B</i>	Ethanol	10	100	4	100	100	-	[67]
<i>Ru-Sn/C</i>	H <sub>2</sub> O	12.5	95	5	91	90	-	[68]
<i>Ir-ReOx/SiO<sub>2</sub></i>	H <sub>2</sub> O	60	50	-	99.9	-	97	[69]

## 1.6 Crotonaldehyde hydrogenation

Crotonaldehyde is another unsaturated aldehyde similar to furfural, which can be derived from soybean oils [40]. Crotonaldehyde is used often as a model compound for unsaturated aldehydes (see Fig. 1.6.1). This is because the absence of a directing group, like the furan ring in furfural, makes the selective hydrogenation of the aldehyde group comparatively more difficult [70]. Consequently, various options have been considered such as sulfur [71-74], NaCl [75], electrophilic sites [34], and ligands [76, 77] that alter the electronic/steric environment of the catalytic surface. All these methods attempt to change the adsorption mode of the unsaturated aldehyde such that C = O adsorption is promoted and the C = C adsorption is hindered.

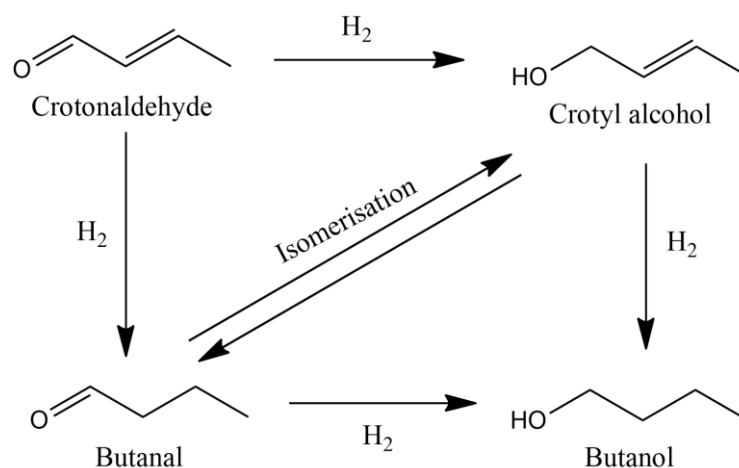


Fig. 1.6.1 Reaction scheme for the hydrogenation of crotonaldehyde.

Therefore, the hydrogenation of the  $C = C$  bond to butanal and then likely to n-butanol cannot be avoided in some catalytic systems (Pt/ $Al_2O_3$  [78], Pd/ $Al_2O_3$  [78], Pd/PEG [79], PdCl<sub>2</sub>(TPPTS)<sub>2</sub> [80] and Cu/ $Al_2O_3$  [74]). Though, n-butanol is also an attractive product as it can be used as a solvent, chemical intermediate and considered as the next generation biofuel due to a 30% higher energy content than ethanol [81].

## 1.7 Single-atom heterogeneous catalysts

Nanoparticles can be shrunk more and more, until they cross a point where they become a few or an isolated atom (not a nanoparticle anymore). In this grey area, the traditional distinctions between homogeneous and heterogeneous catalysts are becoming gradually obscured [82]. The advantage of decreasing the nanoparticle sizes is that atoms below the surface of the nanoparticle typically act as spectator atoms. So are underutilised for catalytic reactions. As the nanoparticle size decreases the number of surface atoms to the number of atoms under the surface increases, thus the dispersion increases (Fig. 1.7.1). As a result, the decrease in nanoparticle size essentially increases the effective concentration of the active material.

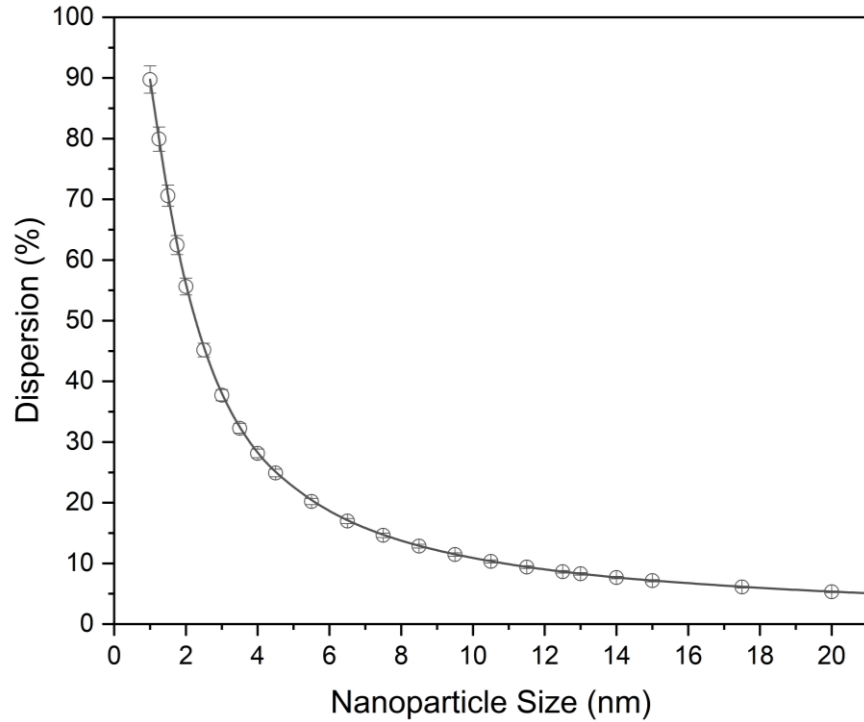


Fig. 1.7.1 Plot of Cu atom dispersion against nanoparticle size. Dispersion was determined assuming the nanoparticles are spherical. The number of Cu atoms on the surface was determined using the area a Cu atom occupies ( $6.80 \text{ \AA}^2$ ) and the surface area of the nanoparticle. The number of atoms below the surface of the nanoparticle was determined by working out the volume of the nanoparticle without the surface atoms. Knowing the radius of the nanoparticle  $R_t$ , one can then determine the radius of the bulk  $R_b$ , by removing the contribution due to the surface atoms ( $R_b = R_t - \text{atomic diameter Cu atom}$ ). The volume of the bulk is then determined using the volume of a sphere. The number of atoms inside the nanoparticles is then calculated by dividing the volume of the bulk with the volume of a Cu unit cell and since each Cu unit cell contains 4 atoms the number of atoms under the surface of the nanoparticle is known. Dispersion finally calculated by [number of surface atoms divided by (surface atoms + atoms under the surface)] times by 100.

There have been several studies considering whether a single atom attached to a support would function as an efficient catalyst [83-85]. Flytzani-Stephanopoulos *et al.* [86] stumbled onto single atoms of Au, present as surface Au-O<sub>x</sub> species functioning as active catalysts for low-temperature water-gas shift reactions. Later work by Flytzani-Stephanopoulos *et al.* [87-89] reported advances in the preparation, characterisation, and catalytic activity of single-atom catalysts for several hydrogenation and oxidation reactions. Such work allowed the field of single atom catalysts to gather much interest over the years (Fig. 1.7.2).

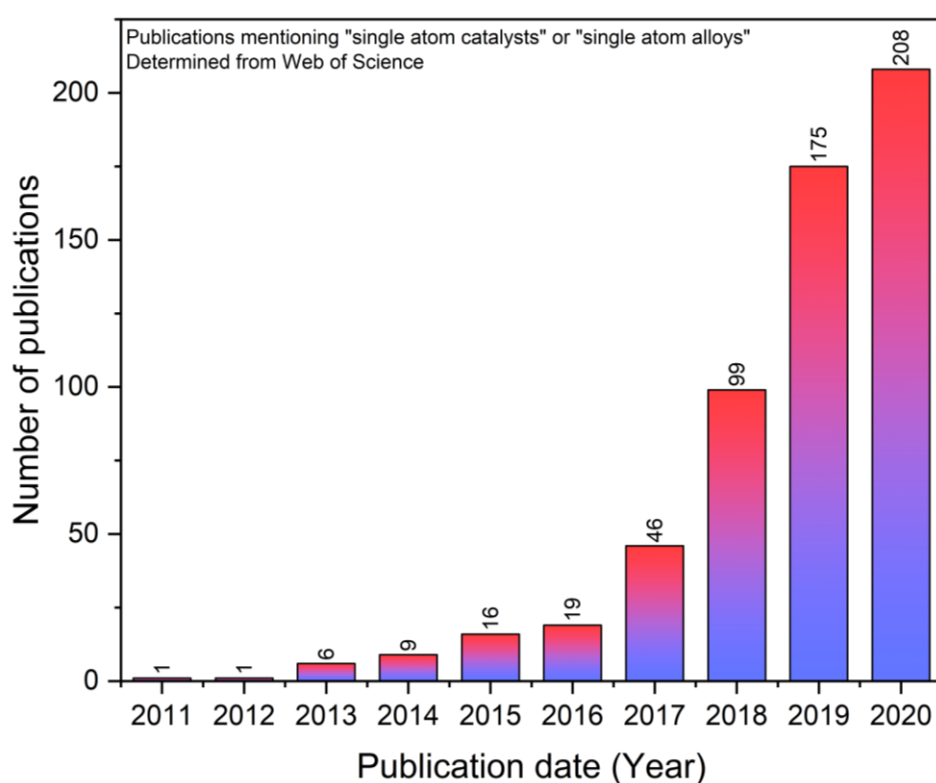


Fig. 1.7.2 Publications mentioning "single-atom catalysts" and "single-atom alloys" registered by Web of Science.

Single-atom catalysts were also found to be highly selective and active compared to their nanoparticle counterparts. Wei *et al.* [90] reported single-atom Pt supported on FeO<sub>x</sub> catalysts for the chemoselective hydrogenation of nitroarenes. The authors reported that their nanoparticle counterparts suffer from low chemoselectivity when more than one reducible groups are present on the target molecule. However, their single-atom catalysts show high activity and high chemoselectivity, even

when the catalyst is reused for a variety of substituted nitroarenes. Specifically, for the hydrogenation of 3-nitrostyrene, Wei *et al.* reported a 20-fold increase in the turnover frequency than the best result found in the literature using the Pt single-atom catalyst with ~99% selectivity. The authors attributed the superior performance to the presence of positively charged platinum atoms and the absence of Pt-Pt metallic bonding, both of which promote the preferential adsorption of nitro groups. The process of creating single-atom catalysts creates a route to temper the reactivity of the very active platinum element. Wei *et al.* took advantage of this by constructing a very selective catalyst with almost trace amounts of precious metal (0.08% Pt).

The whole field of single-atom precious metal catalysts (particularly Pt and Au) has been subject to many initial definitive studies by Flytzani-Stephanopoulos, Sykes and their co-workers [91-93]. A paper by Kyriakou *et al.* [94], reported the creation of a catalyst termed single atom alloys (SAA), in which isolated atoms of Pd deposited on a metallic Cu (111) single crystal, catalysed the selective hydrogenation of acetylene and styrene. Cu was shown to be not very active in its pure state due to its weak hydrogenation activity in dissociating diatomic hydrogen. However, when a small quantity of Pd is added, Cu's hydrogen dissociation capability can be improved [94, 95]. Greater control of the reaction selectivity can also be achieved when using a catalyst designed in this way. The reason for this is that the selectivity of a reaction is most often accomplished by eliminating competitive reactions, which usually require the existence of two or more neighbouring sites. This in turn, improves turnover rate and/or yield for the favoured reaction. Thus, this effect is precisely exploited using single atom alloys for selective hydrogenations. Studies by Kyriakou *et al.* [94, 96] and Pei *et al.* [95] concluded that the conversion of acetylene to ethylene occurs due to H spillover from the single Pd sites to the Cu, where acetylene is adsorbed, and the product is released due to it being weakly adsorbed in the Cu regions. Evidence for this hydrogen spillover has been experimentally observed by Lucci *et al.* [97] on Pt/Cu SAA (see Fig. 1.7.3) where they found Pt atoms in Cu act as both entrance and exit sites for H<sub>2</sub> dissociation and recombination, respectively. With DFT calculations predicting negligible barrier for H<sub>2</sub> dissociation on Pt, which is consistent with the facile dissociative adsorption that was observed [98].

They also interestingly found that the concentration of  $H_2$  desorbing off the surface was higher than the surface coverage of the Pt, indicating the H atoms are spilling over from the Pt sites to the adjacent Cu atom. This confirms the study by Jewels *et al.* [99] previous assignment that H atoms do indeed diffuse across the Cu surface. The single-atom conformation of Pd also gives the catalyst resistance from molecules that adsorb too strongly on two or three-fold sites of the highly active Pd metal. Therefore, the deactivation resistance (e.g. CO resistance) is improved by eliminating those ensembles [100].

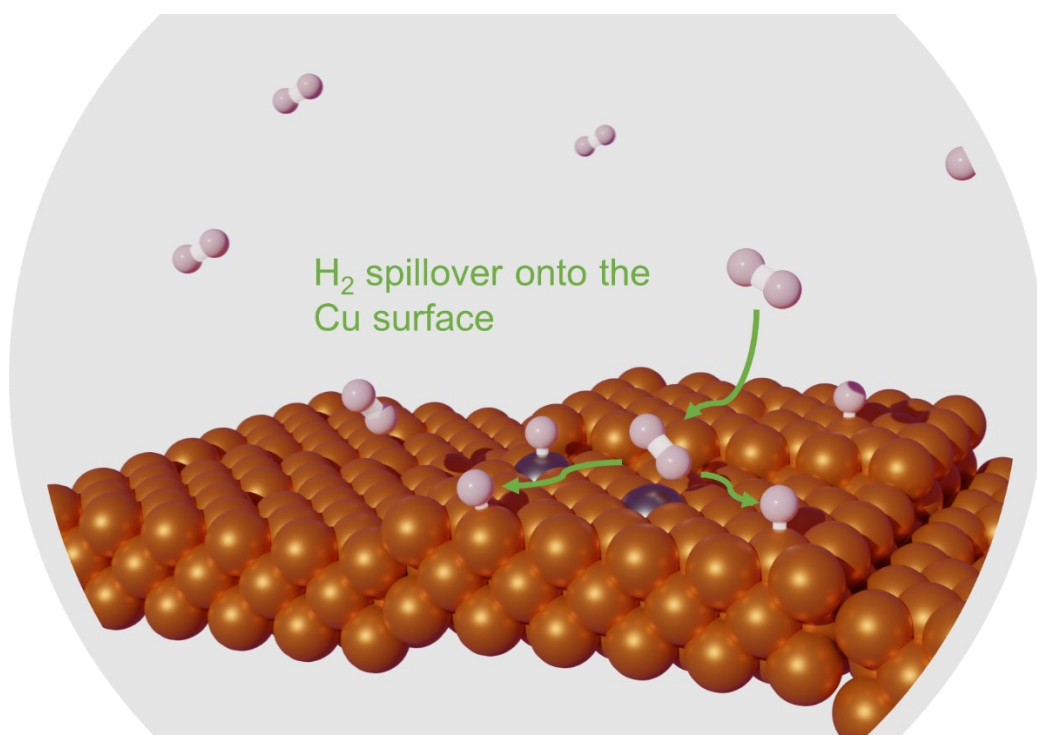


Fig. 1.7.3 Schematic diagram of  $H_2$  dissociation and spillover from isolated Pt atoms onto the Cu surface.

Currently the literature is sparse on single-atom catalysts with only a few reactions and materials being studied. For example, currently, there is no published literature considering the use of single-atom alloy catalysts for the selective hydrogenation of furfural. Therefore, more research into designing different single-atom catalyst compositions and testing of such catalysts in essential reactions will strengthen the literature and unveil the real potential of single-atom catalysts. The crucial challenges outlined by Chen *et al.* [101] for single-atom catalysis are i) characterisation of such catalysts; ii) the strong anchoring of the single-atoms on their supports; iii) reproducible and robust synthesis.

## 1.8 Deactivation of supported metal catalysts

### 1.8.1 Sulfur Poisoning

The original premise of the study of the interaction of sulfur on Cu surfaces is that CO<sub>2</sub> feedstocks usually contain sulfur contaminants. These sulfur atoms adsorb strongly onto the Cu surfaces, blocking the active sites for the desired reactions, which can result in the deactivation of the catalysts [102]. Since sulfur is a common poison for many metallic catalysts [103], the adsorption of the molecule has been intensively studied both experimentally [104] and theoretically [102].

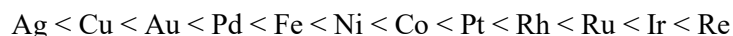
İnoğlu *et al.* [105] observed that the S adsorption energy increases (get weaker) as the sulfur coverage increases, yielding the weakening of the metal-sulfur bond at high coverages. FCC and HCP sites were found to be the most stable sites for sulfur adsorption on Cu surfaces, with FCC sites offering the most stability. Metal d-states have a critical role in explaining the interactions of surface metal atoms with adsorbates. The authors found that surface d-bands were found to generally broaden with increasing sulfur coverage. Consequently, band widening results in a decrease in energy to conserving the d-states. Conversely, if the band narrows it must increase in energy to conserve the d-band state. For most of the highly coordinated sites, it was observed that an adsorbate-induced surface electronic structure modification causes the widening of the surface d-band and the decrease in the d-band centre. Thus, the reactivity of the catalysts is changed by the reduction of the electron-density in the d-states near the Fermi level of the surface, owing to the fundamental fact that sulfur is more electronegative than the metal atoms. Plainly, electron-density is withdrawn from the metal surface due to the difference in electronegativity [106]. Which is important, as the poisoned surfaces will have different electronic properties changing the reactivity of the catalyst.

### 1.8.2 Thermal sintering

Sintering is a major problem for supported catalysts, as the process causes the agglomeration of particles reducing the catalytic activity of the catalyst. Sintered catalysts have a reduced effective concentration of the active material as the reaction typically occurs at the surface. The larger particles will also have a larger quantity of terrace low index surfaces making the surface less reactive.

Consequently, hydrogen dissociation onto the surface will be reduced and in the case of hydrogenation reactions, the activity of the catalysts will be lower.

The major sintering mechanism for metals in the bulk is vacancy diffusion, where it is suggested to be related to the cohesive energy [107]. Hughes [108] gave the following increasing order of stability for metals:



Hughes [108] indicates that silver and copper will be the most susceptible to sintering, mirrored by copper's low Hüttig temperature [109], which is the temperature where the surface atoms become significantly mobile (Hüttig temperature =  $0.3 \times T_m$ , where  $T_m$  is the melting point). Therefore, a copper-based catalyst should be operated at temperatures below 300 °C [107] to halt significant sintering.

### 1.8.3 Carbon deposition (coking)

Possible effects of coking of the metal catalyst include the strong chemisorption of carbon onto the surface as mono or multi-layers. Therefore, blocking the access of reactants to the metallic sites and micro/mesopores. This deactivation mode generally affects catalysts containing Fe, Co and Ni [110]. Copper catalysts are not typically used for Fischer-Tropsch reactions, or processes involving carbonium ion chemistry, so are largely unaffected [107]. Also, copper has a very low activity for breaking C — O bonds or forming C — C, and consequently, wax formation is not a significant problem for CO/H<sub>2</sub> reaction [107]. Such potential problems are further reduced due to copper having to operate at milder temperatures to minimise thermal sintering.

## 1.9 Thesis Aims

The aims of the thesis are to:

- Investigate the effect of three metal precursors in the formation of Cu/Al<sub>2</sub>O<sub>3</sub> catalysts via a simple wet impregnation method. Two different Cu loadings (1 wt% and 5 wt%) will also be investigated, this will give insight into the morphological/electronic changes that occur as the loading is altered. The catalysts will then be tested for the liquid-phase selective hydrogenation of furfural, where the effect of precursor/loading choice on the activity and product selectivity will be understood.
- Investigate, optimise, and characterise the formation of PdCu single atom alloy catalysts synthesised by galvanic replacement techniques. These novel materials will be utilised for the selective hydrogenation of furfural. Consequently, the work will give an understanding of the promotional effect of isolated Pd atoms compared to their Cu and Pd monometallic counterparts.
- Investigate the adoption of the catalysts synthesised throughout this thesis for hydrogenation of crotonaldehyde. The change of the reactant molecule will quantify possible changes in selectivity of the catalysts in the absence of directing groups unlike those present in furfural (furan ring).

## 1.10 References

- [1] D.M. Alonso, J.Q. Bond, J.A. Dumesic, Catalytic conversion of biomass to biofuels, *Green Chem.*, 12 (2010) 1493-1513.
- [2] J.H. Clark, V. Budarin, F.E.I. Deswarte, J.J.E. Hardy, F.M. Kerton, A.J. Hunt, R. Luque, D.J. Macquarrie, K. Milkowski, A. Rodriguez, O. Samuel, S.J. Tavener, R.J. White, A.J. Wilson, Green chemistry and the biorefinery: A partnership for a sustainable future, *Green Chem.*, 8 (2006) 853-860.
- [3] X. Li, P. Jia, T. Wang, Furfural: A Promising Platform Compound for Sustainable Production of C4 and C5 Chemicals, *ACS Catal.*, 6 (2016) 7621-7640.
- [4] Y. Sun, J. Cheng, Hydrolysis of lignocellulosic materials for ethanol production: a review, *Bioresour. Technol.*, 83 (2002) 1-11.
- [5] W.L. Beeson, D.E. Abbey, S.F. Knutsen, Long-term concentrations of ambient air pollutants and incident lung cancer in California adults: results from the AHSMOG study. *Adventist Health Study on Smog, Environ. Health Perspect.*, 106 (1998) 813-823.
- [6] P. Atkins, J.d. Paula, J. Keeler, *Atkins' Physical Chemistry*, 11 ed., Oxford University Press 2017.
- [7] Smokefoot, Energy profile diagram demonstrating the effect of a catalyst, *Wikimedia Commons*, 2013, pp. An energy profile diagram demonstrating the effect of a catalyst for the generic exothermic reaction of  $X + Y \rightarrow Z$ . The catalyst offers an alternate reaction pathway (shown in red) where the rate determining step has a smaller  $\Delta G^\ddagger$ . The relative thermodynamic stabilities remain the same.
- [8] J.W. Niemantsverdriet, *Microscopy and Imaging, Spectroscopy in Catalysis*, Wiley-VCH Verlag GmbH & Co. KGaA, Weinheim, Germany, 2007.

- [9] Z.R. Ismagilov, M.A. Kerzhentsev, Fluidized bed catalytic combustion, *Catal. Today*, 47 (1999) 339-346.
- [10] S. Hu, Y. Guan, Y. Wang, H. Han, Nano-magnetic catalyst KF/CaO-Fe<sub>3</sub>O<sub>4</sub> for biodiesel production, *Applied Energy*, 88 (2011) 2685-2690.
- [11] W. Yang, T.-P. Fellingner, M. Antonietti, Efficient Metal-Free Oxygen Reduction in Alkaline Medium on High-Surface-Area Mesoporous Nitrogen-Doped Carbons Made from Ionic Liquids and Nucleobases, *J. Am. Chem. Soc.*, 133 (2011) 206-209.
- [12] M.J. Taylor, L.J. Durndell, M.A. Isaacs, C.M.A. Parlett, K. Wilson, A.F. Lee, G. Kyriakou, Highly selective hydrogenation of furfural over supported Pt nanoparticles under mild conditions, *Appl. Catal. B*, 180 (2016) 580-585.
- [13] R.C. Jin, The impacts of nanotechnology on catalysis by precious metal nanoparticles, *Nanotechnol. Rev.*, 1 (2012) 31-56.
- [14] A. Wang, J. Li, T. Zhang, Heterogeneous single-atom catalysis, *Nature Reviews Chemistry*, 2 (2018) 65-81.
- [15] T. Muroi, *Role of Precious Metal Catalysts, Noble Metals*, 2012.
- [16] K. Krishna, A. Bueno-López, M. Makkee, J.A. Moulijn, Potential rare earth modified CeO<sub>2</sub> catalysts for soot oxidation: I. Characterisation and catalytic activity with O<sub>2</sub>, *Appl. Catal. B*, 75 (2007) 189-200.
- [17] C.V.S. Almeida, D.S. Ferreira, H. Huang, A.C. Gaiotti, G.A. Camara, A.E. Russell, K.I.B. Eguiluz, G.R. Salazar-Banda, Highly active Pt<sub>3</sub>Rh/C nanoparticles towards ethanol electrooxidation. Influence of the catalyst structure, *Appl. Catal. B*, 254 (2019) 113-127.

- [18] C.C. Pavel, R. Lacal-Arántegui, A. Marmier, D. Schöler, E. Tzimas, M. Buchert, W. Jenseit, D. Blagoeva, Substitution strategies for reducing the use of rare earths in wind turbines, *Resour. Policy*, 52 (2017) 349-357.
- [19] EWI, Rare Earth Materials -China's Role and Emerging Sources, 2011.
- [20] J.S. Kargel, Market Value of Asteroidal Precious Metals in an Age of Diminishing Terrestrial Resources, *Engineering, Construction, and Operations in Space V1996*, pp. 821-829.
- [21] J.B.H. Gordon B. Haxel, and Greta J. Orris, Relative abundance of elements in the Earth's upper crust, Fact Sheet 087-02, U.S. Geological Survey, 2002, pp. Abundance (atom fraction) of the chemical elements in Earth's upper continental crust as a function of atomic number. The rarest elements in the crust (shown in yellow) are the most dense. These are precious gold and the platinum group metals. They were further rarefied in the crust by being siderophile (iron-loving) elements, in the Goldschmidt classification of elements, and have thus been depleted from the crust by being relocated into the Earth's core. Their abundance in meteoroid materials is relatively higher. Additionally, tellurium and selenium have been depleted from the crust due to formation of volatile hydrides.
- [22] K. Oura, V.G. Lifshits, A. Saranin, A.V. Zotov, M. Katayama, *Surface Science*, 1 ed., Springer-Verlag Berlin Heidelberg, Germany, Berlin, Heidelberg, 2003.
- [23] J.E. Lennard-Jones, Processes of adsorption and diffusion on solid surfaces, *Trans. Faraday Society*, 28 (1932) 333-359.
- [24] P. Kratzer, B. Hammer, J.K. Nørskov, Geometric and electronic factors determining the differences in reactivity of H<sub>2</sub> on Cu(100) and Cu(111), *Surf. Sci.*, 359 (1996) 45-53.
- [25] C.Y. Lee, A.E. DePristo, Dissociation dynamics of H<sub>2</sub> on Ni(100), Ni(110), and Ni(111) surfaces, *J. Chem. Phys.*, 84 (1986) 485-495.

- [26] H.F. Berger, E. Grösslinger, K.D. Rendulic, Coupling of vibrational and translational energy in the adsorption of H<sub>2</sub> on Fe(100): state-resolved sticking coefficients, *Surf. Sci.*, 261 (1992) 313-320.
- [27] M. Cacciatore, G.D. Billing, Dissociation and atom recombination of H<sub>2</sub> and D<sub>2</sub> on metallic surfaces: A theoretical survey, *Pure Appl. Chem.*, 68 (1996) 1075-1081.
- [28] N.B. Arboleda, H. Kasai, W.A. Diño, H. Nakanishi, Potential Energy of H<sub>2</sub> Dissociation and Adsorption on Pt(111) Surface: First-Principles Calculation, *Jpn. J. Appl. Phys.*, 46 (2007) 4233-4237.
- [29] B. Hammer, J.K. Nørskov, Electronic factors determining the reactivity of metal surfaces, *Surf. Sci.*, 343 (1995) 211-220.
- [30] H.L. Tierney, A.E. Baber, J.R. Kitchin, E.C.H. Sykes, Hydrogen Dissociation and Spillover on Individual Isolated Palladium Atoms, *Phys. Rev. Lett.*, 103 (2009) 246102.
- [31] K.-G. Fahlbusch, F.-J. Hammerschmidt, J. Panten, W. Pickenhagen, D. Schatkowski, K. Bauer, D. Garbe, H. Surburg, Flavors and Fragrances, *Ullmann's Encyclopedia of Industrial Chemistry*.
- [32] K. Weissermel, H.J. Arpe, *Industrial Organic Chemistry*, Wiley 2008.
- [33] P. Gallezot, D. Richard, Selective Hydrogenation of  $\alpha,\beta$ -Unsaturated Aldehydes, *Catal. Rev. Sci. Eng.*, 40 (1998) 81-126.
- [34] M. Luneau, J.S. Lim, D.A. Patel, E.C.H. Sykes, C.M. Friend, P. Sautet, Guidelines to Achieving High Selectivity for the Hydrogenation of  $\alpha,\beta$ -Unsaturated Aldehydes with Bimetallic and Dilute Alloy Catalysts: A Review, *Chem. Rev.*, 120 (2020) 12834-12872.
- [35] J. March, W.G. Cochran, *Advanced Organic Chemistry: Reactions, Mechanisms, and Structure*, Wiley 1992.

- [36] S.-i. Fukuzawa, T. Fujinami, S. Yamauchi, S. Sakai, 1,2-Regioselective reduction of  $\alpha,\beta$ -unsaturated carbonyl compounds with lithium aluminium hydride in the presence of lanthanoid salts, *J. Chem. Soc., Perkin Trans. 1*, (1986) 1929-1932.
- [37] V. Voorhees, R. Adams, The use of the oxides of platinum for the catalytic reduction of organic compounds. I, *J. Am. Chem. Soc.*, 44 (1922) 1397-1405.
- [38] H.J. Brownlee, C.S. Miner, Industrial Development of Furfural, *Ind. Eng. Chem.*, 40 (1948) 201-204.
- [39] K. Yan, G. Wu, T. Lafleur, C. Jarvis, Production, properties and catalytic hydrogenation of furfural to fuel additives and value-added chemicals, *Renew. Sustain. Energy Rev.*, 38 (2014) 663-676.
- [40] F. Ullmann, *Ullmann's encyclopedia of industrial chemistry*, 7th ed., Wiley-VCH ;, Weinheim, Germany ;, 2009.
- [41] D. Liu, D. Zemlyanov, T. Wu, R.J. Lobo-Lapidus, J.A. Dumesic, J.T. Miller, C.L. Marshall, Deactivation mechanistic studies of copper chromite catalyst for selective hydrogenation of 2-furfuraldehyde, *J. Catal.*, 299 (2013) 336-345.
- [42] R. Rao, A. Dandekar, R.T.K. Baker, M.A. Vannice, Properties of Copper Chromite Catalysts in Hydrogenation Reactions, *J. Catal.*, 171 (1997) 406-419.
- [43] S. Sitthisa, T. Sooknoi, Y. Ma, P.B. Balbuena, D.E. Resasco, Kinetics and mechanism of hydrogenation of furfural on Cu/SiO<sub>2</sub> catalysts, *J. Catal.*, 277 (2011) 1-13.
- [44] G. Machado, S. Leon, F. Santos, R. Lourega, J. Dullius, M. Elizabete Mollmann, P. Eichler, *Literature Review on Furfural Production from Lignocellulosic Biomass*, 2016.
- [45] S. Sitthisa, W. An, D.E. Resasco, Selective conversion of furfural to methylfuran over silica-supported NiFe bimetallic catalysts, *J. Catal.*, 284 (2011) 90-101.

- [46] R.S. Rao, R.T.K. Baker, M.A. Vannice, Furfural hydrogenation over carbon-supported copper, *Catal. Lett.*, 60 (1999) 51-57.
- [47] J. Wu, G. Gao, J. Li, P. Sun, X. Long, F. Li, Efficient and versatile CuNi alloy nanocatalysts for the highly selective hydrogenation of furfural, *Appl. Catal. B*, 203 (2017) 227-236.
- [48] Y. Wang, Y. Miao, S. Li, L. Gao, G. Xiao, Metal-organic frameworks derived bimetallic Cu-Co catalyst for efficient and selective hydrogenation of biomass-derived furfural to furfuryl alcohol, *Mol. Catal.*, 436 (2017) 128-137.
- [49] M. Taylor, The Ultra-Selective Hydrogenation of Furfural on PtCu Supported Bimetallic Nanoparticles and on Pt(111) under Ultra-High Vacuum, CEAC & EBRI, Aston University, 2017.
- [50] S. Iqbal, X. Liu, O.F. Aldosari, P.J. Miedziak, J.K. Edwards, G.L. Brett, A. Akram, G.M. King, T.E. Davies, D.J. Morgan, D.K. Knight, G.J. Hutchings, Conversion of furfuryl alcohol into 2-methylfuran at room temperature using Pd/TiO<sub>2</sub> catalyst, *Catal. Sci. Technol.*, 4 (2014) 2280-2286.
- [51] C. Sun, P. Zeng, M. He, X. He, X. Xie, Morphological effect of non-supported copper nanocrystals on furfural hydrogenation, *Catal. Commun.*, 86 (2016) 5-8.
- [52] C. Zhang, Q. Lai, J.H. Holles, Bimetallic overlayer catalysts with high selectivity and reactivity for furfural hydrogenation, *Catal. Commun.*, 89 (2017) 77-80.
- [53] A.B. Merlo, V. Vetere, J.F. Ruggera, M.L. Casella, Bimetallic PtSn catalyst for the selective hydrogenation of furfural to furfuryl alcohol in liquid-phase, *Catal. Commun.*, 10 (2009) 1665-1669.
- [54] A.B. Merlo, V. Vetere, J.M. Ramallo-López, F.G. Requejo, M.L. Casella, Liquid-phase furfural hydrogenation employing silica-supported PtSn and PtGe catalysts prepared using surface organometallic chemistry on metals techniques, *React. Kinet. Mech. Catal.*, 104 (2011) 467-482.

- [55] M. Lesiak, M. Binczarski, S. Karski, W. Maniukiewicz, J. Rogowski, E. Szubiakiewicz, J. Berłowska, P. Dziugan, I. Witońska, Hydrogenation of furfural over Pd–Cu/Al<sub>2</sub>O<sub>3</sub> catalysts. The role of interaction between palladium and copper on determining catalytic properties, *J. Mol. Catal. A: Chem.*, 395 (2014) 337-348.
- [56] K. Fulajtárova, T. Soták, M. Hronec, I. Vávra, E. Dobročka, M. Omastová, Aqueous phase hydrogenation of furfural to furfuryl alcohol over Pd–Cu catalysts, *Appl. Catal. A Gen.*, 502 (2015) 78-85.
- [57] Y. Nakagawa, K. Takada, M. Tamura, K. Tomishige, Total Hydrogenation of Furfural and 5-Hydroxymethylfurfural over Supported Pd–Ir Alloy Catalyst, *ACS Catal.*, 4 (2014) 2718-2726.
- [58] M.G. Dohade, P.L. Dhepe, Efficient hydrogenation of concentrated aqueous furfural solutions into furfuryl alcohol under ambient conditions in presence of PtCo bimetallic catalyst, *Green Chem.*, 19 (2017) 1144-1154.
- [59] B. Chen, F. Li, Z. Huang, G. Yuan, Tuning catalytic selectivity of liquid-phase hydrogenation of furfural via synergistic effects of supported bimetallic catalysts, *Appl. Catal. A Gen.*, 500 (2015) 23-29.
- [60] S. Huang, N. Yang, S. Wang, Y. Sun, Y. Zhu, Tuning the synthesis of platinum-copper nanoparticles with a hollow core and porous shell for the selective hydrogenation of furfural to furfuryl alcohol, *Nanoscale*, 8 (2016) 14104-14108.
- [61] M.J. Islam, M. Granollers Mesa, A. Osatiashtiani, M.J. Taylor, J.C. Manayil, C.M.A. Parlett, M.A. Isaacs, G. Kyriakou, The effect of metal precursor on copper phase dispersion and nanoparticle formation for the catalytic transformations of furfural, *Appl. Catal. B*, 273 (2020) 119062.
- [62] K. Yan, A. Chen, Selective hydrogenation of furfural and levulinic acid to biofuels on the ecofriendly Cu–Fe catalyst, *Fuel*, 115 (2014) 101-108.

- [63] P.M. Sanjay Srivastava, Jigisha K. Parikh, Ajay K. Dalai, S. S. Amritphale, Anup K. Khare, Cr-free Co-Cu/SBA-15 catalysts for hydrogenation of biomass-derived  $\alpha$ -,  $\beta$ -unsaturated aldehyde to alcohol, *Chinese J. Catal.*, 36 (2015) 933-942.
- [64] S.A. Khromova, M.V. Bykova, O.A. Bulavchenko, D.Y. Ermakov, A.A. Saraev, V.V. Kaichev, R.H. Venderbosch, V.A. Yakovlev, Furfural Hydrogenation to Furfuryl Alcohol over Bimetallic Ni-Cu Sol-Gel Catalyst: A Model Reaction for Conversion of Oxygenates in Pyrolysis Liquids, *Top. Catal.*, 59 (2016) 1413-1423.
- [65] C. Xu, L. Zheng, J. Liu, Z. Huang, Furfural Hydrogenation on Nickel-promoted Cu-containing Catalysts Prepared from Hydrotalcite-Like Precursors, *Chin. J. Chem.* 29 (2011) 691-697.
- [66] S. Wei, H. Cui, J. Wang, S. Zhuo, W. Yi, L. Wang, Z. Li, Preparation and activity evaluation of NiMoB/ $\gamma$ -Al<sub>2</sub>O<sub>3</sub> catalyst by liquid-phase furfural hydrogenation, *Particuology*, 9 (2011) 69-74.
- [67] H. Li, H. Luo, L. Zhuang, W. Dai, M. Qiao, Liquid phase hydrogenation of furfural to furfuryl alcohol over the Fe-promoted Ni-B amorphous alloy catalysts, *J. Mol. Catal. A: Chem.*, 203 (2003) 267-275.
- [68] J.J. Musci, A.B. Merlo, M.L. Casella, Aqueous phase hydrogenation of furfural using carbon-supported Ru and RuSn catalysts, *Catal. Today*, 296 (2017) 43-50.
- [69] S. Liu, Y. Amada, M. Tamura, Y. Nakagawa, K. Tomishige, One-pot selective conversion of furfural into 1,5-pentanediol over a Pd-added Ir-ReOx/SiO<sub>2</sub> bifunctional catalyst, *Green Chem.*, 16 (2014) 617-626.
- [70] M. Tamura, K. Tokonami, Y. Nakagawa, K. Tomishige, Selective Hydrogenation of Crotonaldehyde to Crotyl Alcohol over Metal Oxide Modified Ir Catalysts and Mechanistic Insight, *ACS Catal.*, 6 (2016) 3600-3609.

- [71] M.E. Chiu, G. Kyriakou, F.J. Williams, D.J. Watson, M.S. Tikhov, R.M. Lambert, Sulfur, normally a poison, strongly promotes chemoselective catalytic hydrogenation: stereochemistry and reactivity of crotonaldehyde on clean and S-modified Cu(111), *Chem. Commun.*, (2006) 1283-1285.
- [72] M.E. Chiu, D.J. Watson, G. Kyriakou, M.S. Tikhov, R.M. Lambert, Tilt the Molecule and Change the Chemistry: Mechanism of S-Promoted Chemoselective Catalytic Hydrogenation of Crotonaldehyde on Cu(111), *Angew. Chem. Int. Ed.*, 45 (2006) 7530-7534.
- [73] G.J. Hutchings, F. King, I.P. Okoye, M.B. Padley, C.H. Rochester, Modification of Selectivity in the Hydrogenation of Crotonaldehyde Using Cu/Al<sub>2</sub>O<sub>3</sub> Catalysts Modified with Sulfur Compounds: Effect of Sulfur Source, *J. Catal.*, 148 (1994) 464-469.
- [74] G.J. Hutchings, F. King, I.P. Okoye, C.H. Rochester, Influence of sulphur poisoning of copper/alumina catalyst on the selective hydrogenation of crotonaldehyde, *Appl. Catal. A Gen.*, 83 (1992) L7-L13.
- [75] X.-X. Wang, H.-Y. Zheng, X.-J. Liu, G.-Q. Xie, J.-Q. Lu, L.-Y. Jin, M.-F. Luo, Effects of NaCl on Pt/ZrO<sub>2</sub> catalysts for selective hydrogenation of crotonaldehyde, *Appl. Catal. A Gen.*, 388 (2010) 134-140.
- [76] K.R. Kahsar, D.K. Schwartz, J.W. Medlin, Control of Metal Catalyst Selectivity through Specific Noncovalent Molecular Interactions, *J. Am. Chem. Soc.*, 136 (2014) 520-526.
- [77] H. Liu, Q. Mei, S. Li, Y. Yang, Y. Wang, H. Liu, L. Zheng, P. An, J. Zhang, B. Han, Selective hydrogenation of unsaturated aldehydes over Pt nanoparticles promoted by the cooperation of steric and electronic effects, *Chem. Commun.*, 54 (2018) 908-911.
- [78] B.C. Campo, M.A. Volpe, C.E. Gigola, Liquid-Phase Hydrogenation of Crotonaldehyde over Platinum- and Palladium-Based Catalysts, *Ind. Eng. Chem.*, 48 (2009) 10234-10239.

- [79] F.A. Harraz, S.E. El-Hout, H.M. Killa, I.A. Ibrahim, Catalytic hydrogenation of crotonaldehyde and oxidation of benzene over active and recyclable palladium nanoparticles stabilized by polyethylene glycol, *J. Mol. Catal. A: Chem.*, 370 (2013) 182-188.
- [80] K.-C. Tin, N.-B. Wong, R.-X. Li, Y.-Z. Li, J.-Y. Hu, X.-J. Li, Hydrogenation of crotonaldehyde and cinnamaldehyde catalyzed by water-soluble palladium complex, *J. Mol. Catal. A: Chem.*, 137 (1999) 121-125.
- [81] B. Ndaba, I. Chiyanzu, S. Marx, n-Butanol derived from biochemical and chemical routes: A review, *Biotechnology Reports*, 8 (2015) 1-9.
- [82] J.M. Thomas, R. Raja, Mono-, Bi- and Multifunctional Single-Sites: Exploring the Interface Between Heterogeneous and Homogeneous Catalysis, *Top. Catal.*, 53 (2010) 848-858.
- [83] J.M. Thomas, Z. Saghi, P.L. Gai, Can a Single Atom Serve as the Active Site in Some Heterogeneous Catalysts?, *Top. Catal.*, 54 (2011) 588-594.
- [84] S.L. Wegener, T.J. Marks, P.C. Stair, Design Strategies for the Molecular Level Synthesis of Supported Catalysts, *Acc. Chem. Res.*, 45 (2012) 206-214.
- [85] A. Bruix, Y. Lykhach, I. Matolínová, A. Neitzel, T. Skála, N. Tsud, M. Vorokhta, V. Stetsovych, K. Ševčíková, J. Mysliveček, R. Fiala, M. Václavů, K.C. Prince, S. Bruyère, V. Potin, F. Illas, V. Matolín, J. Libuda, K.M. Neyman, Maximum Noble-Metal Efficiency in Catalytic Materials: Atomically Dispersed Surface Platinum, *Angew. Chem. Int. Ed.*, 53 (2014) 10525-10530.
- [86] Q. Fu, H. Saltsburg, M. Flytzani-Stephanopoulos, Active Nonmetallic Au and Pt Species on Ceria-Based Water-Gas Shift Catalysts, *Science*, 301 (2003) 935-938.
- [87] J.M. Thomas, An Exceptionally Active Catalyst for Generating Hydrogen from Water, *Angew. Chem. Int. Ed.*, 50 (2011) 49-50.

- [88] M. Flytzani-Stephanopoulos, Gold Atoms Stabilized on Various Supports Catalyze the Water–Gas Shift Reaction, *Acc. Chem. Res.*, 47 (2014) 783-792.
- [89] F.R. Lucci, J. Liu, M.D. Marcinkowski, M. Yang, L.F. Allard, M. Flytzani-Stephanopoulos, E.C.H. Sykes, Selective hydrogenation of 1,3-butadiene on platinum–copper alloys at the single-atom limit, *Nat. Commun.*, 6 (2015) 8550.
- [90] H. Wei, X. Liu, A. Wang, L. Zhang, B. Qiao, X. Yang, Y. Huang, S. Miao, J. Liu, T. Zhang, FeO<sub>x</sub>-supported platinum single-atom and pseudo-single-atom catalysts for chemoselective hydrogenation of functionalized nitroarenes, *Nat. Commun.*, 5 (2014) 5634.
- [91] Q. Fu, W. Deng, H. Saltsburg, M. Flytzani-Stephanopoulos, Activity and stability of low-content gold–cerium oxide catalysts for the water–gas shift reaction, *Appl. Catal. B*, 56 (2005) 57-68.
- [92] M. Yang, J. Liu, S. Lee, B. Zugic, J. Huang, L.F. Allard, M. Flytzani-Stephanopoulos, A Common Single-Site Pt(II)–O(OH)<sub>x</sub>– Species Stabilized by Sodium on “Active” and “Inert” Supports Catalyzes the Water-Gas Shift Reaction, *J. Am. Chem. Soc.*, 137 (2015) 3470-3473.
- [93] M. Yang, S. Li, Y. Wang, J.A. Herron, Y. Xu, L.F. Allard, S. Lee, J. Huang, M. Mavrikakis, M. Flytzani-Stephanopoulos, Catalytically active Au-O(OH)<sub>x</sub> species stabilized by alkali ions on zeolites and mesoporous oxides, *Science*, 346 (2014) 1498-1501.
- [94] G. Kyriakou, M.B. Boucher, A.D. Jewell, E.A. Lewis, T.J. Lawton, A.E. Baber, H.L. Tierney, M. Flytzani-Stephanopoulos, E.C. Sykes, Isolated metal atom geometries as a strategy for selective heterogeneous hydrogenations, *Science*, 335 (2012) 1209-1212.
- [95] G.X. Pei, X.Y. Liu, X. Yang, L. Zhang, A. Wang, L. Li, H. Wang, X. Wang, T. Zhang, Performance of Cu-Alloyed Pd Single-Atom Catalyst for Semihydrogenation of Acetylene under Simulated Front-End Conditions, *ACS Catal.*, 7 (2017) 1491-1500.

- [96] G. Kyriakou, E.R.M. Davidson, G. Peng, L.T. Røling, S. Singh, M.B. Boucher, M.D. Marcinkowski, M. Mavrikakis, A. Michaelides, E.C.H. Sykes, Significant Quantum Effects in Hydrogen Activation, *ACS Nano*, 8 (2014) 4827-4835.
- [97] F.R. Lucci, M.D. Marcinkowski, T.J. Lawton, E.C.H. Sykes, H<sub>2</sub> Activation and Spillover on Catalytically Relevant Pt–Cu Single Atom Alloys, *J. Phys. Chem. C*, 119 (2015) 24351-24357.
- [98] Q. Fu, Y. Luo, Catalytic Activity of Single Transition-Metal Atom Doped in Cu(111) Surface for Heterogeneous Hydrogenation, *J. Phys. Chem. C*, 117 (2013) 14618-14624.
- [99] A.D. Jewell, G. Peng, M.F.G. Mattera, E.A. Lewis, C.J. Murphy, G. Kyriakou, M. Mavrikakis, E.C.H. Sykes, Quantum Tunneling Enabled Self-Assembly of Hydrogen Atoms on Cu(111), *ACS Nano*, 6 (2012) 10115-10121.
- [100] J. Liu, F.R. Lucci, M. Yang, S. Lee, M.D. Marcinkowski, A.J. Therrien, C.T. Williams, E.C.H. Sykes, M. Flytzani-Stephanopoulos, Tackling CO Poisoning with Single-Atom Alloy Catalysts, *J. Am. Chem. Soc.*, 138 (2016) 6396-6399.
- [101] Y. Chen, Z. Huang, Z. Ma, J. Chen, X. Tang, Fabrication, characterization, and stability of supported single-atom catalysts, *Catal. Sci. Technol.*, 7 (2017) 4250-4258.
- [102] D.R. Alfonso, A.V. Cugini, D.S. Sholl, Density functional theory studies of sulfur binding on Pd, Cu and Ag and their alloys, *Surf. Sci.*, 546 (2003) 12-26.
- [103] M. May, S. Gonzalez, F. Illas, A systematic density functional study of ordered sulfur overlayers on Cu(111) and Ag(111): Influence of the adsorbate coverage, *Surf. Sci.*, 602 (2008) 906-913.
- [104] C.T. Campbell, B.E. Koel, H<sub>2</sub>S/Cu(111): A model study of sulfur poisoning of water-gas shift catalysts, *Surf. Sci.*, 183 (1987) 100-112.

- [105] N. İnoğlu, J.R. Kitchin, Sulphur poisoning of water-gas shift catalysts: site blocking and electronic structure modification, *Mol. Simul.*, 35 (2009) 936-941.
- [106] J.A. Rodriguez, J. Hrbek, Interaction of Sulfur with Well-Defined Metal and Oxide Surfaces: Unraveling the Mysteries behind Catalyst Poisoning and Desulfurization, *Acc. Chem. Res.*, 32 (1999) 719-728.
- [107] M.V. Twigg, M.S. Spencer, Deactivation of supported copper metal catalysts for hydrogenation reactions, *Appl. Catal. A Gen.*, 212 (2001) 161-174.
- [108] R. Hughes, Deactivation of catalysts by R. Hughes, 1 ed., Academic Press (London), London, 1985.
- [109] M.S. Spencer, Stable and metastable metal surfaces in heterogeneous catalysis, *Nature*, 323 (1986) 685.
- [110] C.H. Bartholomew, Carbon Deposition in Steam Reforming and Methanation, *Catal. Rev. Sci. Eng.*, 24 (1982) 67-112.

## Chapter 2 Experimental

## 2.1 Material synthesis

### 2.1.1 Wet impregnation Cu catalyst synthesis

Appropriate amounts of different Cu precursors including  $\text{Cu}(\text{NO}_3)_2 \cdot x\text{H}_2\text{O}$  (Sigma-Aldrich, 99.999%),  $\text{Cu}(\text{CO}_2\text{CH}_3)_2$  (Sigma-Aldrich, 98%) and  $\text{CuSO}_4 \cdot 5\text{H}_2\text{O}$  (Sigma-Aldrich,  $\geq 98.0\%$ ) were dissolved in deionised water (5 mL). The support, nanophase  $\text{Al}_2\text{O}_3$  (1 g, Alfa Aesar, NanoArc™, 99.5%,  $32\text{-}40\text{ m}^2\text{ g}^{-1}$ ) was then impregnated using the Cu solution. The mixture was stirred for 2 h to ensure homogeneity. The resulting mixture was then dried overnight at  $100\text{ }^\circ\text{C}$ . Finally, the obtained solid was pulverised and calcined in air at  $500\text{ }^\circ\text{C}$ ,  $5\text{ }^\circ\text{C min}^{-1}$ , for 4 h.

The synthesised catalysts were then denoted Cu (N), Cu (A) and Cu (S) for the materials synthesised from copper nitrate, copper acetate and copper sulfate precursors, respectively.

### 2.1.2 Colloidal Cu nanoparticle catalyst synthesis

Colloidal Cu nanoparticles were synthesised using a method reported earlier by Kanzaki *et al.* [1]. DL-1-Amino-2-propanol (AmIP, 2.93 mL, 99.9%, Acros Organics) was added to 7.73 mL of ethylene glycol. Cu (II) acetate (0.6811 g, 98%, Sigma-Aldrich) was then added to the mixture, forming a dark-blue solution with sonication. Once the Cu (II) acetate was dissolved, hydrazine monohydrate (1.83 mL, 98%, Alfa Aesar) was added under vigorous stirring (1100 RPM) and was left to react for approximately 24 h at room temperature. The Cu nanoparticle mixture was then precipitated out by adding it to 25 mL of N, N- dimethylacetamide (DMA, 99%, Acros Organics) under gentle stirring. Subsequently, the Cu nanoparticles were collected via centrifugation and then purified using 25 mL of DMA, toluene (HPLC grade, Fisher Chemical) and hexane (HPLC grade, Fisher Chemical). The resulting nanoparticles were then suspended in 10 mL of ethanol by sonication. In the next step,  $\text{Al}_2\text{O}_3$  (9.9 g, 99.5%,  $32\text{-}40\text{ m}^2\text{ g}^{-1}$ , NanoArc™, Alfa Aesar) was impregnated with the nanoparticle solution (6.6 mL) after the support was mixed with 60 mL of ethanol. The ethanol was then evaporated at room temperature. Finally, the obtained  $\text{Cu}_{100}/\text{Al}_2\text{O}_3$  catalyst was calcined at  $300\text{ }^\circ\text{C}$  for 4 h in static air to remove the AmIP capping agent, followed by reduction at  $230\text{ }^\circ\text{C}$  for 3 h under flowing  $\text{H}_2$ .

### 2.1.3 High loading SAA PdCu catalyst synthesis

The same method as mentioned above (section 2.1.2) was used to synthesise the Cu nanoparticles but scaling up the Cu nanoparticle production 4 times as reported by Kanzaki *et al.* [1]. A final Cu loading of 12.5% was obtained.

For the galvanic replacement (GR) procedure four different synthetic methods were used to investigate how changing the GR process affects their catalytic properties:

*Method 1 (0.1 mM HCl solution):* The Cu/Al<sub>2</sub>O<sub>3</sub> catalyst was initially reduced *in-situ* at 230 °C under flowing H<sub>2</sub> for 3 h in a round-bottom flask. The vessel was then cooled to room temperature under flowing H<sub>2</sub>. The gas was then changed to N<sub>2</sub> and the same vessel was then heated to 100 °C and 18 mL distilled water was added, with stirring set to 700 RPM. The desired amount of Pd (II) nitrate hydrate (99.9%, Alfa Aesar) for an atomic Pd:Cu ratio of 1:90 was dissolved in an aqueous 2 mM HCl solution. 2 mL of this solution was then added to the reduced Cu/Al<sub>2</sub>O<sub>3</sub> mixture and allowed to react/reflux for 20 min under an N<sub>2</sub> atmosphere. The resulting mixture was cooled to room temperature where the catalyst was washed with 300 mL of distilled water via vacuum filtration and dried at 60 °C in an oven overnight.

*Method 2 (aqueous conditions and sonication):* The Cu/Al<sub>2</sub>O<sub>3</sub> catalyst was initially reduced *in-situ* at 230 °C under flowing H<sub>2</sub> for 3 h in a round-bottom flask. The vessel was then cooled to room temperature under flowing H<sub>2</sub>. Then, the gas was changed to N<sub>2</sub> and the same vessel was transferred to a preheated 50 °C ultrasonic bath. The desired amount of Pd (II) nitrate hydrate (99.9%, Alfa Aesar) for an atomic Pd:Cu ratio of 1:90 was dissolved in distilled water. 2 mL of this solution was added to the reduced Cu/Al<sub>2</sub>O<sub>3</sub> mixture and allowed to react for 20 min under an N<sub>2</sub> atmosphere. The subsequent mixture was cooled to room temperature where the catalyst was washed with 300 mL of distilled water via vacuum filtration and dried at 60 °C in an oven overnight.

*Method 3 (2 mM HCl solution):* The Cu/Al<sub>2</sub>O<sub>3</sub> catalyst was initially reduced *in-situ* at 230 °C under flowing H<sub>2</sub> for 3 h in a round-bottom flask. The vessel was then cooled to room temperature under

flowing H<sub>2</sub>. The gas was then changed to N<sub>2</sub> and the same vessel was heated to 100 °C and 18 mL aqueous 2 mM HCl solution was added, with stirring set to 700 RPM. The desired amount of Pd (II) nitrate hydrate (99.9%, Alfa Aesar) for an atomic Pd:Cu ratio of 1:90 was dissolved in an aqueous 2 mM HCl solution. 2 mL of this solution was added to the reduced Cu/Al<sub>2</sub>O<sub>3</sub> mixture and allowed to react/reflux for 20 min under an N<sub>2</sub> atmosphere. The obtained mixture was cooled to room temperature where the catalyst was washed with 300 mL of distilled water via vacuum filtration and dried at 60 °C in an oven overnight.

*Method 4 (0.1 mM HCl solution and sonication):* The Cu/Al<sub>2</sub>O<sub>3</sub> catalyst was initially reduced *in-situ* at 230 °C under flowing H<sub>2</sub> for 3 h in a round-bottom flask. The vessel was then cooled to room temperature under flowing H<sub>2</sub>. The gas was then changed to N<sub>2</sub> and the same vessel was transferred to a preheated 50 °C ultrasonic bath. The desired amount of Pd (II) nitrate hydrate (99.9%, Alfa Aesar) for an atomic Pd:Cu ratio of 1:90 was dissolved in an aqueous 2 mM HCl solution. 2 mL of this solution was added to the reduced Cu/Al<sub>2</sub>O<sub>3</sub> mixture and allowed to react for 20 min under an N<sub>2</sub> atmosphere. The subsequent mixture was cooled to room temperature where the catalyst was washed with 300 mL of distilled water via vacuum filtration and dried at 60 °C in an oven overnight.

The resulting catalysts were denoted Pd<sub>1</sub> Cu<sub>n</sub> (12% MX) where *n* represents the proportion of Cu atoms per each atom of Pd incorporated, which was determined with ICP-OES, while X represents the synthetic method that was used (X = 1 to 4).

#### 2.1.4 Low loading SAA PdCu catalyst synthesis

The PdCu single atom alloy catalysts were synthesised using galvanic replacement [2, 3]. The Cu/Al<sub>2</sub>O<sub>3</sub> catalyst was initially reduced *in-situ* at 230 °C under flowing H<sub>2</sub> for 3 h in a round-bottom flask. The vessel was then cooled to room temperature under flowing H<sub>2</sub>. The gas was then changed to N<sub>2</sub> and the same vessel was heated to 100 °C and 18 mL of distilled water was subsequently added, with stirring set to 700 RPM. The desired amount of Pd (II) nitrate hydrate (99.9%, Alfa Aesar) was dissolved in an aqueous 2 mM HCl solution. 2 mL of this solution was added to the reduced Cu/Al<sub>2</sub>O<sub>3</sub> mixture and allowed to react/reflux for 20 min under an N<sub>2</sub> atmosphere. The subsequent mixture was cooled to

room temperature where the catalysts were washed with 300 mL of distilled water via vacuum filtration and dried at 60 °C in an oven overnight. The resulting catalysts were denoted Pd<sub>1</sub>Cu<sub>n</sub> (12% MX) where *n* represents the proportion of Cu atoms per each atom of Pd incorporated, which was determined with ICP-OES.

### 2.1.5 Colloidal Pd nanoparticle catalyst synthesis

Supported Pd nanoparticles on Al<sub>2</sub>O<sub>3</sub> were synthesised using a method previously reported for Pt nanoparticles [3, 4]. Briefly, 10 mL of ethylene glycol and 50 µL of aqueous 1 M (NaOH) was refluxed at 120 °C. To the hot ethylene glycol, a solution of Na<sub>2</sub>PdCl<sub>4</sub> (10.6 mM, 99.99%, Sigma Aldrich) and polyvinylpyrrolidone (PVP) (91 mM, 40,000 MW, Alfa Aesar) in a 9:1 per volume of ethylene glycol:water was added slowly over 1 h. The now turned black mixture was stirred for an additional 20 min and cooled to room temperature. The nanoparticles were then collected by multiple acetone washes and centrifugation and the resulting solid pellet was dispersed in EtOH. The support (Al<sub>2</sub>O<sub>3</sub>, NanoArc™) was impregnated with the nanoparticle suspension and dried overnight. Finally, the Pd<sub>100</sub>/Al<sub>2</sub>O<sub>3</sub> catalyst was calcined at 300 °C for 4 h in static air.

## 2.2 Material Characterisation

### 2.2.1 Powder X-ray diffraction (XRD)

XRD is a non-destructive quantitative technique, which involves x-rays being fired typically at a solid sample which then diffract by elastic scattering, so the diffracted electromagnetic radiation is of the same energy but varies in the direction compared to the incident beam (Fig. 2.2.1). The incident beam scatters on the crystals, giving rise to destructive and constructive interference depending on the angle of the incident beam. The type of interference is characteristic of a specific crystal structure. Bragg's law (Equation 2.2.1) can be used to understand the constructive interference.

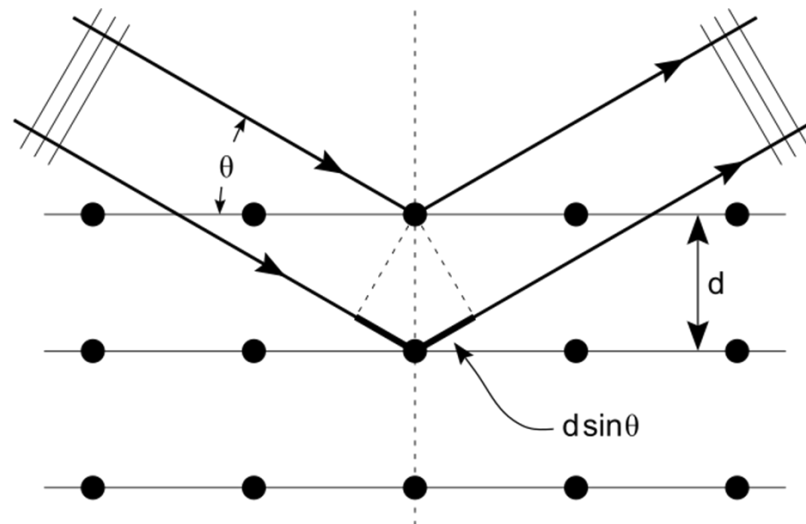


Fig. 2.2.1 Bragg diffraction from a cubic crystal lattice [5].

$$n\lambda = 2d\sin\theta$$

Equation 2.2.1 Bragg law where  $\lambda$  = wavelength of the x-ray,  $n$  = multiplication integer (order of reflection),  $d$  = interplanar distance and  $\theta$  = diffraction angle -.

The x-rays are generated in an x-ray tube consisting of two metal electrodes under vacuum (Fig. 2.2.2a). Electrons are produced by heating a tungsten filament cathode, which then fires and accelerates electrons at the water-cooled anode. The accelerated electrons are then able to knock out the anode's

core electrons, creating core holes that result in decay via x-ray fluorescence. X-ray fluorescence occurs when the electrons in the higher orbitals fall into the core-hole, releasing a characteristic x-ray photon that has the energy between the two orbitals involved. Consequently, different orbitals can be involved in the x-ray fluorescence, producing several characteristic x-rays being emitted from the anode (Fig. 2.2.2b). Thus, a typical XRD x-ray source will contain three main wavelengths  $K_{\alpha 1}$ ,  $K_{\alpha 2}$  and  $K_{\beta}$  each of which will give their own peak for each theoretical diffraction peak. Although a monochromatic x-ray source would be ideal, Ni  $K_{\beta}$  filters (and Göbel mirrors) can be used to reduce the intensity of the Cu  $K_{\beta}$  radiation significantly. A Ni  $K_{\beta}$  filter [6] consists of a 0.02 mm thin Ni foil where the Ni's core electrons can absorb the Cu  $K_{\beta}$  radiation and eject the excited electron from the atom. The physics of this process is essentially x-ray absorption spectroscopy (section 2.2.3) where the probability of x-rays being absorbed by a certain element changes as the energy of the x-ray radiation is changed. But overall, Cu  $K_{\beta}$  radiation has enough energy to do this process while the Cu  $K_{\alpha}$  radiation is not energetic enough to eject the Ni core electrons and thus, the Ni absorption edge lies between the Cu  $K_{\beta}$  and Cu  $K_{\alpha}$  wavelengths. Therefore, the Cu  $K_{\beta}$  radiation intensity is selectively more reduced than the Cu  $K_{\alpha}$ . However, the  $K_{\alpha 1}$  and  $K_{\alpha 2}$  doublet is typically present in most diffractometers since expensive monochromators are required to filter out the  $K_{\alpha 2}$  contamination.

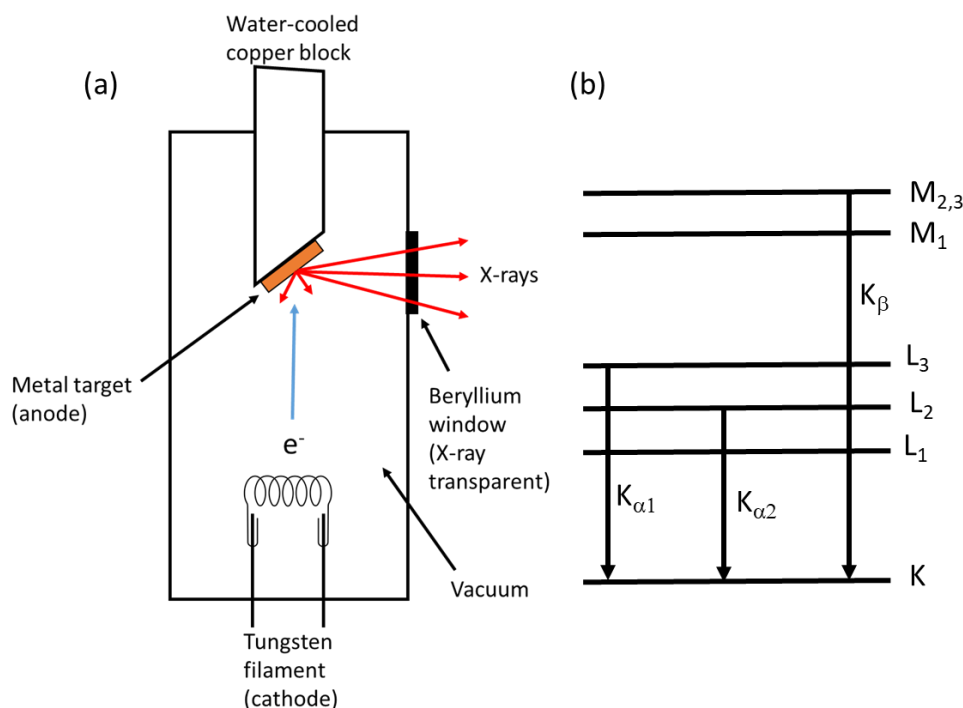


Fig. 2.2.2 (a) Schematic of a basic x-ray tube and (b) electron transitions in an atom, which produce the characteristic  $K_{\alpha 1}$ ,  $K_{\alpha 2}$  and  $K_{\beta}$  x-rays after core-hole creation.

XRD not only can identify which crystals are present in the sample but also can determine the size of the crystallites. The arithmetic mean domain size of the nanoparticles was determined via the Whole Powder Pattern Modelling (WPPM) method [7, 8], utilising the PM2K software [9]. This procedure allows one to extract microstructural information from diffraction patterns via nonlinear least-squares routine, with the observed diffractions profile arising from a convolution of instrumental and sample-related physical effects. Hence, the analysis is directly made in terms of physical models of microstructure and/or lattice defects [7, 10, 11]. The instrumental contribution was estimated by modelling the peak profiles from the NIST SRM 1976b corundum standard, according to the Caglioti *et al.* relationship [12]. The slight Gaussian micro-strain broadening arising from the SRM 1976b [13] was assumed negligible compared to the broadening from the nanosized copper phase. The background was synthesised using a combination of a Chebyshev polynomial and an exponential decay. The crystalline domains were assumed to be spherical and distributed according to a log-normal size distribution. The volume-weighted crystallite size was estimated with the Scherrer equation and the

integral breadth method, which use Equation 2.2.2 and the FWHM or the integrated intensity divided by the peak height for the Scherrer and integral breadth method, respectively.

$$\tau = \frac{K\lambda}{\beta\cos\theta}$$

*Equation 2.2.2 Scherrer equation where  $\tau$  = mean crystallite size,  $K$  = shape factor,  $\lambda$  = X-ray wavelength,  $\beta$  = full-width at half maxima (FWHM) or integral breadth and  $\theta$  = Bragg angle.*

Powder X-ray diffraction data were collected using a Bruker D8 Advance Bragg–Brentano diffractometer equipped with a Lynxeye PSD detector and with Cu  $K\alpha_{1,2}$  radiation (40 kV and 40 mA, 0.2 mm Ni  $K\beta$  absorber, 2.5° Soller Slits, 10–80°  $2\theta$  range, a virtual step scan of 0.02°  $2\theta$ , virtual time per step of 1 or 8 s). The powdered samples were top-loaded into poly(methyl methacrylate) (PMMA) sample holders. *In-situ* XRD measurements were conducted with an Anton-Paar XRK-900 reaction chamber in the parallel beam geometry using a Göbel mirror, 0.2 mm slits and 2.5° Soller slits. Diffractograms were then collected with a virtual step scan of  $2\theta = 0.02^\circ$  and virtual time per step of 2 s in a flowing 20% H<sub>2</sub>/80% He atmosphere.

### 2.2.2 X-ray photoelectron spectroscopy (XPS) and x-ray excited Auger electron spectroscopy (XAES)

XPS is a surface-sensitive technique where up to 10 nanometres of the sample (depending on the x-ray energy and the material) is probed to determine the oxidation state, depth profile, and surface elemental composition. XPS involves the sample being irradiated with x-rays (typically using monochromatic Al  $K\alpha_1$  radiation), which can eject core electrons (if sufficient energy is applied) and photoelectrons leave the sample (depicted in Fig. 2.2.3). The photoelectron is then detected, and the kinetic energy is measured. Upon ejection, an unstable core-hole is left, which then decays either by x-ray fluorescence or an Auger transition. The Auger transition involves the core-hole being filled by an electron transition from a less tightly bound electron in the upper electron levels. The transfer of this electron (often called the down electron) releases energy, which can be emitted once again as x-ray fluorescence or transferred to a third electron. The third electron is known as the Auger electron, which escapes to the vacuum which is then detected like the photoelectron in the XPS process. This process of detecting the Auger electron is called x-ray excited Auger spectroscopy (XAES) or Auger spectroscopy (AES) if the core-hole is created by an incident electron [14].

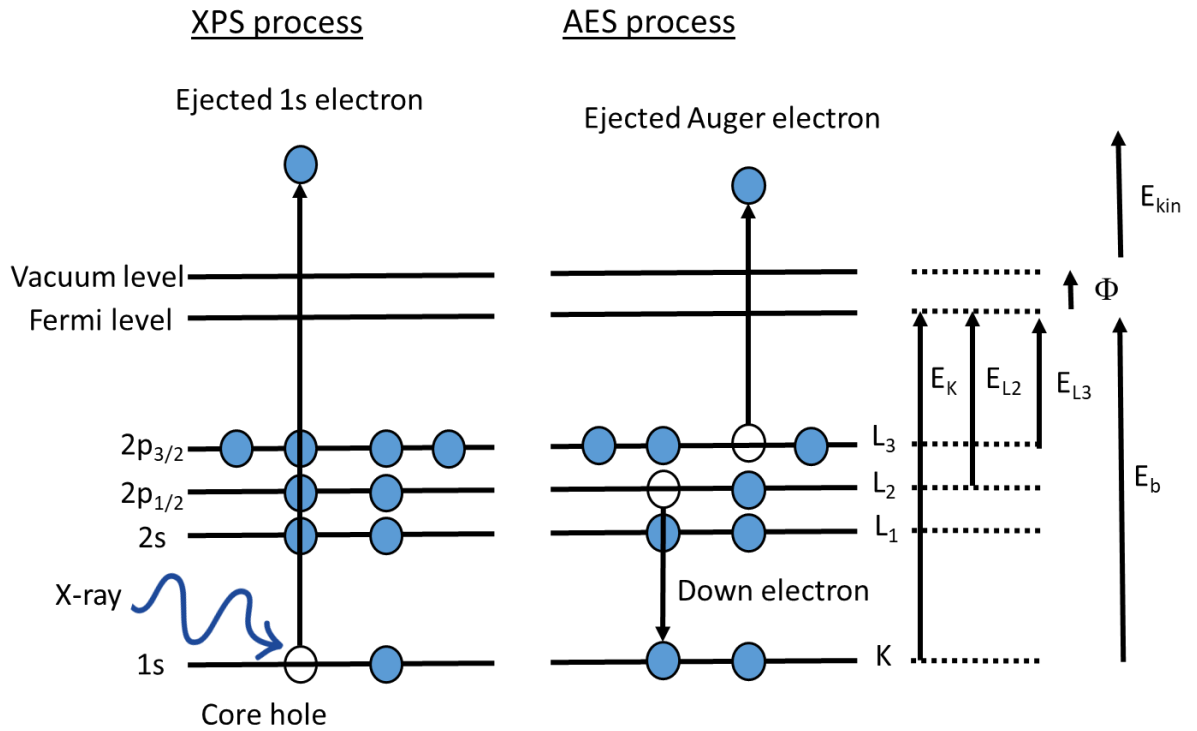


Fig. 2.2.3 Schematic illustration of photo-ionisation of a core electron and the subsequent decay of the core-hole via an Auger transition.  $E_{kin}$  = Kinetic energy of photoelectron/Auger electron,  $E_b$  = electron binding energy,  $\Phi$  = work function and  $E_K$ ,  $E_{L2}$ ,  $E_{L3}$  represent the binding energy of electrons in the K, L2 and L3 orbitals, respectively.

The kinetic energy of the photoelectron is dependent on the energy of the x-ray radiation used,  $h\nu$ , the core electron's binding energy,  $E_b$ , and the work function of the metal,  $\phi$ , (Equation 2.2.3).

$$E_{kin} = h\nu - E_b - \phi$$

Equation 2.2.3 X-ray photoelectron spectroscopy equation.

In contrast, the kinetic energy of the Auger electron is independent of the energy of the incident photon or electron. The kinetic energy is, however, dependent on the orbitals involved in the three-electron process which is summarised in Fig. 2.2.3 and described by Equation 2.2.4.

$$E_{kin} = E_K - E_{L_1} - E_{L_3} - \phi$$

Equation 2.2.4 Auger spectroscopy equation.

The surface sensitivity of XPS and AES arises from the fact that these core-level spectroscopies only detect electrons that can escape the sample into the vacuum of the instrument and reach the detector. For the ejected electrons to escape the sample, inelastic scattering may occur in several discrete energy loss events such as plasmon excitations, electron-hole pair excitations and core-level ionisation events. The average distance that such electrons with a given energy can travel between successive inelastic collisions is defined by the inelastic mean free path (IMFP). So, only the ejected electron emissions near the surface of the material have the lowest probability of energy loss and escaping.

The modified Auger parameter  $\alpha'$  was defined as the sum of the photoelectron binding energy and the Auger electron kinetic energy [15]. The extra-atomic relaxation energy was defined as half the change in the modified Auger parameter compared to bulk Cu [16]. The modified Auger parameter is a final state effect, which also provides an estimate of the relaxation energy/screening energy in the presence of core holes [17], while also not suffering from charging and inadequate calibration problems [14]. The relaxation energy can be interpreted as a secondary process where the surrounding electrons react to the sudden appearance of a positive core-hole after photoemission. The screening of the core-hole by the influx of electrons lowers the measured  $E_b$  [18]. The relaxation energy can be partitioned into intra-atomic and extra-atomic relaxation energy; with the former remaining constant for core-electrons in an atom, while the latter varies with changes in the chemical and physical states. The extra-atomic relaxation energy is defined as half the change in the modified Auger parameter compared to bulk Cu [16]. Finally, the modified Auger parameter,  $\alpha'$ , is defined as the sum of the photoelectron binding energy and the Auger electron kinetic energy [15]. A high  $\alpha'$  indicates higher relaxation energy or improved screening energy, which can be due to a greater number of atoms able to screen the core-hole better after photoemission or due to the polarisability of the support.

The catalyst dispersion can also be calculated by XPS, which was first reported by Kerkhof *et al.* [19]. Their theoretical model for supported metal catalyst consists of an active phase located on sheets of support. The thickness ( $t$ ) of these sheets can be estimated from the density ( $\rho_s$ ) and the surface area of the support ( $S_0$ ) shown in Equation 2.2.5:

$$t = \frac{2}{\rho_s S_0}$$

Equation 2.2.5 Thickness of support sheets.

A dimensionless parameter ( $\beta$ ) is also calculated from the thickness of the support sheets ( $t$ ) and the inelastic mean free path of a photoelectron ejected from a Cu 2p<sub>3/2</sub> orbital (~554 eV, catalytic active material) through the support phase ( $\lambda_s$ ) which can be acquired from Tanuma *et al.* [20]. The expression is shown in Equation 2.2.6.

$$\beta = \frac{t}{\lambda_s}$$

Equation 2.2.6 Dimensionless parameter  $\beta$ .

Theoretical XPS intensity ratio of supported phase ( $p$ ) and the support ( $s$ ) for the supported catalyst ( $I_p^o/I_s^o$ ) [19], was predicted with a maximum error of 10% with Equation 2.2.7.

$$\left(\frac{I_p^o}{I_s^o}\right) = \left(\frac{p}{s}\right) \frac{\sigma_p \beta (1 + e^{-\beta})}{\sigma_s 2 (1 - e^{-\beta})}$$

Equation 2.2.7 Theoretical XPS intensity ratio of supported phase ( $p$ ) and the support ( $s$ ) for a supported catalyst.

Where ( $p/s$ ) is the bulk atomic ratio of the supported phase ( $p$ ) and the support ( $s$ ).  $\sigma_p$  and  $\sigma_s$  are the Schofield photoelectron cross-sections for the supported phase and the support, respectively.

The dispersion was determined according to Equation 2.2.8, reported by Park *et al.* [21], where  $I_p$  and  $I_s$  are the integrated intensity of the Cu 2p<sub>3/2</sub> peak and Al 2p (taking into account the transmission

function), respectively. Deconvolution of the overlapped Cu 3p and Al 2p signal was achieved by following the procedure outlined by Park *et al.* [21]. A similar process was carried out to find Pd dispersion, where in this case the Pd is the supported phase and the Cu is the support.

$$Dispersion (\%) = \left( \frac{I_p}{I_s} \right) \div \left( \frac{I_p^0}{I_s^0} \right) \times 100$$

*Equation 2.2.8 XPS calculated dispersion.*

XP and XAE spectra were acquired on a Kratos AXIS Supra spectrometer, equipped with a charge neutraliser and monochromated Al K $\alpha$  x-ray source (1486.7 eV) with energies referenced to adventitious carbon at 284.8 eV using CasaXPS version 2.3.19PR1.0.

### 2.2.3 X-ray absorption spectroscopy (XAS)

XAS is another core-level spectroscopy that can give insight into structural and electronic information while requiring minimal sample preparation. XAS involves an incoming photon (that has a specific energy) interacting with a core-level electron, ejecting the electron into some unoccupied state above the Fermi energy propagating away, leaving behind a core-hole. The unstable core-hole then decays (1 to 2 femtoseconds) by x-ray fluorescence or an Auger transition in the same manner as described in the previous section. The absorption of this photon can then be quantified through the measuring of the reduction of intensity of the transmitted beam, or the x-ray fluorescence or Auger electrons emitted from the sample. The energy of the incident photons is then changed slightly, and the process is repeated, giving an x-ray absorption spectrum. Unlike the other core-level spectroscopies mentioned, XAS is mostly limited to purpose-built facilities at synchrotrons, as an x-ray source capable of being energy-tuneable, monochromatic, and having enough flux to get adequate signal: noise is difficult in laboratory-based systems. Although it is not impossible [22], they are limited to very concentrated samples.

X-ray absorption spectra for the monometallic Cu catalysts were collected at B18 XAS beamline at Diamond Light Source. A double-crystal Si (111) monochromator was used to scan x-ray energies from -200 to 800 eV relative to the Cu K-edge (8979 eV). Each catalyst was reduced *ex-situ*, then the XAS measurement was conducted in transmission mode with 3 repeats; the data was subsequently merged for further XANES and EXAFS analysis using Athena and Artemis (FEFF6 code) software packages [23].

Furthermore, the x-ray absorption spectra for the single atom alloy catalysts were also collected at B18 XAS beamline at Diamond Light Source, UK. A double-crystal Si (311) monochromator was used to scan x-ray energies from -200 to 800 eV relative to the Pd K-edge (24350 eV). Following *ex-situ* reduction, samples were loaded into 3 mm capillaries and the XAS measurement was conducted in fluorescence mode (multi-element Ge detector at 45° to the sample) with 5 scans. Pseudo-*in-situ* XAS was conducted using a gas-tight cell with aluminised Kapton windows (shown in Fig. 2.2.4); the

catalysts were pelletised and reduced in 5% H<sub>2</sub>/95% He at 300 °C. Subsequently, without exposure to atmospheric oxygen, they were loaded into the cell in an N<sub>2</sub> filled glove box. Spectra were collected in fluorescence mode with 35 scans. XAS data were analysed with Athena and Artemis (FEFF6 code) [23], the accompanying reference spectra were calibrated to 24350 eV, aligned and merged before analysis. FEFF scattering paths were calculated using Cu and CuO CIF files, with the absorber replaced with Pd. Samples denoted re-oxidised and reduced represent samples measured *ex-situ* using a capillary and a gas-tight pellet cell, respectively.

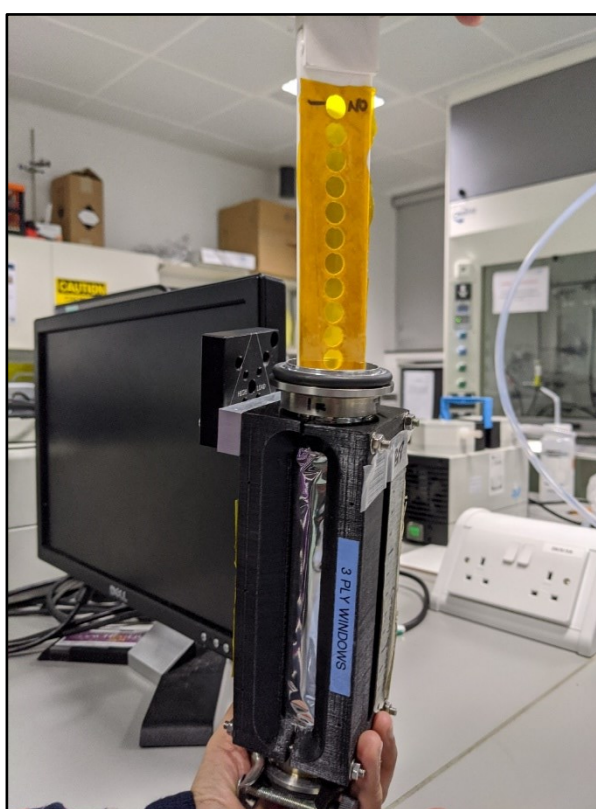


Fig. 2.2.4 Gas-tight cell for air-sensitive samples for XAS experiments.

### 2.2.4 Inductively coupled plasma optical emission spectroscopy (ICP-OES)

In ICP-OES a liquid sample is pumped into a nebuliser and enters with a carrier gas (Ar) as a mist into a spray chamber (Fig. 2.2.5). The spray is then ionised by the inductively coupled plasma, and the analysed material is broken up into its constituent ionised atoms. The resulting ions recombine and produce electromagnetic emissions. The wavelength of these electromagnetic emissions is characteristic of the elements present in the sample, and their intensities are proportional to their concentration. Therefore, the concentration of elements can be determined by comparing the intensity of emissions with a set of standards samples with known amounts of the desired elements. Due to the elemental overlap of the emissions, at least three different emissions or wavelengths were investigated to obtain accurate results.

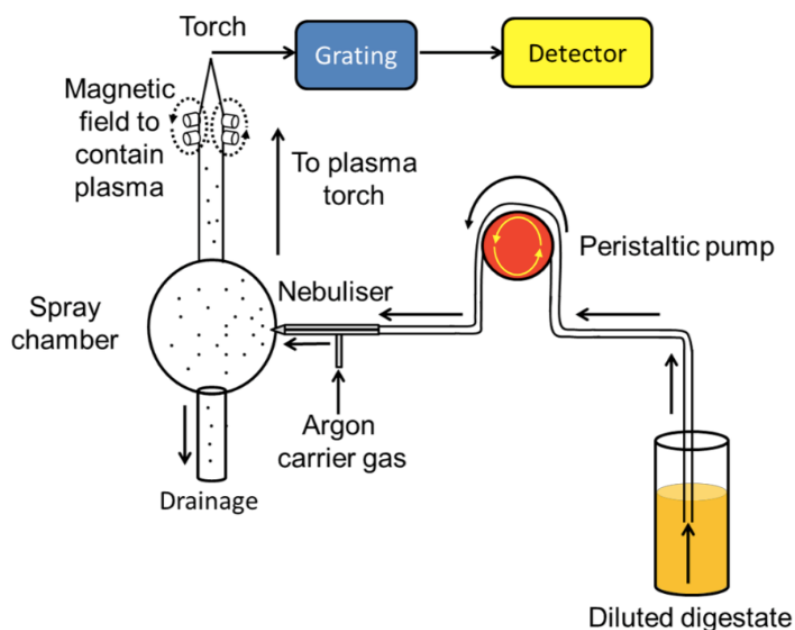


Fig. 2.2.5 Typical ICP-OES schematic showing the process of the sample solution reaching the plasma torch.

The bulk metal content was determined using ICP-OES on a Thermo Scientific iCAP 7400 Duo. The samples (10 mg) were digested with 2 mL of HCl (37%, VWR Chemicals) and 5 mL (>95%, Fisher Scientific) H<sub>2</sub>SO<sub>4</sub>; the mixture was then heated to 280 °C for 1 h to ensure complete dissolution of Al<sub>2</sub>O<sub>3</sub> support. After cooling to room temperature, 3 mL of HNO<sub>3</sub> (68%, VWR Chemicals) was added to confirm the complete dissolution of Cu nanoparticles. The digestant was then topped up to 10 mL to

account for any evaporation losses. Finally, the digestant was diluted 10 times with deionised water before the ICP-OES analysis. However, for the case of the 1 wt% SAA catalysts, this final dilution step was not conducted.

### 2.2.5 Scanning transmission electron microscopy (STEM)

Similar to transmission electron microscopy (TEM), STEM images are formed by electrons transmitting through the sample. However, unlike typical TEM, in STEM the electron beam is focused into a sub-nanometre sized spot which is scanned over the sample in a rastering fashion. The rastering of the beam is done with the scanning coils, and various signals can be collected as a function of the position of the probe to construct STEM images of the sample. It should be noted that in STEM, only the information of the transmitted beam is utilised. Bright-field (BF), dark-field (DF) and high-angle annular dark-field (HAADF) images can all be collected depending on the scattering angle of the transmitted electron beam. As shown in Fig. 2.2.6, the BF detector is aligned with the aperture and used for low angle scattering electrons. Surrounding the BF is the annular DF detector, for low to high scattering angle electrons. Finally, around them, there is the annular HAADF detector for collecting high scattering angle electrons. With BF-STEM, the electrons that are collected have minimal/no change in the angular coordination after passing through the sample. The low scattering angle is due to these electrons having not travelled very close to the positively charged nucleus of the atoms. In some regard, BF-STEM is comparable to HRTEM but lacking the high signal-to-noise of the latter [24]. Nonetheless, BF-STEM is valuable as it can be acquired simultaneously with DF-STEM images. As mentioned earlier, DF-STEM involves collecting only those electrons that have been scattered away from their incident direction by the nucleus of the analysed atoms. A high signal-to-noise is achieved with these images, as only the deflected electrons by the sample are detected and because of the vacuum, electrons travelling through the column do not scatter and contribute to the image. Thus, the DF-images are good at distinguishing the nanostructures, with the empty spaces represented by the dark area of the images. In addition, DF-images also allow the discrimination of atoms as different atoms have unique scattering factors, giving rise to different STEM intensities. This leads to the so-called Z-contrast as the scattering factors are a strong function of Z. Therefore, atoms with a small difference in atomic numbers, like Cu ( $Z=29$ ) and Al ( $Z=13$ ), are difficult to differentiate. Similarly, for HAADF, only electrons that have a very high scattering angle (e.g., those scattered from high Z atoms) are detected providing in-depth information at the atomic scale.

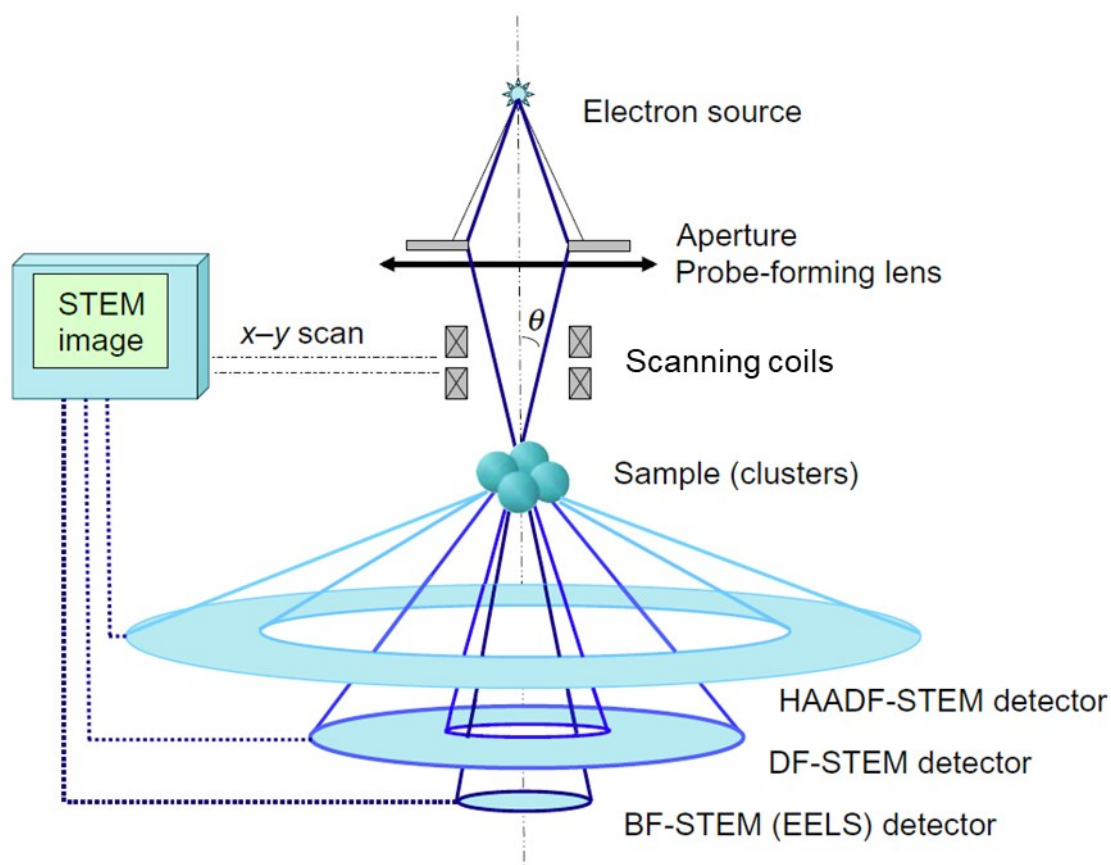


Fig. 2.2.6 Schematic diagram of the operating principle of scanning transmission electron microscopy. Modified from referenced [24].

STEM images were acquired on a Cs aberration-corrected JEOL 2100F microscope operating at 200 kV, using a Gatan Ultrascan 4000 digital camera. Samples were prepared by dispersion in methanol by sonication, followed by deposition on 300-mesh carbon-supported Cu grids and drying at 60 °C. ImageJ 1.52a software was used for image analysis.

### 2.2.6 N<sub>2</sub> Porosimetry

The surface area was determined by the Brunauer–Emmett–Teller (BET) equation (Equation 2.2.9) utilising N<sub>2</sub> physisorption. N<sub>2</sub> porosimetry is a technique that is used to acquire information about the textural properties of solid materials. This is done by N<sub>2</sub> physisorption at -196 °C where N<sub>2</sub> molecules get adsorbed onto the surface via weak van der Waals intermolecular forces, and then the amount of surface-bound N<sub>2</sub> is used to determine monolayer coverage. Brunauer–Emmett–Teller (BET) model is an expanded version of the Langmuir model. The Langmuir model assumes the energy of adsorption is much higher for the first layer than any subsequent layers such that the formation of multi-layers only occurs at higher pressures. However, according to the BET model, the adsorbed molecules in the first layer act as sites for the second layer molecules and so on. It is also assumed that the adsorption interaction of all layers above the first is identical [25]. Consequently, Brunauer, Emmett and Teller were able to derive their linear BET equation (Equation 2.2.9), assuming that the multi-layer has an infinite thickness at  $p/p_0 = 1$ .

$$\frac{p}{n(p_0 - p)} = \frac{C - 1}{n_m C} \times \frac{p}{p_0} + \frac{1}{n_m C}$$

*Equation 2.2.9 BET linear equation.*

where  $p$  is pressure,  $p_0$  is saturation pressure,  $n$  is the total number of adsorbed molecules,  $n_m$  is the monolayer capacity, and  $C$  is an empirical constant that is assumed to be exponentially related to the net heat of adsorption (energy of the adsorption of the initial layer ( $E_1$ ) minus the energy of subsequent layers ( $E_L$ )), determined by Equation 2.2.10.

$$C \approx \exp\left(\frac{E_1 - E_L}{RT}\right)$$

*Equation 2.2.10 Determination of  $C$ , net heat of adsorption for the BET linear equation.*

The constant  $C$  was established to account for the interactions between the subsequent layers of N<sub>2</sub>. The specific surface area is calculated from the linear region of the BET plot (typically pressure range

$p/p_0 = 0.03 - 0.18$ ), indicating monolayer coverage. The specific surface area was calculated according to Equation 2.2.11.

$$SSA = \frac{n_m N_A \sigma}{m_s}$$

*Equation 2.2.11 BET specific surface area calculation. where BET specific surface area (SSA) is related to  $n_m$  utilising  $\sigma$ , the effective cross-sectional area of  $N_2$  ( $0.162 \text{ nm}^2$ ) at  $-196 \text{ }^\circ\text{C}$ ,  $N_A$ , Avogadro's number and  $m_s$ , the mass of the sample (g).*

BET surface areas were determined via  $N_2$  physisorption using a Quantachrome Nova 4000 instrument. Approximately 50 mg of the sample was degassed at  $120 \text{ }^\circ\text{C}$  for 2 h before analysis at  $-196 \text{ }^\circ\text{C}$ .

### 2.2.7 H<sub>2</sub>-Temperature Programmed Reduction (H<sub>2</sub>-TPR)

H<sub>2</sub>-TPR experiments give an insight into the consumption of H<sub>2</sub> as the sample is heated. Consequently, the reducibility of the catalyst can be explored. A thermal conductivity detector (TCD) is used to understand the changes in the gas composition since it is correlated to the thermal conductivity of the gas.

H<sub>2</sub>-TPR was conducted on a Quantachrome ChemBET Pulsar equipped with a TCD detector (150 mA). 100 mg of catalyst was loaded into a quartz wool plugged u-shaped glass tube and degassed/dried under N<sub>2</sub> flow at 100 °C for 30 min. TPR analysis was subsequently conducted under 5% H<sub>2</sub>/95% N<sub>2</sub> (40 mL min<sup>-1</sup>) at a heating rate of 6 °C min<sup>-1</sup> to 300 °C.

### 2.2.8 Thermal Gravimetric Analysis with Mass Spectrometry (TGA-MS)

TGA involves analysing the mass change of a sample continuously as the temperature changes. Phase transitions, absorption, adsorption, and desorption, as well as chemical phenomena such as chemisorption, thermal decomposition, and solid-to-gas reactions (e.g., oxidation or reduction), can be studied using this measurement. Mass spectrometry can be coupled with a TGA instrument to determine the gaseous products released from the sample.

TGA was conducted on a Mettler Toledo TGA/DSC1 Star System under an N<sub>2</sub> purge gas (60 ml min<sup>-1</sup>) interfaced to a ThermoStar TM GSD 301 T3 mass spectrometer. The colloiddally capped Cu/Al<sub>2</sub>O<sub>3</sub> catalyst (20 mg) was loaded into an alumina crucible and heated from 40 to 800 °C with a heating rate of 10 °C min<sup>-1</sup>.

## 2.3 Catalytic testing

### 2.3.1 Hydrogenation of furfural using monometallic Cu catalysts

*In-situ* reduction and catalytic reactions were performed in a H.E.L DigiCAT high-pressure reactor system operating 3 × 50 mL stainless steel autoclaves (Fig. 2.3.1). The reactors were loaded with 30 mg of catalyst and reduced under flowing H<sub>2</sub> at 300 °C for 0.5 h (ramp rate: 5 °C min<sup>-1</sup>). After cooling to room temperature under flowing H<sub>2</sub>, the autoclaves were purged with He and then sealed to prevent oxidation. While He was flowing, 10 mL of the reaction mixture consisting of MeOH (Fisher Scientific, HPLC grade), furfural (0.02 M, Sigma Aldrich, 99%) and the internal standard decane (0.02 M, Sigma Aldrich, 99%), were injected into each reactor. The mixtures were degassed for 10 min in flowing He before pressurising with H<sub>2</sub> (BOC, 99.995%). The reactors were then heated to 50 °C and stirred at 600 RPM using magnetic stirrers. The reaction was carried out for 7 h before being cooled and depressurised to atmospheric pressure. Aliquots of the reaction mixture (0.2 mL) were taken and analysed offline without further dilution using a Bruker Scion 456 GC equipped with a Zebron ZB-5 (5%-phenyl-95%-dimethylpolysiloxane, 30 m × 0.53 mm × 1.50 µm) capillary column and a flame ionisation detector (FID). The concentration of the products was determined through the normalisation of the individual peak areas with the internal standard, as well as the use of 5-point calibration standards of the pure compounds. All peaks in the chromatograph were identified by GC-MS (Shimadzu GC-MS QP2010 SE). The carbon mass balance of the catalytic testing was determined to be ~97%.

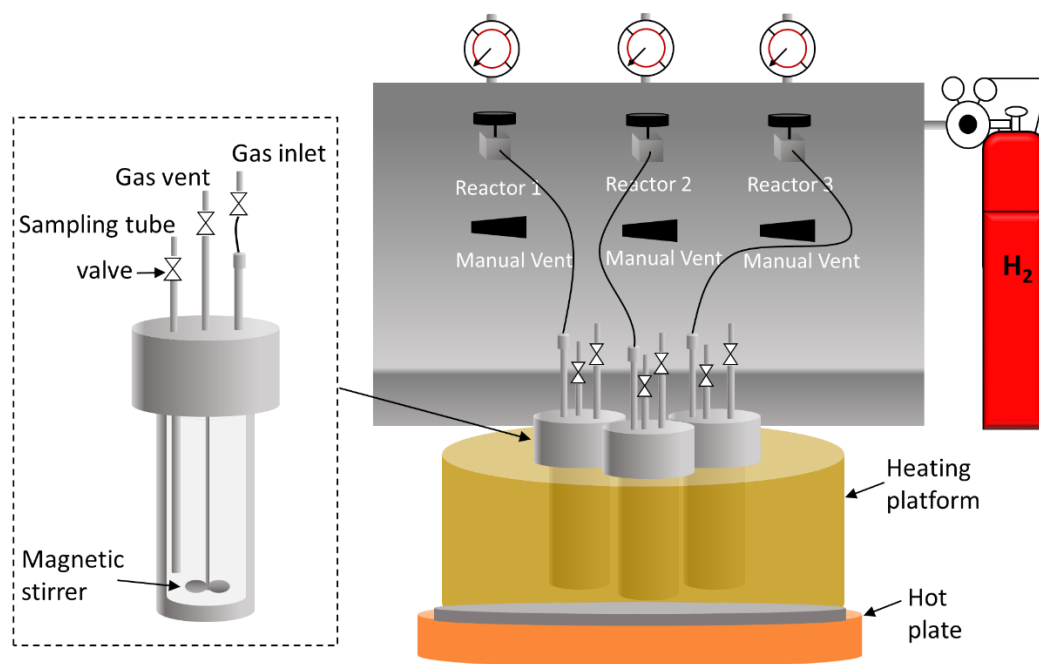


Fig. 2.3.1 Schematic diagram of the H.E.L. Digicat reactor system

### 2.3.1.1 Sulfur leaching and homogenous catalytic tests

The sulfur was leached off the calcined Cu sulfate derived catalyst by ageing it in MeOH at 50 °C for 7 h. The resulting catalyst and supernatant fluid were collected via centrifugation. The leached catalyst was then dried overnight and was reduced *in-situ* before the catalytic testing. The catalytic activity of the dissolved species in the supernatant fluid was investigated by adding furfural and decane to the liquid before starting the reaction.

### 2.3.2 Hydrogenation of furfural using single atom alloy catalysts

*In-situ* reduction and catalytic reactions were performed in a H.E.L DigiCAT high-pressure reactor system operating  $2 \times 50$  mL stainless steel autoclaves (Fig. 2.3.1). The reactors were loaded with 30 mg of catalyst and reduced under flowing  $H_2$  at 300 °C for 0.5 h (ramp rate: 5 °C  $min^{-1}$ ). After cooling to room temperature under flowing  $H_2$ , the autoclaves were purged with  $H_2$  and then sealed to prevent oxidation. While  $H_2$  was flowing, 10 mL of the reaction mixture consisting of MeOH (Fisher Scientific, HPLC grade), furfural (0.02 M, Sigma Aldrich, 99%) and the internal standard butanol (0.02 M, Alfa Aesar, 99%), was injected into each reactor. The mixtures were degassed for 10 min in flowing He before pressurising with  $H_2$  (BOC, 99.995%). The reactors were then heated to 50 °C and stirred at 600 RPM using magnetic stirrers. The reaction was carried out for 7 h before being cooled and depressurised to atmospheric pressure. Aliquots of the reaction mixture (0.2 mL) were taken and analysed offline after a 1:10 dilution (with MeOH) using a Shimadzu GC-FID 2010 Plus equipped with a ZB-WAX (polyethylene glycol, 30 meters  $\times$  0.32 mm  $\times$  0.50  $\mu m$ ) capillary column. The concentration of the products was determined through the normalisation of the individual peak areas with the internal standard, as well as the use of 5-point calibration standards of the pure compounds. All peaks in the chromatograph were identified via GC-MS (Shimadzu GC-MS QP2010 SE).

### 2.3.3 Hydrogenation of crotonaldehyde

*In-situ* reduction and catalytic reactions were performed in a H.E.L DigiCAT high-pressure reactor system operating 2 × 50 mL stainless steel autoclaves (Fig. 2.3.1). The reactors were loaded with 30 mg of catalyst and reduced under flowing H<sub>2</sub> at 300 °C for 0.5h (ramp rate: 5 °C min<sup>-1</sup>). After cooling to room temperature under flowing H<sub>2</sub>, the autoclaves were purged with H<sub>2</sub> and then sealed to prevent oxidation. A reaction solution was made consisting of crotonaldehyde (0.02 M, Sigma Aldrich, ≥99.5%) and the internal standard dioxane (0.02 M, anhydrous, Sigma Aldrich, 99.8%) in MeOH. The reaction solution was then placed in an ultrasonic bath for 5 minutes to ensure solubility and the dissolved gases are removed. Under H<sub>2</sub> flow, 10 mL was injected into each reactor. The mixture was then pressurised with 1.5 bar of H<sub>2</sub> (BOC, 99.995%). Subsequently, the reactors were heated to 50 °C and stirred at 600 RPM using magnetic stirrers. The reaction was carried out for 7 h before being cooled and depressurised to atmospheric pressure. Aliquots of the reaction mixture (0.2 mL) were taken and analysed offline after a 1:4 dilution (with MeOH) using a Shimadzu GC-FID 2010 Plus equipped with a ZB-WAX capillary column. The concentration of the products was determined through the normalisation of the individual peak areas with the internal standard, as well as the use of 5-point calibration standards of the pure compounds. All peaks in the chromatograph were identified via GC-MS (Shimadzu GC-MS QP2010 SE).

### 2.3.4 Recyclability tests

After the catalysts were recovered by centrifugation, they were washed with MeOH three times. The materials were then dried overnight at 100 °C and *in-situ* reduced before testing. The reaction scale was adjusted depending on the amount of catalyst recovered.

### 2.3.5 Calculations for the catalytic experiments

Conversion of the reactant was calculated according to Equation 2.3.1.

$$\text{Conversion (\%)} = \left( \frac{[R]_0 - R_t}{R_0} \right) \times 100$$

*Equation 2.3.1 Conversion calculation. where  $[R]_0$  is the concentration of the reactant at time 0 and  $[R]_t$  is the concentration of the reactant at time  $t$ .*

Products selectivity were calculated according to Equation 2.3.2.

$$S_{\text{product (l)}} (\%) = \left( \frac{C_{\text{product (l)}}}{\sum C_{\text{product}}} \right) \times 100$$

*Equation 2.3.2 Selectivity calculation. where  $S$  is the selectivity (%) and  $C$  is the concentration (M).*

Initial rates of reactant consumption were calculated according to Equation 2.3.3. The reported initial rate was determined after the induction period for a time range of 1 hour.

$$\text{Initial rate (mol h}^{-1}\text{)} = - \left( \frac{\Delta m_{\text{reactant}} (\text{mol})}{\Delta t (\text{h})} \right)$$

*Equation 2.3.3 Initial rate calculation. where  $m_{\text{reactant}}$  is the mol of reactant and  $t$  is time in hours.*

Active Cu sites per catalyst were calculated using Equation 2.3.4.

$$\text{Active Cu sites (mol)} = \left( \frac{\text{Dispersion (\%)}}{100} \times \text{mol of Cu in the catalyst} \right)$$

*Equation 2.3.4 Moles of Cu active sites. where dispersion was calculated from the XPS data and mol of Cu in the catalyst was determined from ICP-OES.*

Turnover frequencies were calculated according to Equation 2.3.5.

$$\text{TOF (h}^{-1}\text{)} = \left( \frac{\text{Initial rate of reactant consumption (mol h}^{-1}\text{)}}{\text{Active Cu sites (mol)}} \right)$$

*Equation 2.3.5 Turnover frequency calculation*

Furfuryl alcohol/metal mole ratio per hour or simply called productivity was determined according to Equation 2.3.6.

$$\text{Productivity (h}^{-1}\text{)} = \left( \frac{\text{mol of furfuyl alcohol produced}}{\text{mol of metal in catalyst} \times \text{reaction time (h)}} \right)$$

*Equation 2.3.6 Furfuryl alcohol/metal mole ratio per hour calculation*

Turnover frequency\* (TOF\*) was determined according to Equation 2.3.7.

$$\text{TOF}^* \text{ (h}^{-1}\text{)} = \left( \frac{\text{mol of reactant consumed}}{\text{mol of promoting metal in catalyst} \times \text{reaction time (h)}} \right)$$

*Equation 2.3.7 Turnover frequency\* (TOF\*) and metal content was determined from ICP-OES.*

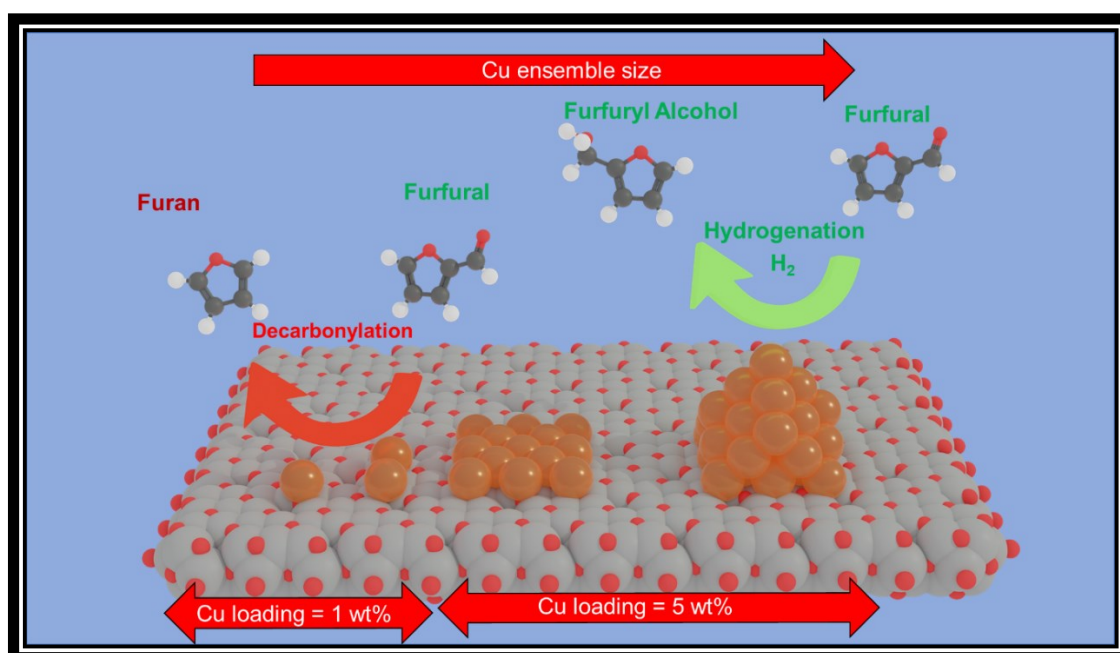
## 2.4 References

- [1] M. Kanzaki, Y. Kawaguchi, H. Kawasaki, Fabrication of Conductive Copper Films on Flexible Polymer Substrates by Low-Temperature Sintering of Composite Cu Ink in Air, *ACS Appl. Mater. Interfaces*, 9 (2017) 20852-20858.
- [2] F.R. Lucci, J. Liu, M.D. Marcinkowski, M. Yang, L.F. Allard, M. Flytzani-Stephanopoulos, E.C.H. Sykes, Selective hydrogenation of 1,3-butadiene on platinum–copper alloys at the single-atom limit, *Nat. Commun.*, 6 (2015) 8550.
- [3] M.J. Taylor, S.K. Beaumont, M.J. Islam, S. Tsatsos, C.A.M. Parlett, M.A. Issacs, G. Kyriakou, Atom efficient PtCu bimetallic catalysts and ultra dilute alloys for the selective hydrogenation of furfural, *Appl. Catal. B*, 284 (2021) 119737.
- [4] M.M. Koebel, L.C. Jones, G.A. Somorjai, Preparation of size-tunable, highly monodisperse PVP-protected Pt-nanoparticles by seed-mediated growth, *J. Nanopart. Res.*, 10 (2008) 1063-1069.
- [5] Hydrargyrum, Bragg diffraction from a cubic crystal lattice, Wikimedia Commons, 2011, pp. The incoming beam (coming from upper left) causes each scatterer to re-radiate a small portion of its intensity as a spherical wave. If scatterers are arranged symmetrically with a separation  $d$ , these spherical waves will be in sync (add constructively) only in directions where their path-length difference  $2d \sin \theta$  equals an integer multiple of the wavelength  $\lambda$ . In that case, part of the incoming beam is deflected by an angle  $2\theta$ , producing a reflection spot in the diffraction pattern.
- [6] V. Pecharsky, P. Zavalij, *Fundamentals of Powder Diffraction and Structural Characterization of Materials*, Springer US2005.
- [7] P. Scardi, M. Leoni, Whole powder pattern modelling, *Acta Crystallogr. A*, 58 (2002) 190-200.

- [8] P. Scardi, M. Leoni, M. D'Incau, Whole Powder Pattern Modelling of cubic metal powders deformed by high energy milling, *Z. Kristallogr. Cryst. Mater.*, 222 (2007) 129.
- [9] M. Leoni, T. Confente, P. Scardi, PM2K: A flexible program implementing Whole Powder Pattern Modelling, *Zeitschrift für Kristallographie Supplements*, 23 (2006) 249-254.
- [10] M. Leoni, P. Scardi, Line profile analysis: pattern modelling versus profile fitting, *J. Appl. Crystallogr.*, 39 (2006) 24-31.
- [11] P. Scardi, M. Leoni, Whole Powder Pattern Modelling: Theory and Applications, in: E.J. Mittemeijer, P. Scardi (Eds.) *Diffraction Analysis of the Microstructure of Materials*, Springer Berlin Heidelberg, Berlin, Heidelberg, 2004, pp. 51-91.
- [12] G. Caglioti, A. Paoletti, F.P. Ricci, On resolution and luminosity of a neutron diffraction spectrometer for single crystal analysis, *Nucl. Instrum. Methods*, 9 (1960) 195-198.
- [13] D.R. Black, D. Windover, M.H. Mendenhall, A. Henins, J. Filliben, J.P. Cline, Certification of Standard Reference Material 1976B, *Powder Diffr.*, 30 (2015) 199-204.
- [14] S. Hofmann, *Auger- and X-Ray Photoelectron Spectroscopy in Materials Science: A User-Oriented Guide*, Springer Berlin Heidelberg 2012.
- [15] S.W. Gaarenstroom, N. Winograd, Initial and final state effects in the ESCA spectra of cadmium and silver oxides, *J. Chem. Phys.*, 67 (1977) 3500-3506.
- [16] G. Moretti, Auger parameter and Wagner plot in the characterization of chemical states by X-ray photoelectron spectroscopy: a review, *J. Electron. Spectrosc. Relat. Phenom.*, 95 (1998) 95-144.
- [17] A. Thøgersen, S. Diplas, J. Mayandi, T. Finstad, A. Olsen, J.F. Watts, M. Mitome, Y. Bando, An experimental study of charge distribution in crystalline and amorphous Si nanoclusters in thin silica films, *J. Appl. Phys.*, 103 (2008) 024308.

- [18] S.P. Kowalczyk, L. Ley, R.L. Martin, F.R. McFeely, D.A. Shirley, Relaxation and final-state structure in XPS of atoms, molecules, and metals, *Faraday Discuss.*, 60 (1975) 7-17.
- [19] F.P.J.M. Kerkhof, J.A. Moulijn, Quantitative analysis of XPS intensities for supported catalysts, *J. Phys. Chem.*, 83 (1979) 1612-1619.
- [20] H. Shinotsuka, S. Tanuma, C.J. Powell, D.R. Penn, Calculations of electron inelastic mean free paths. X. Data for 41 elemental solids over the 50 eV to 200 keV range with the relativistic full Penn algorithm, *Surf. Interface Anal.*, 47 (2015) 871-888.
- [21] P.W. Park, J.S. Ledford, The influence of surface structure on the catalytic activity of alumina supported copper oxide catalysts. Oxidation of carbon monoxide and methane, *Appl. Catal. B*, 15 (1998) 221-231.
- [22] W. Błachucki, J. Czapla-Masztafiak, J. Sá, J. Szlachetko, A laboratory-based double X-ray spectrometer for simultaneous X-ray emission and X-ray absorption studies, *J. Anal. At. Spectrom.*, 34 (2019) 1409-1415.
- [23] B. Ravel, M. Newville, ATHENA, ARTEMIS, HEPHAESTUS: data analysis for X-ray absorption spectroscopy using IFEFFIT, *J. Synchrotron Radiat.*, 12 (2005) 537-541.
- [24] Z. Li, Chapter 5 - Scanning Transmission Electron Microscopy Studies of Mono- and Bimetallic Nanoclusters, in: R.L. Johnston, J.P. Wilcoxon (Eds.) *Frontiers of Nanoscience*, Elsevier 2012, pp. 213-247.
- [25] G. Ertl, H. Knözinger, J. Weitkamp, *Handbook of heterogeneous catalysis*, (2008).

# Chapter 3 The effect of metal precursor on copper phase dispersion and nanoparticle formation for the catalytic transformations of furfural.



### 3.1 Introduction

Current industrial practices for the manufacture of furfuryl alcohol in various countries such as the Dominican Republic, Brazil, South Africa and China all use copper chromate [1, 2]. Such materials have been a benchmark for the past 90 years [3-6] using temperatures of  $\sim 200$  °C and pressures of greater than 30 bar. But, there has been increasing concern about the environmental friendliness of chromite-based catalysts, as they lead to the formation of toxic chromic oxide causing severe environmental problems. Also on the industrial scale, this contributes to safe large-scale disposal challenges (especially with countries with less stringent environmental regulations) and contamination of the products downstream. So, there is a drive for energy-efficient and environmentally friendly alternative processes and materials, which can perform at milder temperature and pressure constraints.

In the literature, many chromate substitute catalysts have been investigated for the gas and liquid-phase transformation of furfural implementing Ir, Pd, Pt, Ru, Ni, Co and Cu [7-12]. Such investigations have shown that the catalytic reaction is dependent on the affinity of reactants for the metal, both in terms of hydrogen-metal and furfural-metal interaction [13, 14]. Taylor *et al.* [15] investigated the effect of support on the Pt catalysed liquid phase hydrogenation of furfural to furfuryl alcohol. The authors studied a variety of supports of different acidity, surface-area, and crystallinity. Despite their major physicochemical differences, supports like MgO, CeO<sub>2</sub> and  $\gamma$ -Al<sub>2</sub>O<sub>3</sub> were reported to perform well. The absence of strong metal-support interactions was reported, however, the support selection appeared to be important to achieve a good dispersion of the metal. In the current work, crystalline nano-Al<sub>2</sub>O<sub>3</sub> was used to allow the active Cu phase to be more accessible to the substrate as compared, for instance with standard porous aluminas (same with other mesoporous materials) which regularly suffer from mass transfer problems as well as the blocking of pores and deterioration of the surface area at high temperatures/prolonged use.

The modification of copper surfaces with sulfur was thoroughly studied for the hydrogenation of crotonaldehyde, both on single crystals and dispersed catalysts [16-20]. Lambert and co-workers [17, 21] found that sulfur atoms activate the copper surface towards the chemoselective transformation of

crotonaldehyde. It was reported this was due to sulfur-induced rehybridization of the adsorbed reactant, which lead to the weakening of the intermolecular bonding and tilting of the C = O and C = C groups with respect to the surface, thus facilitating the interaction with adsorbed hydrogen. Their observations also support earlier investigations by Hutchings *et al.* [16, 19, 20], sulfur promotes crotyl alcohol formations using Cu/Al<sub>2</sub>O<sub>3</sub> catalysts. Conversely, May *et al.* [22] reported that sulfur addition can act as a poison, since it changes the electron characteristics of the surface, such as the work function, altering the metal-metal distances in the top-most atomic row.

This chapter investigates the effect of metal precursors in the generation of Cu/Al<sub>2</sub>O<sub>3</sub> catalysts via a simple wet impregnation method as is commercially used to synthesis heterogeneous catalysts. The synthesis was investigated in two separate Cu loadings the first one leading to the creation of metal nanoparticles. The second one, leading to the formation of a highly dispersed Cu phase consisting mostly of single atoms and dimers on the alumina surface. By utilising a mechanism by which Cu binds to the alumina's surface before the catalytically necessary reduction, rows of copper ions are formed at low coverage. As the loading/calcination temperature increases paracrystalline and finally crystalline CuO is generated [23]. The role of sulfur impurities on the catalyst surface was also investigated by comparing Cu/Al<sub>2</sub>O<sub>3</sub> catalysts prepared using two sulfur-free precursors and one sulfur-containing precursor. The role of sulfur was studied as the literature lacked studies examining Cu catalytic systems on the hydrogenation of furfural, as in some cases, as mentioned earlier, sulfur can act as a promoter or a poison. Consequently, the structure sensitivity of the reaction and the effect of the chosen metal precursor was also explored which has not been previously.

## 3.2 Characterisation of Cu-based catalysts

### 3.2.1 Elemental and Surface Area Analysis

Table 3.2.1 shows the elemental analysis and the surface area measurements of the supported catalysts after calcination and reduction. The Cu loading was found close to the nominal loading but the observable differences in loading between the precursors are due to the differences in the thermal stability and reducibility of the precursors [24-26]. It is reported by Ghose *et al.* [24] that decomposition of  $\text{Cu}(\text{NO}_3)_2 \cdot 3\text{H}_2\text{O}$  in air is followed by the melting of nitrate crystals then the formation of  $[\text{Cu}(\text{NO}_3)_2 \cdot 3\text{Cu}(\text{OH})_2]$  crystals and finally, with the formation of CuO at 310 °C. Also, the breakdown of  $\text{Cu}(\text{CO}_2\text{CH}_3)_2 \cdot \text{H}_2\text{O}$  occurs under 500 °C [25], where dehydration takes place, forming peroxides which decompose into a mixture of Cu,  $\text{Cu}_2\text{O}$  and CuO. Cu and  $\text{Cu}_2\text{O}$  are then oxidised to CuO between 302-500 °C in air. In contrast,  $\text{CuSO}_4$  higher thermal stability in air results in a decomposition temperature of 598 °C [27], with  $\text{CuO} \cdot \text{SO}_3$  intermediate compounds also being formed. In a reductive  $\text{H}_2$  atmosphere, CuO is readily reduced to Cu between 200-300 °C, while  $\text{CuSO}_4$  starts to reduce at 300 °C [28]. Examining the isotherms of the reduced materials shows Type II isotherms (Fig. 3.2.1), suggesting they are non-porous/macroporous, however, the small noticeable hysteresis may have arisen from experimental error or slight defects in the structure or the Cu/Al interfaces causing filling (by  $\text{N}_2$  molecules) of such voids/steps. While the surface area measurements of the catalytic materials are observed to be largely unchanged to the bare support. However, the lower noticeable surface of the 5

wt% Cu/Al<sub>2</sub>O<sub>3</sub> (S) may likely be due to the formation of low surface area Al<sub>2</sub>(SO<sub>4</sub>) through the reaction with the Al<sub>2</sub>O<sub>3</sub> and SO<sub>3</sub> [29].

*Table 3.2.1. Bulk elemental analysis and surface area measurements. Catalysts synthesised using copper nitrate, copper acetate and copper sulfate pentahydrate were denoted (N), (A) and (S), respectively.*

Catalyst	Nominal Cu loading (wt%)	Actual Cu loading <sup>a</sup> (wt%)	Surface area <sup>b</sup> (m <sup>2</sup> g <sup>-1</sup> )
Cu/ Al <sub>2</sub> O <sub>3</sub> (N)	1.0	0.83 ± 0.04	36 ± 2
Cu / Al <sub>2</sub> O <sub>3</sub> (A)	1.0	0.91 ± 0.05	35 ± 2
Cu/ Al <sub>2</sub> O <sub>3</sub> (S)	1.0	0.66 ± 0.08	39 ± 2
Cu/Al <sub>2</sub> O <sub>3</sub> (N)	5.0	4.22 ± 0.32	34 ± 2
Cu / Al <sub>2</sub> O <sub>3</sub> (A)	5.0	4.56 ± 0.36	33 ± 2
Cu/ Al <sub>2</sub> O <sub>3</sub> (S)	5.0	4.22 ± 0.31	30 ± 2
Al <sub>2</sub> O <sub>3</sub>	-	-	38 ± 2

<sup>a</sup> ICP-OES, <sup>b</sup> BET

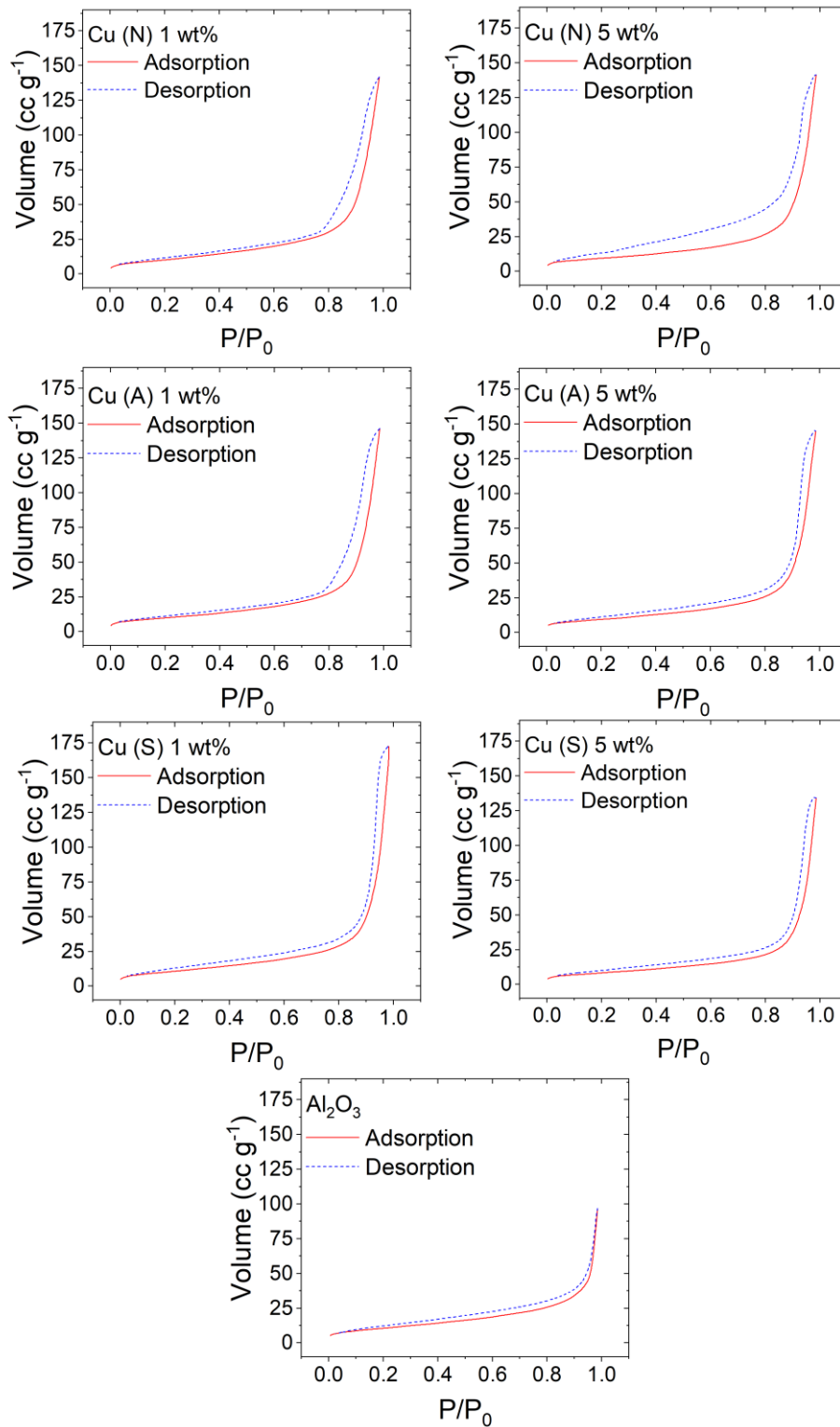


Fig. 3.2.1 Isotherm for Cu/Al<sub>2</sub>O<sub>3</sub> catalysts as well as the bare support.

### 3.2.2 Powder X-Ray Diffraction (PXRD)

Fig. 3.2.2 (a) illustrates *ex-situ* XRD diffractograms from the copper catalysts used in this study after reduction at 300 °C for 0.5 h. The characteristic of nano-crystalline  $\gamma$ -Al<sub>2</sub>O<sub>3</sub> (JCPDS card No. 29-0063) and  $\delta$ -Al<sub>2</sub>O<sub>3</sub> (JCPDS card No. 46-1215), as well as a small impurity of  $\theta$ -Al<sub>2</sub>O<sub>3</sub> phase (JCPDS card No. 11-0517) broad reflections but visible reflections are observed. Qualitatively examining the diffractograms, the nano-crystalline alumina's long-range order appears to be unchanged after Cu deposition. This suggests the copper phase did not appreciably alter the alumina morphology after the various thermal processing steps. In the case of 5 wt% Cu catalysts, the estimated Cu lattice parameters of 3.628 Å (Table 3.2.2) were found to be close to that of bulk Cu (JCPDS card No. 40836). The observation of Cu reflections indicates the Cu phase is predominately in its metallic state after *ex-situ* reduction since diffraction peaks of CuO and Cu<sub>2</sub>O at 35.5° and 42.7° could not be resolved [30]. Diffraction peaks associated with Cu species were not detected for the 1 wt% Cu samples in both their calcined and reduced state (Fig. 3.2.2); in agreement with STEM, suggesting the Cu phase is highly dispersed resulting in extremely broad diffraction peaks.

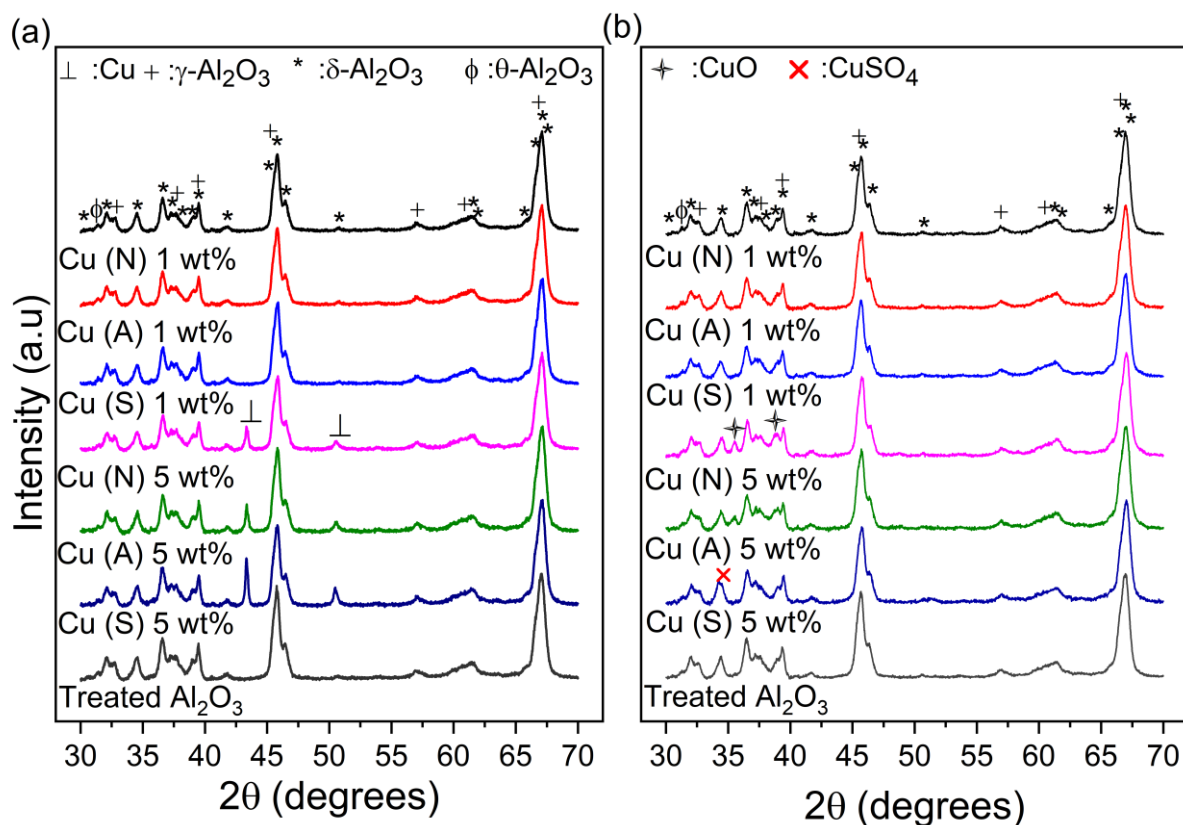


Fig. 3.2.2 XRD patterns of (a) reduced and (b) calcined Cu/Al<sub>2</sub>O<sub>3</sub> catalysts synthesised from their respective copper nitrate (N), copper acetate (A) and copper sulfate (S) precursors at loadings of 5 wt% and 1 wt%.

Table 3.2.2 Tabulated crystallite sizes, particle sizes, lattice parameters and bond lengths. Catalysts synthesised using copper nitrate, copper acetate and copper sulfate pentahydrate were denoted (N), (A) and (S), respectively.

Catalyst	Nominal Cu loading (wt%)	Cu crystallite size <sup>a</sup> (nm)	Cu crystallite size <sup>b</sup> (nm)	Cu particle size <sup>c</sup> (nm)	Cu lattice parameter <sup>b</sup> (Å)	WPPM Fit
Cu/Al <sub>2</sub> O <sub>3</sub> (N)	1	-	-	-	-	-
Cu/Al <sub>2</sub> O <sub>3</sub> (A)	1	-	-	-	-	-
Cu/Al <sub>2</sub> O <sub>3</sub> (S)	1	-	-	-	-	-
Cu/Al <sub>2</sub> O <sub>3</sub> (N)	5	19.6 ± 4.1	13.2 ± 9.5	3.9 ± 1.9	3.628	4.3% <sup>d</sup> , 67.7 <sup>e</sup>
Cu/Al <sub>2</sub> O <sub>3</sub> (A)	5	19.7 ± 4.3	13.0 ± 9.4	6.8 ± 5.5	3.628	4.3% <sup>d</sup> , 67.7 <sup>e</sup>
Cu/Al <sub>2</sub> O <sub>3</sub> (S)	5	24.7 ± 2.8	18.7 ± 12.9	12.8 ± 9.3	3.627	4.2% <sup>d</sup> , 69.5 <sup>e</sup>

<sup>a</sup> Integral breadth method via XRD, <sup>b</sup> WPPM via XRD, <sup>c</sup> STEM, <sup>d</sup> Rwp and <sup>e</sup> WSS.

To examine composition changes of the Cu phase during the reduction step, *in-situ* XRD diffraction experiments were conducted on one sulfur-free and sulfur containing catalysts. Fig. 3.2.3a shows CuO forms after calcination for the 5 wt% Cu/Al<sub>2</sub>O<sub>3</sub> (A) catalyst. And it only starts to reduce into metallic Cu between 100 to 200 °C with both the features of CuO and Cu at 200 °C. At 300 °C, the CuO phase is fully reduced to Cu. Increasing the temperature further appears to not considerably increase the

crystallite size but increase the Cu crystallinity (monitored by the increased Cu (111) reflection intensity). In contrast, the 5 wt% Cu/Al<sub>2</sub>O<sub>3</sub> (S) catalyst (Fig. 3.2.3b) shows CuSO<sub>4</sub> reflections at 25 °C, indicating the calcination at 500 °C for 4 h cannot reduce CuSO<sub>4</sub> completely to CuO. In a similar manner as for the sulfur-free catalyst at 200 °C both the CuSO<sub>4</sub> and Cu is present, and at 300 °C CuSO<sub>4</sub> is reduced to Cu.

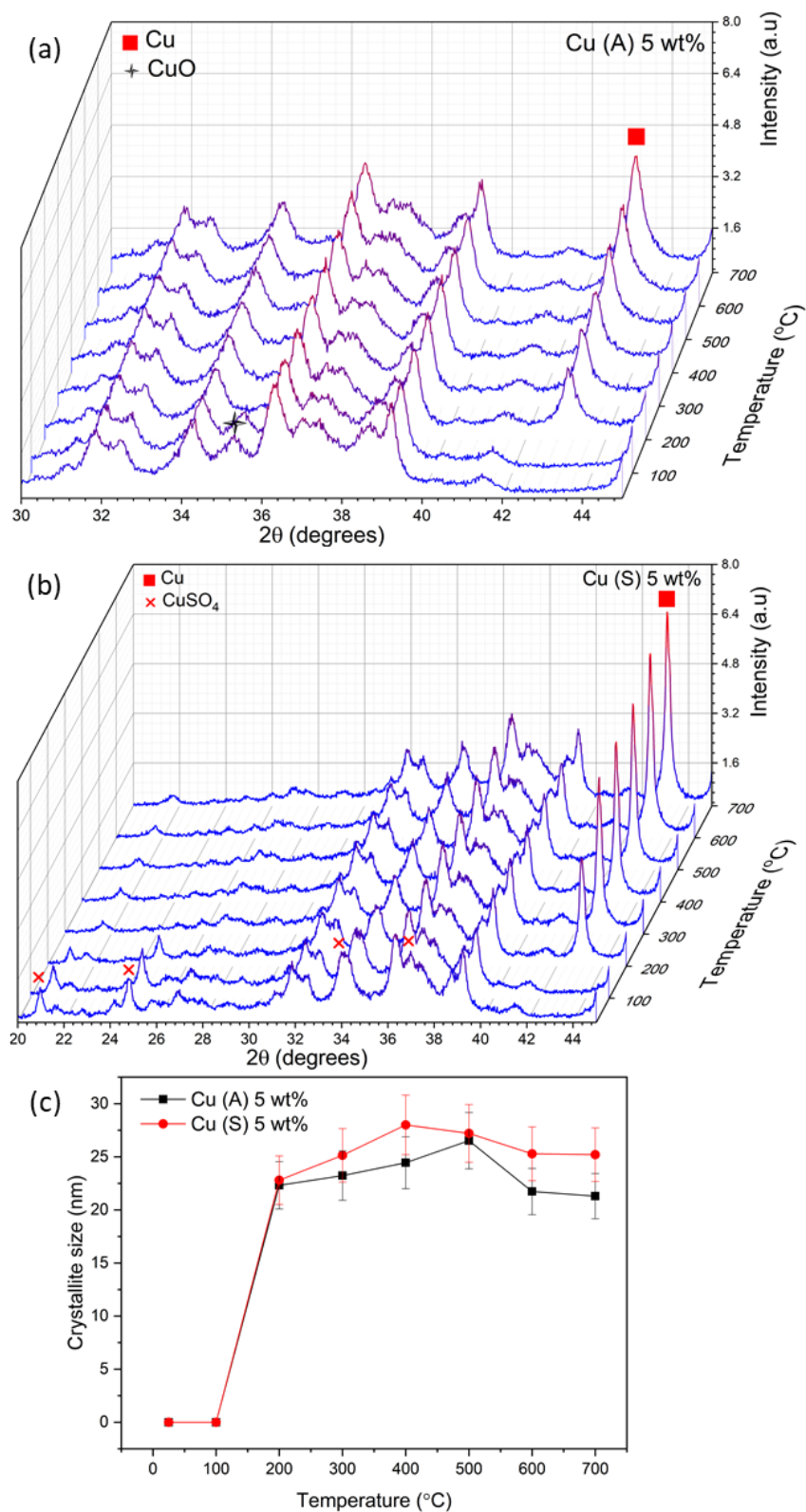


Fig. 3.2.3 In-situ XRD diffractograms of (a) 5 wt% Cu/Al<sub>2</sub>O<sub>3</sub> (A), (b) 5 wt% Cu/Al<sub>2</sub>O<sub>3</sub> (S) catalysts and (c) the change in volume-weighted Cu crystallite size in a reductive atmosphere (20% H<sub>2</sub>/80% He gas flow) between 25-700 °C.

### 3.2.3 Scanning Transmission Electron Microscopy (STEM)

Investigation of the 1 wt% Cu/Al<sub>2</sub>O<sub>3</sub> catalysts with STEM could not establish the existence of any Cu regions. Possibly owing to the combination of low Z-contrasts between Cu and Al entities and the presence of highly dispersed Cu phase embedded onto the Al<sub>2</sub>O<sub>3</sub> superstructure are not resolved. The interpreted EXAFS data, discussed later, suggests the Cu atoms exist mostly as single/dimer species on the surface of the Al<sub>2</sub>O<sub>3</sub> support. In contrast, STEM images of the 5 wt% catalysts (Fig. 3.2.4) show the detection of Cu particles after *ex-situ* reduction. The calculated particle sizes (assuming monocrystallinity) by PXRD of the 5 wt% Cu/Al<sub>2</sub>O<sub>3</sub> (N) and (A) appears to be similar when calculated through both methods (integral breadth and WPPM). But, the trend is not seen in the STEM measured particle sizes, due to the low Z-contrast ratios active-phase and alumina support and the difficulty of identifying small species. Resulting in the overestimating particle size. The conjunction of the PXRD and STEM analysis of the 5 wt% Cu/Al<sub>2</sub>O<sub>3</sub> (N) and (A) catalysts imply that part of the copper-phase is absent of consistent geometric structure. The strange structure is attributed to the mechanism by which the Cu<sup>2+</sup> species are bound to the alumina surface, whereby the Cu<sup>2+</sup> species (from CuO) proceeding calcination are coordinated as rows of copper ions in a tetrahedral/octahedral symmetry via alumina's oxygen atoms, extending alumina's oxide network [23, 31]. As a result, an isolated or paracrystalline CuO phase is formed on the alumina's surface, observed by the estimated ~100% Cu dispersion of the 1 wt% calcined catalyst in Table 3.2.4. In the case of their higher loaded counterparts. Marion *et al.* [31] suggest increasing the loading causes the Cu to oversaturate the alumina's surface, such that the octahedral Cu species begin to sinter into particles from a layered structure during calcination. Consequently, explaining why both layered structures and particles are reported. After reduction, the Cu dispersion is discovered to decrease which is thought to be due to the breakdown of the strong Cu-O links to the support. Thus, allowing Cu atoms to be more mobile resulting in the layered and particle

arrangement. The measured lattice spacing of such layered structures shown in Fig. 3.2.4b is found to be 0.205 nm, indicative of the Cu (111) lattice plane [32].

In contrast, the 5 wt% Cu/Al<sub>2</sub>O<sub>3</sub> (S) displays large distinct particles approximately 12.8nm with a large standard deviation of 9.3 nm. The larger particle size, when compared to the other Cu precursors, is credited to the incomplete CuSO<sub>4</sub> decomposition to CuO (CuSO<sub>4</sub> reflections at 20.7° and 24.6° are observed in the calcined sample, Fig. 3.2.2b). Causing the remaining CuSO<sub>4</sub> to reduce completely from CuSO<sub>4</sub> to Cu into larger particles. The particle size distributions from STEM and computed from XRD using WPPM (Fig. 3.2.5) was found to quite consistent considering XRD has a tough time measuring very small crystallite sizes (below 3 nm). Since broad reflections arising from small crystallites become difficult to resolve from the background (due to destructive interference of the signal). One can also observe that the simple line profile analysis via the integral breadth method is inadequate in this system as a volume-weighted crystallite size is calculated. This leads to crystallite or particle size (assuming particles are monocrystalline) considerably larger than particle size determined from STEM and WPPM (Fig. 3.2.5).

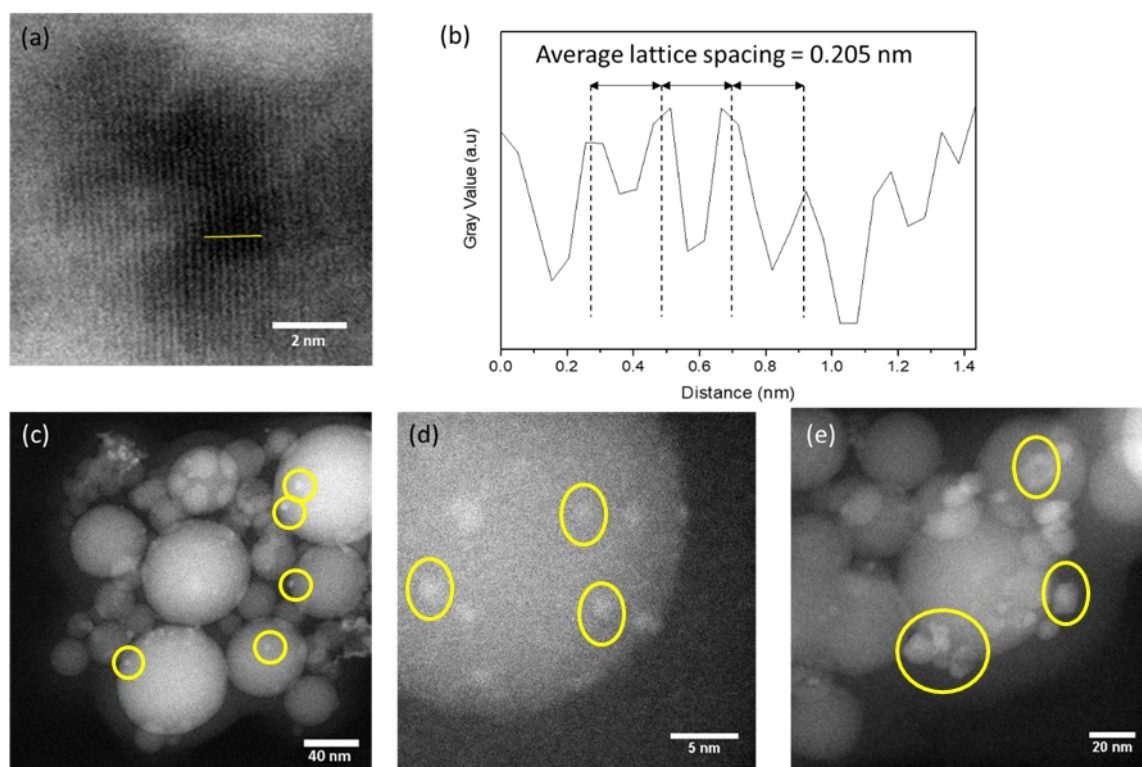


Fig. 3.2.4 Bright and Dark field STEM images and interplanar spacing measurement of (a) 5 wt% Cu/Al<sub>2</sub>O<sub>3</sub> (A), (b) lattice spacing of 5 wt% Cu/Al<sub>2</sub>O<sub>3</sub>, area of measurement indicated by a yellow line. (c) 5 wt% Cu/Al<sub>2</sub>O<sub>3</sub> (A, low magnification), (d) 5.0 wt% Cu/Al<sub>2</sub>O<sub>3</sub> (N) and (e) 5.0 wt% Cu/Al<sub>2</sub>O<sub>3</sub> (S).

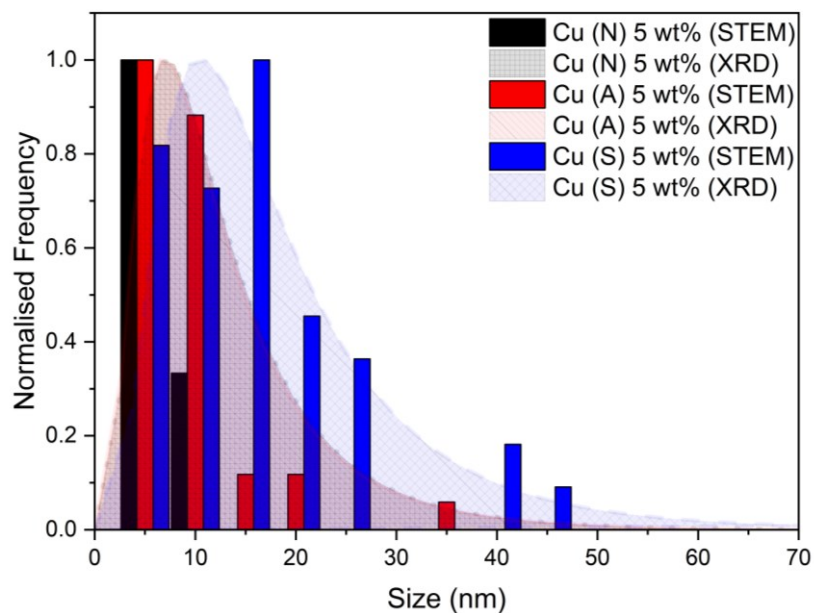


Fig. 3.2.5 Copper size distribution for 5 wt% Cu/Al<sub>2</sub>O<sub>3</sub> catalysts after reduction. STEM (histogram, roughly 100 particles counted for each catalysts) and WPPM result (lognormal distributions).

### 3.2.4 X-ray Photoelectron Spectroscopy (XPS) and X-ray excited Auger Electron Spectroscopy (XAES)

Fig. 3.2.6a displays XPS spectra of catalysts reduced *ex-situ* along with the CuO and Cu<sub>2</sub>O reference standards. All six catalytic materials show the characteristic Cu 2p doublet with the Cu 2p<sub>3/2</sub> transition centred at ~932.8 eV. The absence of the strong shake-up satellites at ~942.6 eV and ~962.3 eV, particularly for the nominal 1 wt% Cu/Al<sub>2</sub>O<sub>3</sub> catalysts, suggests the absence of Cu<sup>2+</sup> species (CuO or CuSO<sub>4</sub>) and that the Cu is mainly in its Cu<sup>0</sup> or Cu<sup>+</sup> oxidation state. Catalysts with a nominal copper loading of 5 wt% but, show a noticeable presence of the shake-up satellite, suggesting that these materials contain more CuO than the 1 wt% Cu/Al<sub>2</sub>O<sub>3</sub> catalysts. Oxidation of the catalyst is expected as the samples have been exposed to the atmosphere before analysis. The compositional differences between 1 wt% and 5 wt% can be due to the mechanism of Cu nanoparticle oxidation, where initially it forms Cu<sub>2</sub>O [33] and then transforms into CuO (on the surface) [34, 35] and since the 5 wt% have more Cu available, the faster the full oxidation occurs. The Cu 2p binding energies of Cu<sup>+</sup> and Cu<sup>0</sup> are very similar, and deconvolution of the spectra is difficult, however, the chemical shift in Auger spectroscopy is more prominent. The L<sub>3</sub>VV Auger spectrum of the reference Cu<sub>2</sub>O spectrum is found shifted substantially to lower kinetic energies compared to bulk metallic Cu. Though it should be noted, x-ray induced reduction can occur, altering the observed composition.

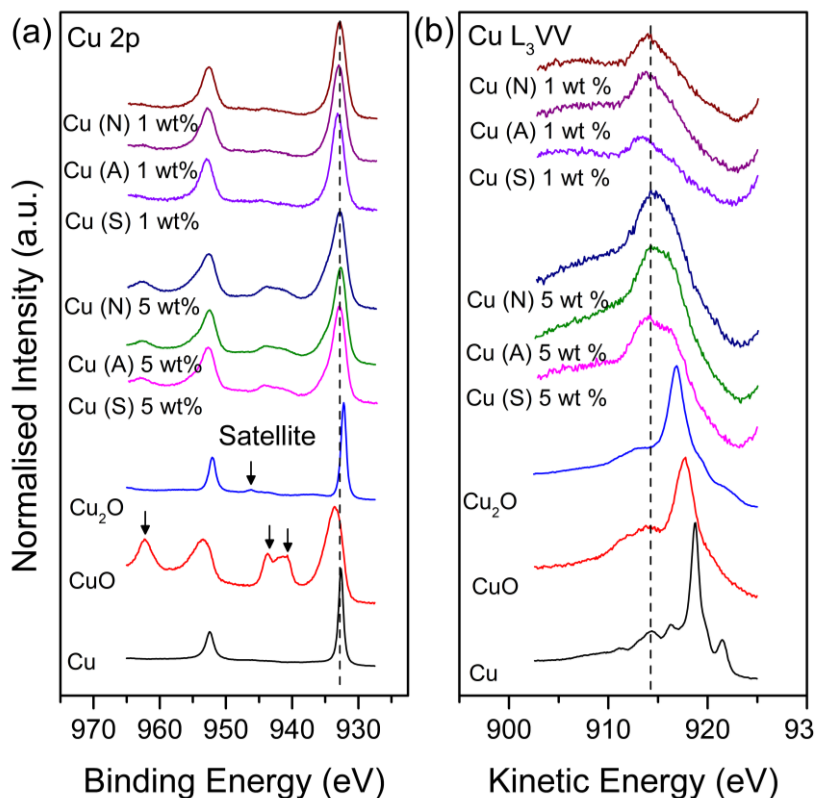


Fig. 3.2.6 High resolution stacked XPS and XAES spectra of the (a) Cu 2p and (b) Cu  $L_3VV$  for the six Cu/Al<sub>2</sub>O<sub>3</sub> catalysts after calcination and reduction at 500 °C and 300 °C respectively. Reference spectra of the Cu, CuO and Cu<sub>2</sub>O [36] are also presented.

Auger spectra of the catalysts are attenuated compared to the bulk reference materials, and the peaks found shifted to lower kinetic energies (Fig. 3.2.6b and Table 3.2.3). This observation was also reported previously [37-40], finding that the binding energies, Auger lines and consequently the modified Auger parameter,  $\alpha'$  is very sensitive to the metal-support effects and particle size. The modified Auger parameter is a final state effect, providing an estimate of the relaxation energy/screening energy in the presence of core holes [41], while also not suffering from charging and inadequate calibration aberrations [42]. The relaxation energy can be interpreted as a secondary process where the surrounding electrons react to the sudden appearance of a positive core-hole after photoemission. The screening of the core-hole by the influx of electrons lowers the measured  $E_b$  [43]. The relaxation energy can be partitioned into intra-atomic relaxation energy and extra-atomic relaxation energy; with the former remaining constant for core-electrons in a given atom, while the latter varies with changes in the chemical and physical states. A high  $\alpha'$  indicates higher relaxation energy or improved screening

energy. This can be caused by a greater number of atoms able to screen the core-hole better after photoemission when examining differently size copper structures or different polarizable supports.

*Table 3.2.3. Summarised binding energies for Cu 2p<sub>3/2</sub>, kinetic energies for the Auger Cu L<sub>3</sub>VV transitions, modified Auger parameters for copper catalysts and change in relaxation energy compared to bulk Cu for catalysts and reference materials.*

Sample	Cu 2p 3/2 E <sub>b</sub> (eV)	Cu L <sub>3</sub> VV E <sub>k</sub> (eV)	Modified Auger parameter α' (eV)	Change in relaxation energy ΔR (eV)
Cu/Al <sub>2</sub> O <sub>3</sub> (N) 1 wt%	932.82	914.09	1846.91	2.24
Cu/Al <sub>2</sub> O <sub>3</sub> (A) 1 wt%	932.97	913.76	1846.73	2.33
Cu/Al <sub>2</sub> O <sub>3</sub> (S) 1 wt%	933.13	913.41	1846.54	2.42
Cu/Al <sub>2</sub> O <sub>3</sub> (N) 5 wt%	932.78	914.93	1847.71	1.84
Cu/Al <sub>2</sub> O <sub>3</sub> (A) 5 wt%	932.68	914.69	1847.37	2.01
Cu/Al <sub>2</sub> O <sub>3</sub> (S) 5 wt%	932.88	914.73	1847.61	1.88
CuSO <sub>4</sub>	935.42	915.40	1850.82	0.28
CuO	933.62	917.78	1851.40	-0.01
Cu <sub>2</sub> O	932.29	916.70	1848.99	1.20
Cu**	932.63	918.75	1851.30	0.00

\*\* Cu 2p 3/2 was calibrated to the ISO standard of 932.63 eV.

In agreement with the current work, the Auger parameter of the catalysts to be on average ~1847.0 eV, drastically lower than that of bulk copper ( $\alpha'_{\text{bulk}} = 1851.3$  eV, shown in Table 3.2.3). The shift is contributed largely to the polarizability of the support [40]. Assessing the modified Auger parameter between the catalysts of different loadings, summarised in Table 3.2.3, the  $\alpha'$  is observed to increase with increasing copper ensemble size. A similar trend is seen in the change of the relaxation energy in reference to bulk copper,  $\Delta R$ . All catalysts exhibit stark changes in their relaxation energies compared to bulk copper. Remarkably, the 1 wt% Cu/Al<sub>2</sub>O<sub>3</sub> catalysts exhibit larger changes in their approximated  $\Delta R$  values compared to their higher Cu loading counterparts. Assumed to be due to the diminishing number of Cu atoms in their nanostructures and the greater interaction with the support due to the higher dispersion (Table 3.2.4). Consequently, the Auger parameter can give an insight into the dispersion/oxidation state of the active phase which crucial for active catalytic materials. As mentioned previously (section 3.2.3), the XPS calculated Cu dispersion decreases considerably after the reduction of the catalyst which can be understood by the reduction of the Cu-O support links, allowing the Cu species to be more mobile and sintering into larger structures. The stacked spectra in Fig. 3.2.6 possibly

suggest an oxidised outer surface layer comprised mostly of CuO, especially for the 5 wt% Cu/Al<sub>2</sub>O<sub>3</sub> catalysts, and an underlying Cu<sup>0</sup> bulk which was confirmed by XRD in Fig. 3.2.2a. The data endorse Rhodin's findings that at room temperature, oxidation occurs swiftly for the first few seconds or minutes. After which a thin oxide layer forms (~0.5 nm) and the rate of oxidation falls to negligible values [44]. Thus, explaining why an oxide layer is not detected in the diffractogram (Fig. 3.2.2a).

Table 3.2.4 Calculated particle size and dispersion from XPS for the six monometallic catalysts in both their calcined and reduced (*ex-situ*) state.

Catalyst	Bulk Cu loading (wt%)	Treatment	XPS particle size (nm)	Dispersion (%)
Cu/Al <sub>2</sub> O <sub>3</sub> (N) 1 wt%	0.8	Calcined	-	100.0 ± 10.0
		Reduced	0.8 ± 0.1	67.3 ± 6.7
Cu/Al <sub>2</sub> O <sub>3</sub> (A) 1 wt%	0.9	Calcined	-	99.6 ± 10.0
		Reduced	0.6 ± 0.1	74.7 ± 7.5
Cu/Al <sub>2</sub> O <sub>3</sub> (S) 1 wt%	0.6	Calcined	-	99.7 ± 10.0
		Reduced	0.9 ± 0.1	60.2 ± 6.0
Cu/Al <sub>2</sub> O <sub>3</sub> (N) 5 wt%	4.2	Calcined	3.4 ± 0.3	28.8 ± 2.9
		Reduced	5.4 ± 0.5	18.8 ± 1.9
Cu/Al <sub>2</sub> O <sub>3</sub> (A) 5 wt%	4.6	Calcined	2.1 ± 0.2	41.4 ± 4.1
		Reduced	5.1 ± 0.5	19.8 ± 2.0
Cu/Al <sub>2</sub> O <sub>3</sub> (S) 5 wt%	4.2	Calcined	4.2 ± 0.4	23.9 ± 2.4
		Reduced	5.1 ± 0.5	19.6 ± 2.0

The S 2p region was also probed (Fig. 3.2.7a), catalysts derived from copper sulfate displayed a peak at ~169.2 eV, indicative of sulfate species (bulk sulfur has a binding energy of 164.0 eV [45]). However, it should be reiterated that *in-situ* PXRD measurements Fig. 3.2.3b did not show any reflections that can be assigned to CuSO<sub>4</sub> when reduced at 300 °C and above. It is also known that Al<sub>2</sub>(SO<sub>4</sub>)<sub>3</sub> could also be formed from the decomposition of CuSO<sub>4</sub> via the reaction between SO<sub>3</sub> and Al<sub>2</sub>O<sub>3</sub> [46]. The XPS results, however, suggest that sulfate species may remain in an amorphous fashion on the copper surface at 300 °C. In contrast, the N 1s region of the XPS did not detect nitrate compounds (Fig. 3.2.7b), indicating the nitrate precursor decomposed fully without leaving trace nitrates.

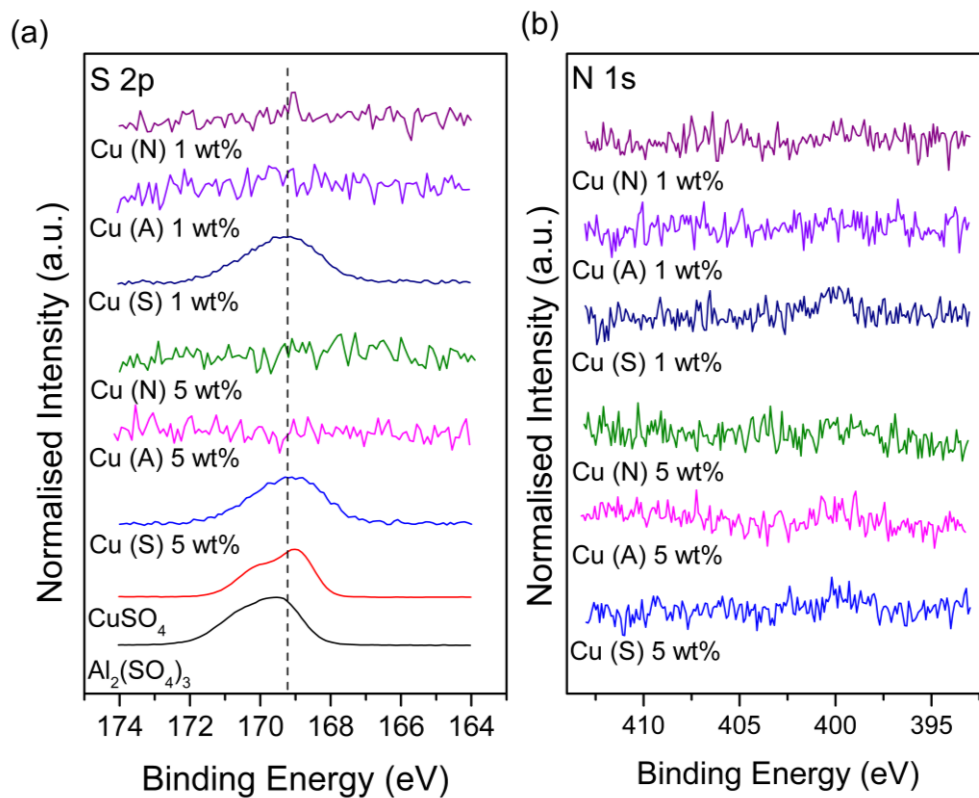


Fig. 3.2.7 High resolution stacked XPS of the (a) S 2p and (b) N 1s for the six Cu/Al<sub>2</sub>O<sub>3</sub> catalysts after calcination and reduction at 500 °C and 300 °C respectively. Reference spectra of the CuSO<sub>4</sub> and Al<sub>2</sub>(SO<sub>4</sub>)<sub>3</sub> are also presented.

### 3.2.5 X-ray Absorption Spectroscopy (XAS)

Linear combination fitting (LCF) was performed on the Cu K-edge XANES spectra (Fig. 3.2.8) and summarised in Table 3.2.5. The disparity in the metallic Cu composition between the 5 wt% Cu/Al<sub>2</sub>O<sub>3</sub> is due to particle size, as the larger the particle, the lower the surface area and less oxidation occurs. LCF did not show the presence of a metallic Cu phase for the 1 wt% catalysts. While an inadequate fit was deconvoluted with CuO but even so, the absorption edge was observed to be shifted to higher energies suggesting the presence of Cu ions, possibly bound to the alumina support.

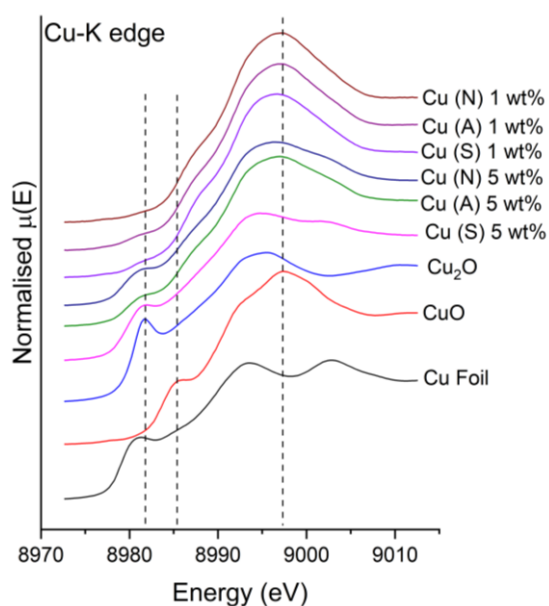


Fig. 3.2.8 Normalised Cu-K edge XANES spectra of six Cu/Al<sub>2</sub>O<sub>3</sub> catalysts (reduced ex-situ) and reference standards.

Table 3.2.5 Cu K edge energies and XANES linear combination fitting.

Sample	Edge energy (eV)	Cu (%)	CuO (%)	Cu <sub>2</sub> O (%)	R factor
Cu/Al <sub>2</sub> O <sub>3</sub> (N) 1 wt%	8980.9	0	100	0	0.027
Cu/Al <sub>2</sub> O <sub>3</sub> (A) 1 wt%	8980.0	0	100	0	0.022
Cu/Al <sub>2</sub> O <sub>3</sub> (S) 1 wt%	8980.4	0	100	0	0.023
Cu/Al <sub>2</sub> O <sub>3</sub> (N) 5 wt%	8979.4	32.6	67.4	-	0.008
Cu/Al <sub>2</sub> O <sub>3</sub> (A) 5 wt%	8979.7	18.6	81.4	-	0.01
Cu/Al <sub>2</sub> O <sub>3</sub> (S) 5 wt%	8979.7	41.5	24.2	34.4	0.001
Cu <sub>2</sub> O	8980.6	-	-	-	-
CuO	8983.9	-	-	-	-
Cu	8979.0	-	-	-	-

EXAFS model fitting displayed in Fig. 3.2.9 and summarised in Table 3.2.6 reinforce the earlier characterisation data. The EXAFS spectra in R-space (phase uncorrected) presented in Fig. 3.2.9b imply the 1 wt% Cu/Al<sub>2</sub>O<sub>3</sub> catalysts lack long-range order as the signal quickly attenuated after the Cu-O shell (1.96 Å). In contrast, the Cu foil spectrum has a strong photon scattering 6 Å away from the absorbing atom. Though the scattering signal is expected to attenuate quickly with disordered/less-coordinated systems like nanoparticles [47]. In addition, the coordination number of these oxidised catalysts suggest the Cu atoms are almost entirely coordinated to oxygen. Also, the lack of the Cu-Cu scattering path (arising from Cu-O-Cu bonds at 2.90 Å) normal for CuO, together with the XANES implies that the Cu atoms are likely coordinated with oxygen atoms on the alumina support. The copper impregnation process was investigated by Cheah *et al.* [48, 49] via XAS suggests the Cu/ $\gamma$ -Al<sub>2</sub>O<sub>3</sub> system consists of octahedral Cu<sup>2+</sup> (O, OH)<sub>6</sub> species. These species are appearing on the surface as monomeric, dimeric and oligomeric hydroxo-bridged with Cu-O equatorial bond lengths of 1.95 Å. Further operando XAS studies by Cassinelli *et al.* [50] indicates that once the catalyst is calcined the octahedral Cu<sup>2+</sup> (O, OH)<sub>6</sub> structure persists. Proceeding reduction (250 °C in an H<sub>2</sub>/He atmosphere) however, they report the incomplete reduction of the Cu<sup>2+</sup> species to Cu<sup>+</sup> and Cu<sup>0</sup>. In the present case (reduction at 300 °C in H<sub>2</sub>), the reduction of the Cu<sup>2+</sup> species follows with the reduction of such hydroxo-bridges leaving behind a metallic Cu-Cu bond, creating a paracrystalline structure (as discussed earlier in section 3.2.3) and when exposed to the atmosphere (during sample transfer), an oxide passivation layer forms. The lack of Cu-Cu coordination for the 1 wt% catalyst (N) (Table 3.2.6) suggests the Cu atoms after reduction are atomically dispersed (single-atom catalyst) while the remaining 1 wt% catalysts comprise isolated/dimer Cu atoms (due to the average coordination being <1 for Cu-Cu) on the alumina's surface [23]. The 5 wt% Cu/Al<sub>2</sub>O<sub>3</sub> (A) catalyst's Cu-Cu bond seems to be noticeably more strained (longer bond lengths) and lower coordination compared to its similar loaded counterparts. This suggests that this catalyst has a transitional morphology between the other 5 wt% catalysts and the 1 wt% catalysts. The shorter Cu-O bond lengths observed for the 5 wt% is explained by the presence of sintered particles with an oxide layer consisting of Cu<sub>2</sub>O (1.88 Å) and CuO (1.96 Å).

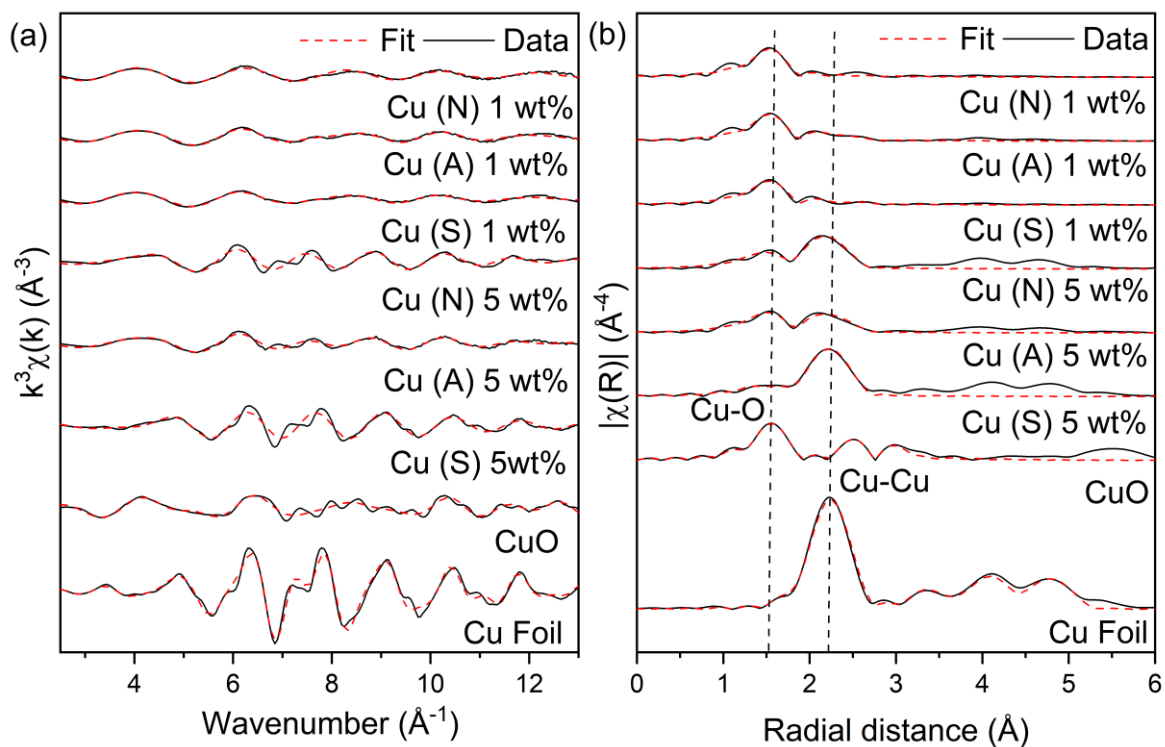


Fig. 3.2.9 EXAFS spectra in (a) *k*-space (*k*-weight = 3) and (b) *R*-space (*k*-weight = 3) for the ex-situ reduced Cu/Al<sub>2</sub>O<sub>3</sub> catalysts along with Cu and CuO reference foil/powder. A *k* range of 3.0 – 12.8 Å<sup>-1</sup> was used to Fourier transform and analyse the data.

Table 3.2.6 EXAFS model fitting of reduced ex-situ Cu/Al<sub>2</sub>O<sub>3</sub> catalysts, Cu and CuO reference foil/powder.

Sample	Shell	CN	R (Å)	$\sigma^2$ (Å <sup>2</sup> )	$\Delta E_0$ (eV)	R factor
Cu foil	Cu-Cu	12	2.551 ± 0.054	9.3 ± 0.8	2.96 ± 0.84	0.0270
CuO	Cu-O	4	1.956 ± 0.004	3.2 ± 0.5	5.74 ± 0.50	0.0013
Cu/Al <sub>2</sub> O <sub>3</sub> (N) 1 wt%*	Cu-O	3.0 ± 0.3	1.953 ± 0.010	4.9 ± 1.3	-2.93 ± 1.46	0.0087
Cu/Al <sub>2</sub> O <sub>3</sub> (N) 1 wt%#	Cu-Cu	0.4 ± 0.3	2.569 ± 0.024	8.0 ± 6.5	-3.40 ± 1.0	0.0097
	Cu-O	3.0 ± 0.2	1.950 ± 0.007	4.8 ± 0.9		
Cu/Al <sub>2</sub> O <sub>3</sub> (A) 1 wt%*#	Cu-O	2.9 ± 0.6	1.959 ± 0.020	5.1 ± 2.5	-1.78 ± 2.62	0.0265
Cu/Al <sub>2</sub> O <sub>3</sub> (A) 1 wt%	Cu-Cu	0.9 ± 0.3	2.577 ± 0.011	8.9 ± 3.0	-3.14 ± 0.93	0.0081
	Cu-O	2.8 ± 0.2	1.950 ± 0.007	4.9 ± 0.8		
Cu/Al <sub>2</sub> O <sub>3</sub> (S) 1 wt%*#	Cu-O	3.2 ± 0.6	1.967 ± 0.019	6.7 ± 2.6	-2.85 ± 2.46	0.0242
Cu/Al <sub>2</sub> O <sub>3</sub> (S) 1 wt%	Cu-Cu	0.7 ± 0.6	2.605 ± 0.024	11.7 ± 7.5	-3.82 ± 1.31	0.0141
	Cu-O	3.1 ± 0.3	1.960 ± 0.010	6.3 ± 1.3		
Cu/Al <sub>2</sub> O <sub>3</sub> (N) 5 wt%	Cu-Cu	3.7 ± 0.6	2.554 ± 0.012	8.9 ± 1.3	-7.69 ± 1.93	0.0111
	Cu-O	2.7 ± 0.6	1.919 ± 0.017	9.2 ± 3.2		
Cu/Al <sub>2</sub> O <sub>3</sub> (A) 5 wt%	Cu-Cu	2.0 ± 0.4	2.564 ± 0.011	8.5 ± 1.7	-5.11 ± 1.74	0.0120
	Cu-O	2.8 ± 0.3	1.938 ± 0.013	7.1 ± 1.7		
Cu/Al <sub>2</sub> O <sub>3</sub> (S) 5 wt%	Cu-Cu	4.8 ± 0.8	2.543 ± 0.012	8.5 ± 1.4	2.00 ± 1.84	0.0145
	Cu-O	1.7 ± 0.7	1.884 ± 0.024	11.8 ± 8.3		

CN, average coordination number; R, the distance between the absorber and backscattered atoms.  $\sigma^2$  multiplied by  $10^3$ , Debye-Waller factor;  $\Delta E_0$ , the photoelectron energy origin; R-factor, the closeness of fit. \* Model assuming Cu atoms are atomically dispersed, and #model assumed not to represent Cu local environment.

### 3.3 Catalytic testing

The performance of the Cu-based catalysts created by wet impregnation was explored for the selective furfural hydrogenation at 50 °C in methanol at 1.5 and 10 bar of hydrogen. The catalyst characterisation has been summarised in Table 3.3.1. The conversion of furfural can follow several pathways, illustrated in Fig. 3.3.1. In the absence of any solid material, neither hydrogenation nor decarbonylation reactions were observed. With minimal conversion, the parent Al<sub>2</sub>O<sub>3</sub> support was found to favour decarbonylation or acetalisation reaction while being inactive to hydrogenation reactions (Table 3.3.2).

*Table 3.3.1 Bulk elemental analysis, surface area measurements, Cu crystallite, Cu particle size analysis and EXAFS determined structure. Catalysts synthesised using copper nitrate, copper acetate and copper sulfate pentahydrate were denoted (N), (A) and (S), respectively.*

Catalyst	Nominal Cu loading (wt%)	Actual Cu loading <sup>a</sup> (wt%)	Surface area <sup>b</sup> (m <sup>2</sup> g <sup>-1</sup> )	Cu crystallite size <sup>c</sup> (nm)	Cu particle size <sup>d</sup> (nm)	EXAFS structure
Cu/Al <sub>2</sub> O <sub>3</sub> (N)	1.0	0.83 ± 0.04	36 ± 2	-	-	Isolated atoms
Cu/Al <sub>2</sub> O <sub>3</sub> (A)	1.0	0.91 ± 0.05	35 ± 2	-	-	Isolated atoms and dimers
Cu/Al <sub>2</sub> O <sub>3</sub> (S)	1.0	0.66 ± 0.08	39 ± 2	-	-	Isolated atoms and dimers
Cu/Al <sub>2</sub> O <sub>3</sub> (N)	5.0	4.22 ± 0.32	34 ± 2	13.2 ± 9.5	3.9 ± 1.9	Small nanoparticles
Cu/Al <sub>2</sub> O <sub>3</sub> (A)	5.0	4.56 ± 0.36	33 ± 2	13.0 ± 9.4	6.8 ± 5.5	Paracrystalline structure
Cu/Al <sub>2</sub> O <sub>3</sub> (S)	5.0	4.22 ± 0.31	30 ± 2	18.7 ± 12.9	12.8 ± 9.3	Large nanoparticles
Al <sub>2</sub> O <sub>3</sub>	-	-	38 ± 2	-	-	-

<sup>a</sup> Determined by ICP-OES, <sup>b</sup> BET surface area from N<sub>2</sub> porosimetry, <sup>c</sup> WPPM via XRD, <sup>d</sup> STEM

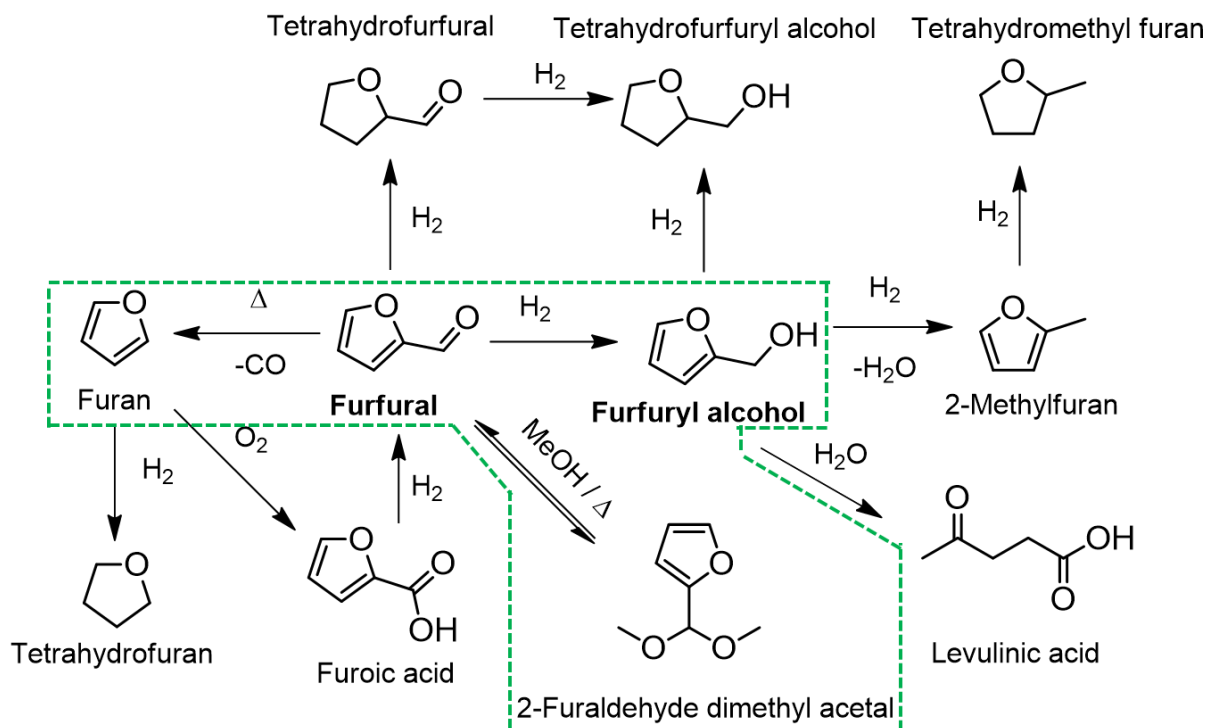


Fig. 3.3.1 Reaction scheme for upgrading furfural [51].

Table 3.3.2 Summary of blanks and bare support catalytic data for the hydrogenation of furfural. Reaction conditions: 7 h, 50 °C, 1.5 bar and 10 bar of  $H_2$ , 600 RPM, and 30 mg of catalyst.

Catalyst	$H_2$ pressure (bar)	Conversion (%)	Furfuryl alcohol S (%)	Furan S (%)	FDMA S (%)
Blank	1.5	1.1 ± 0.1	0.0	0.0	100 ± 5.0
	10	1.6 ± 0.1	0.0	0.0	100 ± 5.0
$Al_2O_3$	1.5	1.1 ± 0.1	0.0	1.0 ± 0.1	99.0 ± 5.0
	10	0.5 ± 0.1	0.0	1.5 ± 0.1	98.5 ± 4.9

In all cases, for the supported Cu-based catalysts, the selective hydrogenation of furfural to furfuryl alcohol was observed and are tabulated in Table 3.3.3. The catalysts were generally discovered to be highly selective to furfuryl alcohol due to the reaction parameters being tuned to favour furfuryl alcohol formation and the inherent selectivity of Cu surfaces [9, 14, 51]. However, the introduction of sulfur via  $CuSO_4$  derived catalysts were found to severely alter the direction of the reaction towards the acetalisation pathway, producing 2-furaldehyde dimethyl acetal (FDMA, Fig. 7.1.1 GCMS spectrum in the appendices), which is a high-cost compound that can be fed into subsequent reactions such as the

Mukaiyama aldol reaction [52]. Furfural conversion was observed to decrease using the materials synthesised from the following metal precursors copper acetate > copper nitrate > copper sulfate. Increasing the pressure of the hydrogen was found to increase the conversion and selectivity towards furfuryl alcohol as the abundance of adsorbed hydrogens makes the pathway more favourable. The low activity of the material synthesised from the sulfate precursor was also accompanied by the production of furan arising from the decarbonylation of furfural and the formation of the acetalisation product FDMA.

Table 3.3.3. Summary of catalytic data for the hydrogenation of furfural using copper catalysts. Reaction conditions: 7 h, 50 °C, 1.5 bar and 10 bar of H<sub>2</sub>, 600 RPM, and 30 mg of catalyst.

Cu precursor	Nominal Cu wt%	H <sub>2</sub> pressure (bar)	Conversion (%)	Furfuryl alcohol S (%)	Furan S (%)	FDMA S (%)
Nitrate	1.0	1.5	9.2 ± 0.5	86.3 ± 4.3	13.7 ± 0.7	0
	5.0		14.1 ± 0.7	94.6 ± 4.7	5.4 ± 0.3	0
	1.0	10	99.3 ± 5.0	99.8 ± 5.0	0.2 ± 0.1	0
	5.0		99.0 ± 5.0	99.5 ± 5.0	0.5 ± 0.1	0
Acetate	1.0	1.5	24.2 ± 1.2	96.0 ± 4.8	4.0 ± 0.2	0
	5.0		47.7 ± 2.4	97.6 ± 4.9	2.4 ± 0.1	0
	1.0	10	99.0 ± 5.0	99.8 ± 5.0	0.2 ± 0.1	0
	5.0		99.4 ± 5.0	99.6 ± 5.0	0.4 ± 0.1	0
Sulfate	1.0	1.5	2.2 ± 0.1	5.1 ± 0.3	61.4 ± 3.1	33.5 ± 1.7
	5.0		7.8 ± 0.4	0.8 ± 0.1	11.3 ± 0.6	89 ± 4.5
	1.0	10	94.9 ± 4.7	94.7 ± 4.7	0.3 ± 0.1	5.1 ± 0.3
	5.0		91.8 ± 4.6	83.5 ± 4.2	0.9 ± 0.1	15.6 ± 0.8

*Rounding errors may be present.*

The reaction profiles of 1 wt% Cu/Al<sub>2</sub>O<sub>3</sub> catalysts for the selective hydrogenation of furfural operating at a mild pressure of 1.5 bar are illustrated in Fig. 3.3.2a. An induction period of 5 to 6 h is noticed where the catalysts are mostly inactive in terms of conversion and furfural alcohol production; most clear for the Cu/Al<sub>2</sub>O<sub>3</sub> (N) and (A) catalysts. Performing the reaction at a higher hydrogen pressure of 10 bar, the induction period is alleviated to ~1 h (Fig. 3.3.2b). This phenomenon can be thought to be attributed to insufficient hydrogen adsorption on the surface, limiting activity or the formation of surface oxide on the copper surface. Arising from pre-dissolved oxygen in the reaction mixture or the *in-situ* reduction procedure at 300 °C for 0.5 h being inadequate. Performing a more rigorous *in-situ*

reduction strategy (320 °C for 0.5 h) had left the induction period unchanged suggesting the reduction procedure was adequate. DFT calculations [53] suggests that CuO is unable to catalyse the reactions due to being unable to produce atomic hydrogen which would enable hydrogenation reactions until the oxide had been reduced. While as expected, the induction period is found inversely proportional to hydrogen partial pressures which have been examined previously by Kim *et al.* [54] via time-resolved XRD and XAS. The authors found the reduction of CuO being complex, involving an induction period and the embedding of hydrogen into the bulk oxide. Their *in-situ* experimentation indicates that under a large supply of hydrogen the reduction process completely reduces the CuO to metallic Cu. This is done without the formation of an intermediate or suboxide (i.e., no Cu<sub>2</sub>O or Cu<sub>4</sub>O<sub>3</sub>) with an apparent activation-energy of 60.7 kJ mol<sup>-1</sup>, while the value for Cu<sub>2</sub>O is 114.7 kJ mol<sup>-1</sup>. Consequently, at low hydrogen partial pressures intermediate oxides are formed that have a higher activation-energy for the final reduction step lengthening the observed induction period. While the possible explanation could be insufficient hydrogen adsorption on the surface, limiting the initial rate of hydrogenation. As the reaction progresses, sufficient adsorbed hydrogen is available for the reaction to progress unhindered. Either way, a poison is present at the start of the reaction in the form of oxide or insufficient hydrogen coverage, observed as an induction period.

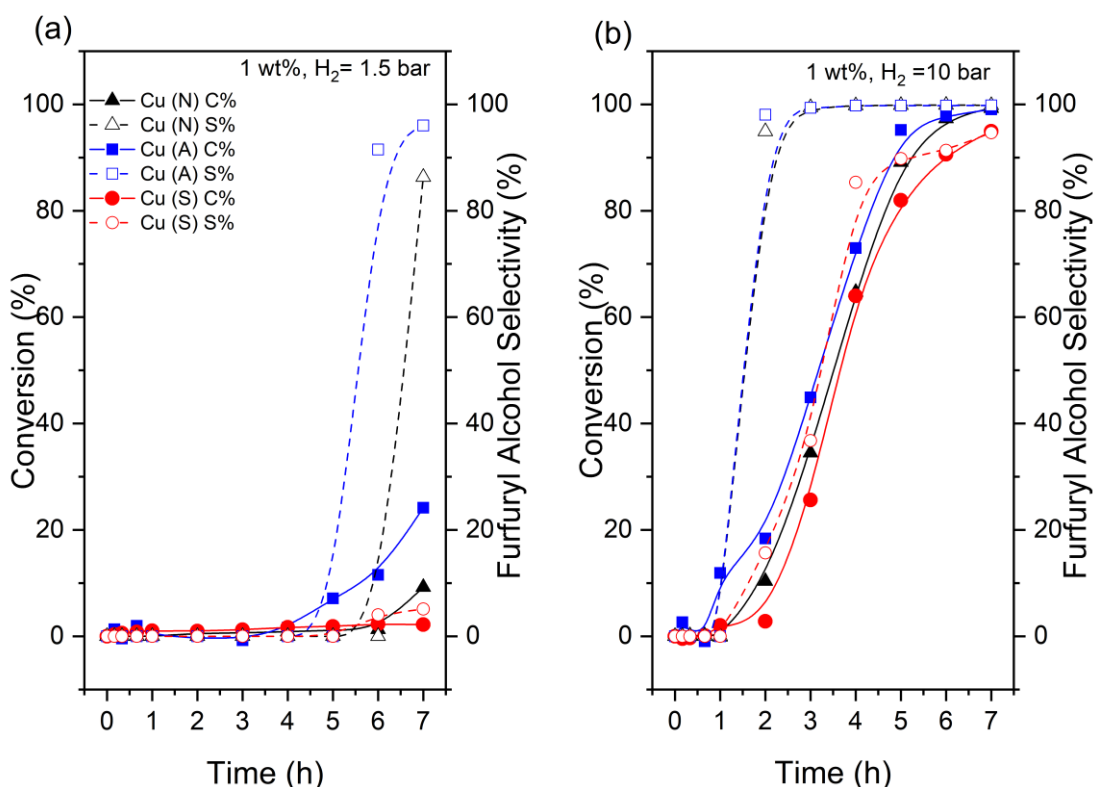


Fig. 3.3.2 The reaction profiles of furfural conversion and furfuryl alcohol selectivity. Reaction conditions: 50 °C, (a) 1.5 bar and (b) 10 bar of H<sub>2</sub>, 600 RPM, 30 mg of catalyst and using supported 1 wt% Cu/Al<sub>2</sub>O<sub>3</sub> catalysts. Solid and dashed lines represent the conversion and selectivity to furfuryl alcohol, respectively.

Reaction profiles are presented of the 5 wt% Cu/Al<sub>2</sub>O<sub>3</sub> catalysts in Fig. 3.3.3. Evidently, CuSO<sub>4</sub> derived Cu/Al<sub>2</sub>O<sub>3</sub> (S) catalyst, demonstrates the worst furfuryl alcohol selectivity with differences becoming more apparent at 1.5 bar of H<sub>2</sub>. The presence of remnant sulfur species (primarily sulfates) on the surface of the catalyst determined through XPS measurements (Fig. 3.2.7a) is thought to be explained by these species. The catalyst deactivation arising from sulfur species is likely related to S being more electronegative than the Cu, thus withdrawing electron density from the surface and causing an electronic modification to the surface [55]. It should be noted that a DFT study by Kitchin *et al.* [56], reported that sulfur preferentially adsorbs onto the high surface energy and high co-ordinated HCP and FCC sites on the copper surface, which hydrogen also favours to adsorb to [57, 58]. The sulfur contamination further cripples copper's ability to chemisorb hydrogen, an activated process (requires energy) [59] unlike other metals such as Pt, Pd and Ni [60]. Alterations to the surface electron density

permit side reactions to be more prominent such as furan and FDMA formation (observed by the immediate increase in conversion in Fig. 3.3.3b). As the partial pressure of hydrogen is increased (Fig. 3.3.2b and Fig. 3.3.3b), the selectivity is noticed to flip towards furfuryl alcohol as the rate-determining is no longer the adsorption of hydrogen. While the increased acetal formation of the 5 wt% Cu (S) against the lower loading counterpart may arise to due the presence of larger Cu surfaces able to promote the reaction and the greater interaction ability of the sulfur species on the Cu surface.

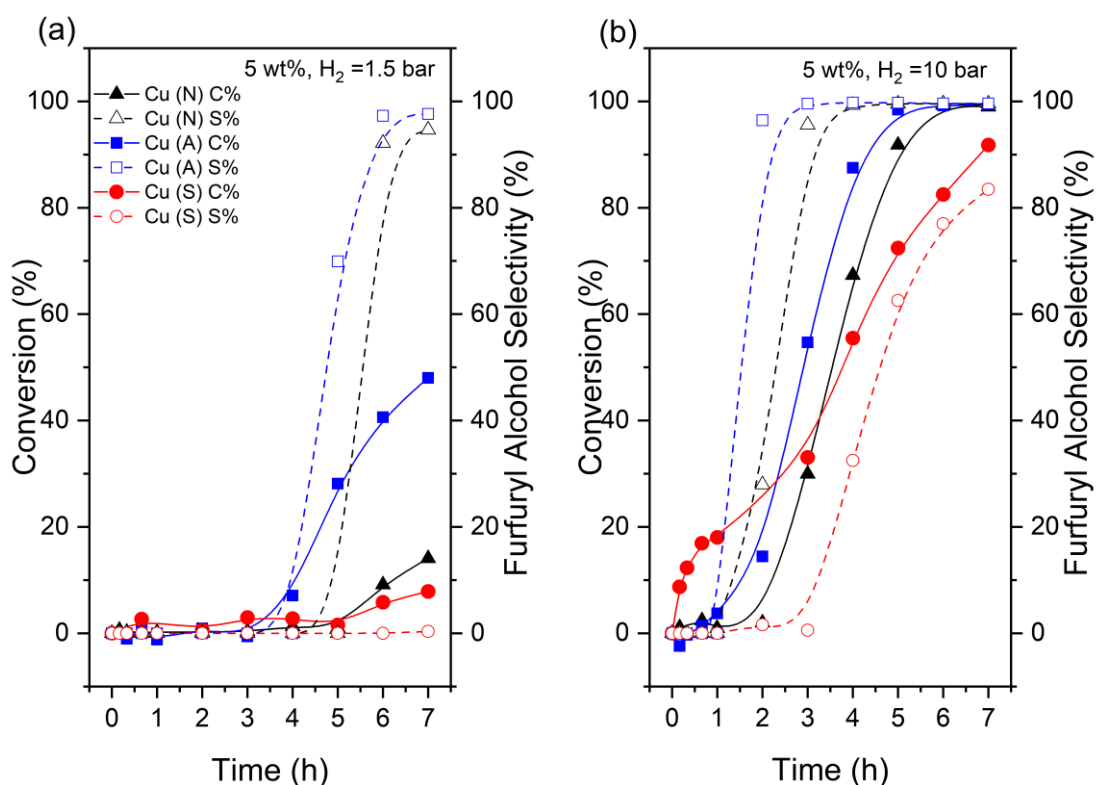


Fig. 3.3.3 The reaction profiles of furfural conversion and furfuryl alcohol selectivity. Reaction conditions: 7 h, 50 °C, (a) 1.5 bar and (b) 10 bar of H<sub>2</sub>, 600 RPM, 30 mg of catalyst and using supported 5 wt% Cu/Al<sub>2</sub>O<sub>3</sub> catalysts. Solid and dashed lines represent the conversion and selectivity to furfuryl alcohol, respectively.

Frequently reported in the literature [15, 61-66], the acetalisation of aldehydes, including furfural (Fig. 3.3.4), in alcoholic solvents is observed. With the presence of Lewis [65, 66] or protic [65] acid catalysts, the acetalisation with alcohols can be achieved. Taylor *et al.* [15] also reported the acetalisation of furfural with their alcoholic solvent utilising supported Pt catalysts. The authors

observed that the hydrogenation of furfural is receptive to the choice of the solvent, with alcohols described as being more active than non-polar solvents. Influencing the current reaction parameters, their findings also suggest that alcohols such as ethanol favours the formation of the undesired acetal products. However, using solvents such as methanol and operating the reaction at lower temperatures was found to suppress the side reaction.

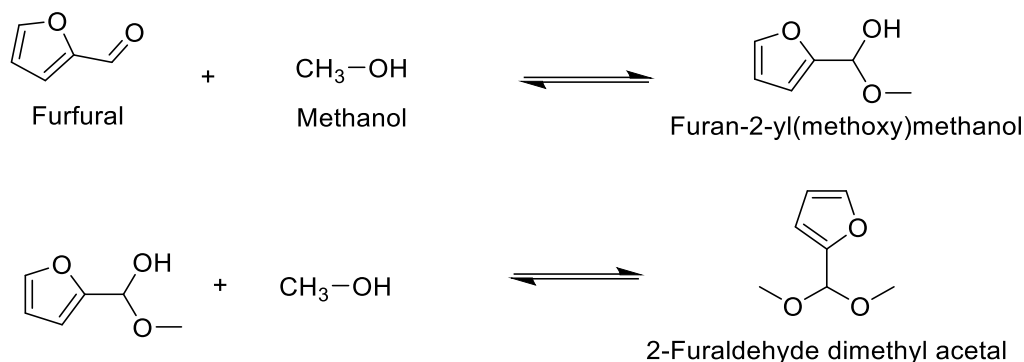


Fig. 3.3.4 Acetalisation of furfural with methanol [15].

As shown in Table 3.3.3, significant FDMA is produced with the sulfate-derived catalysts accredited to sulfur species catalysing the acetalisation of furfural and methanol. In addition, this observation has not yet been reported in this reaction system. Further investigations involved two likely forms of metal sulfates that may be present. The bulk Al<sub>2</sub>(SO<sub>4</sub>)<sub>3</sub> catalyst demonstrated to be the most active, instantly catalysing the reaction at room temperature with minimal agitation (conversion = 92.7%). The remarkable activity and selectivity are attributed to the ‘super Lewis acid sites’ [67] and possibly some homogeneous catalytic character as it was the only catalyst to be completely dissolved into the reaction mixture after 7 hours at 50 °C. Likewise, the bulk CuSO<sub>4</sub> and non-reduced 5 wt% Cu/Al<sub>2</sub>O<sub>3</sub> (S) (CuSO<sub>4</sub> reflections detected in Fig. 3.2.2b and Fig. 3.2.3b) were also found active and selective for these reactions (Table 3.3.4). Note that at an intermediary reduction temperature of 200 °C, the sulfur-derived catalyst has both the characteristics of CuSO<sub>4</sub> and metallic Cu (Fig. 3.2.3b) while the sulfur-free 5.0 wt% Cu/Al<sub>2</sub>O<sub>3</sub> (A) catalyst only has metallic Cu reflections (Fig. 3.2.3a). The resulting catalytic data suggest that sulfate species in the catalyst can direct the reaction towards acetalisation. Leaching of

sulfur was confirmed through ICP-OES of the supernatant fluid after ageing the sulfate-derived catalyst in MeOH for 7 h at 50 °C (section 2.3.1.1). Under identical experimental conditions, the resulting “cleaned” catalyst and the supernatant fluid was able to promote acetalisation via a homogeneous route (Table 3.3.4 and Fig. 3.3.5)

*Table 3.3.4 Summary of catalytic data for the acetalization of furfural using sulfate and sulfate-free catalysts. Reaction conditions: 7 h, 50 °C, 1.5 bar, 600 RPM, and 30 mg of catalyst.*

Catalyst	Reduction temperature (°C)	Conversion (%)	Furfuryl alcohol S (%)	Furan S (%)	FDMA S (%)
Al <sub>2</sub> (SO <sub>4</sub> ) <sub>3</sub>	n/a	84.5 ± 4.2	0	0	100 ± 5.0
CuSO <sub>4</sub>	n/a	89.6 ± 4.5	0	0	100 ± 5.0
Cu/Al <sub>2</sub> O <sub>3</sub> (S) 5.0 wt%	n/a	94.0 ± 4.7	0	0	100 ± 5.0
Cu/Al <sub>2</sub> O <sub>3</sub> (S) 5.0 wt%	200	95.8 ± 4.8	2.3 ± 0.1	0	97.7 ± 4.9
Cu/Al <sub>2</sub> O <sub>3</sub> (A) 5.0 wt%	200	34.0 ± 1.7	98.6 ± 4.9	0	1.4 ± 0.1
Cu/Al <sub>2</sub> O <sub>3</sub> (S) 5.0 wt%	300	7.8 ± 0.4	0.8 ± 0.1	11.3 ± 0.6	89.0 ± 4.5
Cu/Al <sub>2</sub> O <sub>3</sub> (S) 5.0 wt% cleaned*	n/a	70.5 ± 3.5	36.4 ± 1.8	0	63.6 ± 3.2
Supernatant fluid	n/a	93.1 ± 4.7	0	0	100 ± 5.0

\* Catalyst was washed in methanol at 50 °C for 7h before use.

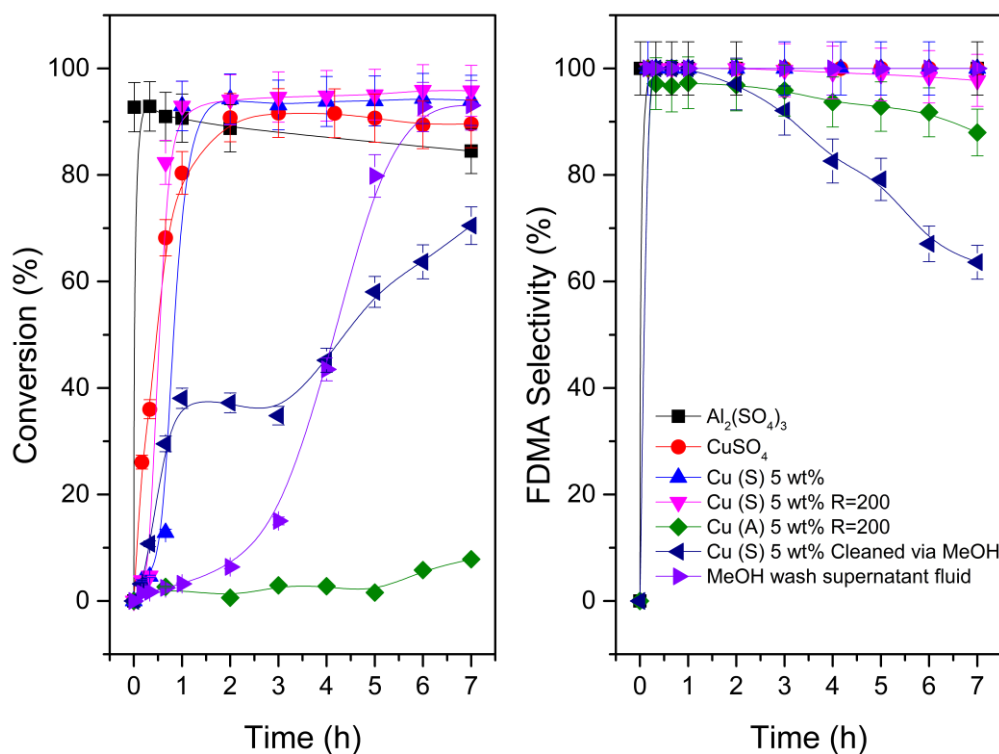


Fig. 3.3.5 Acetalization of furfural with metal sulfate catalyst. The reaction profiles of furfural conversion and 2-furaldehyde dimethyl acetal (FDMA) selectivity. Reaction conditions: 50 °C, 1.5 bar of H<sub>2</sub>, 600 RPM, 30 mg of catalyst and using CuSO<sub>4</sub>, Al<sub>2</sub>(SO<sub>4</sub>)<sub>3</sub> and 5 wt% Cu/Al<sub>2</sub>O<sub>3</sub> catalysts at varying states of reduction.

Table 3.3.3 shows increasing the copper loading of the catalyst and consequently increasing the size of the Cu ensembles, demonstrates an improved conversion and selectivity towards furfuryl alcohol for all the sulfur-free catalysts at low hydrogen pressures. The increased conversion at lower pressures can be simply explained due to the higher copper content and availability of sites able to adsorb hydrogen onto the surface. Whilst, at higher pressures this limiting factor is removed for 1 wt% catalysts. However, once the 1 wt% catalysts have been normalised to metal content (Fig. 3.3.6), they are superior in terms of catalytic activity against their higher loaded counterparts. Turnover frequencies were estimated using dispersions calculated by XPS (Table 3.2.4). TOFs (in Table 3.3.5) suggest that the Cu surface sites in the 1 wt% catalysts are generally better, conceivably due to their lack of coordination and greater reactivity for the transformation of the substrate. Comparing the nitrate and acetate materials, it is also found that they are approximately the same when Cu content/active sites are normalised (Fig.

3.3.6 and Table 3.3.5) for the 1 wt% catalyst with the increased conversion most likely arising due to the most efficient Cu deposition on the support. However, at the Cu 5 wt% loadings the acetate is noticeably better as a higher dispersed Cu phase is formed which can accelerate the reaction at near-ambient hydrogen pressures. Supporting the previous findings, TOFs shows that at milder hydrogen partial pressures, sulfur contaminants could inhibit the formation of active sites compared to the free-sulfur catalysts, or create the same number of active sites but less efficient for hydrogenation.

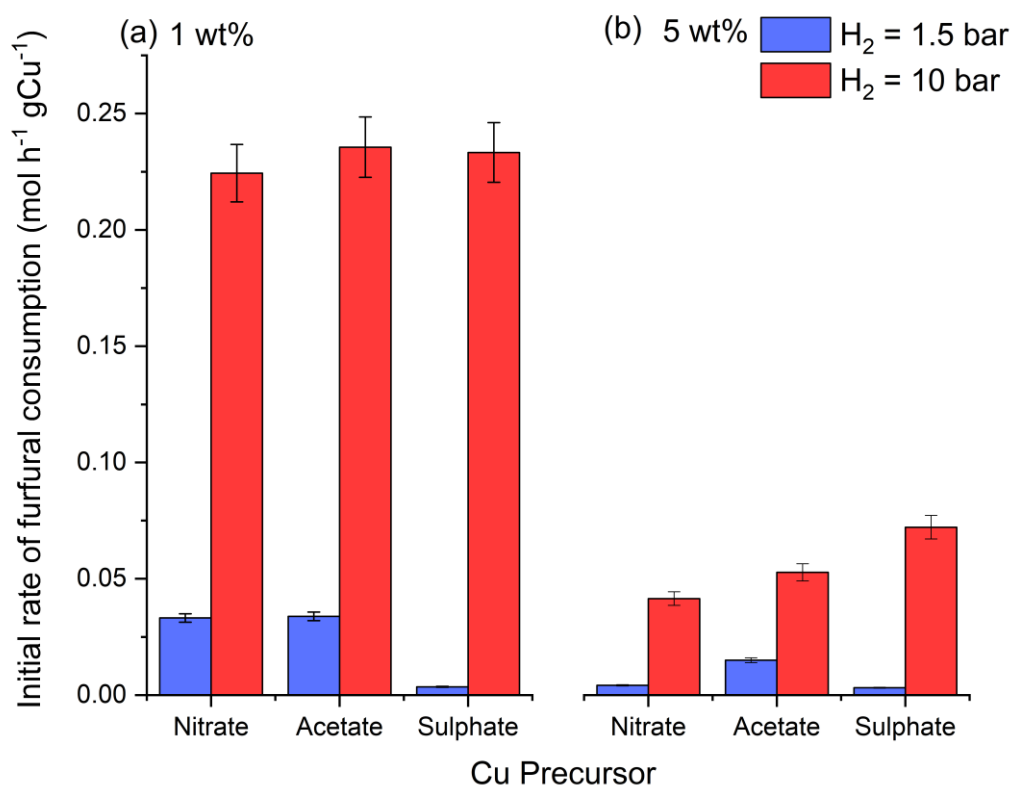


Fig. 3.3.6 Normalised initial rates of furfural consumption per gram of Cu after the induction period across the (a) 1.0 wt% and (b) 5.0 wt% Cu/Al<sub>2</sub>O<sub>3</sub> catalysts at differing hydrogen pressures.

Table 3.3.5 Turnover frequencies for the hydrogenation of furfural using copper catalysts. Reaction conditions: 7 h, 50 °C, 1.5 bar and 10 bar of H<sub>2</sub>, 600 RPM, and 30 mg of catalyst.

Cu precursor	Nominal Cu (wt%)	H <sub>2</sub> pressure (bar)	TOF (h <sup>-1</sup> ) <sup>a</sup>
Nitrate	1	1.5	3.1 ± 0.3
	5		1.4 ± 0.2
	1	10	21.2 ± 2.4
	5		14.0 ± 1.6
Acetate	1	1.5	3.1 ± 0.3
	5		4.8 ± 0.5
	1	10	18.3 ± 2.0
	5		15.7 ± 1.7
Sulfate	1	1.5	0.5 ± 0.1
	5		1.0 ± 0.1
	1	10	30.9 ± 3.4
	5		8.8 ± 1.0

<sup>a</sup> TOF determined from dispersion calculated by XPS.

Across all the catalyst series tested, at near-ambient hydrogen pressures (Table 3.3.3), the furan selectivity is inversely proportional to the Cu loading suggesting the reaction is structure sensitive. Structure sensitivity has been reported previously by Somorjai *et al.* [68] employing supported platinum catalysts. The authors reported that larger Pt particles (7.1 nm) displayed increased selectivity to furfuryl alcohol, while smaller Pt nanoparticles (1.5 nm) were more proficient in accessing the decarbonylation furan pathway. So, similar behaviour is inferred to influence the current behaviour. It is well known that Cu (111) surfaces interact with furfural via its lone pair on the oxygen atom of the carbonyl group. Resulting in a perpendicular  $\eta^1(\text{O})$ -aldehyde conformation [13, 14, 51, 69]. Sitthisa *et al.* [69] suggest this specific conformation is preferred due to the repulsion of the furan ring from the close-packed Cu (111) surface. Due to the overlap of the 3d band of the Cu surface atoms and the anti-bonding orbitals of the aromatic furan ring. The interaction of furfural via this  $\eta^1(\text{O})$ -aldehyde adsorption mode and the instability of the  $\eta^2(\text{C}, \text{O})$ -aldehyde conformation is thought to explain the higher selectivity of the hydrogenation of the C = O bond over decarbonylation observed for Pd catalysts [70]. Generally, as the size of the metal ensemble size decreases, the generation of lower coordination facets are preferred (such as Cu (110) and Cu (100) surfaces). Further theoretical calculations by Sitthisa *et al.* [69], implies that more open Cu (110) planes permits the furan ring to move closer to the surface due to the lower Cu atom density that interacts with the furan ring. Therefore, the 5 wt% catalysts (N and A) are selective

towards furfuryl alcohol at low hydrogen pressures. Decreasing the ensemble size with the 1 wt% catalysts (N and A) the repulsion of the furan ring falls due to the formation of isolated and dimer Cu species and decarbonylation is more favoured.

The recyclability of the 1 wt% and 5 wt% catalysts synthesised from the acetate precursor was also investigated. Once the catalyst was recovered via centrifugation following the reaction, the catalysts were tested under optimal conditions and downscaling the reaction by 15% (since 15% of the catalyst was lost during the recovery process). Table 3.3.6 shows that the activity and selectivity remain unaffected after the reuse of both catalysts.

*Table 3.3.6 Furfural hydrogenation over recycled catalysts. Reaction conditions: 4 h, 50 °C, 10 bar of H<sub>2</sub> and 600 RPM.*

Catalyst	Nominal Cu (wt%)	Hydrogen Pressure (bar)	Conversion (%)	Furfuryl Alcohol S (%)	Furan S (%)	FDMA S (%)
<sup>1</sup> Cu/ Al <sub>2</sub> O <sub>3</sub> (A)	1.0	10	73.0 ± 3.7	99.8 ± 5.0	0.2 ± 0.1	0
<sup>2</sup> Cu/ Al <sub>2</sub> O <sub>3</sub> (A)	1.0	10	72.4 ± 3.6	99.2 ± 5.0	0.8 ± 0.1	0
<sup>1</sup> Cu/ Al <sub>2</sub> O <sub>3</sub> (A)	5.0	10	87.5 ± 4.4	99.8 ± 5.0	0.2 ± 0.1	0
<sup>2</sup> Cu/ Al <sub>2</sub> O <sub>3</sub> (A)	5.0	10	86.3 ± 4.3	99.6 ± 5.0	0.4 ± 0.1	0

Superscripts 1 and 2 indicate the catalyst cycle of testing.

### 3.4 Conclusions

Liquid-phase hydrogenation of furfural was studied with a series of supported monometallic Cu/Al<sub>2</sub>O<sub>3</sub> catalysts synthesised from various Cu metal precursors by wet impregnation. The catalysts' electronic and morphological structure was analysed via ICP-OES, BET, PXRD, STEM, XPS, XAES and XAS. Furfural hydrogenation was receptive to the presence of sulfates in the catalyst, entirely altering the reaction selectivity to the acetalisation pathway of furfural with methanol at over 90% conversion at mild conditions. While at near ambient hydrogen pressures, catalytic tests show that sulfate impurities deactivate the catalyst leading to lower conversion and altered selectivities. It has also been shown that the selective furfural hydrogenation can be structure sensitive, as isolated and dimer Cu atoms were found to promote decarbonylation reactions due to their lower-packed copper structures influencing the interaction of the furan ring with the underlying surface; mimicking platinum group catalysts [13, 70, 71]. In all cases catalysts derived from copper acetate were found to be superior which likely due to their altered structure, suggesting the metal precursor selection appears to be critical to achieving optimal catalytic activity. The mechanism of the precursor decomposition and anchoring onto the support plays a substantial role in the final catalytically active copper morphology. Thus, influencing the synthesis of a cheap, non-toxic, and selective catalyst.

### 3.5 References

- [1] K. Yan, G. Wu, T. Lafleur, C. Jarvis, Production, properties and catalytic hydrogenation of furfural to fuel additives and value-added chemicals, *Renew. Sustain. Energy Rev.*, 38 (2014) 663-676.
- [2] M.J. Taylor, L. Jiang, J. Reichert, A.C. Papageorgiou, S.K. Beaumont, K. Wilson, A.F. Lee, J.V. Barth, G. Kyriakou, Catalytic Hydrogenation and Hydrodeoxygenation of Furfural over Pt(111): A Model System for the Rational Design and Operation of Practical Biomass Conversion Catalysts, *J. Phys. Chem. C*, 121 (2017) 8490-8497.
- [3] F. Ullmann, *Ullmann's encyclopedia of industrial chemistry*, 7th ed., Wiley-VCH ;, Weinheim, Germany ;, 2009.
- [4] D. Liu, D. Zemlyanov, T. Wu, R.J. Lobo-Lapidus, J.A. Dumesic, J.T. Miller, C.L. Marshall, Deactivation mechanistic studies of copper chromite catalyst for selective hydrogenation of 2-furfuraldehyde, *J. Catal.*, 299 (2013) 336-345.
- [5] R. Rao, A. Dandekar, R.T.K. Baker, M.A. Vannice, Properties of Copper Chromite Catalysts in Hydrogenation Reactions, *J. Catal.*, 171 (1997) 406-419.
- [6] H. Adkins, R. Connor, The catalytic hydrogenation of organic compounds over copper chromite, *J. Am. Chem. Soc.*, 53 (1931) 1091-1095.
- [7] J.J. Musci, A.B. Merlo, M.L. Casella, Aqueous phase hydrogenation of furfural using carbon-supported Ru and RuSn catalysts, *Catal. Today*, 296 (2017) 43-50.
- [8] S. Liu, Y. Amada, M. Tamura, Y. Nakagawa, K. Tomishige, One-pot selective conversion of furfural into 1,5-pentanediol over a Pd-added Ir-ReOx/SiO<sub>2</sub> bifunctional catalyst, *Green Chem.*, 16 (2014) 617-626.
- [9] M. Lesiak, M. Binczarski, S. Karski, W. Maniukiewicz, J. Rogowski, E. Szubiakiewicz, J. Berlowska, P. Dziugan, I. Witońska, Hydrogenation of furfural over Pd-Cu/Al<sub>2</sub>O<sub>3</sub> catalysts. The role

of interaction between palladium and copper on determining catalytic properties, *J. Mol. Catal. A: Chem.*, 395 (2014) 337-348.

[10] M.G. Dohade, P.L. Dhepe, Efficient hydrogenation of concentrated aqueous furfural solutions into furfuryl alcohol under ambient conditions in presence of PtCo bimetallic catalyst, *Green Chem.*, 19 (2017) 1144-1154.

[11] H. Li, H. Luo, L. Zhuang, W. Dai, M. Qiao, Liquid phase hydrogenation of furfural to furfuryl alcohol over the Fe-promoted Ni-B amorphous alloy catalysts, *J. Mol. Catal. A: Chem.*, 203 (2003) 267-275.

[12] Y. Wang, Y. Miao, S. Li, L. Gao, G. Xiao, Metal-organic frameworks derived bimetallic Cu-Co catalyst for efficient and selective hydrogenation of biomass-derived furfural to furfuryl alcohol, *Mol. Catal.*, 436 (2017) 128-137.

[13] X. Li, P. Jia, T. Wang, Furfural: A Promising Platform Compound for Sustainable Production of C4 and C5 Chemicals, *ACS Catal.*, 6 (2016) 7621-7640.

[14] Y. Shi, Y. Zhu, Y. Yang, Y.-W. Li, H. Jiao, Exploring Furfural Catalytic Conversion on Cu(111) from Computation, *ACS Catal.*, 5 (2015) 4020-4032.

[15] M.J. Taylor, L.J. Durndell, M.A. Isaacs, C.M.A. Parlett, K. Wilson, A.F. Lee, G. Kyriakou, Highly selective hydrogenation of furfural over supported Pt nanoparticles under mild conditions, *Appl. Catal. B*, 180 (2016) 580-585.

[16] G.J. Hutchings, F. King, I.P. Okoye, M.B. Padley, C.H. Rochester, Modification of Selectivity in the Hydrogenation of Crotonaldehyde Using Cu/Al<sub>2</sub>O<sub>3</sub> Catalysts Modified with Sulfur Compounds: Effect of Sulfur Source, *J. Catal.*, 148 (1994) 464-469.

- [17] M.E. Chiu, G. Kyriakou, F.J. Williams, D.J. Watson, M.S. Tikhov, R.M. Lambert, Sulfur, normally a poison, strongly promotes chemoselective catalytic hydrogenation: stereochemistry and reactivity of crotonaldehyde on clean and S-modified Cu(111), *Chem. Commun.*, (2006) 1283-1285.
- [18] M.V. Twigg, M.S. Spencer, Deactivation of supported copper metal catalysts for hydrogenation reactions, *Appl. Catal. A Gen.*, 212 (2001) 161-174.
- [19] G.J. Hutchings, F. King, I.P. Okoye, C.H. Rochester, Influence of sulphur poisoning of copper/alumina catalyst on the selective hydrogenation of crotonaldehyde, *Appl. Catal. A Gen.*, 83 (1992) L7-L13.
- [20] G.J. Hutchings, F. King, I.P. Okoye, M.B. Padley, C.H. Rochester, Selectivity Enhancement in the Hydrogenation of  $\alpha$ ,  $\beta$ -Unsaturated Aldehydes and Ketones Using Thiophene-Modified Catalysts, *J. Catal.*, 148 (1994) 453-463.
- [21] M.E. Chiu, D.J. Watson, G. Kyriakou, M.S. Tikhov, R.M. Lambert, Tilt the Molecule and Change the Chemistry: Mechanism of S-Promoted Chemoselective Catalytic Hydrogenation of Crotonaldehyde on Cu(111), *Angew. Chem. Int. Ed.*, 45 (2006) 7530-7534.
- [22] M. May, S. Gonzalez, F. Illas, A systematic density functional study of ordered sulfur overlayers on Cu(111) and Ag(111): Influence of the adsorbate coverage, *Surf. Sci.*, 602 (2008) 906-913.
- [23] G. Centi, S. Perathoner, Nature of active species in copper-based catalysts and their chemistry of transformation of nitrogen oxides, *Appl. Catal. A Gen.*, 132 (1995) 179-259.
- [24] J. Ghose, A. Kanungo, Studies on the thermal decomposition of  $\text{Cu}(\text{NO}_3)_2 \cdot 3 \text{H}_2\text{O}$ , *J. Therm. Anal.*, 20 (1981) 459-462.
- [25] Z. Lin, D. Han, S. Li, Study on thermal decomposition of copper(II) acetate monohydrate in air, *J. Therm. Anal. Calorim.*, 107 (2012) 471-475.

- [26] F. Habashi, S.A. Mikhail, K.V. Van, Reduction of sulfates by hydrogen, *Can. J. Chem.*, 54 (1976) 3646-3650.
- [27] A.G. Ostroff, R.T. Sanderson, Thermal stability of some metal sulphates, *J. Inorg. Nucl. Chem.*, 9 (1959) 45-50.
- [28] C. Macken, B.K. Hodnett, Reductive regeneration of sulfated CuO/Al<sub>2</sub>O<sub>3</sub> catalyst-sorbents in hydrogen, methane and steam, *Ind. Eng. Chem.*, 37 (1998) 2611-2617.
- [29] K.S. Yoo, S.D. Kim, S.B. Park, Sulfation of Al<sub>2</sub>O<sub>3</sub> in Flue Gas Desulfurization by CuO/ $\gamma$ -Al<sub>2</sub>O<sub>3</sub> Sorbent, *Ind. Eng. Chem.*, 33 (1994) 1786-1791.
- [30] Y. Yang, D. Xu, Q. Wu, P. Diao, Cu<sub>2</sub>O/CuO Bilayered Composite as a High-Efficiency Photocathode for Photoelectrochemical Hydrogen Evolution Reaction, *Sci. Rep.*, 6 (2016) 35158.
- [31] M.C. Marion, E. Garbowski, M. Primet, Physicochemical properties of copper oxide loaded alumina in methane combustion, *J. Chem. Soc., Faraday Trans.*, 86 (1990) 3027-3032.
- [32] R.G. Haverkamp, A.T. Marshall, D. van Agterveld, Pick your carats: nanoparticles of gold–silver–copper alloy produced in vivo, *J. Nanopart. Res.*, 9 (2007) 697-700.
- [33] R. Nakamura, D. Tokozakura, H. Nakajima, J.-G. Lee, H. Mori, Hollow oxide formation by oxidation of Al and Cu nanoparticles, *J. Appl. Phys.*, 101 (2007) 074303.
- [34] T. Ghodselahi, M.A. Vesaghi, A. Shafiekhani, A. Baghizadeh, M. Lameii, XPS study of the Cu@Cu<sub>2</sub>O core-shell nanoparticles, *Appl. Surf. Sci.*, 255 (2008) 2730-2734.
- [35] B. Wei, N. Yang, F. Pang, J. Ge, Cu<sub>2</sub>O–CuO Hollow Nanospheres as a Heterogeneous Catalyst for Synergetic Oxidation of CO, *J. Phys. Chem. C*, 122 (2018) 19524-19531.
- [36] A.J. Barlow, R.T. Jones, A.J. McDonald, P.J. Pigram, XPSSurfA: An open collaborative XPS data repository using the CMSShub platform, *Surf. Interface Anal.*, 50 (2018) 527-540.

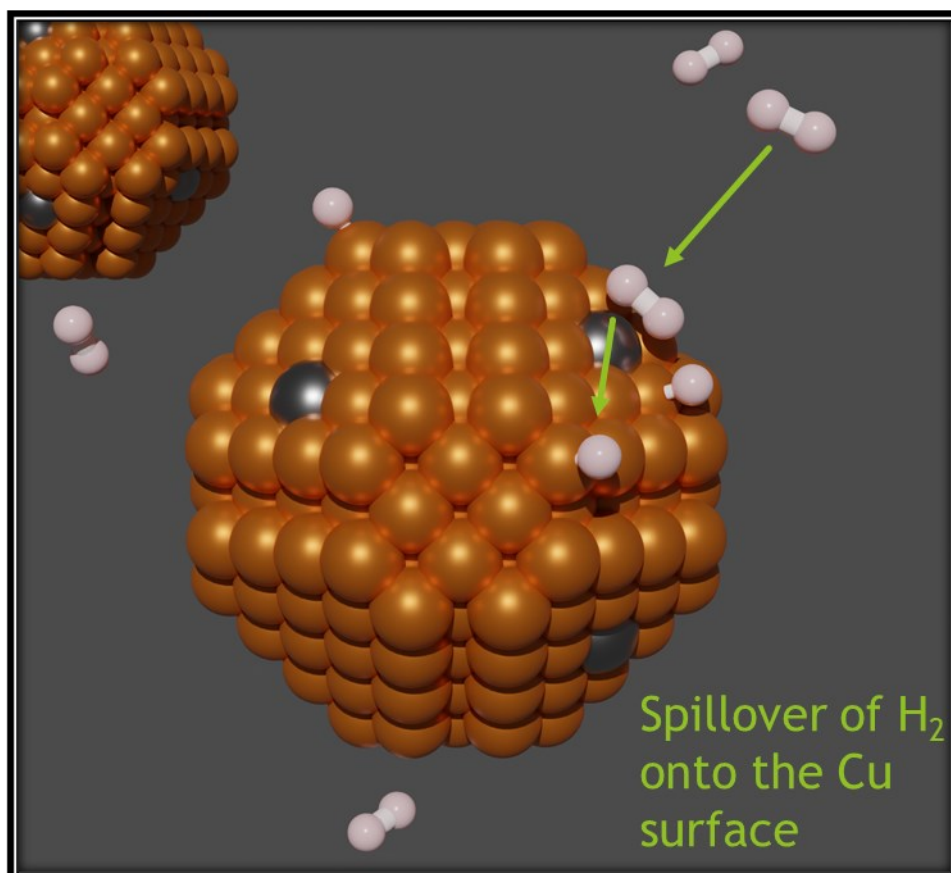
- [37] J.P. Espinós, J. Morales, A. Barranco, A. Caballero, J.P. Holgado, A.R. González-Elipe, Interface Effects for Cu, CuO, and Cu<sub>2</sub>O Deposited on SiO<sub>2</sub> and ZrO<sub>2</sub>. XPS Determination of the Valence State of Copper in Cu/SiO<sub>2</sub> and Cu/ZrO<sub>2</sub> Catalysts, *J. Phys. Chem. B*, 106 (2002) 6921-6929.
- [38] O.P.H. Vaughan, G. Kyriakou, N. Macleod, M. Tikhov, R.M. Lambert, Copper as a selective catalyst for the epoxidation of propene, *J. Catal.*, 236 (2005) 401-404.
- [39] Y.T. Wu, E. Garfunkel, T.E. Madey, Initial stages of Cu growth on ordered Al<sub>2</sub>O<sub>3</sub> ultrathin films, *J. Vac. Sci. Technol. A.*, 14 (1996) 1662-1667.
- [40] J. Batista, A. Pintar, J.P. Gomilšek, A. Kodre, F. Bornette, On the structural characteristics of  $\gamma$ -alumina-supported Pd–Cu bimetallic catalysts, *Appl. Catal. A Gen.*, 217 (2001) 55-68.
- [41] A. Thøgersen, S. Diplas, J. Mayandi, T. Finstad, A. Olsen, J.F. Watts, M. Mitome, Y. Bando, An experimental study of charge distribution in crystalline and amorphous Si nanoclusters in thin silica films, *J. Appl. Phys.*, 103 (2008) 024308.
- [42] S. Hofmann, Auger- and X-Ray Photoelectron Spectroscopy in Materials Science: A User-Oriented Guide, Springer Berlin Heidelberg 2012.
- [43] S.P. Kowalczyk, L. Ley, R.L. Martin, F.R. McFeely, D.A. Shirley, Relaxation and final-state structure in XPS of atoms, molecules, and metals, *Faraday Discuss.*, 60 (1975) 7-17.
- [44] T.N. Rhodin, Low Temperature Oxidation of Copper. I. Physical Mechanism1a, *J. Am. Chem. Soc.*, 72 (1950) 5102-5106.
- [45] Y.M. Shul'ga, V.I. Rubtsov, V.N. Vasilets, A.S. Lobach, N.G. Spitsyna, E.B. Yagubskii, EELS, XPS and IR study of C<sub>60</sub>·2S<sub>8</sub> compound, *Synth. Met.*, 70 (1995) 1381-1382.

- [46] D. Bahrin, Subagjo, H. Susanto, Effect of Regeneration Temperature on Particle Characteristics and Extent of Regeneration of Saturated SO<sub>2</sub>-Adsorption of CuO/ $\gamma$ -Al<sub>2</sub>O<sub>3</sub> Adsorbent, *Procedia Chem.*, 16 (2015) 723-727.
- [47] S. Calvin, XAFS for Everyone, Taylor & Francis, 2013.
- [48] S.-F. Cheah, G.E. Brown, G.A. Parks, XAFS Spectroscopy Study of Cu(II) Sorption on Amorphous SiO<sub>2</sub> and  $\gamma$ -Al<sub>2</sub>O<sub>3</sub>: Effect of Substrate and Time on Sorption Complexes, *J. Colloid Interface Sci.*, 208 (1998) 110-128.
- [49] S.-F. Cheah, G.E. Brown, Jr., G.A. Parks, XAFS study of Cu model compounds and Cu<sup>2+</sup> sorption products on amorphous SiO<sub>2</sub>,  $\gamma$ -Al<sub>2</sub>O<sub>3</sub>, and anatase, *Am. Mineral.*, 85 (2000) 118-132.
- [50] W.H. Cassinelli, L. Martins, A.R. Passos, S.H. Pulcinelli, A. Rochet, V. Briois, C.V. Santilli, Correlation between Structural and Catalytic Properties of Copper Supported on Porous Alumina for the Ethanol Dehydrogenation Reaction, *ChemCatChem*, 7 (2015) 1668-1677.
- [51] R. Mariscal, P. Maireles-Torres, M. Ojeda, I. Sadaba, M. Lopez Granados, Furfural: a renewable and versatile platform molecule for the synthesis of chemicals and fuels, *Energy Environ. Sci.*, 9 (2016) 1144-1189.
- [52] X. Meng, H. Pan, T. Zhong, X. Zhang, Unique chemoselective Mukaiyama aldol reaction of silyl enol diazoacetate with aldehydes and acetals catalyzed by MgI<sub>2</sub> etherate, *Tetrahedron*, 75 (2019) 130682.
- [53] G. Hao, R. Zhang, J. Li, B. Wang, Q. Zhao, Insight into the effect of surface structure on H<sub>2</sub> adsorption and activation over different CuO(111) surfaces: A first-principle study, *Comput. Mater. Sci.*, 122 (2016) 191-200.

- [54] J.Y. Kim, J.A. Rodriguez, J.C. Hanson, A.I. Frenkel, P.L. Lee, Reduction of CuO and Cu<sub>2</sub>O with H<sub>2</sub>: H Embedding and Kinetic Effects in the Formation of Suboxides, *J. Am. Chem. Soc.*, 125 (2003) 10684-10692.
- [55] J.A. Rodriguez, J. Hrbek, Interaction of Sulfur with Well-Defined Metal and Oxide Surfaces: Unraveling the Mysteries behind Catalyst Poisoning and Desulfurization, *Acc. Chem. Res.*, 32 (1999) 719-728.
- [56] N. İnoğlu, J.R. Kitchin, Sulphur poisoning of water-gas shift catalysts: site blocking and electronic structure modification, *Mol. Simul.*, 35 (2009) 936-941.
- [57] P. Kratzer, B. Hammer, J.K. Nørskov, Geometric and electronic factors determining the differences in reactivity of H<sub>2</sub> on Cu(100) and Cu(111), *Surf. Sci.*, 359 (1996) 45-53.
- [58] B. Hammer, M. Scheffler, K.W. Jacobsen, J.K. Nørskov, Multidimensional Potential Energy Surface for H<sub>2</sub> Dissociation over Cu(111), *Phys. Rev. Lett.*, 73 (1994) 1400-1403.
- [59] C.S. Alexander, J. Pritchard, Chemisorption of hydrogen on evaporated copper films, *J. Chem. Soc., Faraday Trans.1*, 68 (1972) 202-215.
- [60] M. Cacciatore, G.D. Billing, Dissociation and atom recombination of H<sub>2</sub> and D<sub>2</sub> on metallic surfaces: A theoretical survey, *Pure Appl. Chem.*, 68 (1996) 1075-1081.
- [61] P.D. Vaidya, V.V. Mahajani, Kinetics of Liquid-Phase Hydrogenation of Furfuraldehyde to Furfuryl Alcohol over a Pt/C Catalyst, *Ind. Eng. Chem.*, 42 (2003) 3881-3885.
- [62] A.B. Merlo, V. Vetere, J.F. Ruggera, M.L. Casella, Bimetallic PtSn catalyst for the selective hydrogenation of furfural to furfuryl alcohol in liquid-phase, *Catal. Commun.*, 10 (2009) 1665-1669.

- [63] P. Mäki-Arvela, L.-P. Tiainen, A.K. Neyestanaki, R. Sjöholm, T.-K. Rantakylä, E. Laine, T. Salmi, D.Y. Murzin, Liquid phase hydrogenation of citral: suppression of side reactions, *Appl. Catal. A Gen.*, 237 (2002) 181-200.
- [64] P.G.N. Mertens, F. Cuypers, P. Vandezande, X. Ye, F. Verpoort, I.F.J. Vankelecom, D.E. De Vos, Ag<sup>0</sup> and Co<sup>0</sup> nanocolloids as recyclable quasihomogeneous metal catalysts for the hydrogenation of  $\alpha,\beta$ -unsaturated aldehydes to allylic alcohol fragrances, *Appl. Catal. A Gen.*, 325 (2007) 130-139.
- [65] F.A.J. Meskens, *Methods for the Preparation of Acetals from Alcohols or Oxiranes and Carbonyl Compounds*, *Synthesis*, 1981 (1981) 501-522.
- [66] R. Kumar, A.K. Chakraborti, Copper(II) tetrafluoroborate as a novel and highly efficient catalyst for acetal formation, *Tetrahedron Lett.*, 46 (2005) 8319-8323.
- [67] J.-H. Lin, C.-S. Chen, H.-L. Ma, C.-Y. Hsu, H.-W. Chen, Synthesis of MWCNTs on CuSO<sub>4</sub>/Al<sub>2</sub>O<sub>3</sub> using chemical vapor deposition from methane, *Carbon*, 45 (2007) 223-225.
- [68] V.V. Pushkarev, N. Musselwhite, K. An, S. Alayoglu, G.A. Somorjai, High Structure Sensitivity of Vapor-Phase Furfural Decarbonylation/Hydrogenation Reaction Network as a Function of Size and Shape of Pt Nanoparticles, *Nano Lett.*, 12 (2012) 5196-5201.
- [69] S. Sitthisa, T. Sooknoi, Y. Ma, P.B. Balbuena, D.E. Resasco, Kinetics and mechanism of hydrogenation of furfural on Cu/SiO<sub>2</sub> catalysts, *J. Catal.*, 277 (2011) 1-13.
- [70] V. Vorotnikov, G. Mpourmpakis, D.G. Vlachos, DFT Study of Furfural Conversion to Furan, Furfuryl Alcohol, and 2-Methylfuran on Pd(111), *ACS Catal.*, 2 (2012) 2496-2504.
- [71] S. Sitthisa, W. An, D.E. Resasco, Selective conversion of furfural to methylfuran over silica-supported NiFe bimetallic catalysts, *J. Catal.*, 284 (2011) 90-101.

## Chapter 4 PdCu single atom alloys for the selective hydrogenation of furfural





## 4.1 Introduction

In the earlier chapter, it is shown that Cu catalysts derived from Cu acetate are optimal for the selective hydrogenation of furfural. However, while Cu is very selective for the reaction, it lacks the activity that other more expensive metals such as Ir, Pt, Pd and Ru can provide [1-6].

In most cases, only the surface atoms of the nanoparticle are the active sites, whereas those inside the nanoparticle are spectators. For example, in a 5 nm particle, only about 22% of the atoms are available for catalysis, which leads to inefficient use of precious metals (Fig. 1.7.1). This is problematic since the scarce nature of precious metals requires intensive mining operations that are environmentally damaging [7]. Catalysts that use more abundant elements normally need harsher conditions and/or augmentation of their catalytic activity by combining them with precious metals [3]. A method of improving atom efficiency is to develop more and more dispersed catalysts up to the atomic limit. This is where single-atom catalysis exists, where traditional heterogeneous and homogeneous distinctions become blurred [8]. Several investigations have been published on whether a single atom attached to the support would work as an efficient catalyst [9-11]. Flytzani-Stephanopoulos *et al.* [12] stumbled onto single atoms of Au, present as surface Au-O<sub>x</sub> species serving as effective catalysts for the low-temperature water-gas shift reaction, as they found no evidence of Au nanoparticles taking part as the active species. Various other studies have investigated single-atom catalysts (SAC) theoretically and experimentally looking at unique preparation methods and catalytic processes [13-18]. Advantages of single atoms include incredible activity [19] with chemoselectivity due to the isolated active sites. As one can expect, there is better control of sites compared to a nanoparticle where multiple different active sites are present (e.g., on different surfaces such as 111, 110 and 100). A subclass of SACs supported on typically a base metal such as copper were reported initially by Kyriakou *et al.* [20]. The Pd atoms were deposited on a Cu (111) surface in Ultra High Vacuum (UHV) conditions, where they observed stable isolated Pd species via LT-STM (low-temperature scanning tunnelling microscopy) and named the structure as a single-atom alloy (SAA). Various DFT studies also supported their findings that the isolated Pd atoms present can act as entry and exit sites for hydrogen dissociation and recombination

with the reported activation energy dropping from 0.4 eV (Cu 111) to  $\sim 0.02$  eV with the SAA [16, 20-22]. These fundamental experiments in UHV led to the development of actual SAA catalysts used in various catalytic reactions [15, 18, 23, 24].

This chapter investigates the synthesis of atom efficient SAA catalysts for selective hydrogenation of furfural. In this chapter the Cu nanoparticle formation was controlled colloiddally, as it was previously shown in Chapter 3 how wet impregnation creates a range of different nanostructures. The resulting monodisperse Cu nanoparticle will be used as a sacrificial host for the Pd atoms to be implanted. Since hydrogen dissociation is an activated process on Cu surfaces, the isolated Pd atoms will enhance hydrogen dissociation and spillover hydrogen onto the copper surface, increasing the activity of the catalyst. Investigations will also be conducted to optimise the catalytic behaviour by adjusting synthetic parameters. Due to the lack of experimental studies on whether the isolated surface Pd atoms can sink into the nanoparticle, XAS experiments will be used to give insight into this.

## 4.2 Characterisation of alumina supported catalysts

### 4.2.1 PdCu SAA catalysts 12 wt%

#### 4.2.1.1 Elemental and Surface Area Analysis

Bulk elemental analysis of the 12 wt% catalytic materials (Table 4.2.1) shows that adjusting the galvanic replacement (GR) method to synthesise the SAA catalysts can significantly affect the final loading of both Cu and Pd. GR is a simple way to prepare bimetallic nanostructures using metal hosts as templates for the minority metal [18, 25, 26]. In the present case, the Pd (II) precursors are reduced by the Cu<sup>0</sup> ( $\text{Cu} + \text{Pd}^{2+} \rightarrow \text{Cu}^{2+} + \text{Pd}$ ). The process is rationalised by Cu having the lower reduction potential ( $\text{Cu}^{2+}/\text{Cu}$ ,  $E^0 = +0.340$  V) compared to Pd ( $\text{Pd}^{2+}/\text{Pd}$ ,  $E^0 = +0.575$  V) so enabling the electron transfer from Cu to Pd. Utilising method 1 (M1), causes the least amount of leaching of the host 12% Cu/Al<sub>2</sub>O<sub>3</sub> catalyst but also leading to the lowest resulting Pd loading. While M3's conditions observed to be the harshest utilising 2 mM HCl (20 times more concentrated than M1) causing substantial leaching of the Cu phase. The purpose of the HCl in the procedure is to dissolve any surface Cu oxide that may be present as the GR reaction will be severely hindered [15] while the metallic Cu phase should be more chemically resistant to HCl [27].

*Table 4.2.1 Bulk elemental analysis, for the 12 wt% PdCu catalysts determined by ICP-OES.*

Sample	GR method	Pd loading (wt%)	Cu loading (wt%)
Cu <sub>100</sub> (12%)	-	-	12.525 ± 0.250
Pd <sub>1</sub> Cu <sub>153</sub> (12% M1)	0.1mM HCl, 100 °C	0.132 ± 0.005	12.476 ± 0.123
Pd <sub>1</sub> Cu <sub>100</sub> (12% M2)	Aqueous media, sonication, 50 °C	0.189 ± 0.015	11.341 ± 0.215
Pd <sub>1</sub> Cu <sub>98</sub> (12% M3)	2.0 mM HCl, 100 °C	0.175 ± 0.006	10.262 ± 0.047
Pd <sub>1</sub> Cu <sub>93</sub> (12% M4)	0.1 mM HCl, sonication, 50 °C	0.199 ± 0.016	11.076 ± 0.175

It has also been shown the reduction of Pd<sup>2+</sup> and Pt<sup>2+</sup> can be accelerated by sonication [18, 25, 26] with PdCu SAA catalysts previously being synthesised this way [18]. Therefore, sonication was implemented for methods 2 and 4 (M2 and M4). Sonication caused the noticeable dissolution of the Cu nanoparticles, observed by the reduction in the Cu loading which has been reported earlier [28] and has

been further exacerbated with the addition of 0.1 mM HCl (M4). But as previously reported, the GR reaction was found significantly enhanced by increased Pd uptake.

Porosimetry of the bare  $\text{Al}_2\text{O}_3$  support (Fig. 4.2.1) showed that it has a type II isotherm with a surface area of  $38.2 \text{ m}^2\text{g}^{-1}$  indicating the material is non-porous/macro-porous. The data is consistent with the manufactured specifications that the material is composed of non-porous crystalline nanoparticles. Only the bare support was investigated as the previous chapter showed minimal differences in surface area between the catalysts.

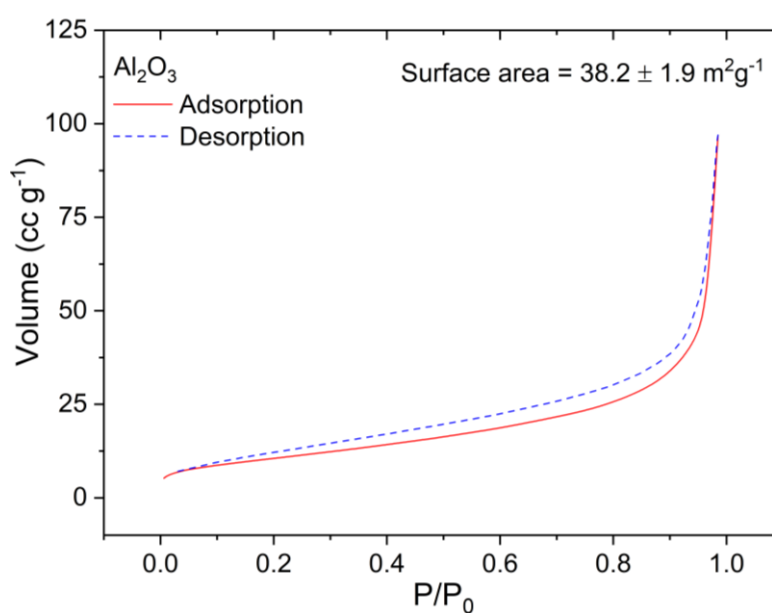


Fig. 4.2.1 BET isotherm for the bare  $\text{Al}_2\text{O}_3$  support.

#### 4.2.1.2 Powder X-ray Diffraction (PXRD)

Fig. 4.2.2 displays the *ex-situ* reduced (300 °C, 0.5 h) diffractograms for the 12 wt% loaded catalysts. The diffractograms show broad but discernible reflections characteristic of nano-crystalline  $\gamma$ -Al<sub>2</sub>O<sub>3</sub> (JCPDS card No. 29-0063) and  $\delta$ -Al<sub>2</sub>O<sub>3</sub> (JCPDS card No. 46-1215), and a small impurity arising from the  $\theta$ -Al<sub>2</sub>O<sub>3</sub> phase (JCPDS card No. 11-0517). Qualitatively examining the alumina diffraction data, the morphology of the support after Cu and Pd deposition seems largely unchanged. The host Cu<sub>100</sub> (12%) catalyst shows observable diffraction peaks associated with the copper phase, with a calculated average lattice of 3.621 Å (Table 4.2.2). Similarly, the PdCu bimetallic catalysts also show observable Cu diffraction peaks. However, insignificant changes in the lattice parameters are observed with Pd addition, which contradicts Vegard rule [29] suggestion that the lattice should expand. However, a recent paper by Gamler *et al.* [30] suggests that when there is a lattice mismatch in core-shell bimetallic systems a compressive strain develops, resulting in the diffraction peak shifting to higher angles and the observation of lattice contractions. It should be noted the lattice parameters determined from whole pattern powder modelling (WPPM) lacks the accuracy of methods such as Rietveld refinement as WPPM has only the position of the peaks constrained while the latter has both the position and intensity of the peaks constrained to the crystal structure.

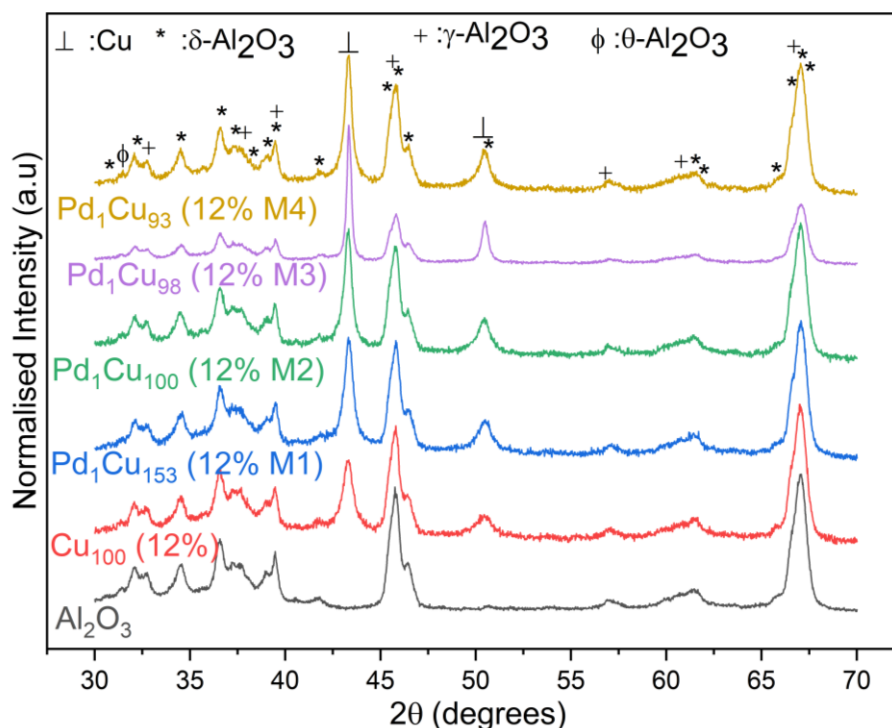


Fig. 4.2.2 XRD diffractograms of reduced ex-situ 12 wt% PdCu species supported on Al<sub>2</sub>O<sub>3</sub> catalysts and the bare support.

Table 4.2.2 Crystallite size and lattice parameters for the 12 wt% PdCu catalysts

Sample	GR method	Crystallite size (nm) <sup>a</sup>	Crystallite size (nm) <sup>b</sup>	Lattice Parameter (Å) <sup>b</sup>
Cu <sub>100</sub> (12%)	-	8.2 ± 0.8	6.4 ± 3.7	3.621
Pd <sub>1</sub> Cu <sub>153</sub> (12% M1)	0.1mM HCl	10.4 ± 1.0	7.7 ± 5.0	3.615
Pd <sub>1</sub> Cu <sub>100</sub> (12% M2)	Aqueous sonication	11.0 ± 1.1	7.1 ± 5.1	3.620
Pd <sub>1</sub> Cu <sub>98</sub> (12% M3)	2.0 mM HCl	21.7 ± 2.2	9.9 ± 8.7	3.617
Pd <sub>1</sub> Cu <sub>93</sub> (12% M4)	0.1 mM HCl sonication	11.9 ± 1.2	5.1 ± 4.0	3.617

<sup>a</sup> Determined by XRD via the integral breadth method, <sup>b</sup> WPPM via XRD

The crystallite size of the host Cu<sub>100</sub> (12%)/Al<sub>2</sub>O<sub>3</sub> is observed to be 6.4 ± 3.7 nm, which is small considering the very high Cu loading of the catalyst. And since the nanoparticles were colloiddally synthesised, the size and shape of the particles can be controlled before deposition onto the support. Similar control of the nanoparticle formation would not be possible for an equivalent wet impregnation synthesis. Consequently, this method has given a good sacrificial platform for the subsequent Pd incorporation. Examining the Cu crystallite sizes in Table 4.2.2, one can observe that as Pd is introduced

onto the host Cu catalyst, the crystallite sizes are within error similar, but the particles generally become less monodisperse (higher standard deviation, WPPM). Mohl *et al.* [25] reported that after the GR process the Cu ions can be reduced again from the solution and deposited onto the nanoparticle. Consequently, this uncontrolled reduction can explain altered the particle size distribution compared to the host catalyst.

The absence of detectable Pd reflections of the bimetallic catalyst in Fig. 4.2.2 indicates the absence of long-range Pd crystalline structure, suggesting the Pd phase is highly dispersed in all these catalysts. It should be also noted Pd ( $29.5^\circ$  for PdO, JCPDS 41-1107) and Cu oxides ( $36.4^\circ$  and  $38.8^\circ$  for  $\text{Cu}_2\text{O}$ , 05-0667 and CuO, JCPDS 45-0937, respectively) were also not detected implying the nanoparticle mostly has taken on a core-shell type structure with a metallic core and an passivation layer.

#### 4.2.1.3 X-ray Photoelectron Spectroscopy (XPS) and X-ray excited Auger Electron Spectroscopy (XAES)

Fig. 4.2.3 shows XPS spectra of the *ex-situ* reduced catalysts along with reference spectra of Cu, CuO, Cu<sub>2</sub>O, Pd and PdO. The characteristic Cu 2p doublet is observed with the Cu 2p<sub>3/2</sub> transition centred at 932.50 eV (Table 4.2.3). The absence of strong shake-up satellites at 942.6 eV and 962.3 eV, shows the absence of Cu<sup>2+</sup> species so, the Cu is largely in its Cu<sup>0</sup> or Cu<sup>+</sup> oxidation state. Note that passivation of the copper nanoparticles is expected after exposure to atmospheric oxygen before analysis. Minimal differences in the Cu 2p<sub>3/2</sub> transition are observed between the catalysts. It should also be noted, the binding energies of Cu<sup>+</sup> and Cu<sup>0</sup> are very similar making deconvolution problematic. With this problem in mind, the composition of the Cu species was determined according to the Cu 2p<sub>3/2</sub> and satellite peaks [31-33]. The surface compositional analysis (Table 4.2.3) shows that overall, the surface Cu species are dominantly in the Cu<sup>0</sup> or Cu<sup>+</sup> state with ~15% composing of Cu<sup>2+</sup> (CuO) supporting the idea of an surface Cu oxide layer.

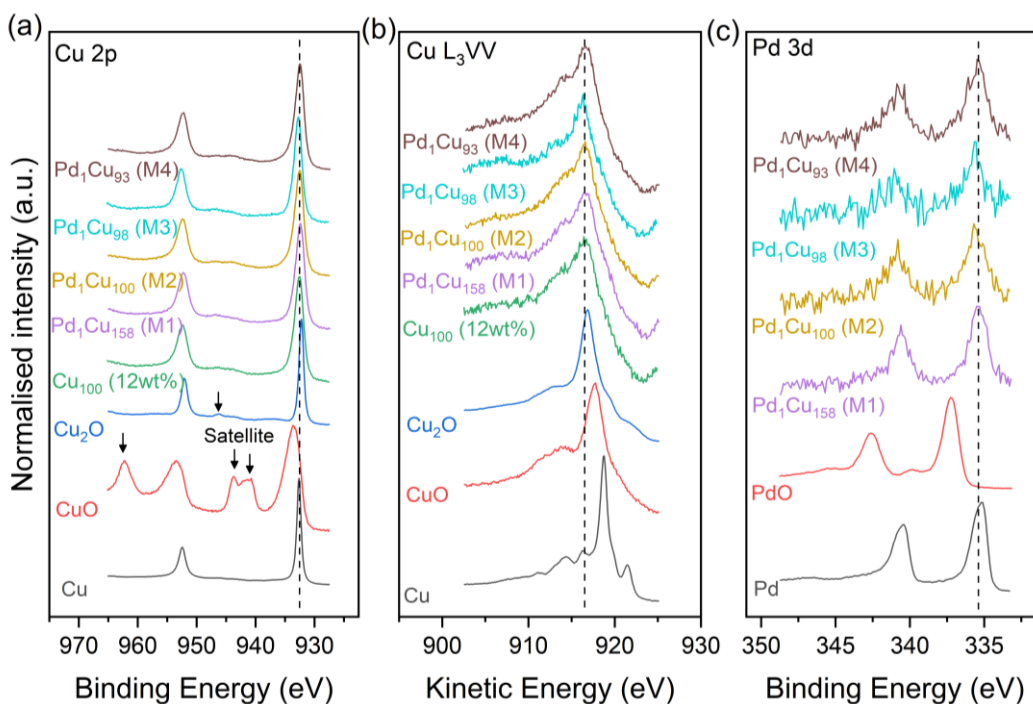


Fig. 4.2.3 High-resolution stacked XPS and XAES spectra of the (a) Cu 2p, (b) Cu L<sub>3</sub>VV and (c) Pd 3d regions for the 12 wt% PdCu catalysts synthesised using different methods after being reduced *ex-situ* at 300 °C for 0.5 h under flowing H<sub>2</sub>.

Table 4.2.3 Summarised binding energies for the Pd 3d<sub>5/2</sub> and Cu 2p<sub>3/2</sub>, kinetic energies for the Auger Cu L<sub>3</sub>VV transitions, surface composition, modified Auger parameters for copper catalysts and change in relaxation energy compared to bulk Cu for the ex-situ reduced 12 wt% catalysts and reference materials.

Sample	Pd 3d <sub>5/2</sub> (eV)	Cu 2p <sub>3/2</sub> (eV)	L <sub>3</sub> VV (eV)	Cu <sup>0</sup> + Cu <sup>+</sup> (%)	Cu <sup>2+</sup> (%)	Modified Auger parameter (eV)	Δ Relaxation energy (eV)
Cu <sub>100</sub> (12%)	-	932.47	916.42	86.2	13.8	1848.89	1.25
Pd <sub>1</sub> Cu <sub>153</sub> (12% M1)	335.41	932.40	916.49	84.4	15.6	1848.89	1.25
Pd <sub>1</sub> Cu <sub>100</sub> (12% M2)	335.70	932.50	916.59	85.4	14.6	1849.09	1.14
Pd <sub>1</sub> Cu <sub>98</sub> (12% M3)	335.47	932.47	916.62	85.4	14.6	1849.09	1.14
Pd <sub>1</sub> Cu <sub>93</sub> (12% M4)	335.65	932.75	916.34	83.6	16.4	1849.09	1.14
CuO	-	933.62	917.78	-	-	1851.40	-0.01
Cu <sub>2</sub> O	-	932.29	916.70	-	-	1848.99	1.20
Cu foil*	-	932.63	918.75	-	-	1851.38	0
PdO	337.26	-	-	-	-	-	-
Pd foil	335.20	-	-	-	-	-	-

\*Cu 2p<sub>3/2</sub> was calibrated to the ISO standard of 932.63 eV.

Contrarily to the small difference in the Cu 2p<sub>3/2</sub> transition binding energy between Cu<sub>2</sub>O and Cu, chemical shifts in the Auger transitions are much more prominent due to the altered pathway for the transition involving electrons closer to the valence electrons, which are involved in bonding [34]. Consequently, the L<sub>3</sub>VV Auger transition for the reference Cu<sub>2</sub>O sample is found shifted to lower kinetic energies (~2 eV) when compared to the reference Cu sample (Table 4.2.3). Cu L<sub>3</sub>VV Auger transitions for the catalysts were found to be comparable to Cu<sub>2</sub>O, though shifted to slightly lower kinetic energies (by 0.1 eV). The modified Auger parameter/relaxation energies which are dependent on initial and final state effects show similar trends suggesting the surface is largely composed of Cu<sub>2</sub>O with the further shift from bulk Cu<sub>2</sub>O due to the polarizable support. The latter point will be discussed further in section 4.2.2.6.

Fig. 4.2.3c shows the attenuated Pd 3d<sub>5/2</sub> transition centred at approximately 335.5 eV, shifted 0.3 eV higher the metallic Pd. This expected result supports the idea that the surface oxidised Cu nanoparticles withdraw electrons from the Pd atoms, therefore increasing the binding energy. It should be noted bulk PdO is not formed as PdO will cause a large binding energy shift of 2.1 eV (Table 4.2.3). So, it is likely that the surface Pd analysed by XPS is likely near or in the Cu oxide layer via Pd-O-Cu/O-Cu-Pd interactions.

Fig. 4.2.4 shows the XPS derived dispersion calculations, giving an insight into the location of the Cu and Pd atoms present in the catalysts. Supported by the previous characterisation techniques, the Pd<sub>1</sub>Cu<sub>153</sub> (12% M1) catalyst seems to be the most unaffected by the GR process by observing similar Cu dispersion values. The calculated Cu dispersion for both catalysts equates to a nanoparticle size  $\sim 10.5 \pm 1.5$  nm (according to the dispersion vs Cu nanoparticle plot in Fig. 1.7.1) which is within error similar to the XRD results. It can be also observed that the Pd<sub>1</sub>Cu<sub>98</sub> (12% M3) catalyst has the lowest dispersion (nanoparticle size of  $\sim 11.0$  nm), though the difference is slight compared to the data from the crystallite size calculations. This can be rationalised by the fact that XPS observe all atoms on the surface no matter if they are in small or larger nanoparticles. While the sonicated catalysts (M2 and M4) appear to have the highest Cu dispersion (nanoparticle sizes of  $\sim 7.5$  nm and  $\sim 6.8$  nm, respectively) which is consistent with sonication's ability to break up aggregates [28]. However, sonication can promote the Kirkendall effect [26, 35], whereby the diffusion of elements like Pt into Cu is faster than the opposite reaction. Consequently, the promotion of the diffusion of the Pd into the bulk of the copper phase is detected by the decrease in the Pd dispersion. Though, the bimetallic catalyst synthesised from method 1 (Pd<sub>1</sub>Cu<sub>153</sub> (12% M1)) appears to have the highest relative surface Pd concentration (highest Pd dispersion). Such results are consistent with previous observations [36] that core-shell morphology is favoured when the GR process occurs slowly, while harsher conditions (in the current case, 2 mM HCl and sonication) promote full alloy formation. High surface Pd concentration is crucial, as surface Pd species are responsible for the enhanced hydrogen dissociation capability of the catalyst. This is due to the Pd surface atoms acting as entrance and exit sites for hydrogen dissociation and the subsequent spillover onto the copper phase [37] where the rest of the reaction takes place.

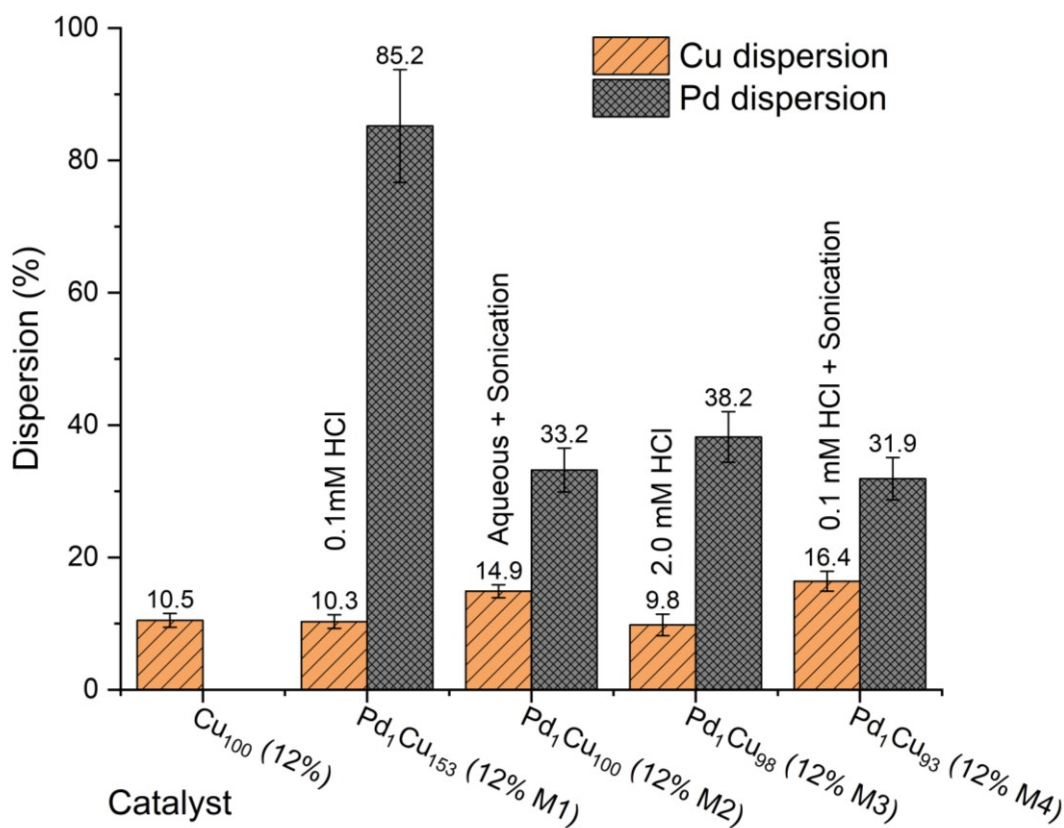


Fig. 4.2.4 XPS derived dispersions for the 12 wt% PdCu catalysts synthesised using different methods after being reduced *ex-situ* at 300 °C for 0.5 h under flowing H<sub>2</sub>.

It has been reported by Elzey *et al.* [38] that Cu nanoparticles aged in aqueous HCl (25 mM) solutions in air can form a paratacamite (Cu<sub>2</sub>(OH)<sub>3</sub>Cl) phase. The Cl 2s/2p region of the survey spectrum (Fig. 4.2.5) for the Pd<sub>1</sub>Cu<sub>98</sub> (12% M3) catalyst is unable to detect the presence of Cl. The absence of Cl suggests that in 2 mM HCl aqueous conditions, detectable Cl is not formed on the nanoparticle after reduction at 300 °C. The survey spectrum also shows the absence of any other contamination other than adventitious carbon which is thought to be deposited from the atmosphere and is typically comprised of short-chain and possibly polymeric carbon compounds [39].

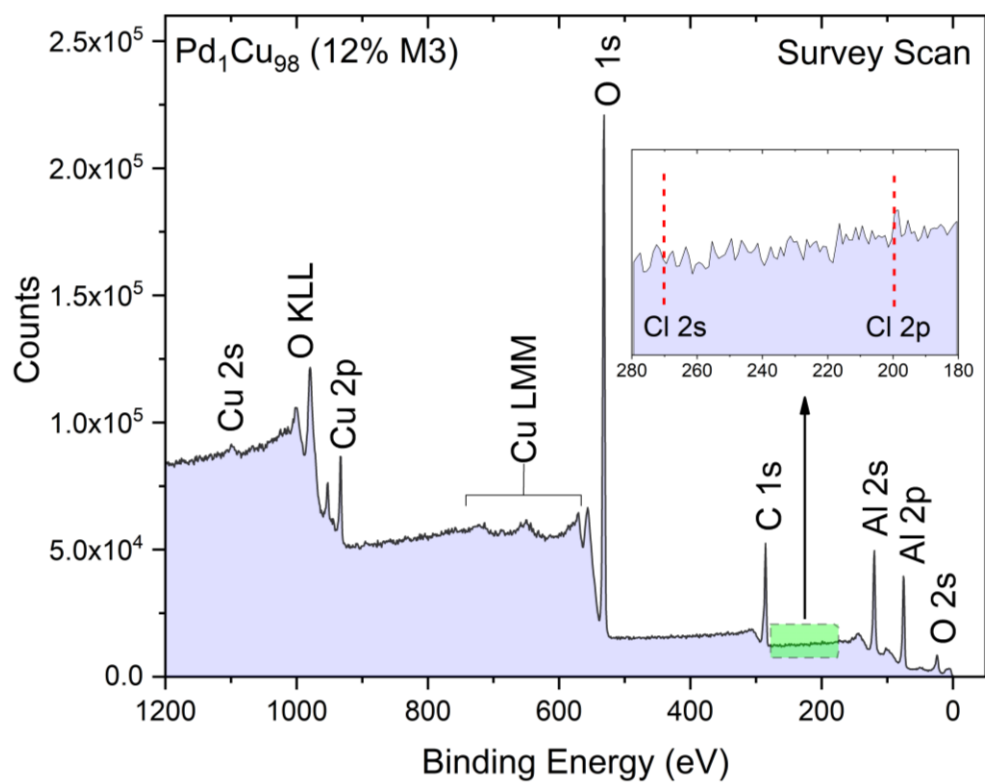


Fig. 4.2.5 Survey XPS spectrum of the ex-situ reduced  $\text{Pd}_1\text{Cu}_{98}$  (12% M3) catalyst with an insert of the  $\text{Cl } 2s$  and  $2p$  region.

#### 4.2.1.4 X-ray Absorption Spectroscopy (XAS)

The PdCu catalyst synthesised via method 1 (Pd<sub>1</sub>Cu<sub>158</sub> (12% M1)) was chosen for XAS analysis, as the catalyst was found to be the most promising from the Pd dispersion and the later shown catalytic testing data. The EXAFS modelling is displayed in Table 4.2.4 and Fig. 4.2.6, the fitting was completed by assuming the Cu structure was largely unchanged with one of the Cu atoms replaced with Pd. The data suggests the absence of Pd-Pd coordination at 2.742 Å. Therefore, a single scattering path (Pd-Cu) was included in the fit relating to the bonding between the Cu atoms and Pd atom. After the first coordination shell, the intensity of the oscillations (in R-space) quickly falls away which suggests that the structure is quite disordered after the first-shell or lack of adequate signal to noise. The data, therefore, suggest the Pd atoms have successfully been atomically dispersed throughout the Cu phase without clustering of the Pd atoms. This conclusion can be further supported by the calculated Pd-Cu bond length of 2.572 Å, which matches well to the bulk Cu-Cu bond length of 2.551 Å considering the slightly larger Pd atomic radius (1.40 Å) compared to Cu (1.35 Å). It should be noted that EXAFS can only distinguish similar bond length elements if the difference in the atomic number is approximately at least 3 (for higher atomic number elements this can increase to 5-7), as the difference in the computed intensity of the scattering path is nearly identical. In the present case, the difference in the atomic number between Cu and Pd is 17 and have a significant difference in their bond lengths making their differentiation possible.

Table 4.2.4 EXAFS model fitting of the re-oxidised PdCu/Al<sub>2</sub>O<sub>3</sub> catalyst, Pd and Cu reference foils.

Sample	Sample form	Shell	CN	R (Å)	$\sigma^2$ (Å <sup>2</sup> ) $\times 10^3$	$\Delta E_0$ (eV)	R factor
Pd foil	-	Pd-Pd	12	2.742 ± 0.002	5.6 ± 0.4	3.70 ± 0.39	0.0163
Cu foil	-	Cu-Cu	12	2.551 ± 0.054	9.3 ± 0.8	2.96 ± 0.84	0.0270
Pd <sub>1</sub> Cu <sub>158</sub> (12% M1)	Re-oxidised	Pd-Cu	6.2 ± 0.8	2.572 ± 0.007	4.2 ± 0.8	1.40 ± 1.56	0.0063

CN, average coordination number; R, the distance between the absorber and backscattered atoms.  $\sigma^2$  multiplied by  $10^3$ , Debye-Waller factor;  $\Delta E_0$ , the photoelectron energy origin; R-factor, the closeness of fit.

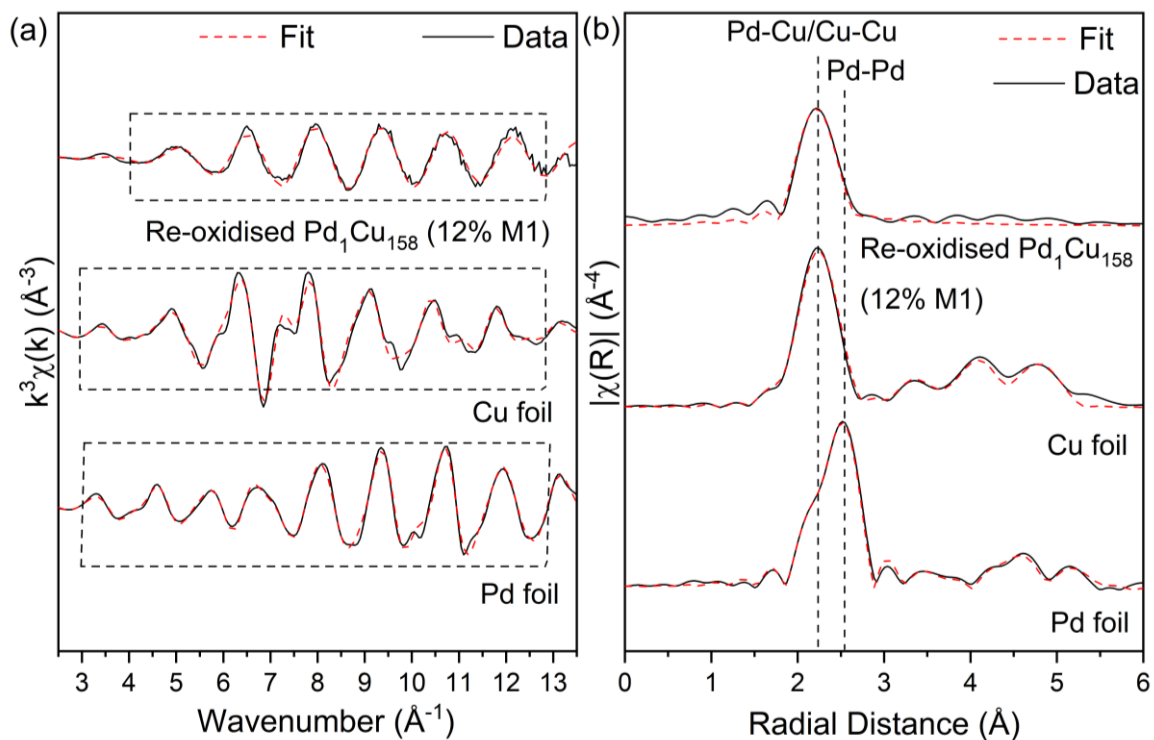


Fig. 4.2.6 EXAFS spectra in  $k$ -space ( $k$ -weight = 3) and (b)  $R$ -space ( $k$ -weight = 3) for the  $\text{Pd}_1\text{Cu}_{158}/\text{Al}_2\text{O}_3$  catalyst (reduced *ex-situ*) along with Pd and Cu reference foils. Dashed-lined rectangles indicate  $k$  ranges over which the data were then Fourier transformed and analysed.

## 4.2.2 PdCu SAA catalysts 1 wt%

### 4.2.2.1 Elemental and Surface Area Analysis

A series of lower Cu loading catalysts were made so that sintering of the nanoparticles due to the high metal content would be less of an issue, thus improving nanoparticle monodispersity. Bulk elemental analysis of the catalytic materials (Table 4.2.5) shows that monometallic catalysts with an approximate Cu/Pd loading of 1 wt% were successfully synthesised. Bimetallic PdCu/Al<sub>2</sub>O<sub>3</sub> catalysts show trace quantities of Pd being incorporated into the monometallic host Cu/Al<sub>2</sub>O<sub>3</sub> catalyst giving Pd:Cu atomic ratios of 1:234, 1:216 and 1:53. Galvanic replacement method 1 was chosen for these catalysts as superior Pd dispersion was achieved with their higher loaded Pd<sub>1</sub>Cu<sub>158</sub> analogue. As mentioned earlier (section 4.2.1.1), a type II isotherm was observed for the bare support with a surface area of 38.2 m<sup>2</sup> g<sup>-1</sup> showing that the material is non-porous/macro-porous.

*Table 4.2.5 Bulk elemental analysis of the 1 wt% catalysts determined by ICP-OES.*

Catalyst	Pd loading <sup>a</sup> (wt%)	Cu loading <sup>a</sup> (wt%)	Pd:Cu atomic ratio
Cu <sub>100</sub>	-	0.9403 ± 0.0267	-
Pd <sub>1</sub> Cu <sub>234</sub>	0.0064 ± 0.0006	0.8947 ± 0.0253	1: 234
Pd <sub>1</sub> Cu <sub>216</sub>	0.0067 ± 0.0006	0.8599 ± 0.0262	1: 216
Pd <sub>1</sub> Cu <sub>53</sub>	0.0296 ± 0.0022	0.9296 ± 0.0232	1: 53
Pd <sub>100</sub>	0.8882 ± 0.0529	-	-

#### 4.2.2.2 Thermogravimetric Analysis with Mass Spectrometry (TGA-MS)

Thermal analysis of the colloiddally capped nanoparticles was performed to understand their decomposition modes during catalyst synthesis. The derivative of the TGA data of the 1-amino-2-propanol ( $C_3H_9NO$ ) capped Cu nanoparticles is shown in Fig. 4.2.7. There is a small mass loss at  $\sim 180$  °C and a larger mass loss at  $\sim 365$  °C which is correlated to the decomposition of the capping agent. MS spectra of the decomposition gases show that the initial small loss at  $\sim 180$  °C is likely due to the formation NO, while at the higher temperatures  $CO_2$  and elemental C was released from the capping agent. Mass spectrometry data, however, did not detect any desorbing 1-amino-2-propanol or other molecules with an Mz of 14, 15, 16, 17, 18, 27 and 60, suggesting the capping agent fully decomposed mainly into NO, C and  $CO_2$ .

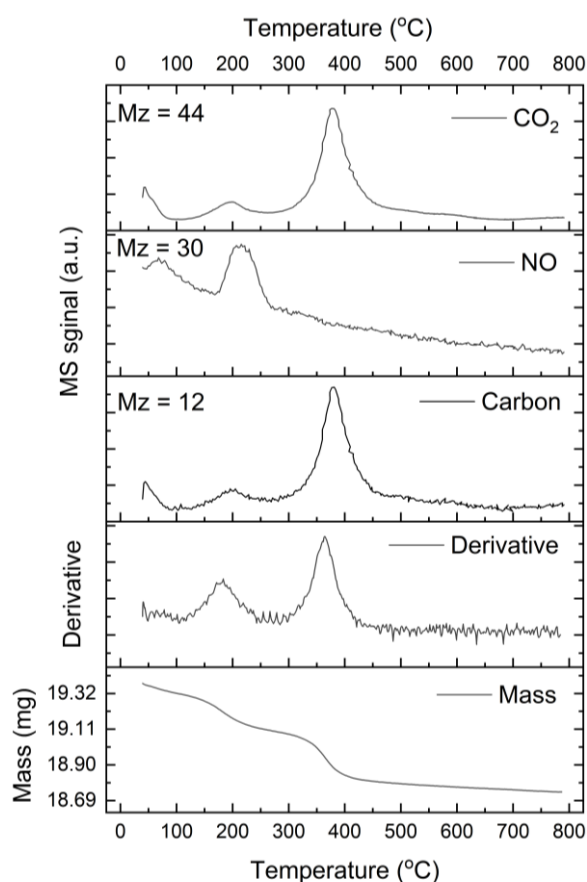


Fig. 4.2.7 TGA-MS data of the 1 wt% colloiddally capped Cu/ $Al_2O_3$  catalyst under flowing  $N_2$  with a heating rate of  $10$  °C  $min^{-1}$ .

#### 4.2.2.3 H<sub>2</sub> Temperature Programmed Reduction (H<sub>2</sub>-TPR)

Following the decomposition of the capping agents, investigations were also conducted to observe the reducibility of the catalysts which is required for catalyst activation. The H<sub>2</sub>-TPR profile shown in Fig. 4.2.8 of the Pd<sub>100</sub> catalyst shows that PdO can reduce to Pd metal at room temperature under flowing H<sub>2</sub> which has also been reported earlier [1]. It has also been reported extensively in the literature that  $\beta$ -hydride species forms when H<sub>2</sub> interacts with Pd which is observed by its decomposition at 94 °C [1, 40-42]. However, this negative decomposition peak is not observed for the SAA catalysts which suggest that such features are below the detection limit (trace Pd loading) and possibly due to the hydride species needing extended Pd surfaces to form [43]. TPR profiles also show that the T<sub>Max</sub> for reduction decreases with Pd addition which is expected as Pd can facilitate hydrogen adsorption through spillover onto the Cu surface [20, 22].

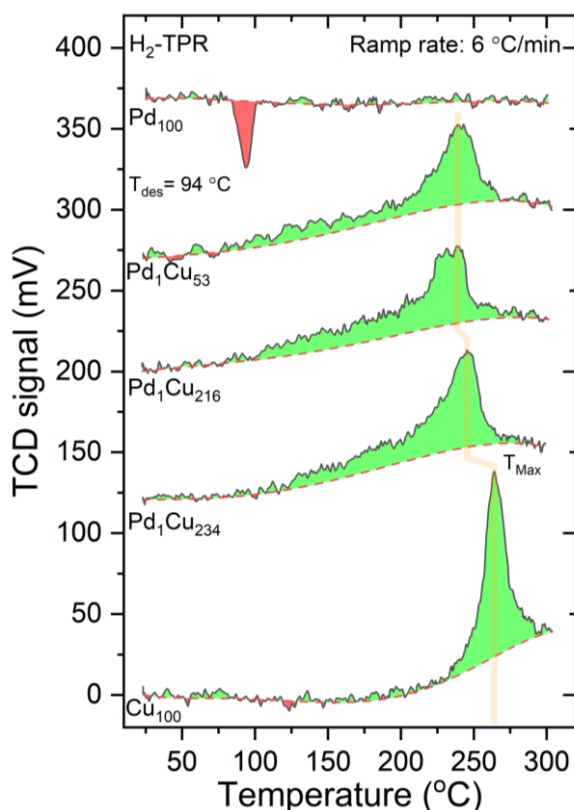


Fig. 4.2.8 H<sub>2</sub> Temperature programmed reduction of Cu, PdCu and Pd catalysts. Gas composition was 5% H<sub>2</sub>/ 95% N<sub>2</sub> v/v at 40 ml/min with a heating rate of approximately 6 °C min<sup>-1</sup>.

#### 4.2.2.4 Powder X-ray Diffraction (PXRD) and Selected Area Electron Diffraction (SAED)

Fig. 4.2.9 shows the catalysts' *ex-situ* PXRD after reduction at 300 °C for 0.5 h. The diffractograms show broad but discernible reflections characteristic of nano-crystalline  $\gamma$ -Al<sub>2</sub>O<sub>3</sub> (JCPDS card No. 29-0063) and  $\delta$ -Al<sub>2</sub>O<sub>3</sub> (JCPDS card No. 46-1215), and a small impurity arising from the  $\theta$ -Al<sub>2</sub>O<sub>3</sub> phase (JCPDS card No. 11-0517). A quantitative examination of the diffractograms shows that the lattice parameters of the alumina phases remain unchanged (Table 4.2.6), suggesting that the copper/palladium phase onto the alumina did not significantly affect the overall morphology of the support. The spots forming rings observed in the SAED images of the catalysts (Fig. 4.2.10) suggest the support is largely polycrystalline, as amorphous materials will form more noticeable diffused rings. It should be noted that only spots relating to the  $\gamma$ -Al<sub>2</sub>O<sub>3</sub> and  $\delta$ -Al<sub>2</sub>O<sub>3</sub> could be distinguished.

Examining the PXRD diffractograms, the host Cu<sub>100</sub>/Al<sub>2</sub>O<sub>3</sub> catalyst did not show any diffraction peaks arising from the copper phase, inferring that the Cu nanoparticles are very small, lacking long-range order, leading to very broad diffraction peaks. In contrast, after galvanic replacement of the Cu with Pd atoms (PdCu catalysts), a broad Cu (111) reflection is observed at 43.4°, and an estimated lattice parameter of 3.623 Å (Table 4.2.6), which is comparable to the 12% Cu<sub>100</sub>/Al<sub>2</sub>O<sub>3</sub> catalyst discussed earlier in section 4.2.1.2. However, the appearance of the Cu (111) reflection only after Pd incorporation can suggest that the GR process itself can increase the order of the Cu such that it is detectable. As was mentioned earlier in section 4.2.1.2, the GR process can cause the Cu ions produced directly from GR or nanoparticle dissolution to be reduced again onto the Cu nanoparticle [25], thus, increasing Cu's apparent crystallinity. Increasing the Pd loading in the catalysts did not show any significant changes in the lattice parameters, and the absence of any Pd reflections suggests the Pd atoms have been incorporated into the Cu phase without forming detectable Pd ensembles or identifiable changes in the Cu structure. As another benchmark catalyst, the monometallic Pd<sub>100</sub>/Al<sub>2</sub>O<sub>3</sub> catalyst showed Pd reflections consistent with that of an Pd crystal structure (JCPDS card No. 05-068). In the diffractograms, Pd (29.5° for PdO, JCPDS 41-1107) and Cu oxides (36.4° and 38.8° for Cu<sub>2</sub>O, 05-0667

and CuO, JCPDS 45-0937, respectively) were not detected implying the nanoparticles are predominately in their metallic state with an oxide passivation layer.

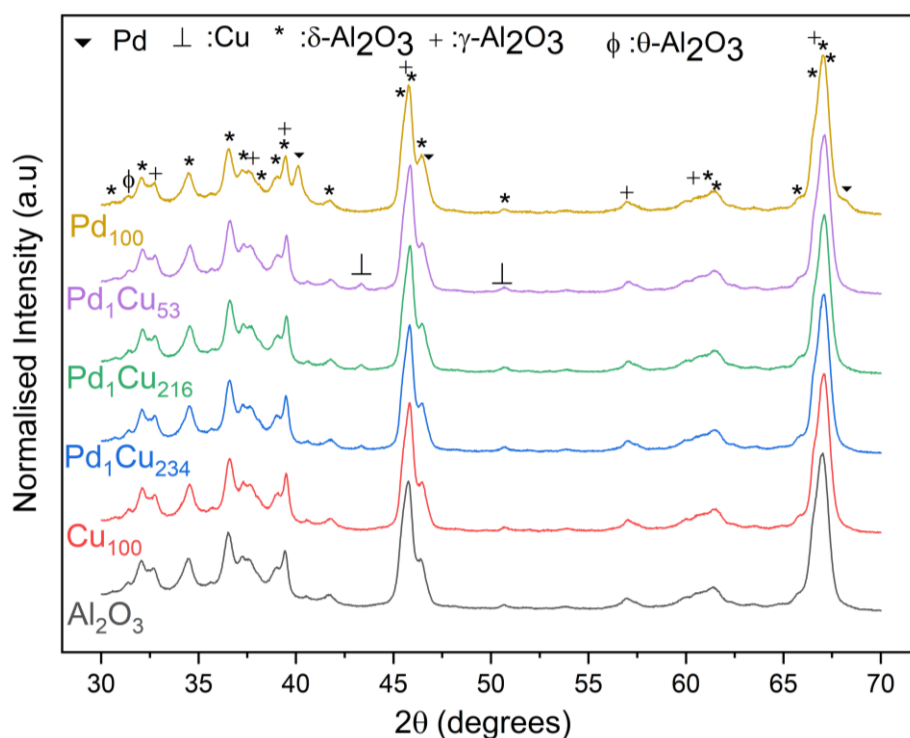
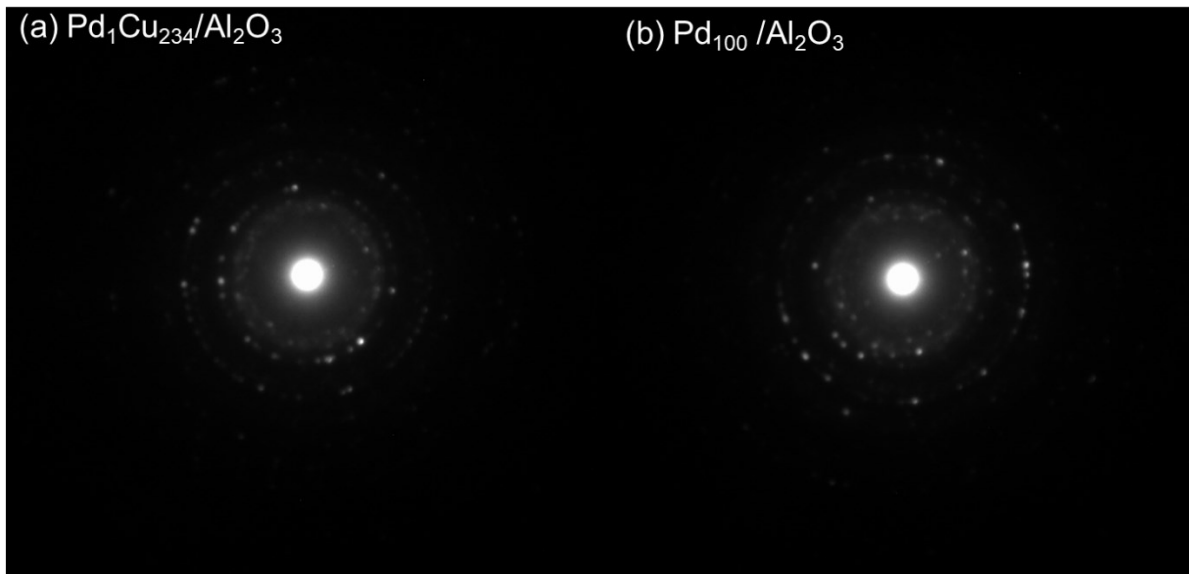


Fig. 4.2.9 XRD diffractograms of the reduced ex-situ Pd, Cu and PdCu species supported on Al<sub>2</sub>O<sub>3</sub> catalysts and the bare support.

Table 4.2.6 Summary of lattice parameters determined from XRD (WPPM) for the 1% catalysts after being reduced ex-situ at 300 °C for 0.5 h under flowing H<sub>2</sub>. For reference data the following JCPDS cards were used 40836, 05-068, 29-0063 and 46-1215 for Cu, Pd, γ- Al<sub>2</sub>O<sub>3</sub> and δ- Al<sub>2</sub>O<sub>3</sub>.

Sample	Cu		Pd	γ- Al <sub>2</sub> O <sub>3</sub>	δ- Al <sub>2</sub> O <sub>3</sub>		
	a (Å)	a (Å)	a (Å)	a (Å)	a (Å)	b (Å)	c (Å)
Reference	3.615	3.889	7.924	7.924	7.956	7.956	11.711
Al <sub>2</sub> O <sub>3</sub>	-	-	7.921	7.921	7.962	7.939	11.746
Cu <sub>100</sub>	-	-	7.917	7.917	7.959	7.934	11.743
Pd <sub>1</sub> Cu <sub>234</sub>	3.622	-	7.914	7.914	7.955	7.933	11.739
Pd <sub>1</sub> Cu <sub>216</sub>	3.624	-	7.916	7.916	7.955	7.934	11.743
Pd <sub>1</sub> Cu <sub>53</sub>	3.623	-	7.917	7.917	7.957	7.934	11.743
Pd <sub>100</sub>	-	3.894	7.915	7.915	7.957	7.928	11.74



*Fig. 4.2.10 SAED images of the reduced ex-situ (a)  $\text{Pd}_1\text{Cu}_{234}$  and (b)  $\text{Pd}_{100}$  catalysts supported on  $\text{Al}_2\text{O}_3$  after being reduced ex-situ at 300 °C for 0.5 h under flowing  $\text{H}_2$ .*

#### 4.2.2.5 Scanning and Transmission Electron Microscopy (STEM/TEM)

Investigation of the Cu<sub>100</sub> catalyst with STEM showed the presence of very small monodisperse Cu nanoparticles with an average size of  $2.7 \pm 0.7$  nm (Fig. 4.2.11a). It should be noted, that this is in stark contrast to the previous Chapter where a wet impregnation synthesis gave rise to isolated and dimer copper atoms embedded onto an Al<sub>2</sub>O<sub>3</sub> surface. As a consequence, wet impregnation typically gave a range of nanostructures, while the colloidal synthesis formed monodisperse nanoparticles ideal for understanding the formation of single-atom alloy catalysts. Nevertheless, the initial replacement of Pd atoms by galvanic replacement causes a slight decrease in the nanoparticle size (Fig. 4.2.11f and Table 4.2.7) for the Pd<sub>1</sub>Cu<sub>234</sub> and Pd<sub>1</sub>Cu<sub>216</sub> catalysts. This observation is likely caused by the initial dissolution of the nanoparticles seen by the reduction in the Cu loading (Table 4.2.5) after the GR process. But, once the Pd concentration was quadrupled (Pd<sub>1</sub>Cu<sub>53</sub> catalyst) the nanoparticles appear to grow into larger particles with sizes of  $7.0 \pm 4.4$  nm (Fig. 4.2.11d). Particle sizes (assuming particles are monocrystalline) were determined via XRD (Table 4.2.7) using both integral breadth and WPPM methods. Particle size analysis between the simple line profile analysis (integral breadth method and the Scherrer equation) and the STEM and WPPM were inconsistent. This can be explained as a volume-weighted crystallite size average is determined using the integral breadth method, which can overestimate crystallite size by rogue large particles. In contrast, values calculated using the WPPM method give an area-weighted average which is influenced less by large particles. WPPM and STEM results support the observation that Cu particle size increase with Pd concentration, which is hypothesised to be attributed to the reduction of Cu ions onto the existing nanoparticles [25], thus possibly explaining why only the Cu peak is seen for the PdCu catalysts. TEM images of the benchmark Pd<sub>100</sub> catalyst (Fig. 4.2.11e) synthesised colloiddally show that the average nanoparticle size is  $5.1 \text{ nm} \pm 2.7 \text{ nm}$  with the presence of larger 10 nm particles supporting the dissimilarity between the TEM and XRD particle sizes.

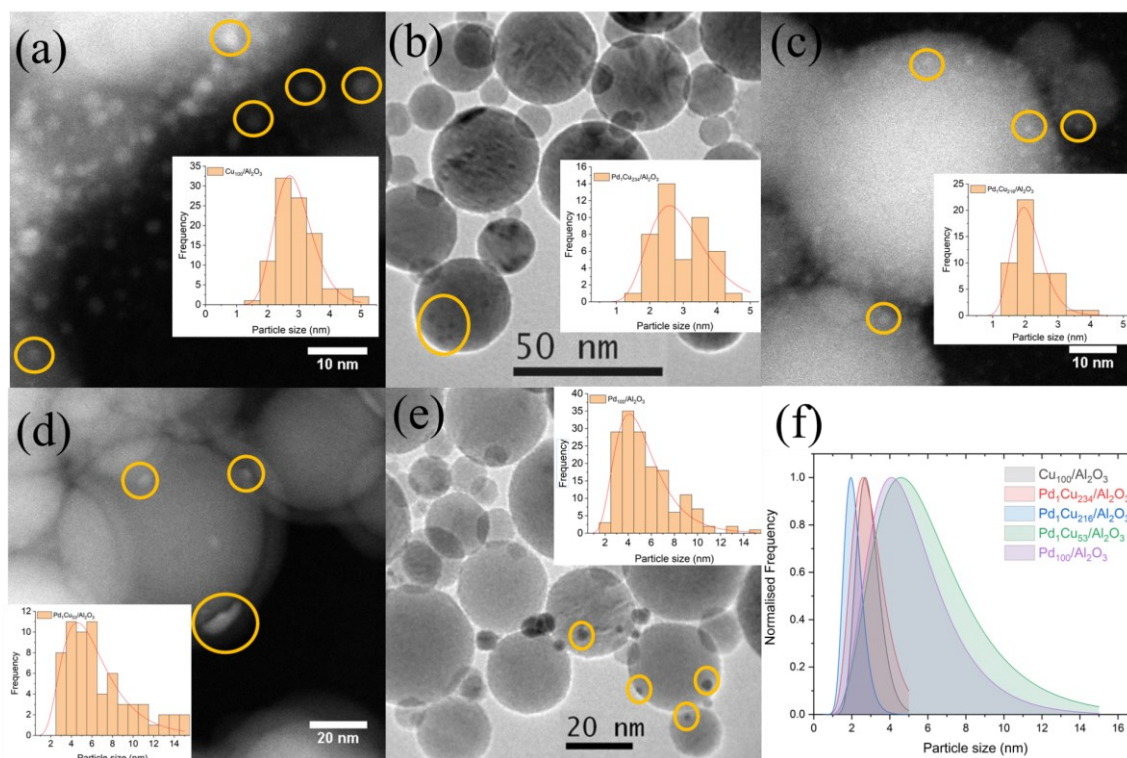


Fig. 4.2.11 STEM/TEM images and particle distributions of (a)  $\text{Cu}_{100}/\text{Al}_2\text{O}_3$ , (b)  $\text{Pd}_1\text{Cu}_{234}/\text{Al}_2\text{O}_3$ , (c)  $\text{Pd}_1\text{Cu}_{216}/\text{Al}_2\text{O}_3$ , (d)  $\text{Pd}_1\text{Cu}_{53}/\text{Al}_2\text{O}_3$ , (e)  $\text{Pd}_{100}/\text{Al}_2\text{O}_3$ , and (f) lognormal STEM/TEM size distributions for the catalysts reduced ex-situ at  $300^\circ\text{C}$  for 0.5 h under flowing  $\text{H}_2$ .

Table 4.2.7 Pd/Cu crystallite and particle size analysis for the 1 wt% catalysts after being reduced ex-situ at  $300^\circ\text{C}$  for 0.5 h under flowing  $\text{H}_2$ .

Catalyst	Pd crystallite/particle size (nm)	Cu crystallite/particle size (nm)
$\text{Cu}_{100}$	-	$2.7 \pm 0.7^{\text{d}}$
$\text{Pd}_1\text{Cu}_{234}$	-	$22.8 \pm 2.3^{\text{b}}$
		$2.3 \pm 2.7^{\text{c}}$
		$2.6 \pm 0.7^{\text{d}}$
$\text{Pd}_1\text{Cu}_{216}$	-	$23.7 \pm 2.4^{\text{b}}$
		$2.0 \pm 2.4^{\text{c}}$
		$2.0 \pm 0.6^{\text{d}}$
$\text{Pd}_1\text{Cu}_{53}$	-	$19.7 \pm 2.0^{\text{b}}$
		$15.2 \pm 8.4^{\text{c}}$
		$7.0 \pm 4.4^{\text{d}}$
$\text{Pd}_{100}$	$14.0 \pm 1.4^{\text{b}}$	-
	$14.0 \pm 6.4^{\text{c}}$	-
	$5.1 \pm 2.7^{\text{d}}$	-

<sup>b</sup> Integral breadth method via XRD, <sup>c</sup> WPPM via XRD, <sup>d</sup> STEM/TEM

#### 4.2.2.6 X-ray Photoelectron Spectroscopy (XPS) and X-ray excited Auger Electron Spectroscopy (XAES)

XPS spectra of the *ex-situ* reduced catalysts along with the reference spectra (Fig. 4.2.12) mirror the spectra reported earlier for the 12% catalysts in section 4.2.1.3. The characteristic Cu 2p doublet is observed with the Cu 2p<sub>3/2</sub> transition centred at 932.75 eV (Table 4.2.8). The absence of strong shake-up satellites at 942.6 eV and 962.3 eV, shows the absence of Cu<sup>2+</sup> species so, the Cu is largely in its Cu<sup>0</sup> or Cu<sup>+</sup> oxidation state due to exposure to atmospheric oxygen. Minimal differences in the Cu 2p<sub>3/2</sub> transition are observed between the catalysts. Surface compositional analysis (Table 4.2.8) shows that much less Cu<sup>2+</sup> (1-3%) compared to the 12% analogue SAA catalysts (15% Cu<sup>2+</sup>) shown earlier. Therefore, the surface Cu species are largely in either the Cu<sup>0</sup> or Cu<sup>+</sup> state. The compositional differences between 1% and 12% can be due to the mechanism of Cu nanoparticle oxidation, where initially it forms Cu<sub>2</sub>O [44] and then transforms into CuO (on the surface) [45, 46] and since the 12% have more Cu available the faster the full oxidation occurs.

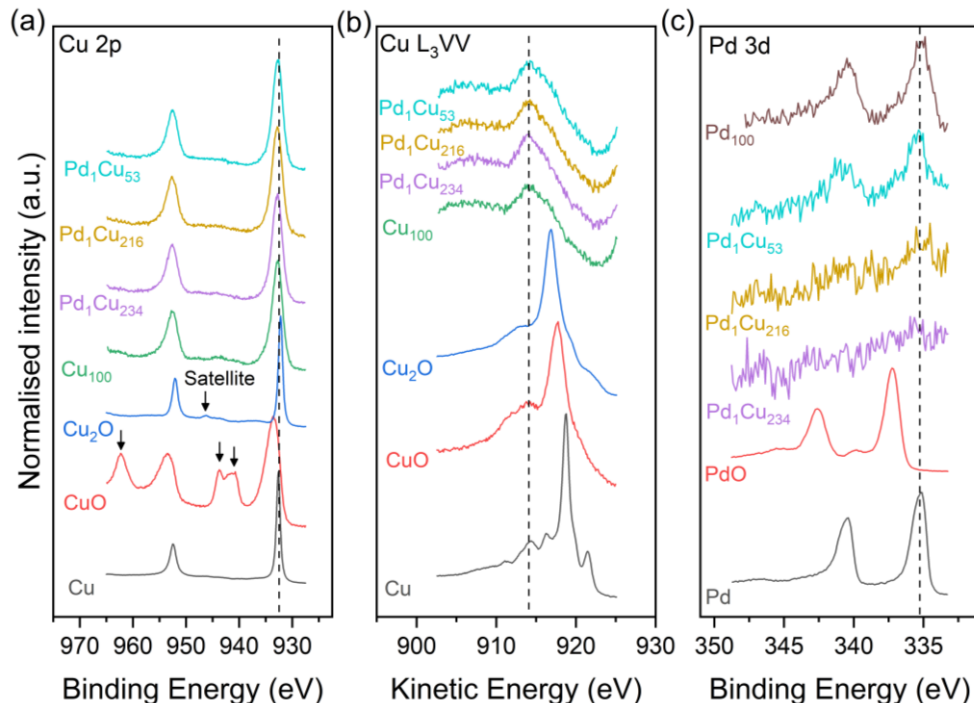


Fig. 4.2.12 High-resolution stacked XPS and XAES spectra of the (a) Cu 2p, (b) Cu L<sub>3</sub>VV and (c) Pd 3d regions for the 1 wt% PdCu catalysts after being reduced *ex-situ* at 300 °C for 0.5 h under flowing H<sub>2</sub>.

Table 4.2.8 Summarised binding energies for Pd 3d<sub>5/2</sub> and Cu 2p<sub>3/2</sub>, kinetic energies for the Auger Cu L<sub>3</sub>VV transitions, surface composition, modified Auger parameters for copper catalysts and change in relaxation energy compared to bulk Cu for the ex-situ reduced catalysts and reference materials.

Sample	Pd 3d <sub>5/2</sub> (eV)	Cu 2p <sub>3/2</sub> (eV)	L <sub>3</sub> VV (eV)	Cu <sup>0</sup> + Cu <sup>+</sup> (%)	Cu <sup>2+</sup> (%)	Modified Auger parameter (eV)	Δ Relaxation energy (eV)
Cu <sub>100</sub>	-	932.75	914.64	96.6	3.4	1847.39	2.00
Pd <sub>1</sub> Cu <sub>234</sub>	-	932.75	914.14	97.2	2.8	1846.89	2.25
Pd <sub>1</sub> Cu <sub>216</sub>	335.53	932.83	914.24	97.6	2.4	1847.07	2.15
Pd <sub>1</sub> Cu <sub>53</sub>	335.34	932.74	914.24	98.9	1.1	1846.98	2.20
Pd <sub>100</sub>	335.06	-	-	-	-	-	-
CuO	-	933.62	917.78	-	-	1851.40	-0.01
Cu <sub>2</sub> O	-	932.29	916.70	-	-	1848.99	1.20
Cu foil*	-	932.63	918.75	-	-	1851.38	0.00
PdO	337.26	-	-	-	-	-	-
Pd foil	335.20	-	-	-	-	-	-

\*Cu 2p<sub>3/2</sub> was calibrated to the ISO standard of 932.63 eV.

The Cu L<sub>3</sub>VV Auger transitions of the catalysts are found to be attenuated and significantly shifted to lower kinetic energies compared to even the Cu<sub>2</sub>O reference. Such observations in the shifts in the Auger transitions and the modified Auger parameter,  $\alpha'$  are not without precedent for supported catalysts [40, 47, 48]. The modified Auger parameter is dependent on both initial and final state effects, providing an estimate of the relaxation/screening energies due to the presence of core-holes [49] while being independent of sample charging and energy calibration problems [50]. It is observed that the  $\alpha'$  of the Cu<sub>100</sub> catalyst to be 1847.4 eV, which is drastically lower than bulk Cu ( $\alpha'_{\text{bulk}} = 1851.38$  eV). The shift is attributed largely to the polarizability of the support [51] which can withdraw electrons from the Cu nanoparticles; reducing the ability of the Cu atoms to screen the core-hole after photoemission. It is well known that the Cu atoms in PdCu bimetallic systems can act as electron donors to Pd atoms [52], whereby a further decrease in screening efficiency of the conduction electrons is observed by the decrease in  $\alpha'$  with Pd introduction. The spectra in Fig. 4.2.12 suggest the surface oxide is most likely comprised of Cu<sub>2</sub>O for the catalysts due to the surface composition analysis and the shift in the Cu L<sub>3</sub>VV transition.

The Pd 3d<sub>5/2</sub> transition of the monometallic benchmark Pd<sub>100</sub>/Al<sub>2</sub>O<sub>3</sub> is found at 335.06 eV consistent with that of bulk metallic Pd (335.20 eV, Table 4.2.8). In addition, PdO could not be detected/deconvoluted via fitting suggesting the Pd present is in its metallic state. A severely attenuated

Pd  $3d_{5/2}$  transition centred at 335.34 eV is observed for the Pd<sub>1</sub>Cu<sub>53</sub> catalyst due to the trace concentration of Pd. The slight observed shift compared to Pd<sub>100</sub> catalyst correlates well with earlier literature [18, 53] due to the Pd-O-Cu interaction on the surface after the passivation of the Cu nanoparticles.

Fig. 4.2.13 shows the XPS derived dispersion calculations and as mentioned earlier, it can give an insight of the location of the Cu and Pd atoms present in the catalysts. For the monometallic Cu<sub>100</sub> catalyst, a dispersion value of  $71.0 \pm 7.1$  % is determined which equates to a spherical nanoparticle size of  $\sim 1.5$  nm (according to the dispersion vs Cu nanoparticle plot in Fig. 1.7.1) which is noticeably smaller than both XRD and STEM measurements. The lower equivalent nanoparticle size can be attributed to the fact that XPS can detect Cu atoms irrespective of them being present in small nanoparticle or large nanoparticles while with STEM/TEM it is difficult to distinguish very small particles from the support because of the Z-contrast. It should be noted that XPS derived dispersion/nanoparticle size come with errors of  $\pm 10\%$  due to assumptions made during the calculation [54]. As observed in the STEM/TEM and XRD data the initial replacement of Cu atoms with Pd atoms appears to not decrease the dispersion of the Cu phase, but with significantly higher Pd loading (Pd<sub>1</sub>Cu<sub>53</sub> catalyst) the dispersion slightly decreases. The Pd dispersion of the monometallic Pd<sub>100</sub> is calculated to be  $22.9 \pm 2.3$  % which equates to a nanoparticle size of  $\sim 5$  nm which is consistent with the TEM data, likely due to the larger Z-contrast between Pd and Al and the presence of larger distinguishable nanoparticles. The significantly increased Pd dispersion of the Pd<sub>1</sub>Cu<sub>216</sub> catalyst compared to the Pd<sub>1</sub>Cu<sub>53</sub> catalyst suggests that the latter has an increased proportion of the Pd atoms sunk into the bulk of the nanoparticle. Due to the trace Pd loading of the Pd<sub>1</sub>Cu<sub>234</sub> catalyst the Pd 3d transition could not be detected (Fig. 4.2.12c) and thus, the dispersion could not be determined.

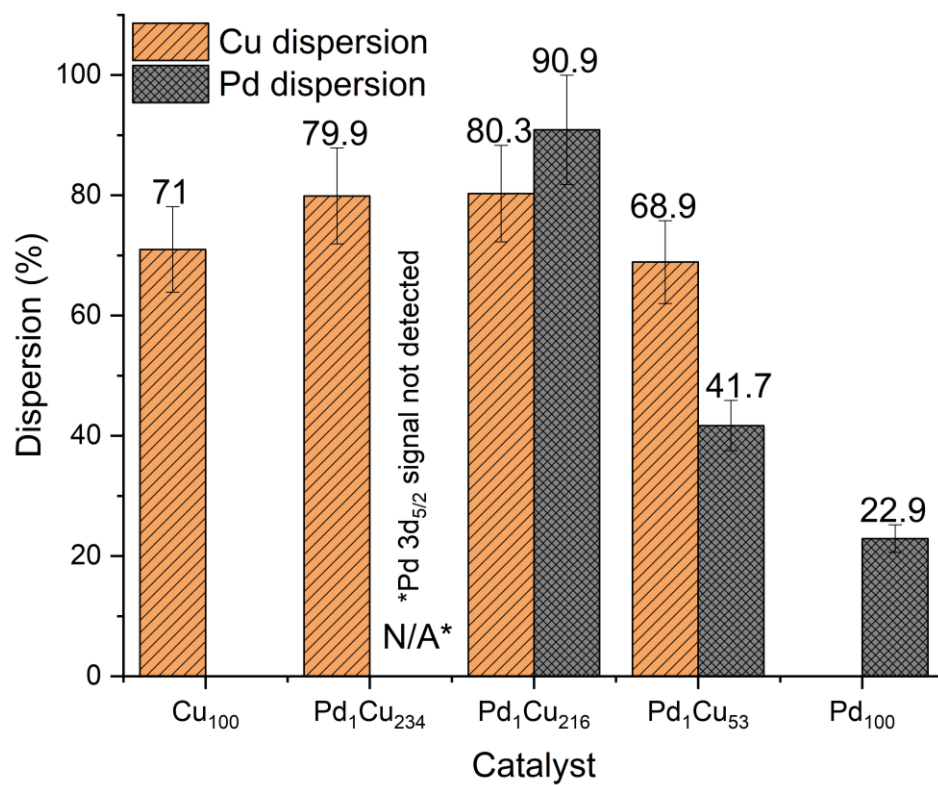


Fig. 4.2.13 XPS derived dispersions for the 1 wt% Cu/PdCu/Pd catalysts after being reduced ex-situ at 300 °C for 0.5 h under flowing H<sub>2</sub>.

#### 4.2.2.7 X-ray Absorption Spectroscopy (XAS)

In Table 4.2.9 and Fig. 4.2.14, the XANES spectra and Pd K edge energy are compared. After reduction, the Pd atoms are slightly negatively charged [23] (discussed previously) while after oxidation the edge is shifted to higher energies due to oxygen withdrawing electron density from its surrounding atoms. The XANES (Fig. 4.2.14) also suggest the Pd species are in their zeroth oxidation state due to the presence of the 2<sup>nd</sup> peak (indicated by the brown arrow) after the edge appearing only after reduction for the Pd<sub>1</sub>Cu<sub>216</sub> catalyst [55].

Table 4.2.9 Pd K edge energies for Pd foil and PdCu catalysts in their reduced and re-oxidised states.

Sample	Sample form	Pd K-edge energy (eV)
Pd foil	-	24350.0
Pd <sub>1</sub> Cu <sub>158</sub> (12% MI)	Re-oxidised	24349.5
Pd <sub>1</sub> Cu <sub>53</sub>	Re-oxidised	24349.6
Pd <sub>1</sub> Cu <sub>53</sub>	Reduced	24348.7
Pd <sub>1</sub> Cu <sub>216</sub>	Re-oxidised	24350.4
Pd <sub>1</sub> Cu <sub>216</sub>	Reduced	24349.5

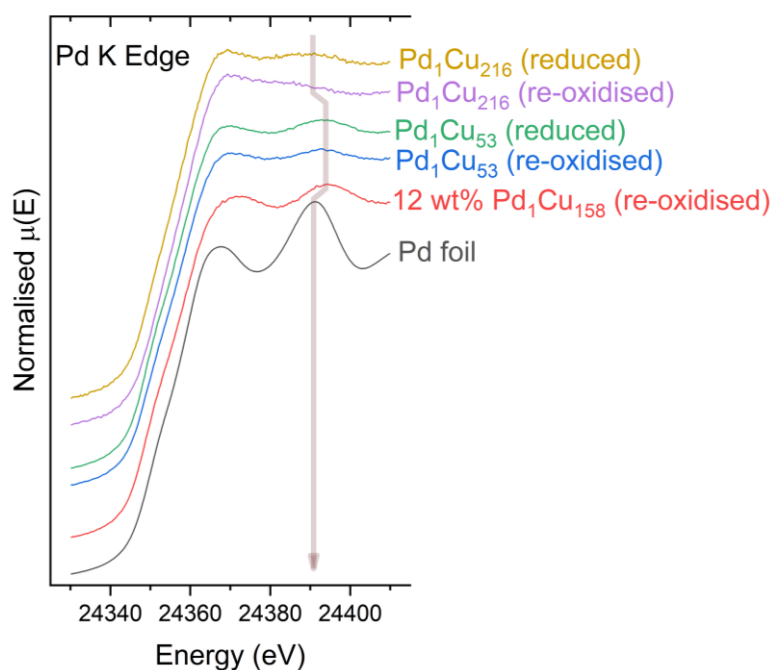


Fig. 4.2.14 Normalised Pd K edge XANES of the PdCu catalysts in their re-oxidised and reduced state.

Table 4.2.10 EXAFS model fitting of the re-oxidised and reduced PdCu/Al<sub>2</sub>O<sub>3</sub> catalysts, Pd and Cu reference foils.

Sample	Sample form	Shell	CN	R (Å)	$\sigma^2$ (Å <sup>2</sup> ) $\times 10^3$	$\Delta E_0$ (eV)	R factor
Pd foil	-	Pd-Pd	12	$2.742 \pm 0.002$	$5.6 \pm 0.4$	$3.70 \pm 0.39$	0.0163
Cu foil	-	Cu-Cu	12	$2.551 \pm 0.054$	$9.3 \pm 0.8$	$2.96 \pm 0.84$	0.0270
Pd <sub>1</sub> Cu <sub>158</sub> (12% M1)	Re-oxidised	Pd-Cu	$6.2 \pm 0.8$	$2.572 \pm 0.007$	$4.2 \pm 0.8$	$1.40 \pm 1.56$	0.0063
Pd <sub>1</sub> Cu <sub>53</sub>	Re-oxidised	Pd-Cu	$5.2 \pm 0.9$	$2.563 \pm 0.011$	$5.5 \pm 1.3$	$0.87 \pm 2.23$	0.0134
Pd <sub>1</sub> Cu <sub>53</sub>	Reduced	Pd-Cu	$5.4 \pm 0.75$	$2.562 \pm 0.087$	$5.1 \pm 1.0$	$1.48 \pm 1.73$	0.0080
Pd <sub>1</sub> Cu <sub>216</sub>	Re-oxidised	Pd-O	$2.5 \pm 1.3$	$2.003 \pm 0.044$	$7.5 \pm 5.8$	$3.31 \pm 5.89$	0.0163
		Pd-Cu	$2.5 \pm 1.0$	$2.564 \pm 0.007$	$4.4 \pm 2.9$		
Pd <sub>1</sub> Cu <sub>216</sub>	Reduced	Pd-Cu	$3.7 \pm 0.9$	$2.551 \pm 0.015$	$5.5 \pm 1.7$	$-0.30 \pm 3.08$	0.0110

CN, average coordination number; R, the distance between the absorber and backscattered atoms.  $\sigma^2$  multiplied by  $10^3$ , Debye-Waller factor;  $\Delta E_0$ , the photoelectron energy origin; R-factor, the closeness of fit.

Pseudo *in-situ* and *ex-situ* EXAFS (Fig. 4.2.15 and Fig. 4.2.16) suggest that Pd atoms have successfully galvanically replaced the Cu atoms on the nanoparticles while remaining atomically dispersed, confirming the formation of the single-atom catalysts. The tabulated (Table 4.2.10) first shell Pd-Cu bond lengths for the reduced Pd<sub>1</sub>Cu<sub>53</sub> and Pd<sub>1</sub>Cu<sub>216</sub> catalysts were found to be  $2.562 \pm 0.011$  Å and  $2.551 \pm 0.015$  Å, which coincides with a Cu-Cu bond ( $2.551 \pm 0.054$  Å). The Pd atoms determined to be missing Pd-Pd ( $2.742$  Å, Pd metal, Fig. 4.2.15b) and bulk alloyed Pd-Cu ( $2.63$  Å, Cu<sub>3</sub>Pd) coordination supporting theoretical calculations [16] that Pd can form a stable single-atom catalyst on Cu (111) surfaces. In addition, the sinusoidal waveform of the EXAFS in k-space (Fig. 4.2.15a) is consistent with the absence of multiple different scattering species in the measured local coordination environment [56]. Coordination numbers of the Pd-Cu shell were found to be  $5.4 \pm 0.75$  (Pd<sub>1</sub>Cu<sub>53</sub>) and  $3.7 \pm 0.9$  (Pd<sub>1</sub>Cu<sub>216</sub>), much lower than the typical FCC bulk and surface (111) coordination numbers of 12 and 9. This suggests the Pd atoms are incorporated on/near the surface in very small nanoparticles with dangling bonds. Pei *et al.* [23] also reported Pd-Cu bond length and coordination of  $2.58$  Å and 11.6 for a PdCu SAC catalyst synthesised via co-impregnation. However, co-impregnation distributes Pd atoms throughout the nanoparticle while galvanic replacement selectively replaces surface atoms explaining the difference in coordination numbers since in one case Pd atoms are distributed homogeneously and the other heterogeneously.

Typically, EXAFS alone does not provide insight into whether the Pd atoms are on the surface or in the bulk since the technique gives the average local environment across the whole sample, and any

attempts to determine such information will usually result in the use of highly correlated parameters producing unreliable results. This point is critical since Pd surface atoms are important in the increased hydrogen dissociation ability of the catalyst [16, 20-22] (atoms below the surface are inaccessible for the reactions) and have not been examined experimentally on real catalysts. However, *in-situ* FTIR methods exist [57] utilising CO as a surface probe molecule, but such experiments rely on the fact that adequate signal: noise is achieved. It is important to determine whether the absence of bridged CO vibrational modes is due to the presence of single atoms or the lack of signal caused by the trace loading of the dopant. DFT calculations suggest Pd and Pt are the most stable on a copper surface due to their relatively lower surface energies and higher deformation energies [16]. To examine this experimentally, the samples were reduced and re-oxidised at room temperature by exposing the sample with atmospheric oxygen. Selectively altering the surface Pd atoms with oxidation allows to easily differentiate surface Pd species from any Pd diffused into the bulk which will be largely unaffected. Pd-O coordination is observed in the Pd<sub>1</sub>Cu<sub>216</sub> catalyst with a reduction in the Pd-Cu coordination from 3.7 to 2.5 suggesting a significant portion of the Pd atoms remain on the surface via selective oxidation. In contrast, the Pd<sub>1</sub>Cu<sub>53</sub> catalysts seem to be largely unaffected by the surface oxidation (a slight drop in Pd-Cu coordination of 0.2), suggesting a significant portion of the atoms have diffused below the topmost layer of the nanoparticle, which supports our XPS findings. The absence of oxygen coordination was also observed in the high loaded PdCu SAA analogue (Pd<sub>1</sub>Cu<sub>153</sub> 12% M1, mentioned earlier in section 4.2.1). It should be noted also that this method is not entirely ideal, as in actual reaction conditions adsorbed hydrogen can stabilise surface Pd atoms bringing more atoms up to the surface [16, 58, 59]. The Pd-O bond length of the Pd<sub>1</sub>Cu<sub>216</sub> catalyst is found to be  $2.003 \pm 0.044$  Å, which is reminiscent of bulk PdO (2.01 Å). This indicates the surface Pd atoms can distort the Cu oxidised phase, as the Cu-O bond lengths are 1.88 Å and 1.96 Å for Cu<sub>2</sub>O and CuO, respectively. Additionally, it can be observed an increase in the Pd-Cu bond lengths with copper oxidation, the largest increase been detected in the Pd<sub>1</sub>Cu<sub>216</sub> catalyst. This can be correlated to the increased perturbation of the underlying Cu lattice of the nanoparticles by the oxide layer.

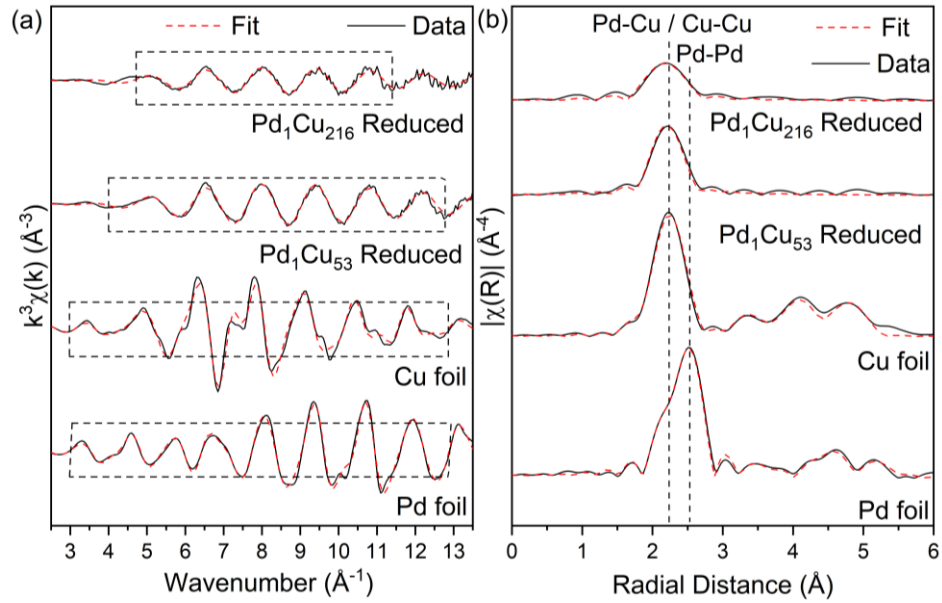


Fig. 4.2.15 (a) Pseudo *in-situ* EXAFS spectra in k-space (k-weight = 3) and (b) R-space (k-weight = 3) for PdCu/Al<sub>2</sub>O<sub>3</sub> catalysts (reduced *ex-situ* and placed in a gas-tight cell via a glovebox to prevent oxidation) along with Pd and Cu reference foils. Dashed-lined rectangles indicate k ranges over which the data were then Fourier transformed and analysed.

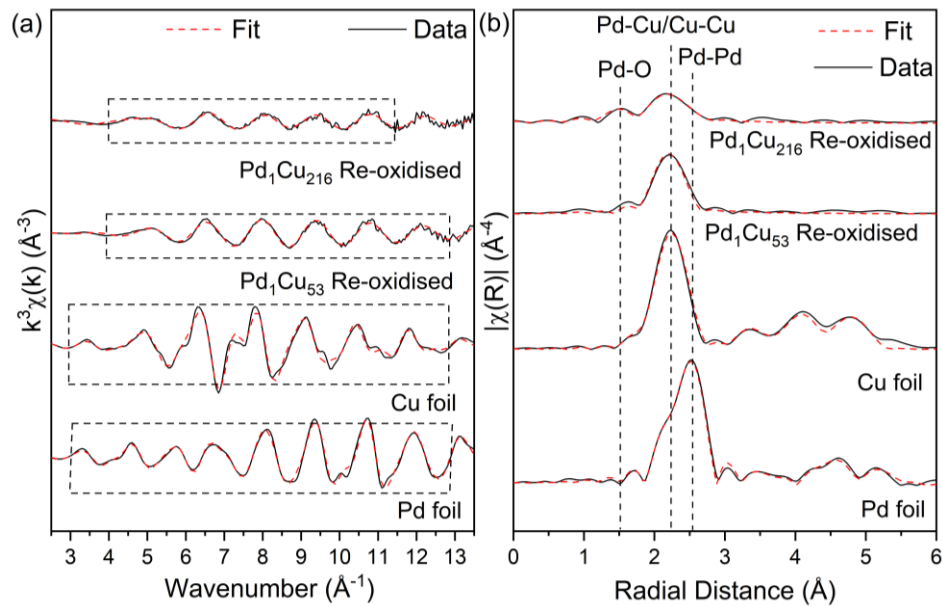


Fig. 4.2.16 (a) EXAFS spectra in k-space (k-weight = 3) and (b) R-space (k-weight = 3) for PdCu/Al<sub>2</sub>O<sub>3</sub> catalysts (reduced *ex-situ*) along with Pd and Cu reference foils. Dashed-lined rectangles indicate k ranges over which the data were then Fourier transformed and analysed.

### 4.3 Catalytic testing

#### 4.3.1 PdCu SAA catalysts 12 wt%

Preliminary experiments on the high loading PdCu determined the optimal synthetic route of the formation of PdCu catalysts used for the synthesis of 1 wt% catalysts. The characterisation of the 12 wt% catalytic materials have been summarised in Table 4.3.1. The method using minimal HCl and without sonication was chosen because the resulting catalyst (Pd<sub>1</sub>Cu<sub>153</sub> 12% M1) displayed superior activity when normalised to both Cu and Pd content (Fig. 4.3.1). The significant alterations in the Cu nanostructure and loading using the harsher GR conditions (methods 3 and 4) appear to significantly decrease the Cu normalised catalytic activity when compared to the host Cu<sub>100</sub> (12%) catalyst. While the Pd<sub>1</sub>Cu<sub>100</sub> (12% M2) catalyst synthesised in aqueous conditions with sonication appears to be the 2<sup>nd</sup> best catalyst as the GR process was milder (when compared to methods 2 and 3) with less leaching occurring. However, the catalytic performance is subpar when compared to the (Pd<sub>1</sub>Cu<sub>158</sub> 12% M1) catalyst which is due to the sonication's ability to promote the diffusion of Pd into the bulk of the nanoparticle (Fig. 4.2.4). Therefore, reducing the Pd surface sites for hydrogen dissociation and hindering its catalytic ability. Overall, the data suggest a mild GR synthetic procedure is required to promote the catalytic activity as it results in minimal changes in the host nanoparticle structure and encourages surface Pd species.

Table 4.3.1 Summary of the characterisation data for the 12 wt% Cu/Al<sub>2</sub>O<sub>3</sub> and PdCu/Al<sub>2</sub>O<sub>3</sub> catalysts.

Sample	GR method	Pd loading (wt%) <sup>a</sup>	Cu loading (wt%) <sup>a</sup>	Crystallite size (nm) <sup>b</sup>	Cu Dispersion (%) <sup>c</sup>	Pd Dispersion (%) <sup>c</sup>
Cu <sub>100</sub> (12%)	-	-	2.525 ± 0.250	6.4 ± 3.7	10.5 ± 1.1	-
Pd <sub>1</sub> Cu <sub>158</sub> (12% M1)	0.1 mM HCl, 100 °C	0.132 ± 0.005	2.476 ± 0.123	7.7 ± 5.0	10.3 ± 1.0	85.2 ± 8.5
Pd <sub>1</sub> Cu <sub>100</sub> (12% M2)	Aqueous media, sonication, 50 °C	0.189 ± 0.015	1.341 ± 0.215	7.1 ± 5.1	14.9 ± 1.5	32.2 ± 3.2
Pd <sub>1</sub> Cu <sub>98</sub> (12% M3)	2.0 mM HCl, 100 °C	0.175 ± 0.006	0.262 ± 0.047	9.9 ± 8.7	9.8 ± 1.0	38.2 ± 3.8
Pd <sub>1</sub> Cu <sub>93</sub> (12% M4)	0.1 mM HCl, sonication, 50 °C	0.199 ± 0.016	1.076 ± 0.175	5.1 ± 4.0	16.4 ± 1.6	31.9 ± 3.2

<sup>a</sup>ICP-OES, <sup>b</sup>WPPM via XRD and <sup>c</sup>XPS.

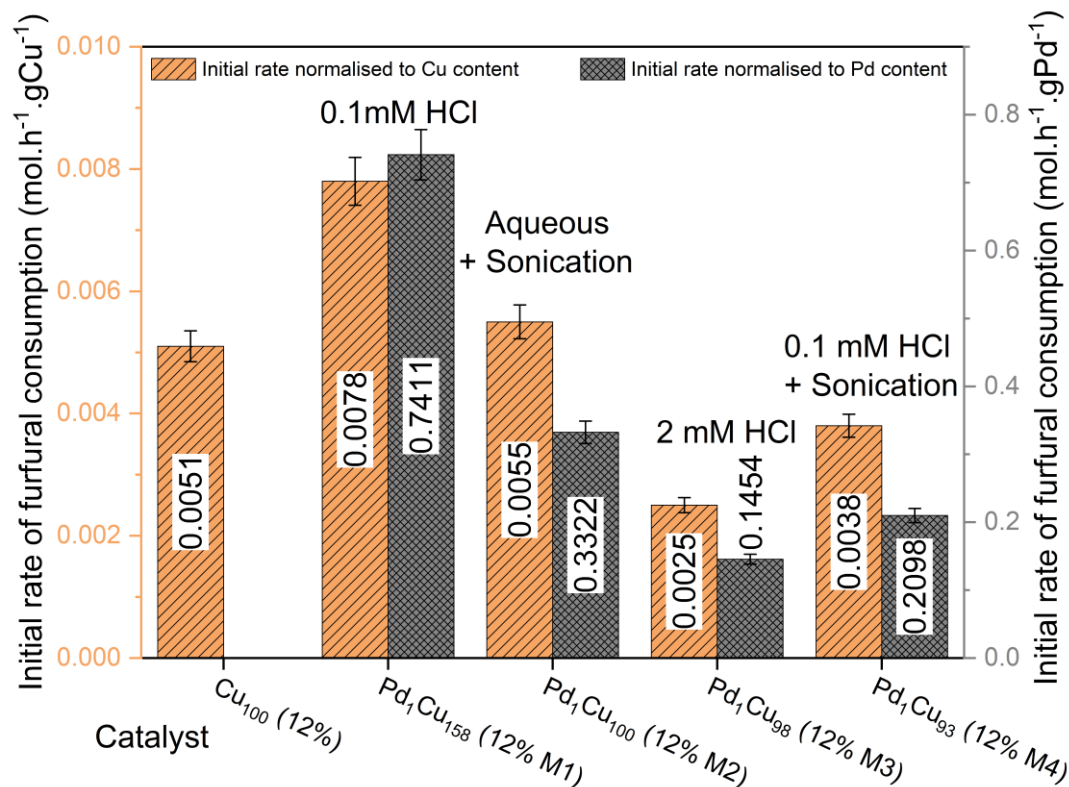


Fig. 4.3.1 Initial rate of the furfural consumption normalised to Cu and Pd content for 12 wt% PdCu catalyst using different GR methods. The initial rate was determined after the induction period for the Cu-based catalysts. Reaction conditions: 7 h, 50 °C, 1.5 bar of H<sub>2</sub>, 600 RPM, 30 mg of catalyst

### 4.3.2 PdCu SAA catalysts 1 wt%

The characterisation data for the 1 wt% catalysts is tabulated in Table 4.3.2.

Table 4.3.2 Summary of the characterisation data for the 1 wt% Al<sub>2</sub>O<sub>3</sub> supported catalysts.

Catalyst	Pd loading <sup>a</sup> (wt%)	Cu loading <sup>a</sup> (wt%)	Pd:Cu atomic ratio	Particle size (nm)	Cu dispersion (%)	Pd dispersion (%)	EXAFS
Cu <sub>100</sub>	-	0.9403 ± 0.0267	-	2.7 ± 0.7 <sup>a</sup>	71.0 ± 7.1	-	-
Pd <sub>1</sub> Cu <sub>234</sub>	0.0064 ± 0.0006	0.8947 ± 0.0253	1: 234	2.6 ± 0.7 <sup>a</sup>	79.9 ± 8.0	N/A	-
Pd <sub>1</sub> Cu <sub>216</sub>	0.0067 ± 0.0006	0.8599 ± 0.0262	1: 216	2.0 ± 0.6 <sup>a</sup>	80.3 ± 8.0	90.9 ± 9.1	SAA
Pd <sub>1</sub> Cu <sub>53</sub>	0.0296 ± 0.0022	0.9296 ± 0.0232	1: 53	7.0 ± 4.4 <sup>a</sup>	68.9 ± 6.9	41.7 ± 4.2	SAA
Pd <sub>100</sub>	0.8882 ± 0.0529	-	-	5.1 ± 2.7 <sup>b</sup>	-	22.9 ± 2.3	-

STEM/TEM <sup>a</sup>Cu and <sup>b</sup>Pd particle size

The catalytic data reveal that adding trace amounts of Pd to the Cu nanoparticles has significantly improved the hydrogenation of furfural at 50 °C with 1.5 bar of hydrogen (Table 4.3.3). The PdCu

catalysts show higher activity than Cu and higher selectivity than Pd. As mentioned in the previous chapter, in absence of any solid catalyst, neither decarbonylation nor hydrogenation reactions were observed. The parent Al<sub>2</sub>O<sub>3</sub> support was also found to be inactive towards the hydrogenation of furfural, favouring the acetalization with methanol, with minimal conversion. The major product observed for all catalysts were furfuryl alcohol (FFA) while other side products were 2-furaldehyde dimethyl acetal (FDMA, Fig. 7.1.1 GCMS spectrum in appendices) and tetrahydrofurfuryl alcohol (THFA). It should be noted, the lower carbon balance of the Pd<sub>100</sub> catalyst is attributed to unquantifiable decomposition/ether products [60].

Table 4.3.3 Summary of the catalytic data for the hydrogenation of furfural using Pd/Cu catalysts. Reaction conditions: 7 h, 50 °C, 1.5 bar, 600 RPM, and 30 mg of catalyst.

Catalyst	Conversion (%)	FFA S (%)	FDMA S (%)	THFA S (%)	Carbon Balance S (%)
Cu <sub>100</sub>	23.1 ± 1.2	98.2 ± 4.9	1.8 ± 0.1	0.0	98.1 ± 4.9
Pd <sub>1</sub> Cu <sub>234</sub>	30.3 ± 1.5	97.9 ± 4.9	2.1 ± 0.1	0.0	96.6 ± 4.8
Pd <sub>1</sub> Cu <sub>216</sub>	40.1 ± 2.0	99.1 ± 5.0	0.9 ± 0.1	0.0	96.9 ± 4.8
Pd <sub>1</sub> Cu <sub>53</sub>	38.2 ± 2.9	98.0 ± 4.9	2.0 ± 0.1	0.0	96.2 ± 4.9
Pd <sub>100</sub>	60.4 ± 3.0	89.7 ± 4.4	2.8 ± 0.2	7.5 ± 0.4	84.4 ± 4.3

*Rounding errors may be present.*

Fig. 4.3.2a indicates an induction period of approximately 1 h where the copper-based catalysts are inactive in terms of conversion. This behaviour is thought to be due to the limited catalytically available adsorbed hydrogen at the start of the reaction either through the formation of surface oxide (from O<sub>2</sub> contamination) or Cu's inability to adequately chemisorb hydrogen. However, the presence of Pd with the SAA catalysts seems to lessen its effects. This is in stark contrast to the monometallic Pd<sub>100</sub> catalyst which lacks any such induction period due to its increased resistance to oxidation, higher reducibility and likely also due to the extended Pd surface to store hydrogen as β-hydride species during the *in-situ* reduction treatment [1, 40-42]. However, the Cu-based catalysts' low activity is offset by its high selectivity. The increased selectivity is due to furfural binding to the surface via the lone pairs in the carbonyl functional group, promoting hydrogenation of the C = O bond instead of the C = C bond [61, 62]. Pd surfaces are very reactive allowing η<sup>2</sup>(C, O)-aldehyde bonding modes, in which both O and C

are bound [62-64]. As a result, unidentified decarboxylation/ethers products are promoted, creating a higher discrepancy in the carbon balance (Fig. 4.3.2b), and the THFA formation is also favoured. Such side products observed for Pd catalysts are not observed with the SAA catalysts since it requires extended Pd surfaces for such side reactions to occur, so the selectivity is provided by the Cu surfaces. The isolated Pd atoms act as entry sites for hydrogen dissociate and adsorb after which they spill over onto the Cu surface [16, 20-22] where they react with the adsorbed substrate.

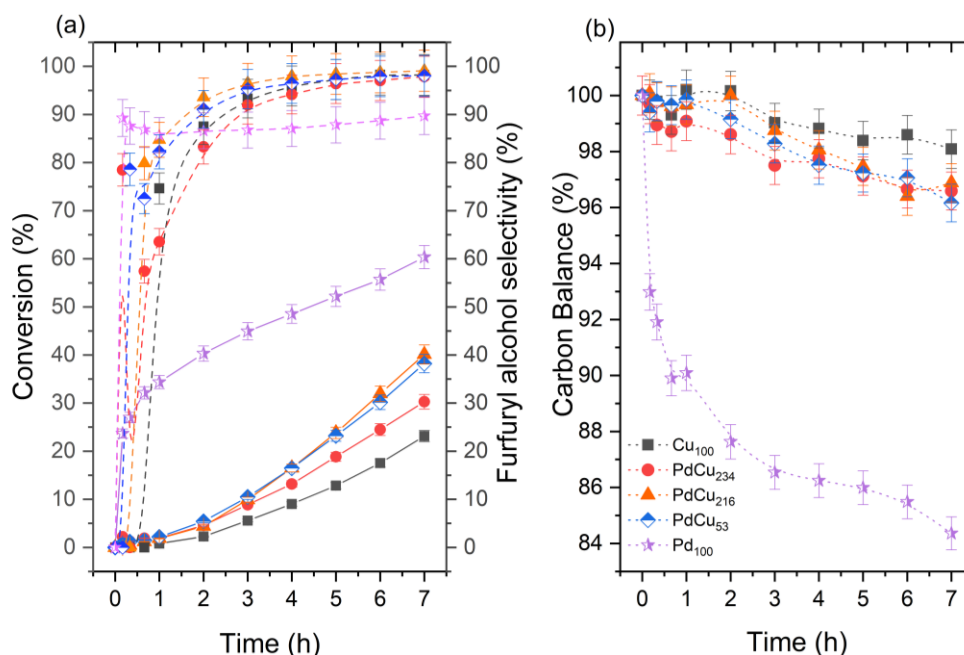


Fig. 4.3.2 The reaction profiles of (a) furfural conversion, selectivity and (b) carbon balance. Reaction conditions: 7 h, 50 °C, 1.5 bar of H<sub>2</sub>, 600 RPM, 30 mg of catalyst. Solid lines, dashed, and dotted lines represent conversion, selectivity, and carbon balance, respectively.

Fig. 4.3.3a demonstrates the activity of the PdCu SAA catalysts are better than their monometallic counterparts when normalised to metal content. Particularly, the Pd<sub>1</sub>Cu<sub>216</sub> catalyst demonstrates an eleven-fold increase in activity compared to the monometallic Pd<sub>100</sub> catalyst due to the lack of spectator Pd atoms in the nanoparticle's bulk. Significant improvements are also observed over the Cu<sub>100</sub> catalyst, showing that trace amounts of Pd atoms can augment the catalytic surface by promoting hydrogen adsorption. The improvement in activity with Pd loading has a diminishing return, with the Pd<sub>1</sub>Cu<sub>216</sub> catalyst being the superior atom-efficient catalyst. It is proposed this trend is due to the Pd atoms being

inaccessible to be used as hydrogen dissociation entry sites since the EXAFS suggests a significant portion of Pd atoms have diffused under the surface of the nanoparticle. Analysing the furfuryl alcohol production profile normalised to the nanoparticle metal (Fig. 4.3.3b) shows that the atomically dispersed Pd<sub>1</sub>Cu<sub>216</sub> catalyst can improve the performance of the Cu host surface to that of the benchmark monometallic Pd<sub>100</sub> catalyst. While it can be clearly seen that both systems follow drastically different reaction mechanisms, explained earlier through the different reactant binding modes/hydrogen storage capability of Pd and Cu majority surfaces.

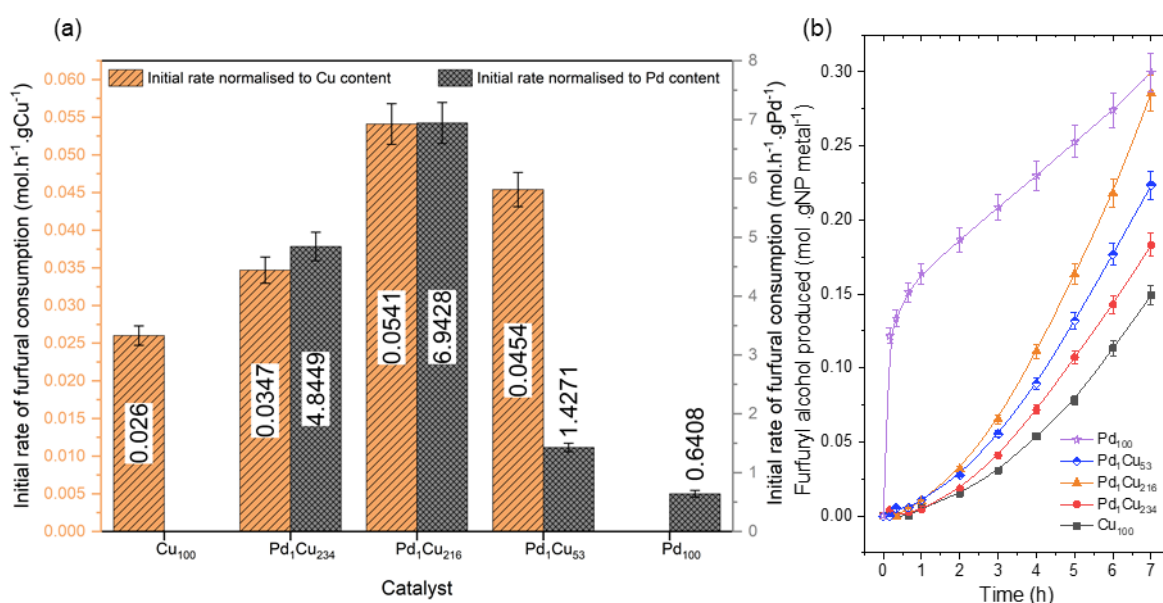


Fig. 4.3.3 (a) Initial rate of the furfural consumption normalised to Cu and Pd content. The initial rate was determined after the induction period for the Cu-based catalysts. (b) Furfuryl alcohol production over time normalised to the majority nanoparticle metal. Reaction conditions: 7 h, 50 °C, 1.5 bar of H<sub>2</sub>, 600 RPM, 30 mg of catalyst.

Turnover frequency (TOF) was determined in Fig. 4.3.4 to determine if the surface-active sites are actually better by removing effect of dispersion of the catalysts. The TOF clearly shows that the introduction of the atomically dispersed Pd atoms increases the catalytic activity of the surface Cu sites with the optimal Pd<sub>1</sub>Cu<sub>216</sub> SAA catalyst increasing Cu TOFs by ~85%. Further increasing the Pd loading with the Pd<sub>1</sub>Cu<sub>53</sub> comes with diminishing returns as the TOFs are not seen to increase which is also observed in the normalised initial rates (Fig. 4.3.3a). When comparing TOFs of the monometallic Pd<sub>100</sub> catalyst to a SAA catalyst shows that the atomically dispersed Pd sites are ~173% more catalytically

active than the typically equivalent surface sites found on Pd nanoparticles. Supporting the previous data, it can be noticed that initially as the Pd loading is increased the activity of the Pd sites also increases to a maximum TOF of  $813 \pm 81 \text{ h}^{-1}$ . Further drastic increases in the Pd loading with the Pd<sub>1</sub>Cu<sub>53</sub> catalyst appears to begin to render the Pd sites less effective, possibly changing their properties to be more like that of a monometallic Pd catalyst. It should be noted that due to the inability to determine the Pd dispersion for the Pd<sub>1</sub>Cu<sub>234</sub> catalyst (lack of Pd 3d signal) it was assumed to be 100% for this TOF calculation.

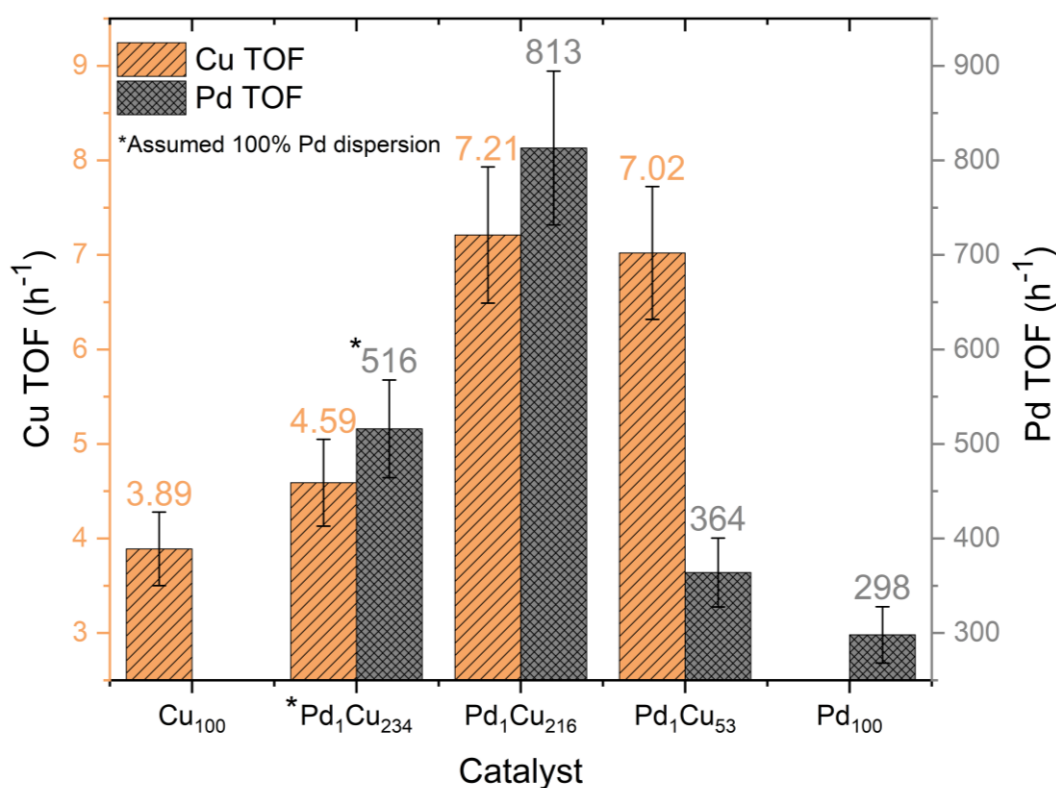


Fig. 4.3.4 Turnover frequency of both Cu and Pd surface atoms for the catalysts determined from the XPS calculated dispersion. Reaction conditions: 7 h, 50 °C, 1.5 bar of H<sub>2</sub>, 600 RPM, 30 mg of catalyst.

Fig. 4.3.5 shows the produced furfuryl alcohol/metal mole ratio per hour (Equation 2.3.6) or simply called productivity ( $\text{h}^{-1}$ ), under mild to moderate reaction temperatures and pressures. The catalysts synthesised in this work and those reported in the literature are compared. The advantages of comparing the mole ratio furfuryl alcohol/metal per hour are that all the active metal content, yield, and reaction time is considered quantifying the best selective atom efficient catalysts. Comparing the monometallic



### 4.3.3 Spent catalyst characterisation and recycling experiments

Comparing the XPS spectra of the spent and fresh Pd<sub>1</sub>Cu<sub>216</sub> catalysts (Fig. 4.3.6a) shows that after recovery, the spent material is significantly oxidised to CuO which is observed by the strong shake-up satellites and the shift of the Cu 2p<sub>3/2</sub> transition by +0.82 eV. Surface compositional analysis in Table 4.3.4 confirms the Cu species are largely in their Cu<sup>2+</sup> oxidation state (77.5%).

*Table 4.3.4 Summarised energies for the Cu 2p<sub>3/2</sub> and the Auger Cu L<sub>3</sub>VV transitions, surface composition, modified Auger parameters and XPS calculated dispersion for the fresh and spent catalysts.*

Sample	State	Cu 2p <sub>3/2</sub> (eV)	L <sub>3</sub> VV (eV)	Cu <sup>0</sup> + Cu <sup>+</sup> (%)	Cu <sup>2+</sup> (%)	Modified Auger parameter (eV)	Cu Dispersion (%)
Pd <sub>1</sub> Cu <sub>216</sub>	Fresh	932.83	914.24	97.6	2.4	1847.07	80.3 ± 8.0
Pd <sub>1</sub> Cu <sub>216</sub>	Spent	933.65	915.05	22.5	77.5	1848.70	70.5 ± 7.1
CuO	-	933.62	917.78	-	-	1851.40	-
Cu <sub>2</sub> O	-	932.29	916.70	-	-	1848.99	-
Cu*	-	932.63	918.75	-	-	1851.38	-

\*Cu 2p<sub>3/2</sub> was calibrated to the ISO standard of 932.63 eV.

As observed for the unused catalyst, the modified Auger parameter is found noticeably lower than bulk Cu ( $\alpha'_{\text{bulk}} = 1851.38$  eV) or that of bulk CuO ( $\alpha'_{\text{CuO}} = 1851.40$ ) for the spent material. Though, the  $\alpha'$  is also shifted by +0.63 eV, like that of Cu<sub>2</sub>O, though due to the satellite structure/compositional analysis it can be presumed the shift arises from the presence of CuO while the overall negative shift of the parameter is due to Cu's close contact to the polarisable support. However, the XPS calculated Cu dispersion values show that there may be some loss in Cu dispersion through nanoparticle sintering.

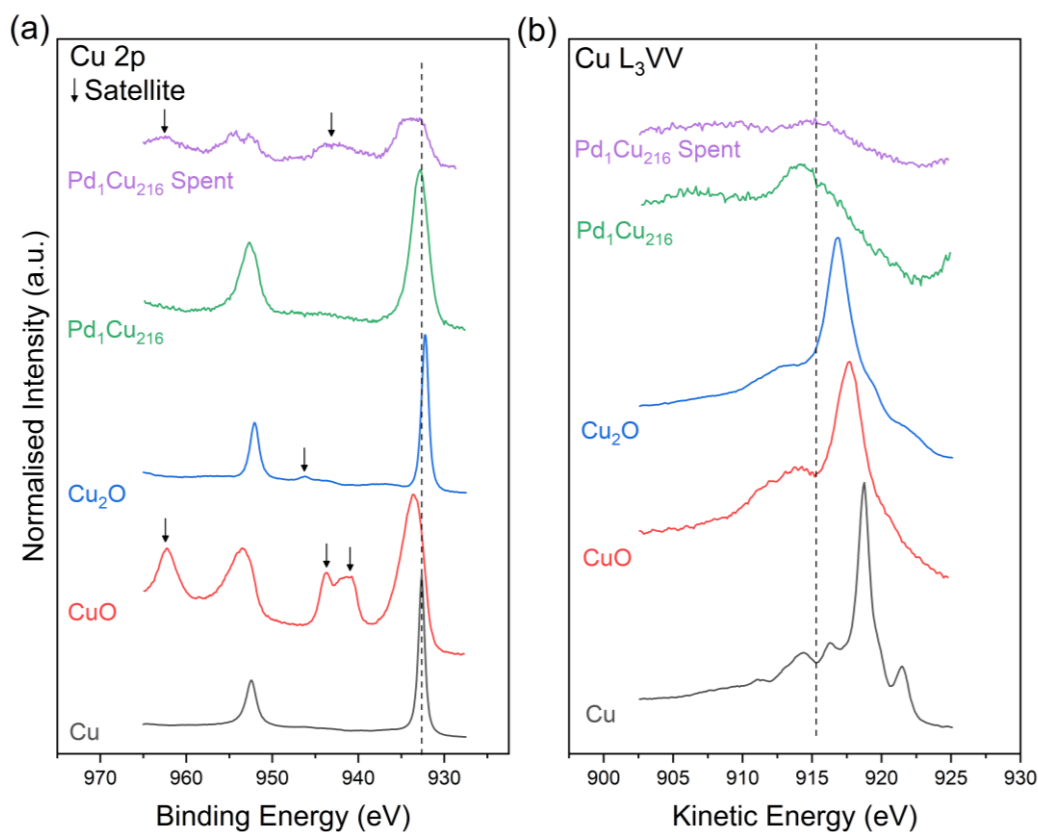


Fig. 4.3.6 High-resolution stacked XPS and XAES spectra of the (a) Cu 2p and (b) Cu L<sub>3</sub>VV regions for the fresh and spent Pd<sub>1</sub>Cu<sub>216</sub> catalyst.

The recyclability of the optimal PdCu SAA catalyst was investigated. The catalysts were recovered after the reaction via centrifugation followed by washing with methanol. Once dried, they were retested. Table 4.3.5 shows that the conversion and selectivity of the catalyst were within error minimally affected after reuse. This is consistent with the ICP-OES analysis of the filtered supernatant fluid as the elemental analysis ruled out Cu leaching.

Table 4.3.5 Furfural hydrogenation over the recycled catalysts. Reaction conditions: 7 h, 50 °C, 1.5 bar of H<sub>2</sub> and 600 RPM.

Catalyst	Conversion (%)	FFA S (%)	FDMA S (%)	THFA S (%)	Carbon Balance S (%)
Pd <sub>1</sub> Cu <sub>216</sub> <sup>1</sup>	40.1 ± 2.0	99.1 ± 5.0	0.9 ± 0.1	0.0	96.9 ± 4.8
Pd <sub>1</sub> Cu <sub>216</sub> <sup>2</sup>	37.5 ± 1.9	97.4 ± 4.9	2.6 ± 0.1	0.0	97.0 ± 4.9

Superscripts 1 and 2 indicate the catalyst cycle of testing.

#### 4.4 Conclusions

A series of bimetallic PdCu catalysts were tested for the selective hydrogenation of furfural under mild conditions. The catalyst morphology and electronic properties were thoroughly studied utilising XRD, XPS, STEM, EXAFS, XANES, TPR and ICP-OES. Catalyst characterisation confirms that Pd atoms were atomically dispersed on the host copper nanoparticle surface, confirming the formation of a single atom catalyst. The combination of pseudo-*in-situ* and *ex-situ* EXAFS suggests that as the Pd loading increases, Pd atoms diffuse into the bulk reducing their catalytic effectiveness. Various modifications to the galvanic replacement process were made, optimising the resulting catalyst for improved catalytic activity. The augmentation of the copper surface with trace amounts of Pd (0.0067 wt%) was found to improve the normalised catalytic activity by eleven-fold when compared to a monometallic Pd catalyst. The synthesised atom efficient catalysts retain Cu's high selectivity attributed to the incredible control of the Pd active sites since they are isolated, which eliminates competitive side-reactions that require more than one Pd neighbouring atom. This work also shows the formation of a single atom alloy catalyst is not enough, but such isolated atoms need to be present on the surface to be taken advantage of. Finally, when compared against the literature (Fig. 4.3.5) it is found that these materials are the most competitive atom efficient catalysts implemented for the selective hydrogenation of furfural to furfuryl alcohol.

## 4.5 References

- [1] M. Lesiak, M. Binczarski, S. Karski, W. Maniukiewicz, J. Rogowski, E. Szubiakiewicz, J. Berłowska, P. Dziugan, I. Witońska, Hydrogenation of furfural over Pd–Cu/Al<sub>2</sub>O<sub>3</sub> catalysts. The role of interaction between palladium and copper on determining catalytic properties, *J. Mol. Catal. A: Chem.*, 395 (2014) 337-348.
- [2] M.J. Taylor, L.J. Durndell, M.A. Isaacs, C.M.A. Parlett, K. Wilson, A.F. Lee, G. Kyriakou, Highly selective hydrogenation of furfural over supported Pt nanoparticles under mild conditions, *Appl. Catal. B*, 180 (2016) 580-585.
- [3] M.J. Taylor, S.K. Beaumont, M.J. Islam, S. Tsatsos, C.A.M. Parlett, M.A. Issacs, G. Kyriakou, Atom efficient PtCu bimetallic catalysts and ultra dilute alloys for the selective hydrogenation of furfural, *Appl. Catal. B*, 284 (2021) 119737.
- [4] M.G. Dohade, P.L. Dhepe, Efficient hydrogenation of concentrated aqueous furfural solutions into furfuryl alcohol under ambient conditions in presence of PtCo bimetallic catalyst, *Green Chem.*, 19 (2017) 1144-1154.
- [5] Y. Nakagawa, K. Takada, M. Tamura, K. Tomishige, Total Hydrogenation of Furfural and 5-Hydroxymethylfurfural over Supported Pd–Ir Alloy Catalyst, *ACS Catal.*, 4 (2014) 2718-2726.
- [6] J.J. Musci, A.B. Merlo, M.L. Casella, Aqueous phase hydrogenation of furfural using carbon-supported Ru and RuSn catalysts, *Catal. Today*, 296 (2017) 43-50.
- [7] EWI, Rare Earth Materials -China's Role and Emerging Sources, 2011.
- [8] J.M. Thomas, R. Raja, Mono-, Bi- and Multifunctional Single-Sites: Exploring the Interface Between Heterogeneous and Homogeneous Catalysis, *Top. Catal.*, 53 (2010) 848-858.
- [9] J.M. Thomas, Z. Saghi, P.L. Gai, Can a Single Atom Serve as the Active Site in Some Heterogeneous Catalysts?, *Top. Catal.*, 54 (2011) 588-594.

- [10] S.L. Wegener, T.J. Marks, P.C. Stair, Design Strategies for the Molecular Level Synthesis of Supported Catalysts, *Acc. Chem. Res.*, 45 (2012) 206-214.
- [11] A. Bruix, Y. Lykhach, I. Matolínová, A. Neitzel, T. Skála, N. Tsud, M. Vorokhta, V. Stetsovych, K. Ševčíková, J. Mysliveček, R. Fiala, M. Václavů, K.C. Prince, S. Bruyère, V. Potin, F. Illas, V. Matolín, J. Libuda, K.M. Neyman, Maximum Noble-Metal Efficiency in Catalytic Materials: Atomically Dispersed Surface Platinum, *Angew. Chem. Int. Ed.*, 53 (2014) 10525-10530.
- [12] Q. Fu, H. Saltsburg, M. Flytzani-Stephanopoulos, Active Nonmetallic Au and Pt Species on Ceria-Based Water-Gas Shift Catalysts, *Science*, 301 (2003) 935-938.
- [13] J.M. Thomas, An Exceptionally Active Catalyst for Generating Hydrogen from Water, *Angew. Chem. Int. Ed.*, 50 (2011) 49-50.
- [14] M. Flytzani-Stephanopoulos, Gold Atoms Stabilized on Various Supports Catalyze the Water-Gas Shift Reaction, *Acc. Chem. Res.*, 47 (2014) 783-792.
- [15] F.R. Lucci, J. Liu, M.D. Marcinkowski, M. Yang, L.F. Allard, M. Flytzani-Stephanopoulos, E.C.H. Sykes, Selective hydrogenation of 1,3-butadiene on platinum-copper alloys at the single-atom limit, *Nat. Commun.*, 6 (2015) 8550.
- [16] Q. Fu, Y. Luo, Catalytic Activity of Single Transition-Metal Atom Doped in Cu(111) Surface for Heterogeneous Hydrogenation, *J. Phys. Chem. C*, 117 (2013) 14618-14624.
- [17] J. Jones, H. Xiong, A.T. DeLaRiva, E.J. Peterson, H. Pham, S.R. Challa, G. Qi, S. Oh, M.H. Wiebenga, X.I. Pereira Hernández, Y. Wang, A.K. Datye, Thermally stable single-atom platinum-on-ceria catalysts via atom trapping, *Science*, 353 (2016) 150.
- [18] M.B. Boucher, B. Zugic, G. Cladaras, J. Kammert, M.D. Marcinkowski, T.J. Lawton, E.C. Sykes, M. Flytzani-Stephanopoulos, Single atom alloy surface analogs in Pd<sub>0.18</sub>Cu<sub>15</sub> nanoparticles for selective hydrogenation reactions, *Phys. Chem. Chem. Phys.*, 15 (2013) 12187-12196.

- [19] H. Wei, X. Liu, A. Wang, L. Zhang, B. Qiao, X. Yang, Y. Huang, S. Miao, J. Liu, T. Zhang, FeOx-supported platinum single-atom and pseudo-single-atom catalysts for chemoselective hydrogenation of functionalized nitroarenes, *Nat. Commun.*, 5 (2014) 5634.
- [20] G. Kyriakou, M.B. Boucher, A.D. Jewell, E.A. Lewis, T.J. Lawton, A.E. Baber, H.L. Tierney, M. Flytzani-Stephanopoulos, E.C. Sykes, Isolated metal atom geometries as a strategy for selective heterogeneous hydrogenations, *Science*, 335 (2012) 1209-1212.
- [21] G. Kyriakou, E.R.M. Davidson, G. Peng, L.T. Roling, S. Singh, M.B. Boucher, M.D. Marcinkowski, M. Mavrikakis, A. Michaelides, E.C.H. Sykes, Significant Quantum Effects in Hydrogen Activation, *ACS Nano*, 8 (2014) 4827-4835.
- [22] H.L. Tierney, A.E. Baber, J.R. Kitchin, E.C.H. Sykes, Hydrogen Dissociation and Spillover on Individual Isolated Palladium Atoms, *Phys. Rev. Lett.*, 103 (2009) 246102.
- [23] G.X. Pei, X.Y. Liu, X. Yang, L. Zhang, A. Wang, L. Li, H. Wang, X. Wang, T. Zhang, Performance of Cu-Alloyed Pd Single-Atom Catalyst for Semihydrogenation of Acetylene under Simulated Front-End Conditions, *ACS Catal.*, 7 (2017) 1491-1500.
- [24] J. Liu, J. Shan, F.R. Lucci, S. Cao, E.C.H. Sykes, M. Flytzani-Stephanopoulos, Palladium–gold single atom alloy catalysts for liquid phase selective hydrogenation of 1-hexyne, *Catal. Sci. Technol.*, 7 (2017) 4276-4284.
- [25] M. Mohl, D. Dobo, A. Kukovecz, Z. Konya, K. Kordas, J. Wei, R. Vajtai, P.M. Ajayan, Formation of CuPd and CuPt Bimetallic Nanotubes by Galvanic Replacement Reaction, *J. Phys. Chem. C*, 115 (2011) 9403-9409.
- [26] Z. Sun, J. Masa, W. Xia, D. König, A. Ludwig, Z.-A. Li, M. Farle, W. Schuhmann, M. Muhler, Rapid and Surfactant-Free Synthesis of Bimetallic Pt–Cu Nanoparticles Simply via Ultrasound-Assisted Redox Replacement, *ACS Catal.*, 2 (2012) 1647-1653.

- [27] S. Elzey, V.H. Grassian, Nanoparticle Dissolution from the Particle Perspective: Insights from Particle Sizing Measurements, *Langmuir*, 26 (2010) 12505-12508.
- [28] S. Pradhan, J. Hedberg, E. Blomberg, S. Wold, I. Odnevall Wallinder, Effect of sonication on particle dispersion, administered dose and metal release of non-functionalized, non-inert metal nanoparticles, *J. Nanopart. Res.*, 18 (2016) 285.
- [29] L. Vegard, Die Konstitution der Mischkristalle und die Raumfüllung der Atome, *Z. Phys.*, 5 (1921) 17-26.
- [30] J.T.L. Gamler, A. Leonardi, X. Sang, K.M. Koczur, R.R. Unocic, M. Engel, S.E. Skrabalak, Effect of lattice mismatch and shell thickness on strain in core@shell nanocrystals, *Nanoscale Advances*, 2 (2020) 1105-1114.
- [31] M.C. Biesinger, Advanced analysis of copper X-ray photoelectron spectra, *Surf. Interface Anal.*, 49 (2017) 1325-1334.
- [32] M.C. Biesinger, B.R. Hart, R. Polack, B.A. Kobe, R.S.C. Smart, Analysis of mineral surface chemistry in flotation separation using imaging XPS, *Miner. Eng.*, 20 (2007) 152-162.
- [33] M.C. Biesinger, B.P. Payne, A.P. Grosvenor, L.W.M. Lau, A.R. Gerson, R.S.C. Smart, Resolving surface chemical states in XPS analysis of first row transition metals, oxides and hydroxides: Cr, Mn, Fe, Co and Ni, *Appl. Surf. Sci.*, 257 (2011) 2717-2730.
- [34] C.D. Wagner, A. Joshi, The auger parameter, its utility and advantages: a review, *J. Electron. Spectrosc. Relat. Phenom.*, 47 (1988) 283-313.
- [35] H. Nakajima, The discovery and acceptance of the Kirkendall Effect: The result of a short research career, *JOM*, 49 (1997) 15-19.

- [36] D. Wang, Y. Li, Bimetallic Nanocrystals: Liquid-Phase Synthesis and Catalytic Applications, *Adv. Mater.*, 23 (2011) 1044-1060.
- [37] F.R. Lucci, M.D. Marcinkowski, T.J. Lawton, E.C.H. Sykes, H<sub>2</sub> Activation and Spillover on Catalytically Relevant Pt–Cu Single Atom Alloys, *J. Phys. Chem. C*, 119 (2015) 24351-24357.
- [38] S. Elzey, J. Baltrusaitis, S. Bian, V.H. Grassian, Formation of paratacamite nanomaterials via the conversion of aged and oxidized copper nanoparticles in hydrochloric acidic media, *J. Mater. Chem.*, 21 (2011) 3162-3169.
- [39] T.L. Barr, S. Seal, Nature of the use of adventitious carbon as a binding energy standard, *J. Vac. Sci. Technol. A*, 13 (1995) 1239-1246.
- [40] J. Batista, A. Pintar, D. Mandrino, M. Jenko, V. Martin, XPS and TPR examinations of  $\gamma$ -alumina-supported Pd-Cu catalysts, *Appl. Catal. A Gen.*, 206 (2001) 113-124.
- [41] F. Cárdenas-Lizana, S. Gómez-Quero, C. Amorim, M.A. Keane, Gas phase hydrogenation of p-chloronitrobenzene over Pd–Ni/Al<sub>2</sub>O<sub>3</sub>, *Appl. Catal. A Gen.*, 473 (2014) 41-50.
- [42] S.F. Parker, H.C. Walker, S.K. Callear, E. Grünwald, T. Petzold, D. Wolf, K. Möbus, J. Adam, S.D. Wieland, M. Jiménez-Ruiz, P.W. Albers, The effect of particle size, morphology and support on the formation of palladium hydride in commercial catalysts, *Chemical Science*, 10 (2019) 480-489.
- [43] P.W. Albers, K. Möbus, C.D. Frost, S.F. Parker, Characterization of  $\beta$ -Palladium Hydride Formation in the Lindlar Catalyst and in Carbon-Supported Palladium, *J. Phys. Chem. C*, 115 (2011) 24485-24493.
- [44] R. Nakamura, D. Tokozakura, H. Nakajima, J.-G. Lee, H. Mori, Hollow oxide formation by oxidation of Al and Cu nanoparticles, *J. Appl. Phys.*, 101 (2007) 074303.

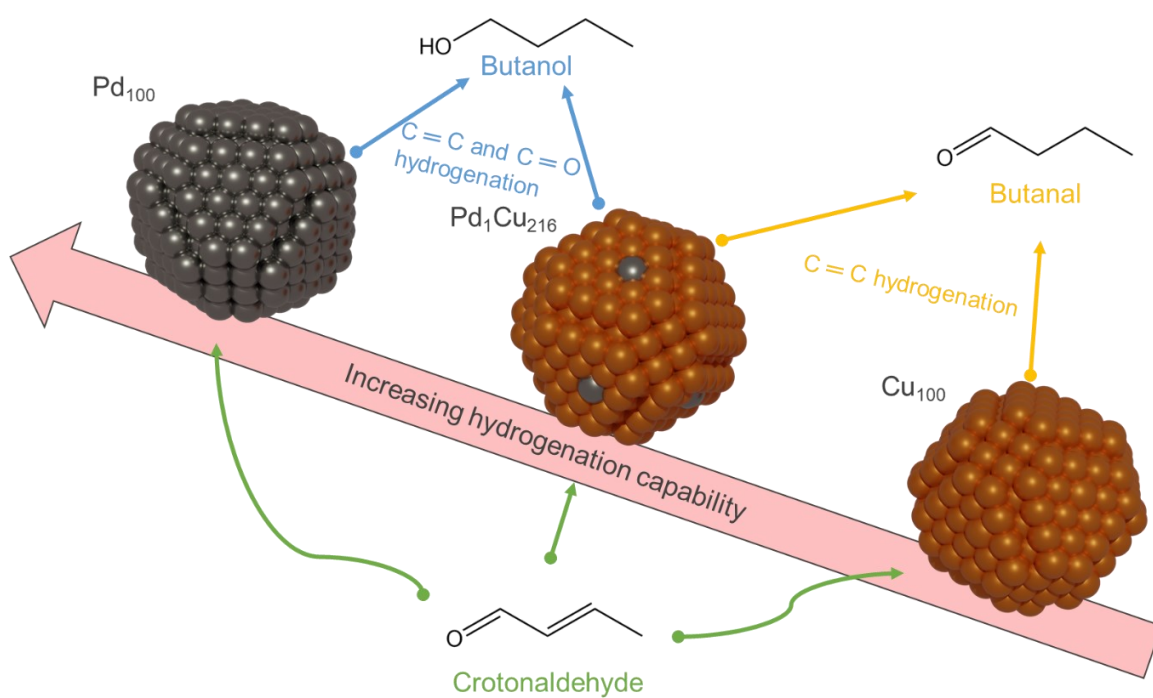
- [45] T. Ghodselahi, M.A. Vesaghi, A. Shafiekhani, A. Baghizadeh, M. Lameii, XPS study of the Cu@Cu<sub>2</sub>O core-shell nanoparticles, *Appl. Surf. Sci.*, 255 (2008) 2730-2734.
- [46] B. Wei, N. Yang, F. Pang, J. Ge, Cu<sub>2</sub>O–CuO Hollow Nanospheres as a Heterogeneous Catalyst for Synergetic Oxidation of CO, *J. Phys. Chem. C*, 122 (2018) 19524-19531.
- [47] O.P.H. Vaughan, G. Kyriakou, N. Macleod, M. Tikhov, R.M. Lambert, Copper as a selective catalyst for the epoxidation of propene, *J. Catal.*, 236 (2005) 401-404.
- [48] M.J. Islam, M. Granollers Mesa, A. Osatiashtiani, M.J. Taylor, J.C. Manayil, C.M.A. Parlett, M.A. Isaacs, G. Kyriakou, The effect of metal precursor on copper phase dispersion and nanoparticle formation for the catalytic transformations of furfural, *Appl. Catal. B*, 273 (2020) 119062.
- [49] A. Thøgersen, S. Diplas, J. Mayandi, T. Finstad, A. Olsen, J.F. Watts, M. Mitome, Y. Bando, An experimental study of charge distribution in crystalline and amorphous Si nanoclusters in thin silica films, *J. Appl. Phys.*, 103 (2008) 024308.
- [50] S. Hofmann, *Auger- and X-Ray Photoelectron Spectroscopy in Materials Science: A User-Oriented Guide*, Springer Berlin Heidelberg 2012.
- [51] J. Batista, A. Pintar, J.P. Gomilšek, A. Kodre, F. Bornette, On the structural characteristics of  $\gamma$ -alumina-supported Pd–Cu bimetallic catalysts, *Appl. Catal. A Gen.*, 217 (2001) 55-68.
- [52] S.V. Myers, A.I. Frenkel, R.M. Crooks, X-ray Absorption Study of PdCu Bimetallic Alloy Nanoparticles Containing an Average of  $\sim$ 64 Atoms, *Chem. Mater.*, 21 (2009) 4824-4829.
- [53] L. Guzzi, Z. Schay, G. Stefler, L.F. Liotta, G. Deganello, A.M. Venezia, Pumice-Supported Cu–Pd Catalysts: Influence of Copper on the Activity and Selectivity of Palladium in the Hydrogenation of Phenylacetylene and But-1-ene, *J. Catal.*, 182 (1999) 456-462.

- [54] F.P.J.M. Kerkhof, J.A. Moulijn, Quantitative analysis of XPS intensities for supported catalysts, *J. Phys. Chem.*, 83 (1979) 1612-1619.
- [55] J. Nilsson, P.-A. Carlsson, H. Grönbeck, M. Skoglundh, First Principles Calculations of Palladium Nanoparticle XANES Spectra, *Top. Catal.*, 60 (2017) 283-288.
- [56] S. Calvin, *XAFS for Everyone*, Taylor & Francis, 2013.
- [57] G.X. Pei, X.Y. Liu, A. Wang, A.F. Lee, M.A. Isaacs, L. Li, X. Pan, X. Yang, X. Wang, Z. Tai, K. Wilson, T. Zhang, Ag Alloyed Pd Single-Atom Catalysts for Efficient Selective Hydrogenation of Acetylene to Ethylene in Excess Ethylene, *ACS Catal.*, 5 (2015) 3717-3725.
- [58] J. Greeley, M. Mavrikakis, Alloy catalysts designed from first principles, *Nat. Mater.*, 3 (2004) 810-815.
- [59] J. Greeley, M. Mavrikakis, Near-surface alloys for hydrogen fuel cell applications, *Catal. Today*, 111 (2006) 52-58.
- [60] S.M. Rogers, C.R.A. Catlow, C.E. Chan-Thaw, A. Chutia, N. Jian, R.E. Palmer, M. Perdjon, A. Thetford, N. Dimitratos, A. Villa, P.P. Wells, Tandem Site- and Size-Controlled Pd Nanoparticles for the Directed Hydrogenation of Furfural, *ACS Catal.*, 7 (2017) 2266-2274.
- [61] S. Sitthisa, T. Sooknoi, Y. Ma, P.B. Balbuena, D.E. Resasco, Kinetics and mechanism of hydrogenation of furfural on Cu/SiO<sub>2</sub> catalysts, *J. Catal.*, 277 (2011) 1-13.
- [62] X. Li, P. Jia, T. Wang, Furfural: A Promising Platform Compound for Sustainable Production of C4 and C5 Chemicals, *ACS Catal.*, 6 (2016) 7621-7640.
- [63] S. Sitthisa, W. An, D.E. Resasco, Selective conversion of furfural to methylfuran over silica-supported NiFe bimetallic catalysts, *J. Catal.*, 284 (2011) 90-101.

- [64] V. Vorotnikov, G. Mpourmpakis, D.G. Vlachos, DFT Study of Furfural Conversion to Furan, Furfuryl Alcohol, and 2-Methylfuran on Pd(111), *ACS Catal.*, 2 (2012) 2496-2504.
- [65] M.M. Villaverde, T.F. Garetto, A.J. Marchi, Liquid-phase transfer hydrogenation of furfural to furfuryl alcohol on Cu–Mg–Al catalysts, *Catal. Commun.*, 58 (2015) 6-10.
- [66] F. Hu, L. Leng, M. Zhang, W. Chen, Y. Yu, J. Wang, J.H. Horton, Z. Li, Direct Synthesis of Atomically Dispersed Palladium Atoms Supported on Graphitic Carbon Nitride for Efficient Selective Hydrogenation Reactions, *ACS Appl. Mater. Interfaces*, 12 (2020) 54146-54154.
- [67] K. Fulajtárova, T. Soták, M. Hronec, I. Vávra, E. Dobročka, M. Omastová, Aqueous phase hydrogenation of furfural to furfuryl alcohol over Pd–Cu catalysts, *Appl. Catal. A Gen.*, 502 (2015) 78-85.
- [68] M.M. Villaverde, N.M. Bertero, T.F. Garetto, A.J. Marchi, Selective liquid-phase hydrogenation of furfural to furfuryl alcohol over Cu-based catalysts, *Catal. Today*, 213 (2013) 87-92.
- [69] S. Bhogeswararao, D. Srinivas, Catalytic conversion of furfural to industrial chemicals over supported Pt and Pd catalysts, *J. Catal.*, 327 (2015) 65-77.
- [70] H. Li, H. Luo, L. Zhuang, W. Dai, M. Qiao, Liquid phase hydrogenation of furfural to furfuryl alcohol over the Fe-promoted Ni-B amorphous alloy catalysts, *J. Mol. Catal. A: Chem.*, 203 (2003) 267-275.
- [71] R. Bardestani, R. Biriaei, S. Kaliaguine, Hydrogenation of Furfural to Furfuryl Alcohol over Ru Particles Supported on Mildly Oxidized Biochar, *Catalysts*, 10 (2020) 934.
- [72] J. Tan, J. Cui, X. Cui, T. Deng, X. Li, Y. Zhu, Y. Li, Graphene-Modified Ru Nanocatalyst for Low-Temperature Hydrogenation of Carbonyl Groups, *ACS Catal.*, 5 (2015) 7379-7384.

- [73] P. Weerachawanasak, P. Krawmanee, W. Inkamhaeng, F.J. Cadete Santos Aires, T. Sooknoi, J. Panpranot, Development of bimetallic Ni-Cu/SiO<sub>2</sub> catalysts for liquid phase selective hydrogenation of furfural to furfuryl alcohol, *Catal. Commun.*, 149 (2021) 106221.
- [74] J. Yu, Y. Yang, L. Chen, Z. Li, W. Liu, E. Xu, Y. Zhang, S. Hong, X. Zhang, M. Wei, NiBi intermetallic compounds catalyst toward selective hydrogenation of unsaturated aldehydes, *Appl. Catal. B*, 277 (2020) 119273.

## Chapter 5 Single atom alloy and monometallic catalysts for the hydrogenation of crotonaldehyde



## 5.1 Introduction

Chapter 3 highlighted the importance of Cu metal precursor selection for the hydrogenation of furfural. While Chapter 4 discussed the excellent promotion of the catalytic activity for base-metal Cu catalysts using atomically dispersed Pd atoms. Since these Chapters focused only on the hydrogenation of furfural, the catalysts will now be utilised for the hydrogenation of a common  $\alpha$ ,  $\beta$  unsaturated aldehyde like crotonaldehyde. In contrast to furfural, crotonaldehyde is a smaller and relatively simpler unsaturated aldehyde. The hydrogenation of this planar  $\pi$ -conjugated molecule is complex and has been studied both experimentally and theoretically [1-8]. The reaction pathway can follow two routes by hydrogenating the C = C or the C = O bond, forming butanal or crotyl alcohol, respectively. Both these molecules can then be hydrogenated to butanol via the reduction of their remaining unsaturated double bond. Thus, the experiments will confirm if a similar promotion of the hydrogenation capability is observed with Pd atoms. Also, crotonaldehyde lacks the furan ring (present in furfural) which directs the reaction by the repulsion of its anti-bonding orbitals with the 3d orbitals of the Cu (111) surface atoms [9] promoting a vertical adsorption. Directing groups are important as the C = C hydrogenation is thermodynamically more favourable by 35 kJ/mol [10]. Consequently, the reactivity will be investigated in the case where C = O hydrogenation will not be specifically preferred. In the absence of these effects, the reactivity changes of the Pd atoms on the copper surface will be examined.

A range of metal catalysts has already been studied for the hydrogenation of crotonaldehyde in the literature such as Ag, Co, Cu, Ir, Mo, Nb, Ni, Pt, Pd, Re, Rh, Ru and W [3, 7, 11-20]. Base-metals such as Ni and Cu [14, 20, 21] are reported to preferentially hydrogenate the C = C bonds, as the crotonaldehyde molecule typically adsorbs flat on the surface. There has been significant interest in Cu-based catalysts [6, 7, 14, 21] for such reactions, as it is inexpensive compared to Pt-based catalysts, and steric [20] and electronic [6] modifications have been employed to promote perpendicular crotonaldehyde adsorption, thus altering the selectivity towards the C = O bond hydrogenation. For example, adsorbed sulfur species have been used to cause a rehybridisation of the adsorbed reactant, resulting in the weakening of the intermolecular bonding and tilting of the C = C and C = O groups

relative to the surface [22], thus, favouring the unsaturated alcohol formation by Cu-based catalysts.

While Pt-based catalysts are reported to show high crotyl alcohol selectivity, due to a similar tilting of the reactant as the coverage of the crotonaldehyde increases [23], Pd catalysts are unselective to which double bond is hydrogenated. Campo *et al.* [13] reported that monometallic Pd catalysts were unselective towards crotyl alcohol. Modification of the Pd with oxidic species [13] or Ni [12] had a minimal effect on changing the selectivity towards crotyl alcohol or the synergistic behaviour. However, it has been reported earlier that the lack of selectivity towards crotyl alcohol may be the result of the isomerisation of crotyl alcohol to butanal (Fig. 1.6.1) promoted by Al<sub>2</sub>O<sub>3</sub>, Cu, Pd, and Ni materials [24-26].

Recently, a few single-atom catalysts have been utilised to develop better atom efficient and selective materials for the hydrogenation of crotonaldehyde. A Pt<sub>1</sub>/MoC catalyst synthesised by Qingyuan *et al.* [27] reported a 4 times increase in TOF of the SAC (1216 h<sup>-1</sup>) versus a monometallic 1% Pt/MoC (299 h<sup>-1</sup>). However, the reported selectivity was found to be approximately equally distributed across the three possible hydrogenation products (butanal, crotyl alcohol and butanol). In contrast, another Rh<sub>1</sub>/MoS<sub>2</sub> SAC synthesised by and Yang *et al.* [17] reported a 100% crotyl alcohol selective catalyst. They attributed the incredible selectivity to a “pocket” like active sites, which promoted vertical adsorption of crotonaldehyde and hydrogenation of only the C = O bond through steric effects. However, such sites lacked the activity (TOF = 64.7 h<sup>-1</sup>) compared to the Pt<sub>1</sub>/MoC catalyst.

This chapter investigates the adoption of the catalysts synthesised in the previous chapters for the hydrogenation of crotonaldehyde. The initial catalytic parameters will be chosen based on the previous furfural experiments to explore how under similar reactions conditions crotonaldehyde hydrogenation differs from furfural. And whether a similar copper catalyst promotion is observed with Pd addition and if Pd atoms can change the reactivity of the base copper catalyst in the absence of directing groups, and vice versa, how the reactivity of atomically dispersed Pd atoms on a Cu surface differs from its Pd monometallic counterpart. Also, the chapter will initially investigate optimising the reaction conditions by adjusting catalyst mass and hydrogen pressure. The novelty of the work comes from the absence of

literature on the metal precursors' effect for Cu catalysts and the use of single-atom alloy catalysts for the hydrogenation of crotonaldehyde.

## 5.2 Catalytic testing

### 5.2.1 Optimisation of the hydrogenation of crotonaldehyde

#### 5.2.1.1 Mass of catalyst

The performance of the monometallic Cu<sub>100</sub> and Pd<sub>100</sub> Al<sub>2</sub>O<sub>3</sub> supported catalysts were first tested under the same reaction conditions for the furfural experiments in the earlier Chapter. Using 30 mg of catalyst, it was found that crotonaldehyde was converted into butanal (Fig. 5.2.1). This occurred through the hydrogenation of the C = C with minimal crotyl alcohol formation but proceeding to fully hydrogenate the molecule to butanal (Table 5.2.1). The lack of crotyl alcohol selectivity is because hydrogenating the C = C bond is thermodynamically and kinetically more favourable than the C = O bond [28]. This is not observed for the furfural experiments in the prior Chapters as crotonaldehyde is absent of directing groups [11] such as furan for furfural, which makes the C = O hydrogenation preferable. Comparing the yield profile of the Cu and Pd-based systems shows the superior hydrogenation capability of Pd, noticed by the complete conversion of crotonaldehyde to butanal within the first 20 minutes. Conversely, an induction period is present for the Cu catalyst and generating butanal over 7 hours. Likewise furfural hydrogenation, the crotonaldehyde reaction seems to form an acetal (crotonaldehyde dimethyl acetal, Fig. 7.1.2 GCMS found in appendices) with methanol, which has also been reported previously [13, 29].

*Table 5.2.1 Summary of the catalytic hydrogenation of crotonaldehyde using monometallic Cu and Pd Al<sub>2</sub>O<sub>3</sub> supported catalysts. Reaction conditions: 7 h, 50 °C, 1.5 bar, 600 RPM, and 30mg or 10 mg of catalyst.*

Catalyst	Mass of catalyst (mg)	Conversion (%)	Butanal S(%)	Butanol S(%)	Crotyl Alcohol S(%)	Acetal S(%)	Initial rate (mol/h·gMetal)
Cu <sub>100</sub>	30	100.0 ± 5.0	87.1 ± 4.4	4.7 ± 0.2	2.5 ± 0.1	5.7 ± 0.3	0.12 ± 0.01
Cu <sub>100</sub>	10	98.1 ± 4.9	93.1 ± 4.7	3.9 ± 0.2	1.5 ± 0.1	1.6 ± 0.1	0.39 ± 0.02
Pd <sub>100</sub>	30	100.0 ± 5.0	92.5 ± 4.6	7.5 ± 0.4	0.0	0.0	2.06 ± 0.10
Pd <sub>100</sub>	10	99.2 ± 5.0	62.8 ± 3.1	37.2 ± 1.9	0.0	0.0	5.69 ± 0.29

*Rounding errors may be present.*

Due to the excellent reactivity of both monometallic catalysts, the mass of the active material used was reduced by 67% to 10 mg. The drastic reduction in mass appears to improve the reactivity for both catalysts. A significant change in selectivity is also observed for the Pd<sub>100</sub> catalyst with a 30% gain in

the butanol selectivity, while the  $\text{Cu}_{100}$  catalyst's selectivity is largely unaffected. The phenomenon of the increase in catalytic activity (initial rates in Table 5.2.1) with less catalyst can be attributed to excess catalytic sites compared to the reactant molecules increasing the competition for reactant molecules. Justifying why normalised initial rates are inversely proportional to the amount of catalyst used.

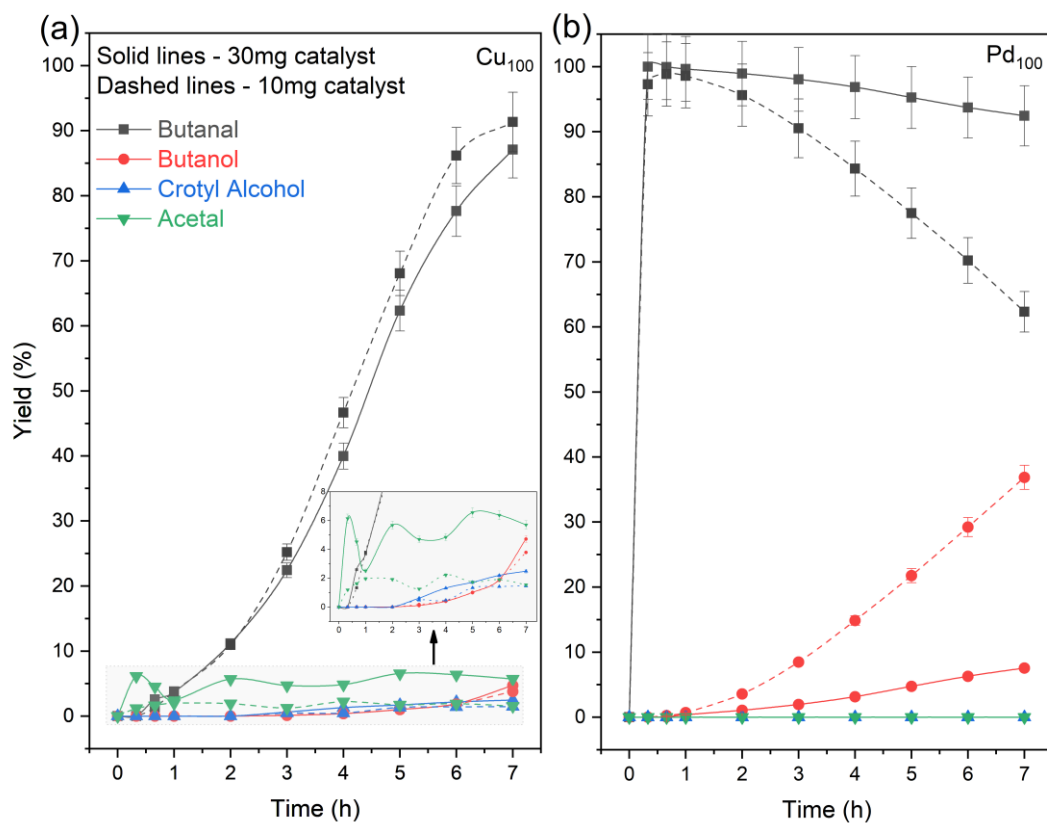


Fig. 5.2.1 Percentage yields of the products formed against time for the monometallic (a)  $\text{Cu}_{100}$  and (b)  $\text{Pd}_{100}$   $\text{Al}_2\text{O}_3$  supported catalysts. Reaction conditions: 7 h, 50 °C, 1.5 bar, 600 RPM, and 30mg or 10 mg of catalyst.

### 5.2.1.2 Hydrogen pressure

The effect of hydrogen pressure was also investigated for the two monometallic catalysts (Fig. 5.2.2 and Table 5.2.2). For both catalysts, the increase of pressure accelerates the formation of butanal. While in the case of Cu the pressure favours the conversion of butanal to butanol, in Pd the formation of this final product is more inhibited. None of the catalysts shows a significant production of crotyl alcohol, and the pressure has a negligible impact on the formation of acetal for the Cu catalyst. The Cu<sub>100</sub> catalyst displays a mediocre initial rate increase of ~10% when H<sub>2</sub> pressure increases from 1.5 to 10 bar, suggesting the surface is still likely to be deficient in adsorbed hydrogen.

The reactivity of the Pd<sub>100</sub> catalyst, however, doesn't follow the reactivity of Pt catalysts, for which high hydrogen pressures enhance butanol formation and low hydrogen pressures improve crotyl alcohol selectivity [16]. The phenomenon with Pd<sub>100</sub> catalyst can likely be explained by the bi-molecular Langmuir-Hinshelwood (LH) reaction mechanism. The LH mechanism for bi-molecular reactions requires both reactant molecules to be adsorbed onto the catalyst surface for the reaction to proceed. So, in the current case, the highest reaction rate of butanal hydrogenation to butanol occurs when both reactants (butanal and hydrogen) have a similar adsorbed surface concentration. It can be proposed that in higher H<sub>2</sub> pressures condition (10 bar), an excess of hydrogen is available on the surface. Hence, there is not enough butanal on the surface to react to form butanol. Contrarily, at 1.5 bar of H<sub>2</sub>, the imbalance of adsorbed reactant is less severe, so the yield of butanol is greater. In the case of Pt, the difference can be hypothesised to their different adsorption strengths of the reactants, where even at higher pressures there is still insufficient hydrogen on the surface to be detrimental to the selectivity.

Finally, the conversion of crotonaldehyde to butanal (C = C hydrogenation) seems to increase with pressure for both Pd and Pt [16] catalysts. This may suggest an Eley-Rideal mechanism for this reaction since even when the surface is oversaturated with hydrogen, the reactant can interact with the adsorbed hydrogen and reduce the C = C bond.

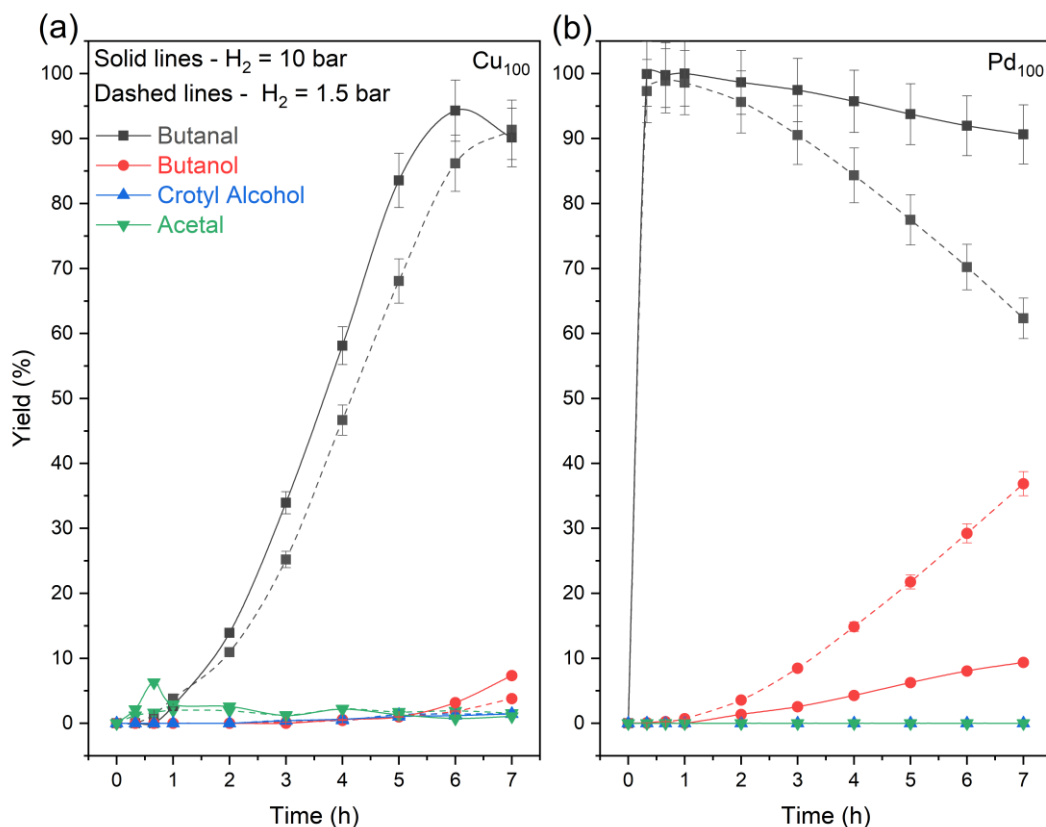


Fig. 5.2.2 Percentage yields of the products formed against time for the monometallic (a)  $\text{Cu}_{100}$  and (b)  $\text{Pd}_{100}$   $\text{Al}_2\text{O}_3$  supported catalysts. Reaction conditions: 7 h, 50 °C, 1.5 bar or 10 bar, 600 RPM, and 10 mg of catalyst.

Table 5.2.2 Summary of the catalytic hydrogenation of crotonaldehyde using monometallic Cu and Pd  $\text{Al}_2\text{O}_3$  supported catalysts. Reaction conditions: 7 h, 50 °C, 1.5 or 10 bar, 600 RPM, and 10 mg of catalyst.

Catalyst	$\text{H}_2$ pressure (bar)	Conversion (%)	Butanal S(%)	Butanol S(%)	Crotyl Alcohol S(%)	Acetal S(%)	Initial rate (mol/h.gMetal)
$\text{Cu}_{100}$	1.5	98.1 ± 4.9	93.1 ± 4.7	3.9 ± 0.2	1.5 ± 0.1	1.6 ± 0.1	0.39 ± 0.02
$\text{Cu}_{100}$	10	100.0 ± 5.0	90.2 ± 4.5	7.3 ± 0.4	1.5 ± 0.1	1.1 ± 0.1	0.43 ± 0.02
$\text{Pd}_{100}$	1.5	99.2 ± 5.0	62.8 ± 3.1	37.2 ± 1.9	0.0	0.0	5.69 ± 0.29
$\text{Pd}_{100}$	10	100.0 ± 5.0	90.6 ± 4.5	9.4 ± 0.5	0.0	0.0	5.77 ± 0.29

Rounding errors may be present.

## 5.2.2 PdCu SAA catalysts

Table 4.3.2 summarises the characterisation data of the 1 wt% PdCu SAA catalysts, which was discussed in depth in Chapter 4. In summary, three bimetallic PdCu catalysts were synthesised by galvanic replacement, where a monometallic  $\text{Cu}/\text{Al}_2\text{O}_3$  catalyst was used as the template. Bulk elemental analysis showed that trace amounts of Pd were incorporated into the nanoparticles with

EXAFS determining the Pd species where atomically dispersed on the Cu nanoparticles. Thus, confirming the formation of single-atom catalysts, specifically single-atom alloy catalysts. EXAFS and XPS characterisation differentiated the catalysts by suggesting that the Pd<sub>1</sub>Cu<sub>216</sub> catalyst had a larger ratio of Pd atoms remaining on the surface of the nanoparticle than the higher Pd loaded Pd<sub>1</sub>Cu<sub>53</sub> catalyst.

Table 5.2.3 Summary of the characterisation data for the 1 wt% Al<sub>2</sub>O<sub>3</sub> supported catalysts.

Catalyst	Pd loading <sup>a</sup> (wt%)	Cu loading <sup>a</sup> (wt%)	Pd:Cu atomic ratio	Particle size (nm)	Cu dispersion (%)	Pd dispersion (%)	EXAFS
Cu <sub>100</sub>	-	0.9403 ± 0.0267	-	2.7 ± 0.7 <sup>a</sup>	71.0 ± 7.1	-	-
Pd <sub>1</sub> Cu <sub>234</sub>	0.0064 ± 0.0006	0.8947 ± 0.0253	1: 234	2.6 ± 0.7 <sup>a</sup>	79.9 ± 8.0	N/A	-
Pd <sub>1</sub> Cu <sub>216</sub>	0.0067 ± 0.0006	0.8599 ± 0.0262	1: 216	2.0 ± 0.6 <sup>a</sup>	80.3 ± 8.0	90.9 ± 9.1	SAA
Pd <sub>1</sub> Cu <sub>53</sub>	0.0296 ± 0.0022	0.9296 ± 0.0232	1: 53	7.0 ± 4.4 <sup>a</sup>	68.9 ± 6.9	41.7 ± 4.2	SAA
Pd <sub>100</sub>	0.8882 ± 0.0529	-	-	5.1 ± 2.7 <sup>b</sup>	-	22.9 ± 2.3	-

STEM/TEM <sup>a</sup>Cu and <sup>b</sup>Pd particle size

The catalytic performance of the Pd augmented Cu-based SAA catalysts was explored for the hydrogenation of crotonaldehyde at 50 °C with 1.5 bar of hydrogen. The transformation of crotonaldehyde can follow various pathways which have been summarised in Fig. 5.2.3. In the absence of any Cu/Pd material, hydrogenation reactions were not observed (Table 5.2.4). Only the acetalisation of crotonaldehyde with the solvent was observed with the parent Al<sub>2</sub>O<sub>3</sub> support and without any solid material.

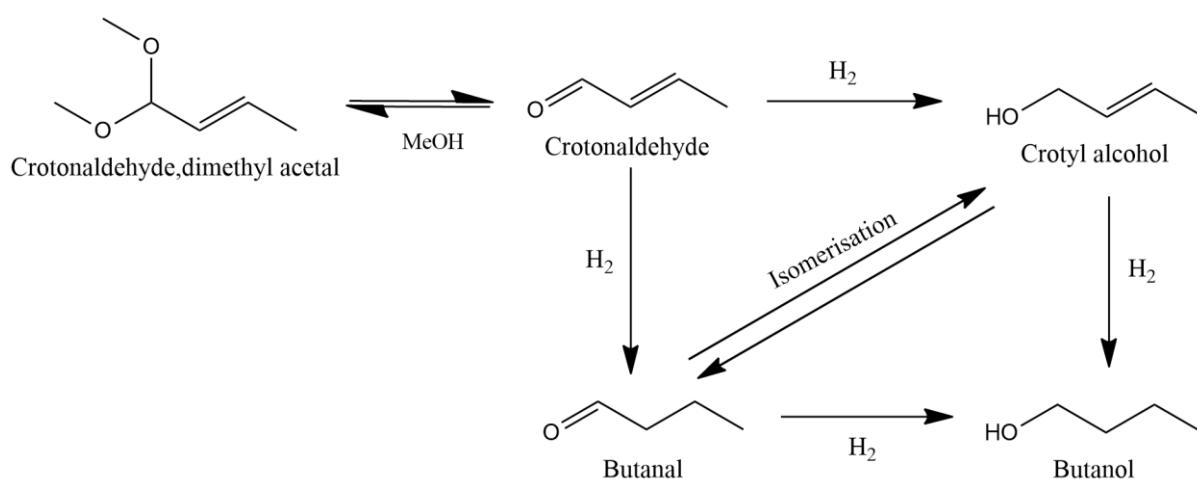


Fig. 5.2.3 Reaction scheme for the transformation of crotonaldehyde.

Table 5.2.4 Summary of blanks and bare support catalytic data for the hydrogenation of crotonaldehyde. Reaction conditions: 7 h, 50 °C, 1.5 bar, 600 RPM, and 10 mg of catalyst.

Catalyst	Conversion (%)	Butanal S (%)	Butanol S (%)	Crotyl Alcohol S (%)	Acetal S (%)
Blank	4.7 ± 0.2	0.0	0.0	0.0	100 ± 5.0
Al <sub>2</sub> O <sub>3</sub>	1.3 ± 0.1	0.0	0.0	0.0	100 ± 5.0

The catalytic data show that adding trace amounts of Pd to the Cu nanoparticles has significantly improved the hydrogenation of crotonaldehyde (Table 5.2.5). The PdCu SAA catalysts are found to promote hydrogenation of both the C = C and C = O bonds compared to the host Cu<sub>100</sub> catalyst, which only improves the former. Thus, “fast-forwarding” the reaction as higher conversions are reached of butanal to butanol. But, like the monometallic catalysts mentioned earlier, the catalysts appear to initially promote the hydrogenation of the C = C bond to butanal with minimal selectivity to crotyl alcohol (C = O bond). The inability to adequately hydrogenate the C = O bond first in crotonaldehyde but facilely with furfural can be traced to the furan ring being electronically repulsed from the Cu (111) surface. Thus, promoting a perpendicular  $\eta^1(\text{O})$ -aldehyde conformation [9] and the selective hydrogenation of the C = O bond. While for crotonaldehyde, XANES experiments by Chiu *et al.* [14] suggest that on Cu (111) surfaces crotonaldehyde adsorbs flat on the surface, which is attributed to the lack of selectivity to the C = O bond. Since the PdCu SAA catalysts in the present work derive their selectivity from the host nanoparticle’s bonding modes, the preference for C = C hydrogenation is understandable. While DFT calculations on Pd (111) surfaces found crotonaldehyde followed a similar binding mode, parallel to the surface via the C = C and C = O bonds. As a result, these conformations promoted either the full hydrogenation to butane or partially to butanal [4].

Table 5.2.5 Summary of the catalytic data for the hydrogenation of crotonaldehyde using Pd/Cu catalysts. Reaction conditions: 7 h, 50 °C, 1.5 bar, 600 RPM, and 10 mg of catalyst.

Catalyst	Conversion (%)	Butanal S (%)	Butanol S (%)	Crotyl Alcohol S (%)	Acetal S (%)
Cu <sub>100</sub>	98.1 ± 4.9	93.1 ± 4.7	3.9 ± 0.2	1.5 ± 0.1	1.6 ± 0.1
Pd <sub>1</sub> Cu <sub>234</sub>	99.3 ± 5.0	84.3 ± 4.4	13.3 ± 0.5	1.5 ± 0.1	1.0 ± 0.1
Pd <sub>1</sub> Cu <sub>216</sub>	99.7 ± 5.0	75.1 ± 3.8	22.0 ± 1.1	1.6 ± 0.1	1.3 ± 0.1
Pd <sub>1</sub> Cu <sub>53</sub>	99.0 ± 5.0	77.4 ± 4.1	20.8 ± 0.8	1.2 ± 0.1	0.6 ± 0.1
Pd <sub>100</sub>	99.2 ± 5.0	62.8 ± 3.1	37.2 ± 1.9	0.0	0.0

Rounding errors may be present.

Fig. 5.2.4a illustrates that all the catalysts can achieve 100% crotonaldehyde conversion over 7 h at 50 °C and 1.5 bar, albeit by different pathways. The conversion profiles are also reminiscent of furfural experiments with these catalysts in the earlier chapter, but with higher activity. Consistent with the catalytic data in the previous chapters, an induction period of 0.67 - 1 h are observed for all the copper-based catalysts where the conversion is suppressed. As mentioned previously, the behaviour is assumed to be because of the limited catalytically available hydrogen at the beginning of the reaction, either through the formation of surface oxide (from O<sub>2</sub> contamination) or Cu's inability to adequately chemisorb hydrogen. But the presence of Pd with the SAA catalysts appears to lessen its effects. This is in stark contrast to the monometallic Pd<sub>100</sub> catalyst, lacking any such induction period due to its increased resistance to oxidation, higher reducibility and likely again due to the extended Pd surface to store hydrogen as β-hydride species during the *in-situ* reduction treatment [30-33].

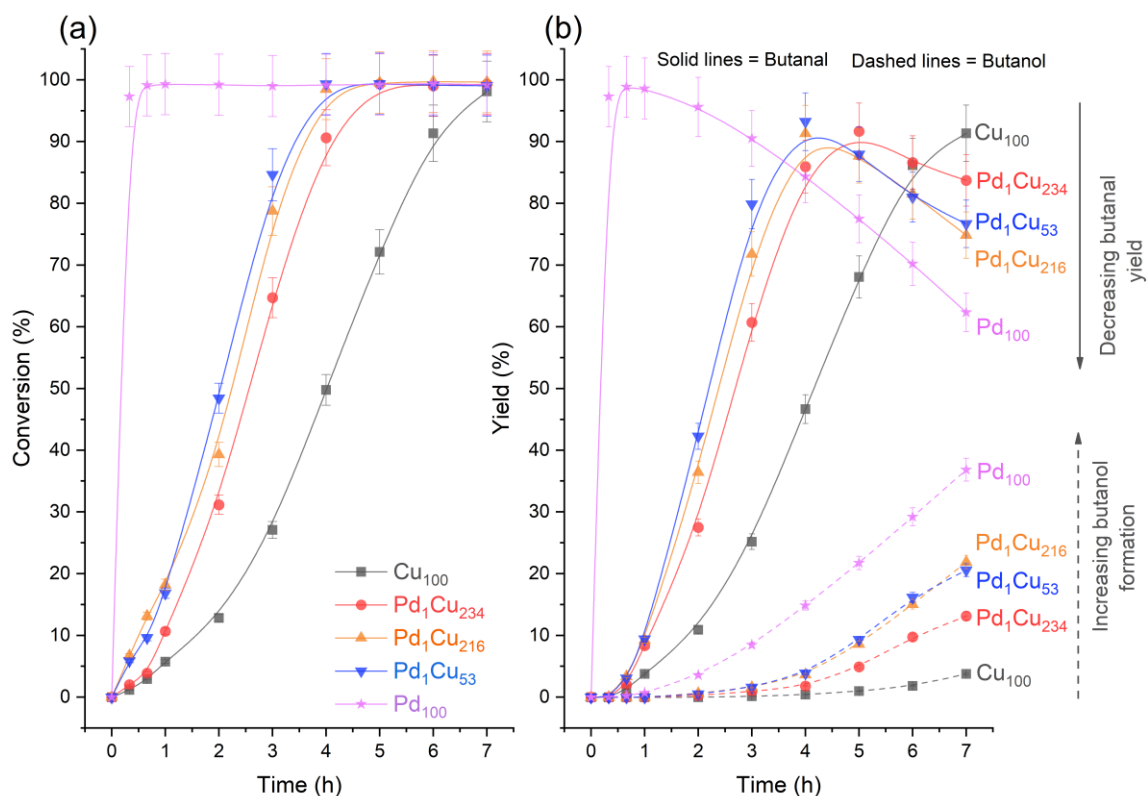


Fig. 5.2.4 The reaction profiles of (a) crotonaldehyde conversion and (b) yield of major products across monometallic and bimetallic catalysts. Reaction conditions: 7 h, 50 °C, 1.5 bar, 600 RPM, and 10 mg of catalyst.

Normalising the reaction in Fig. 5.2.5 facilitates the comparison of the catalytic behaviour

irrespective of activity and reaction time. In general, all the Cu-based catalysts follow a similar trend (especially for Fig. 5.2.5b), corroborating the idea that the Pd atoms fast-forward the hydrogenation of butanal to butanol. However, examining Fig. 5.2.5a there is a slight difference in the initial reaction pathway for the Pd<sub>1</sub>Cu<sub>216</sub> and Pd<sub>1</sub>Cu<sub>53</sub> catalysts, which can be attributed to the higher selectivity towards the acetal at the start of the reaction. Though, as the reaction progresses, the acetal is likely converted back to the reactant as the reactant is consumed. It should be noted that the Pd<sub>100</sub> trend can be misleading as 0 – 97% conversion (and 0 – 97% butanal yield) is only characterised by 2 data points, meaning the reaction pathway of this phase cannot be determined.

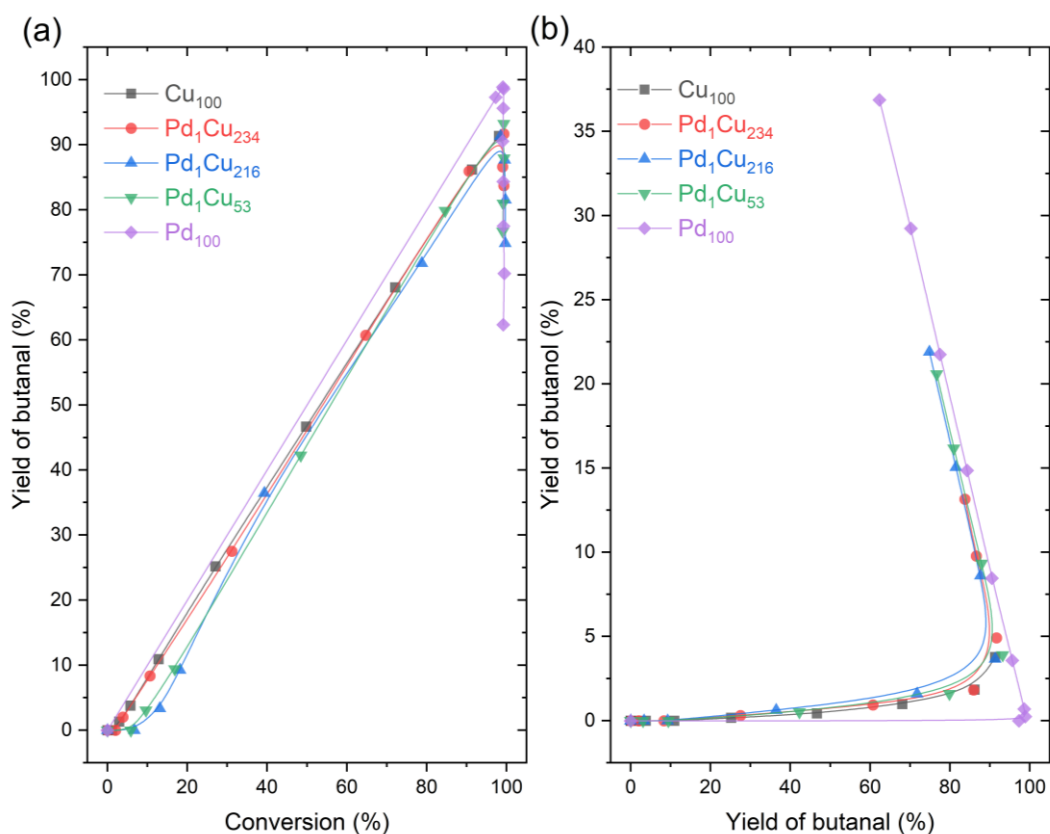


Fig. 5.2.5 (a) Yield of butanal vs conversion and (b) yield of butanol vs yield of butanal reaction graphs. Reaction conditions: 7 h, 50 °C, 1.5 bar, 600 RPM, and 10 mg of catalyst

Analysing the yields, it can be speculated that in all the catalytic systems tested the reaction proceeds largely by the hydrogenation of crotonaldehyde to butanal (via the C = C bond) and then the subsequent reduction of butanal to butanol (via the C = O bond) [3]. However, past studies [24-26] suggest the

mechanism may be more complex as butanal may also be formed from crotyl alcohol acting as an intermediate, isomerising into the saturated aldehyde (Fig. 5.2.3). As it was also reported for Cu-Cr catalysts that the activity for forming crotyl alcohol is lower than its isomerisation reaction, so the majority of crotyl alcohol may be transformed into butanal [25]. To understand this reaction better further experiments were conducted replacing the reactant, crotonaldehyde with crotyl alcohol under the same conditions (Table 5.2.6 and Fig. 5.2.6). Both monometallic catalysts were found to be able to isomerise crotyl alcohol to butanal but with a major selectivity towards crotyl alcohol's hydrogenation to butanol. Also, unsurprisingly the Pd<sub>100</sub> catalyst was found to be significantly more active in hydrogenating to butanol compared to the Cu<sub>100</sub> catalyst. The data also provides some evidence why the Pd<sub>100</sub> catalyst is entirely unselective towards crotyl alcohol, as it is quickly either converted to butanol or butanal. However, since the crotyl alcohol intermediate is not detected, it is likely crotyl alcohol is not initially formed.

*Table 5.2.6 Summary of the catalytic data for the hydrogenation of crotyl alcohol using monometallic Pd/Cu catalysts. Reaction conditions: 7 h, 50 °C, 1.5 bar, 600 RPM, and 10 mg of catalyst.*

Catalyst	Conversion (%)	Butanal S (%)	Butanol S (%)	Carbon balance (%)
Cu <sub>100</sub>	12.3 ± 0.6	5.5 ± 0.3	94.5 ± 4.8	100 ± 5.0
Pd <sub>100</sub>	95.3 ± 4.8	9.4 ± 0.5	90.6 ± 4.5	92.1 ± 4.6

*Rounding errors may be present.*

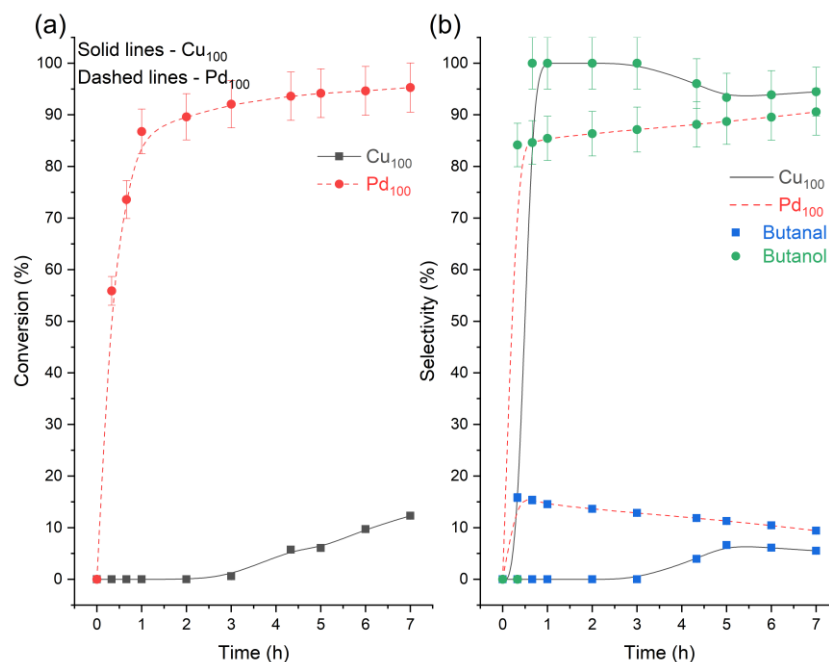


Fig. 5.2.6 The reaction profiles of (a) crotyl alcohol conversion and (b) product selectivity across the monometallic catalysts. Reaction conditions: 7 h, 50 °C, 1.5 bar, 600 RPM, and 10 mg of catalyst.

Nevertheless, the  $\text{Cu}_{100}$  catalyst is shown to be the least active for forming butanol from crotonaldehyde but augmenting with Pd improved its yield (~500% butanol yield increase). The enhanced hydrogenation capability of the PdCu SAA catalysts can once again be credited to the isolated Pd atoms acting as entry sites for hydrogen to dissociate and spill over onto the Cu surface [34-37] where they react with the adsorbed substrate.

Mirroring the furfural experiments, the PdCu SAA materials are considerably more atom efficient catalysts than their monometallic counterparts (Fig. 5.2.7). Principally, the  $\text{Pd}_1\text{Cu}_{216}$  catalyst demonstrates a nineteen-fold increase in activity compared to the monometallic  $\text{Pd}_{100}$  catalyst, which is due to the lack of spectator Pd atoms in the nanoparticle's bulk. Substantial improvements are also observed over the  $\text{Cu}_{100}$  catalyst at 1.5 bar and 10 bar (~two-fold increase in both cases, Table 5.2.2), thus, demonstrating the synergistic behaviour of Pd atoms on Cu surfaces for the hydrogenation of crotonaldehyde. The  $\text{Pd}_1\text{Cu}_{234}$  and  $\text{Pd}_1\text{Cu}_{216}$  catalysts show that adding trace amounts of Pd have the greatest effect, while further Pd addition has a diminishing return in the activity. It is proposed this trend

is due to the Pd atoms being inaccessible as hydrogen dissociation entry sites since the EXAFS suggests a considerable quantity of the Pd atoms have diffused under the surface of the nanoparticle for the Pd<sub>1</sub>Cu<sub>53</sub> catalyst.

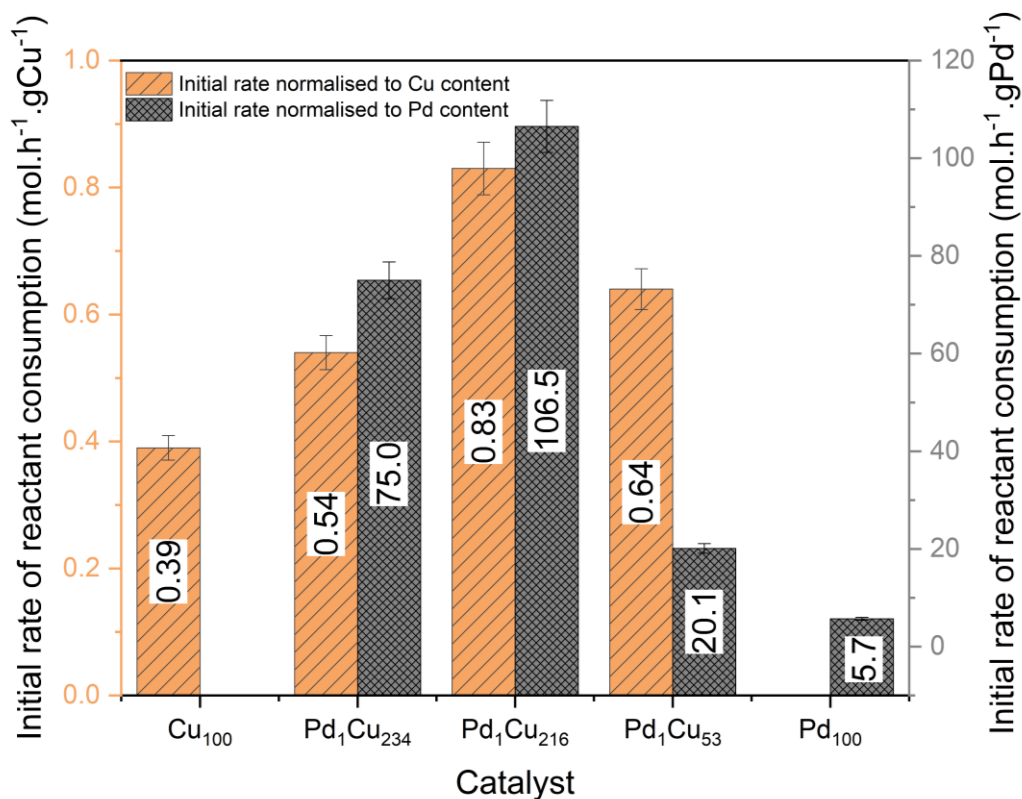


Fig. 5.2.7 Initial rate of the crotonaldehyde consumption normalised to Cu and Pd content. The initial rate was determined after the induction period for the Cu-based catalysts. Reaction conditions: 7 h, 50 °C, 1.5 bar, 600 RPM, and 10 mg of catalyst.

TOFs were determined in Fig. 5.2.8 to identify whether the synergistic effect of the atomically dispersed Pd atoms were due to the difference in the dispersion of the catalysts. The TOF indicates the introduction of the atomically dispersed Pd atoms augments the catalytic activity of the surface Cu sites. For example, the optimal Pd<sub>1</sub>Cu<sub>216</sub> catalyst boosts Cu TOFs by ~90%. Further raising the Pd loading with the Pd<sub>1</sub>Cu<sub>53</sub> comes with diminishing returns as the TOF and normalised initial rates (Fig. 5.2.7) are not promoted. Comparing TOFs of the monometallic Pd<sub>100</sub> catalyst to an SAA catalyst shows that the atomically dispersed Pd sites are ~373% more catalytically active than the equivalent surface sites found on Pd nanoparticles. Supporting the furfural experiments, it can also be noticed that initially as the Pd

loading is increased, the activity of the Pd sites also increases to a maximum TOF of  $12500 \pm 125 \text{ h}^{-1}$ . Further drastic increases in the Pd loading with the  $\text{Pd}_1\text{Cu}_{53}$  catalyst appears to begin to render the Pd sites less effective, possibly changing their properties to be more like that of a monometallic Pd catalyst. It should be noted that due to the inability to determine the Pd dispersion for the  $\text{Pd}_1\text{Cu}_{234}$  catalyst (lack of Pd 3d signal) it was assumed to be 100% for this TOF calculation.

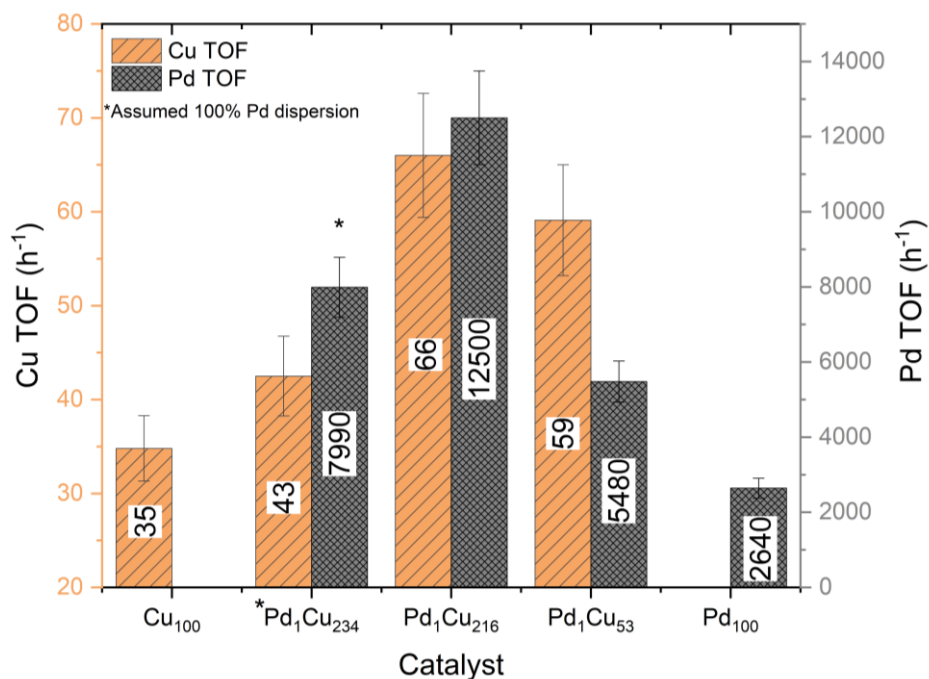


Fig. 5.2.8 Turnover frequency of both Cu and Pd surface atoms for the catalysts determined from the XPS calculated dispersion. Reaction conditions: 7 h, 50 °C, 1.5 bar, 600 RPM, and 10 mg of catalyst.

### 5.2.2.1 Spent catalyst characterisation and recycling experiments

Comparing the XPS spectra of the spent and unused  $\text{Pd}_1\text{Cu}_{216}$  catalysts (Fig. 5.2.9a) shows that like the furfural experiments, the spent catalyst is significantly oxidised to CuO, which is observed by the shake-up satellites and the broadening of the Cu  $2p_{3/2}$  transition to higher energies. Supporting this, the surface compositional analysis in Table 4.3.4 confirms the Cu species are largely in their  $\text{Cu}^{2+}$  oxidation state (58.7%) which is not as pronounced as with furfural.

Table 5.2.7 Summarised energies for the Cu 2p<sub>3/2</sub> and the Auger Cu L<sub>3</sub>VV transitions, surface composition, modified Auger parameters and XPS calculated dispersion for the unused and spent catalysts.

Sample	State	Cu 2p <sub>3/2</sub> (eV)	L <sub>3</sub> VV (eV)	Cu <sup>0</sup> + Cu <sup>+</sup> (%)	Cu <sup>2+</sup> (%)	Cu Dispersion (%)
Pd <sub>1</sub> Cu <sub>216</sub>	Fresh	932.83	914.24	97.6	2.4	80.3 ± 8.0
Pd <sub>1</sub> Cu <sub>216</sub>	Spent	932.73	N/A	41.3	58.7	61.5 ± 6.2
CuO	-	933.62	917.78	-	-	-
Cu <sub>2</sub> O	-	932.29	916.70	-	-	-
Cu*	-	932.63	918.75	-	-	-

\*Cu 2p<sub>3/2</sub> was calibrated to the ISO standard of 932.63 eV.

The spectrum of the spent material is also found to be severely attenuated compared to the unused catalyst, which is likely due to the small amount of catalyst used and recovered from the catalytic testing. Consequently, the position of the Cu L<sub>3</sub>VV Auger transition cannot accurately be determined (Fig. 5.2.9b). The XPS calculated Cu dispersion values show that there is some loss in Cu dispersion likely through nanoparticle sintering.

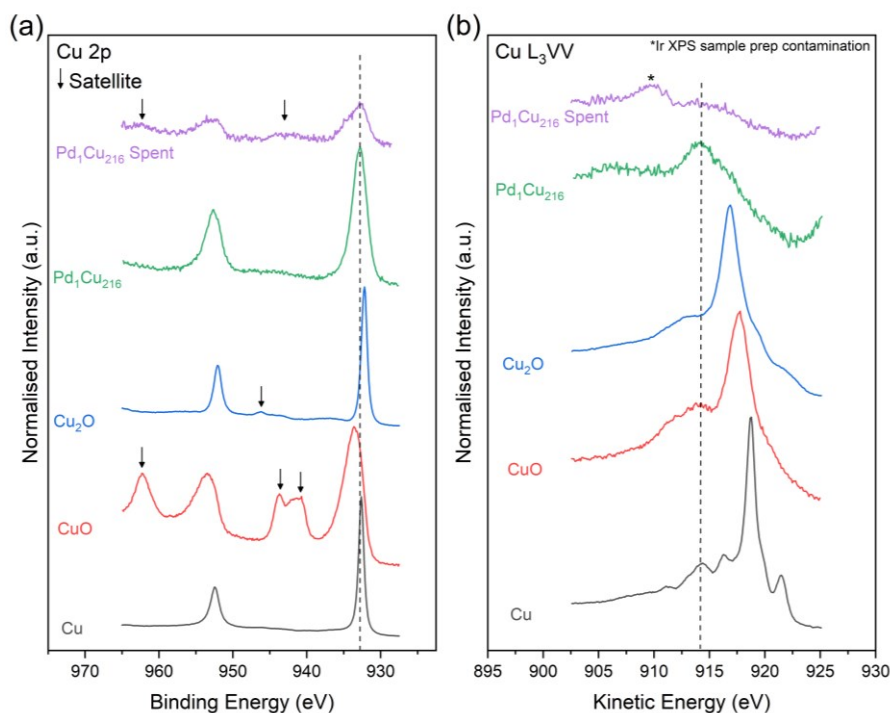


Fig. 5.2.9 High-resolution stacked XPS and XAES spectra of the (a) Cu 2p and (b) Cu L<sub>3</sub>VV regions for the unused and spent Pd<sub>1</sub>Cu<sub>216</sub> catalyst.

The recyclability of the catalysts was investigated. The catalysts were recovered after the reaction via centrifugation, followed by washing with methanol. Once dried, they were retested at 75% scale. Table 4.3.5 shows that the conversion and selectivity of the catalysts were within error minimally

affected after reuse. This is consistent with the ICP-OES analysis of the filtered supernatant fluid as the elemental analysis ruled out Cu leaching.

*Table 5.2.8 Crotonaldehyde hydrogenation over the recycled catalysts. Reaction conditions: 7 h, 50 °C, 1.5 bar, 600 RPM, and 10 mg of catalyst.*

Catalyst	Conversion (%)	Butanal S (%)	Butanol S (%)	Crotyl Alcohol S (%)	Acetal S (%)
Cu <sub>100</sub> <sup>1</sup>	98.1 ± 4.9	93.1 ± 4.7	3.9 ± 0.2	1.5 ± 0.1	1.6 ± 0.1
Cu <sub>100</sub> <sup>2</sup>	98.1 ± 4.9	94.4 ± 4.7	1.9 ± 0.1	1.6 ± 0.1	2.1 ± 0.1
Pd <sub>1</sub> Cu <sub>216</sub> <sup>1</sup>	99.7 ± 5.0	75.1 ± 3.8	22.0 ± 1.1	1.6 ± 0.1	1.3 ± 0.1
Pd <sub>1</sub> Cu <sub>216</sub> <sup>2</sup>	99.2 ± 5.0	73.7 ± 3.7	23.7 ± 1.2	1.5 ± 0.1	1.2 ± 0.1
Pd <sub>1</sub> Cu <sub>53</sub> <sup>1</sup>	99.0 ± 5.0	77.4 ± 4.1	20.8 ± 0.8	1.2 ± 0.1	0.6 ± 0.1
Pd <sub>1</sub> Cu <sub>53</sub> <sup>2</sup>	99.0 ± 5.0	77.8 ± 4.2	18.2 ± 0.6	1.6 ± 0.1	2.3 ± 0.1
Pd <sub>100</sub> <sup>1</sup>	99.7 ± 5.0	62.8 ± 3.1	37.2 ± 1.9	0.0	0.0
Pd <sub>100</sub> <sup>2</sup>	100.0 ± 5.0	65.3 ± 3.3	34.7 ± 1.7	0.0	0.0

Superscripts 1 and 2 indicate the catalyst cycle of testing.

### 5.2.3 Cu/Al<sub>2</sub>O<sub>3</sub> wet impregnation catalysts

The characterisation of the Cu/Al<sub>2</sub>O<sub>3</sub> catalysts discussed in depth in Chapter 3 is summarised in Table 3.3.1. In summary, six catalysts were synthesised by wet impregnation with three different Cu precursors (nitrate, acetate, and sulfate) and at two loadings of 1 wt% and 5 wt%. EXAFS analysis suggested at 1 wt% the Cu phase formed into isolated and dimer atoms attached to the support. While at 5 wt%, the sulfate derived catalyst formed larger defined nanoparticles, the nitrate formed small nanoparticles, and the acetate formed a layered/paracrystalline structure.

*Table 5.2.9 Bulk elemental analysis, surface area measurements, Cu crystallite, Cu particle size analysis and EXAFS determined structure. Catalysts synthesised using copper nitrate, copper acetate and copper sulfate pentahydrate were denoted (N), (A) and (S), respectively.*

Catalyst	Nominal Cu loading (wt%)	Actual Cu loading <sup>a</sup> (wt%)	Surface area <sup>b</sup> (m <sup>2</sup> g <sup>-1</sup> )	Cu crystallite size <sup>c</sup> (nm)	Cu particle size <sup>d</sup> (nm)	EXAFS structure
Cu/Al <sub>2</sub> O <sub>3</sub> (N)	1.0	0.83 ± 0.04	35.9 ± 1.8	-	-	Isolated atoms
Cu/Al <sub>2</sub> O <sub>3</sub> (A)	1.0	0.91 ± 0.05	35.0 ± 1.8	-	-	Isolated atoms and dimers
Cu/Al <sub>2</sub> O <sub>3</sub> (S)	1.0	0.66 ± 0.08	38.8 ± 1.9	-	-	Isolated atoms and dimers
Cu/Al <sub>2</sub> O <sub>3</sub> (N)	5.0	4.22 ± 0.32	33.5 ± 1.7	13.2 ± 9.5	3.9 ± 1.9	Small nanoparticles
Cu/Al <sub>2</sub> O <sub>3</sub> (A)	5.0	4.56 ± 0.36	33.3 ± 1.7	13.0 ± 9.4	6.8 ± 5.5	Paracrystalline structure
Cu/Al <sub>2</sub> O <sub>3</sub> (S)	5.0	4.22 ± 0.31	29.7 ± 1.5	18.7 ± 12.9	12.8 ± 9.3	Large nanoparticles

<sup>a</sup>Determined by ICP-OES, <sup>b</sup>BET surface area from N<sub>2</sub> porosimetry, <sup>c</sup>WPPM via XRD, <sup>d</sup>STEM

The catalytic data of the Cu/Al<sub>2</sub>O<sub>3</sub> catalysts derived from wet impregnation in Table 5.2.10 is found to mirror the reactivity of the earlier shown PdCu catalysts. In all cases, the wet impregnation monometallic catalysts are found to be more selective towards the complete hydrogenation of crotonaldehyde compared to the monometallic colloidal Cu<sub>100</sub> catalyst (4% butanol selectivity, Table 5.2.5). The difference in selectivity can be due to the different ratios of active sites present in the wet impregnation catalysts as a range of Cu nanostructures are formed (Table 3.3.1) from the synthetic process.

The effect of remnant sulfate species appears to have a minimal effect on the hydrogenation of crotonaldehyde when compared to furfural (Chapter 3). For example, the acetal, butanol and crotyl alcohol selectivity were largely unaffected by the choice of the precursor. However, it should be noted it is widely reported in the literature that sulfur can be beneficial to promote crotyl alcohol selectivity [7, 14, 21, 38, 39]. Lambert *et al.* [6, 14] found that sulfur atoms activate the copper surface towards the

chemoselective transformation of crotonaldehyde. It was found that the presence of S adatoms electronically perturbs and strongly tilts the reactant favouring C = O over C = C hydrogenation. Their observations also support earlier investigations by Hutchings *et al.* [7, 21, 39], sulfur promotes crotyl alcohol formations using Cu/Al<sub>2</sub>O<sub>3</sub> catalysts under atmospheric conditions. The ineffectiveness of sulfates in the current work may likely be due to the source of sulfur, where in the literature S<sub>2</sub> and thiophene are used and the location of sulfur species. As the previous studies feed the sulfur source with the reactant so sulfur species are adsorbed on the surface instead of being embedded in the Cu nanostructure, which likely is the case with the sulfate-derived catalysts. Thus, the source of sulfur and the location may have different degrees of effectiveness in changing the reactivity. Though the 5 wt% (S) catalyst appears to have the lowest conversion (88% versus 99%) across the 5 wt% catalysts suggesting the sulfate may be detrimental through site blocking.

Table 5.2.10 Summary of the catalytic data for the hydrogenation of crotonaldehyde using Cu/Al<sub>2</sub>O<sub>3</sub> catalysts derived from different metal precursors. Reaction conditions: 7 h, 50 °C, 1.5 bar, 600 RPM, and 10 mg of catalyst.

Cu precursor	Nominal Cu wt%	Conversion (%)	Butanal S (%)	Butanol S (%)	Crotyl alcohol S (%)	Acetal S (%)
Nitrate	1	98.5 ± 4.9	86.7 ± 4.4	10.4 ± 0.4	1.5 ± 0.1	1.4 ± 0.1
	5	98.9 ± 4.9	83.8 ± 4.5	12.5 ± 0.3	2.1 ± 0.1	1.6 ± 0.1
Acetate	1	100.0 ± 5.0	68.4 ± 3.4	30.4 ± 1.5	0.9 ± 0.1	0.3 ± 0.1
	5	99.2 ± 5.0	80.5 ± 4.3	16.5 ± 0.5	1.8 ± 0.1	1.2 ± 0.1
Sulfate	1	99.0 ± 4.9	84.6 ± 4.2	11.9 ± 0.6	1.9 ± 0.1	1.6 ± 0.1
	5	88.1 ± 4.4	88.0 ± 4.6	10.5 ± 0.3	1.0 ± 0.1	0.6 ± 0.1

*Rounding errors may be present.*

The conversion profiles in Fig. 5.2.10a shows once again, an induction period is present for all the catalysts. Such results are consistent with all the catalytic data presented in this thesis. Whereby the Cu-based catalysts are inactive at the start of the reaction where reduced activity is observed. However, while the catalyst is inactive in terms of hydrogenation reactions (Fig. 5.2.10) there is an uptick in the reversible acetalisation reactions which is especially noticeable for the 5 wt% Cu (A) catalyst (Fig. 5.2.10a). After the induction period, crotonaldehyde is hydrogenated to butanal across all the catalysts with the acetate derived catalysts being superior. The superior activity of the acetate can likely be attributed to the different modes of decomposition of the precursors during the synthesis (Chapter 3)

creating further dispersed paracrystalline nanostructure. Another observation that can be made is the 1 wt% (A) appears to be significantly more active at fully hydrogenating crotonaldehyde to butanol when compared against its higher loaded counterpart.

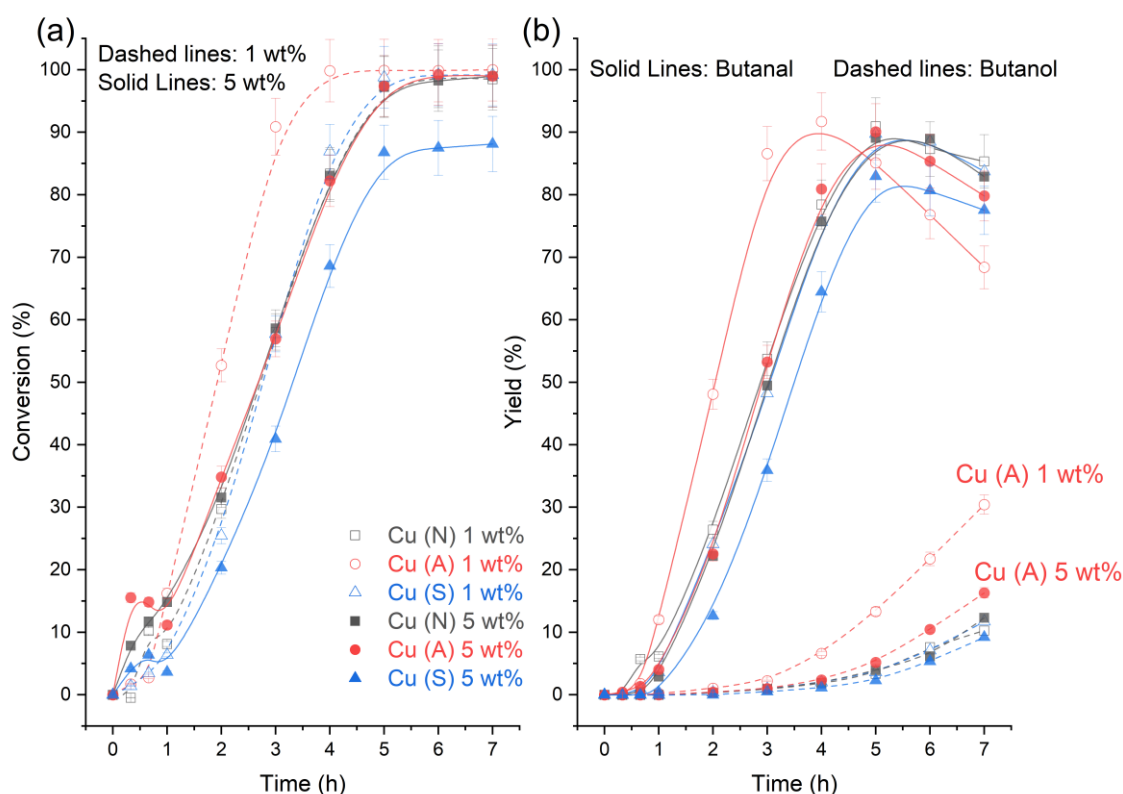


Fig. 5.2.10 The reaction profiles of (a) crotonaldehyde conversion and (b) yield of major products across the 1 wt% and 5 wt% Cu/Al<sub>2</sub>O<sub>3</sub> wet impregnation catalysts. Reaction conditions: 7 h, 50 °C, 1.5 bar, 600 RPM, and 10 mg of catalyst.

Fig. 5.2.11a shows the initial rates normalised to Cu content and TOFs. Such values support the initial observation that sulfate content has a minor non-beneficial effect compared to the furfural experiments (5 wt% catalysts). While the initial rates and TOFs of sulfur-free 5 wt% catalysts indicate the active sites are largely identical. However, in the case of the 1 wt% catalysts sulfur does not seem to affect the active sites performing just as well as the acetate derived catalyst. Like the 5 wt% catalysts, the effect of metal precursor choice appears not to substantially affect the activity of the sites for the hydrogenation to butanal. But looking at the initial rate of consumption of butanal to butanol (Fig.

5.2.11b) the acetate derived catalysts are excellent at hydrogenating the C = O bond to butanol. Overall, the 1 wt% catalysts are found to be more active than the 5 wt% in terms of TOFs and normalised initial rates, likely due to the highly dispersed nature of the Cu species into isolated and small clusters of Cu atoms.

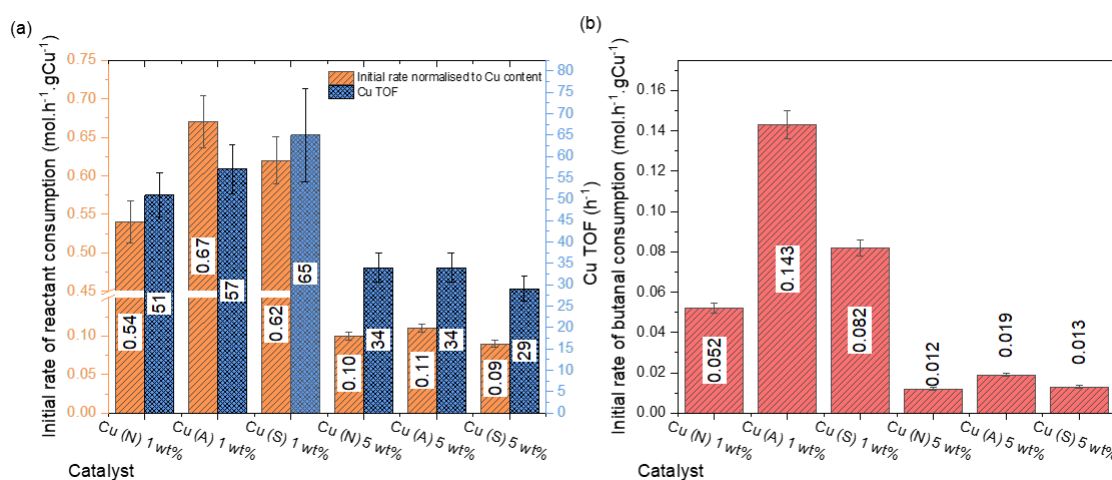


Fig. 5.2.11 (a) Normalised initial rates of crotonaldehyde consumption per gram of Cu and TOF (b) Normalised initial rates of butanal consumption after the induction period across the 1 wt% and 5 wt% Cu/Al<sub>2</sub>O<sub>3</sub> catalysts.

## 5.2.4 Catalyst performance against literature

Finally, the catalysts in this Chapter were compared against the literature in Fig. 5.2.12. The catalyst performance was calculated by TOF\* (promoting metal content, Equation 2.3.7) quantifying the most active atom efficient catalyst. It should also be noted the colour of the spheres represents which metal is used for the calculation. Pd, Pt, Ir, Ag, Ni, Cu, Ru, Rh, Au and Co represent sphere colours dark grey, blue, red, purple, green, orange, greenish-yellow, yellow, cyan, and brown, respectively. The Cu (A) 1 wt% synthesised by wet impregnation is more active than the colloiddally synthesised Cu<sub>100</sub> catalyst, likely due to isolated atom and dimer Cu atoms. However, both monometallic Cu catalysts were found to be superior compared to a Cu-Cr catalyst reported in the literature [25]. The most active catalyst reported in the literature is a Pt<sub>1</sub>/MoC single-atom catalyst (SAC) [27] (TOF\* = 1216 h<sup>-1</sup>) but operating at moderate reaction conditions (100 °C, 20 bar). Nevertheless, the TOF\* for the SAA catalysts in this work are between 2000 – 11,000 h<sup>-1</sup> while operating at milder conditions.

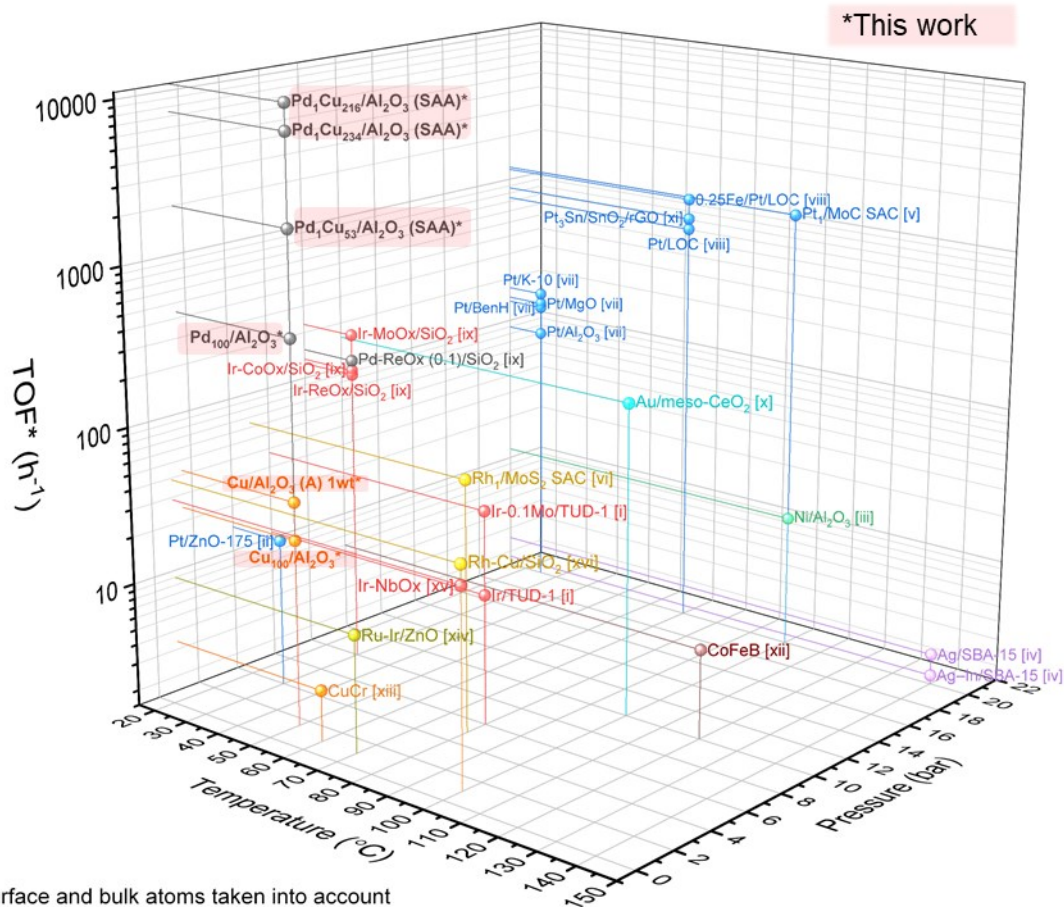


Fig. 5.2.12 TOF\* ( $h^{-1}$ ) of catalysts from this work and various catalysts found in the literature under low to moderate conditions ( $<150\text{ }^{\circ}C$  and  $<20\text{ bar}$ ). TOF\* calculation took in consideration both metal atoms on the surface and in the bulk. Reference represented by the square bracketed Roman numerals [i]=[40], [ii]=[41], [iii]=[20], [iv]=[18], [v]=[27], [vi]=[17], [vii]=[16], [viii]=[42], [ix]=[11], [x]=[43], [xi]=[44], [xii]=[45], [xiii]=[25], [xiv]=[46], [xv]=[47] and [xvi]=[48]. Log<sub>10</sub> scale is used for the TOF\* ( $h^{-1}$ ) z-axis and the colour of the spheres represents which metal is used for the calculation. Pd, Pt, Ir, Ag, Ni, Cu, Ru, Rh, Au and Co represent sphere colours dark grey, blue, red, purple, green, orange, greenish-yellow, yellow, cyan, and brown, respectively.

### 5.3 Conclusions

A series of bimetallic PdCu catalysts were tested for the hydrogenation of crotonaldehyde under mild conditions. The augmentation of the copper surface with trace amounts of Pd (0.0067 wt%) was found to improve the normalised catalytic activity by nineteen-fold and two-fold when compared to the monometallic Pd and Cu catalysts, respectively. Atomically dispersed Pd atoms augmentation was also found to improve the hydrogenation capability of the  $\text{Cu}_{100}/\text{Al}_2\text{O}_3$  catalyst by “fast-forwarding” the reaction, and consequently, increasing the yield of butanol by 4.8 times. Also adding trace amounts of Pd has a far greater effect on the hydrogenation capability of copper catalysts than increasing the pressure to 10 bar (from 1.5 bar). However, the promotion of crotyl alcohol selectivity was not observed. This is due to the inherent lack of selectivity of Cu surfaces under the current conditions. as Cu surfaces can also isomerise crotonaldehyde to butanal and hydrogenate it to butanol. This work confirms the formation of a single atom alloy catalyst is not enough, but such isolated atoms need to be present on the surface to be taken advantage of. In addition, the work also shows the selectivity of the SAA is constrained to the reactivity of the host nanoparticle. For example, on Cu surfaces, furfural’s C = O bond is selectively hydrogenated (Chapter 4) while for crotonaldehyde it is not because of the different adsorption mode of the molecule.

The effect of Cu metal precursor selection was also tested for the crotonaldehyde hydrogenation using supported monometallic catalysts. The presence of remnant sulfates from catalyst synthesis was found to have a minor non-beneficial effect on the reaction. The promotion effect reported in the literature [7, 21, 39] was not observed, which is likely to be due to the source and location of the sulfur species on the catalytic surface. Like the furfural experiments in Chapter 3, the acetate derived catalysts were found to be optimal for the hydrogenation reactions, in this case, for the hydrogenation of crotonaldehyde to butanol.

## 5.4 References

- [1] P. Mäki-Arvela, L.-P. Tiainen, A.K. Neyestanaki, R. Sjöholm, T.-K. Rantakylä, E. Laine, T. Salmi, D.Y. Murzin, Liquid phase hydrogenation of citral: suppression of side reactions, *Appl. Catal. A Gen.*, 237 (2002) 181-200.
- [2] P. Gallezot, D. Richard, Selective Hydrogenation of  $\alpha,\beta$ -Unsaturated Aldehydes, *Catal. Rev. Sci. Eng.*, 40 (1998) 81-126.
- [3] A.R. McInroy, A. Uhl, T. Lear, T.M. Klapötke, S. Shaikhutdinov, S. Schaueremann, G. Rupprechter, H.-J. Freund, D. Lennon, Morphological and chemical influences on alumina-supported palladium catalysts active for the gas phase hydrogenation of crotonaldehyde, *J. Chem. Phys.*, 134 (2011) 214704.
- [4] W. Shi, L. Zhang, Z. Ni, X. Xiao, S. Xia, Adsorption and hydrogenation mechanism of crotonaldehyde on a Pd(111) surface by periodic DFT calculations, *RSC Adv.*, 4 (2014) 27003-27012.
- [5] M. Luneau, J.S. Lim, D.A. Patel, E.C.H. Sykes, C.M. Friend, P. Sautet, Guidelines to Achieving High Selectivity for the Hydrogenation of  $\alpha,\beta$ -Unsaturated Aldehydes with Bimetallic and Dilute Alloy Catalysts: A Review, *Chem. Rev.*, 120 (2020) 12834-12872.
- [6] M.E. Chiu, D.J. Watson, G. Kyriakou, M.S. Tikhov, R.M. Lambert, Tilt the Molecule and Change the Chemistry: Mechanism of S-Promoted Chemoselective Catalytic Hydrogenation of Crotonaldehyde on Cu(111), *Angew. Chem. Int. Ed.*, 45 (2006) 7530-7534.
- [7] G.J. Hutchings, F. King, I.P. Okoye, C.H. Rochester, Influence of sulphur poisoning of copper/alumina catalyst on the selective hydrogenation of crotonaldehyde, *Appl. Catal. A Gen.*, 83 (1992) L7-L13.
- [8] P. Mäki-Arvela, J. Hájek, T. Salmi, D.Y. Murzin, Chemoselective hydrogenation of carbonyl compounds over heterogeneous catalysts, *Appl. Catal. A Gen.*, 292 (2005) 1-49.

- [9] S. Sitthisa, T. Sooknoi, Y. Ma, P.B. Balbuena, D.E. Resasco, Kinetics and mechanism of hydrogenation of furfural on Cu/SiO<sub>2</sub> catalysts, *J. Catal.*, 277 (2011) 1-13.
- [10] C. Mohr, P. Claus, Hydrogenation Properties of Supported Nanosized Gold Particles, *Sci. Prog.*, 84 (2001) 311-334.
- [11] M. Tamura, K. Tokonami, Y. Nakagawa, K. Tomishige, Selective Hydrogenation of Crotonaldehyde to Crotyl Alcohol over Metal Oxide Modified Ir Catalysts and Mechanistic Insight, *ACS Catal.*, 6 (2016) 3600-3609.
- [12] G. Budroni, S.A. Kondrat, S.H. Taylor, D.J. Morgan, A.F. Carley, P.B. Williams, G.J. Hutchings, Selective deposition of palladium onto supported nickel – bimetallic catalysts for the hydrogenation of crotonaldehyde, *Catal. Sci. Technol.*, 3 (2013) 2746-2754.
- [13] B.C. Campo, M.A. Volpe, C.E. Gigola, Liquid-Phase Hydrogenation of Crotonaldehyde over Platinum- and Palladium-Based Catalysts, *Ind. Eng. Chem.*, 48 (2009) 10234-10239.
- [14] M.E. Chiu, G. Kyriakou, F.J. Williams, D.J. Watson, M.S. Tikhov, R.M. Lambert, Sulfur, normally a poison, strongly promotes chemoselective catalytic hydrogenation: stereochemistry and reactivity of crotonaldehyde on clean and S-modified Cu(111), *Chem. Commun.*, (2006) 1283-1285.
- [15] F.A. Harraz, S.E. El-Hout, H.M. Killa, I.A. Ibrahim, Catalytic hydrogenation of crotonaldehyde and oxidation of benzene over active and recyclable palladium nanoparticles stabilized by polyethylene glycol, *J. Mol. Catal. A: Chem.*, 370 (2013) 182-188.
- [16] I. Kun, G. Szöllösi, M. Bartók, Crotonaldehyde hydrogenation over clay-supported platinum catalysts, *J. Mol. Catal. A: Chem.*, 169 (2001) 235-246.
- [17] Y. Lou, Y. Zheng, X. Li, N. Ta, J. Xu, Y. Nie, K. Cho, J. Liu, Pocketlike Active Site of Rh1/MoS<sub>2</sub> Single-Atom Catalyst for Selective Crotonaldehyde Hydrogenation, *J. Am. Chem. Soc.*, 141 (2019) 19289-19295.

- [18] L. Tian, Q. Yang, Z. Jiang, Y. Zhu, Y. Pei, M. Qiao, K. Fan, Highly chemoselective hydrogenation of crotonaldehyde over Ag–In/SBA-15 fabricated by a modified “two solvents” strategy, *Chem. Commun.*, 47 (2011) 6168-6170.
- [19] X.-X. Wang, H.-Y. Zheng, X.-J. Liu, G.-Q. Xie, J.-Q. Lu, L.-Y. Jin, M.-F. Luo, Effects of NaCl on Pt/ZrO<sub>2</sub> catalysts for selective hydrogenation of crotonaldehyde, *Appl. Catal. A Gen.*, 388 (2010) 134-140.
- [20] J. Yu, Y. Yang, L. Chen, Z. Li, W. Liu, E. Xu, Y. Zhang, S. Hong, X. Zhang, M. Wei, NiBi intermetallic compounds catalyst toward selective hydrogenation of unsaturated aldehydes, *Appl. Catal. B*, 277 (2020) 119273.
- [21] G.J. Hutchings, F. King, I.P. Okoye, M.B. Padley, C.H. Rochester, Modification of Selectivity in the Hydrogenation of Crotonaldehyde Using Cu/Al<sub>2</sub>O<sub>3</sub> Catalysts Modified with Sulfur Compounds: Effect of Sulfur Source, *J. Catal.*, 148 (1994) 464-469.
- [22] X. Li, P. Jia, T. Wang, Furfural: A Promising Platform Compound for Sustainable Production of C<sub>4</sub> and C<sub>5</sub> Chemicals, *ACS Catal.*, 6 (2016) 7621-7640.
- [23] A.J. Urquhart, F.J. Williams, O.P.H. Vaughan, R.L. Cropley, R.M. Lambert, Adsorbate conformation determines catalytic chemoselectivity: crotonaldehyde on the Pt(111) surface, *Chem. Commun.*, (2005) 1977-1979.
- [24] H. Noller, W.M. Lin, Activity and selectivity of Ni-CuAl<sub>2</sub>O<sub>3</sub> catalysts for hydrogenation of crotonaldehyde and mechanism of hydrogenation, *J. Catal.*, 85 (1984) 25-30.
- [25] R. Rao, A. Dandekar, R.T.K. Baker, M.A. Vannice, Properties of Copper Chromite Catalysts in Hydrogenation Reactions, *J. Catal.*, 171 (1997) 406-419.
- [26] J. Šimoník, L. Beránek, Mono and bimolecular mechanisms in the catalytic isomerization of crotyl alcohol to butyraldehyde, *J. Catal.*, 24 (1972) 348-351.

- [27] Q. Bi, X. Yuan, Y. Lu, D. Wang, J. Huang, R. Si, M. Sui, F. Huang, One-Step High-Temperature-Synthesized Single-Atom Platinum Catalyst for Efficient Selective Hydrogenation, *Research*, 2020 (2020) 9140841.
- [28] L.A. Saudan, Hydrogenation Processes in the Synthesis of Perfumery Ingredients, *Acc. Chem. Res.*, 40 (2007) 1309-1319.
- [29] F. Zaragoza, V. Heinze, Direct C-4 arylation of crotonaldehyde with arenediazonium tetrafluoroborates, *Tetrahedron Lett.*, 52 (2011) 4678-4680.
- [30] M. Lesiak, M. Binczarski, S. Karski, W. Maniukiewicz, J. Rogowski, E. Szubiakiewicz, J. Berlowska, P. Dziugan, I. Witońska, Hydrogenation of furfural over Pd–Cu/Al<sub>2</sub>O<sub>3</sub> catalysts. The role of interaction between palladium and copper on determining catalytic properties, *J. Mol. Catal. A: Chem.*, 395 (2014) 337-348.
- [31] J. Batista, A. Pintar, D. Mandrino, M. Jenko, V. Martin, XPS and TPR examinations of  $\gamma$ -alumina-supported Pd-Cu catalysts, *Appl. Catal. A Gen.*, 206 (2001) 113-124.
- [32] F. Cárdenas-Lizana, S. Gómez-Quero, C. Amorim, M.A. Keane, Gas phase hydrogenation of p-chloronitrobenzene over Pd–Ni/Al<sub>2</sub>O<sub>3</sub>, *Appl. Catal. A Gen.*, 473 (2014) 41-50.
- [33] S.F. Parker, H.C. Walker, S.K. Callear, E. Grünewald, T. Petzold, D. Wolf, K. Möbus, J. Adam, S.D. Wieland, M. Jiménez-Ruiz, P.W. Albers, The effect of particle size, morphology and support on the formation of palladium hydride in commercial catalysts, *Chemical Science*, 10 (2019) 480-489.
- [34] G. Kyriakou, E.R.M. Davidson, G. Peng, L.T. Roling, S. Singh, M.B. Boucher, M.D. Marcinkowski, M. Mavrikakis, A. Michaelides, E.C.H. Sykes, Significant Quantum Effects in Hydrogen Activation, *ACS Nano*, 8 (2014) 4827-4835.

- [35] G. Kyriakou, M.B. Boucher, A.D. Jewell, E.A. Lewis, T.J. Lawton, A.E. Baber, H.L. Tierney, M. Flytzani-Stephanopoulos, E.C. Sykes, Isolated metal atom geometries as a strategy for selective heterogeneous hydrogenations, *Science*, 335 (2012) 1209-1212.
- [36] H.L. Tierney, A.E. Baber, J.R. Kitchin, E.C.H. Sykes, Hydrogen Dissociation and Spillover on Individual Isolated Palladium Atoms, *Phys. Rev. Lett.*, 103 (2009) 246102.
- [37] Q. Fu, Y. Luo, Catalytic Activity of Single Transition-Metal Atom Doped in Cu(111) Surface for Heterogeneous Hydrogenation, *J. Phys. Chem. C*, 117 (2013) 14618-14624.
- [38] M.V. Twigg, M.S. Spencer, Deactivation of supported copper metal catalysts for hydrogenation reactions, *Appl. Catal. A Gen.*, 212 (2001) 161-174.
- [39] G.J. Hutchings, F. King, I.P. Okoye, M.B. Padley, C.H. Rochester, Selectivity Enhancement in the Hydrogenation of  $\alpha$ ,  $\beta$ -Unsaturated Aldehydes and Ketones Using Thiophene-Modified Catalysts, *J. Catal.*, 148 (1994) 453-463.
- [40] Y.-M. Xu, W.-B. Zheng, Y.-M. Hu, C. Tang, A.-P. Jia, J.-Q. Lu, The effects of MoOx decoration on the selective hydrogenation of crotonaldehyde over MoOx-promoted Ir/TUD-1 catalysts, *J. Catal.*, 381 (2020) 222-233.
- [41] J. Hidalgo-Carrillo, M.A. Aramendía, A. Marinas, J.M. Marinas, F.J. Urbano, Support and solvent effects on the liquid-phase chemoselective hydrogenation of crotonaldehyde over Pt catalysts, *Appl. Catal. A Gen.*, 385 (2010) 190-200.
- [42] F. Hou, H. Song, H. Zhao, J. Zhao, J. Yang, L. Yan, L. Chou, The chemoselective hydrogenation of crotonaldehyde over PtFe catalysts supported on La<sub>2</sub>O<sub>2</sub>CO<sub>3</sub> nanorods, *React. Kinet. Mech. Catal.*, 122 (2017) 117-133.

- [43] M.-M. Wang, L. He, Y.-M. Liu, Y. Cao, H.-Y. He, K.-N. Fan, Gold supported on mesostructured ceria as an efficient catalyst for the chemoselective hydrogenation of carbonyl compounds in neat water, *Green Chem.*, 13 (2011) 602-607.
- [44] J. Shi, M. Zhang, W. Du, W. Ning, Z. Hou, SnO<sub>2</sub>-isolated Pt<sub>3</sub>Sn alloy on reduced graphene oxide: an efficient catalyst for selective hydrogenation of C=O in unsaturated aldehydes, *Catal. Sci. Technol.*, 5 (2015) 3108-3112.
- [45] Y. Pei, P. Guo, M. Qiao, H. Li, S. Wei, H. He, K. Fan, The modification effect of Fe on amorphous CoB alloy catalyst for chemoselective hydrogenation of crotonaldehyde, *J. Catal.*, 248 (2007) 303-310.
- [46] Q. Yu, X. Zhang, B. Li, J. Lu, G. Hu, A. Jia, C. Luo, Q. Hong, Y. Song, M. Luo, Effect of reduction temperature on Ru-Ir/ZnO catalyst for selective hydrogenation of crotonaldehyde, *J. Mol. Catal. A: Chem.*, 392 (2014) 89-96.
- [47] M. Tamura, K. Tokonami, Y. Nakagawa, K. Tomishige, Effective NbO<sub>x</sub>-Modified Ir/SiO<sub>2</sub> Catalyst for Selective Gas-Phase Hydrogenation of Crotonaldehyde to Crotyl Alcohol, *ACS Sustain. Chem. Eng.*, 5 (2017) 3685-3697.
- [48] P. Reyes, G. Pecchi, J.L.G. Fierro, Surface Structures of Rh-Cu Sol-Gel Catalysts and Performance for Crotonaldehyde Hydrogenation, *Langmuir*, 17 (2001) 522-527.

## Chapter 6 Conclusions and Future work

## 6.1 Conclusions

### 6.1.1 Effect of metal precursors on nanoparticle morphology for the copper catalysed transformation of furfural

This thesis set out to explore the hydrogenation of  $\alpha$ ,  $\beta$  unsaturated aldehydes with inexpensive Cu-based catalysts. The first study (Chapter 3) looked at the liquid-phase hydrogenation of furfural with a series of supported monometallic Cu/Al<sub>2</sub>O<sub>3</sub> catalysts synthesised via various Cu metal precursors by wet impregnation. With the loadings also being changed, ICP-OES, BET, PXRD, STEM, XPS, XAES and XAS suggested a range of Cu nanostructures were formed from isolated Cu atoms embedded onto the support to island type structures and defined nanoparticles (Fig. 6.1.1). Furfural hydrogenation was sensitive to the presence of sulfates in the catalyst. Sulfates altered the reaction selectivity to the acetalisation pathway of furfural with methanol at over 90% conversion in mild conditions. While at near ambient hydrogen pressures, catalytic tests show that sulfate impurities deactivate the catalyst leading to lower conversion and altered selectivities. Catalytic data also suggested the reaction is likely structure sensitive, as isolated and dimer Cu atoms were found to promote decarbonylation reactions due to their lower-packed copper structures reducing the repulsion of the furan ring with the underlying surface. Consistently, however, catalysts derived from copper acetate were found to be superior, suggesting the metal precursor selection appears to be critical to achieving optimal catalytic activity via changes in the Cu nanostructures.

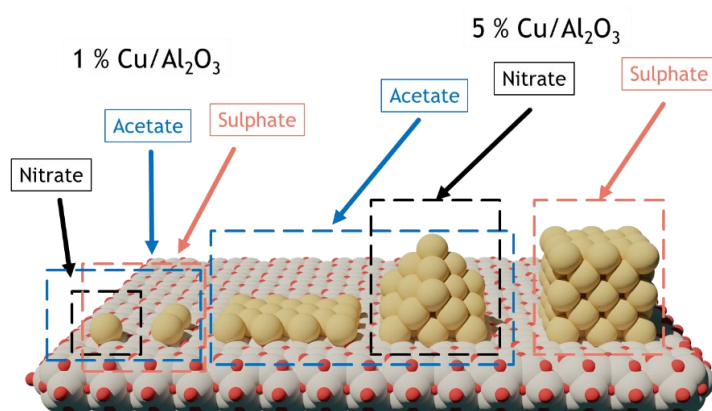


Fig. 6.1.1 Schematic representation of the Cu nanostructures observed as the Cu precursor and loading are altered.

### 6.1.2 PdCu single atom alloys for the hydrogenation of furfural

Following the research on monometallic Cu catalysts in Chapter 3, Cu catalysts were enhanced with the introduction of Pd atoms in Chapter 4. A series of PdCu/Al<sub>2</sub>O<sub>3</sub> catalysts were made from a host colloiddally synthesised Cu<sub>100</sub>/Al<sub>2</sub>O<sub>3</sub> catalyst using galvanic replacement techniques. The catalyst morphology and electronic properties were thoroughly studied utilising XRD, XPS, STEM, XANES, EXAFS, TPR and ICP-OES. The material characterisation confirmed that Pd atoms were atomically dispersed on the host copper nanoparticle surface, confirming the formation of a single atom catalyst or specifically a single atom alloy catalyst (SAA). The combination of pseudo-*in-situ* and *ex-situ* EXAFS suggested that as the Pd loading increases, Pd atoms diffuse into the bulk reducing their catalytic effectiveness. Various optimisations were made to the galvanic replacement synthetic method; finding mild reaction conditions encouraged Pd atoms to stay on the surface. The augmentation of the copper surface with trace amounts of Pd (0.0067 wt%) was found to be the most effective and improve the normalised catalytic activity by eleven-fold when compared to a monometallic Pd catalyst. The synthesised atom efficient SAA catalysts retain Cu's high selectivity attributed to the incredible control of the Pd active sites since they are isolated. Therefore, eliminating competitive side-reactions that require more than one Pd neighbouring atom. The work also highlighted the effectiveness of different SAA catalysts, where the catalysts with the largest portion of precious metal atoms on the surface performing the best.

### 6.1.3 Single-atom alloy and monometallic catalysts for the hydrogenation of crotonaldehyde

Finally, the catalysts synthesised were tested for the hydrogenation of another  $\alpha$ ,  $\beta$  unsaturated aldehyde. Crotonaldehyde was chosen as it lacked the directing group present in furfural (furan ring), so the catalysts can be examined in a situation where C = O hydrogenation is not specifically preferred. Similarly, to the furfural experiments, the addition of trace amounts of Pd (0.0067 wt%) onto the Cu surface was found to improve the normalised catalytic activity by nineteen-fold and two-fold when compared to the monometallic Pd and Cu catalysts, respectively. The atomically dispersed Pd atoms

were also observed to improve the hydrogenation capability of the  $\text{Cu}_{100}/\text{Al}_2\text{O}_3$  catalyst by “fast-forwarding” the reaction, increasing the yield of butanol by 4.8 times. In addition, adding trace amounts of Pd has a far greater effect on the hydrogenation capability of copper catalysts than increasing the pressure to 10 bar (from 1.5 bar). However, unlike the previous experiments, the PdCu SAA catalysts were not selective to crotyl alcohol (selective  $\text{C} = \text{O}$  hydrogenation) due to the inherent lack of selectivity of Cu surfaces without the furan directing group. Thus, these experiments confirm the selectivity of the SAA catalysts is constrained by the reactivity of the host nanoparticle.

The catalytic data of the effect of metal precursor showed that remnant sulfate species were found to have a minor non-beneficial effect on the reaction. The promotional effect observed previously [1-3] was not observed, which is likely to be due to the source and location of the sulfur species on the catalytic surface. The acetate derived catalysts were once again found to be superior for the hydrogenation of crotonaldehyde to butanol. Specifically, the 1 wt% (A) catalyst was found to be optimal for the formation of butanol, which was likely due to its highly dispersed Cu phase.

## 6.2 Future work

To understand the Cu-based catalysts better, more characterisations could have been conducted in an inert atmosphere to prevent surface oxidation. This would have been most beneficial for surface sensitive techniques like XPS and XAES, as more robust links could be made between the characterisation data and the catalysis.

Further investigations could be conducted to understand the  $\text{Cu}/\text{Al}_2\text{O}_3$  catalyst wet impregnation synthesis better. The most useful technique to probe this would be performing the calcination and reduction step *in-situ* with XANES and EXAFS. For example, creating a 1 wt% catalyst with Cu acetate both the C K-edge and Cu L-edge can be followed, thus the oxidation and the local coordination environment changes could be understood as atomic and dimeric Cu atoms are formed.

All the hydrogenation reactions presented in this thesis could also benefit from the conversion of batch reactors to continuous flow reactors. Such reactors are more industrially relevant as the advantages

include simpler catalyst activation, scale-up, space reduction, energy efficiency, and waste reduction. Operando experiments can also be easily conducted with such reactors as the reactant is passed through the catalyst bed. Both the electronic and local environments of the catalyst and the reactant can be tracked with XAS in real-time under real reaction conditions. Data on the stability/reusability of the single-atom catalysts can also be collected as the catalyst ages in the reactor. So, the deactivation modes of such catalysts can be easily understood.

Finally, the scaling up of the synthesis of single atom alloy catalysts could be investigated to see whether the atomically dispersed Pd atoms can be maintained and if they could be mass produced for industry. Further applications of such catalysts also be explored for their use in automotive catalytic converters and fuel cells where different metallic compositions would be required.

### 6.3 References

- [1] G.J. Hutchings, F. King, I.P. Okoye, M.B. Padley, C.H. Rochester, Modification of Selectivity in the Hydrogenation of Crotonaldehyde Using Cu/Al<sub>2</sub>O<sub>3</sub> Catalysts Modified with Sulfur Compounds: Effect of Sulfur Source, *J. Catal.*, 148 (1994) 464-469.
- [2] G.J. Hutchings, F. King, I.P. Okoye, C.H. Rochester, Influence of sulphur poisoning of copper/alumina catalyst on the selective hydrogenation of crotonaldehyde, *Appl. Catal. A Gen.*, 83 (1992) L7-L13.
- [3] G.J. Hutchings, F. King, I.P. Okoye, M.B. Padley, C.H. Rochester, Selectivity Enhancement in the Hydrogenation of  $\alpha$ ,  $\beta$ -Unsaturated Aldehydes and Ketones Using Thiophene-Modified Catalysts, *J. Catal.*, 148 (1994) 453-463.

## Chapter 7 Appendices

## 7.1 Figures

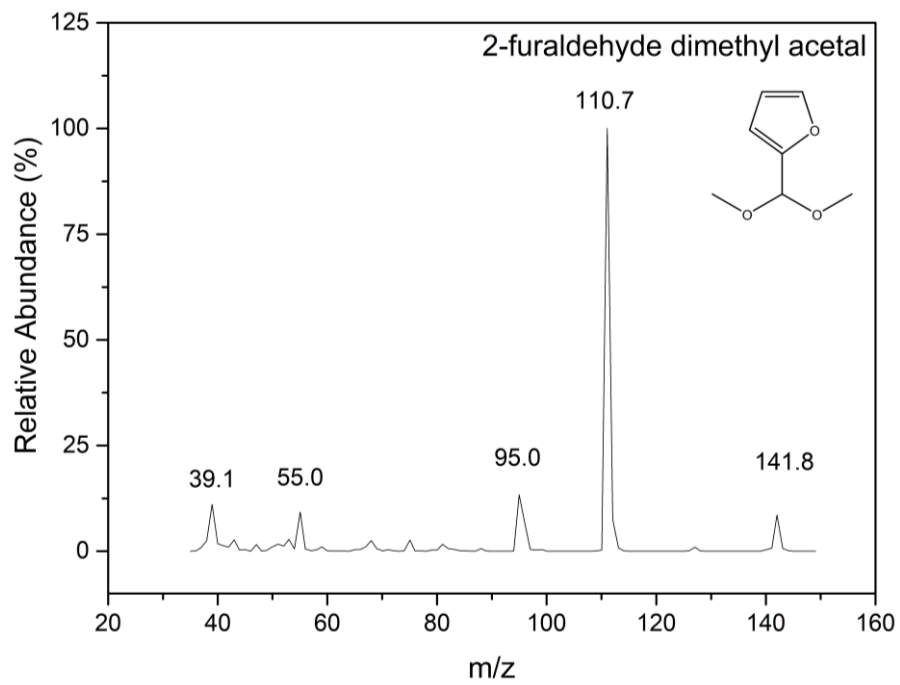


Fig. 7.1.1 MS spectrum 2-furaldehyde dimethyl acetal [1].

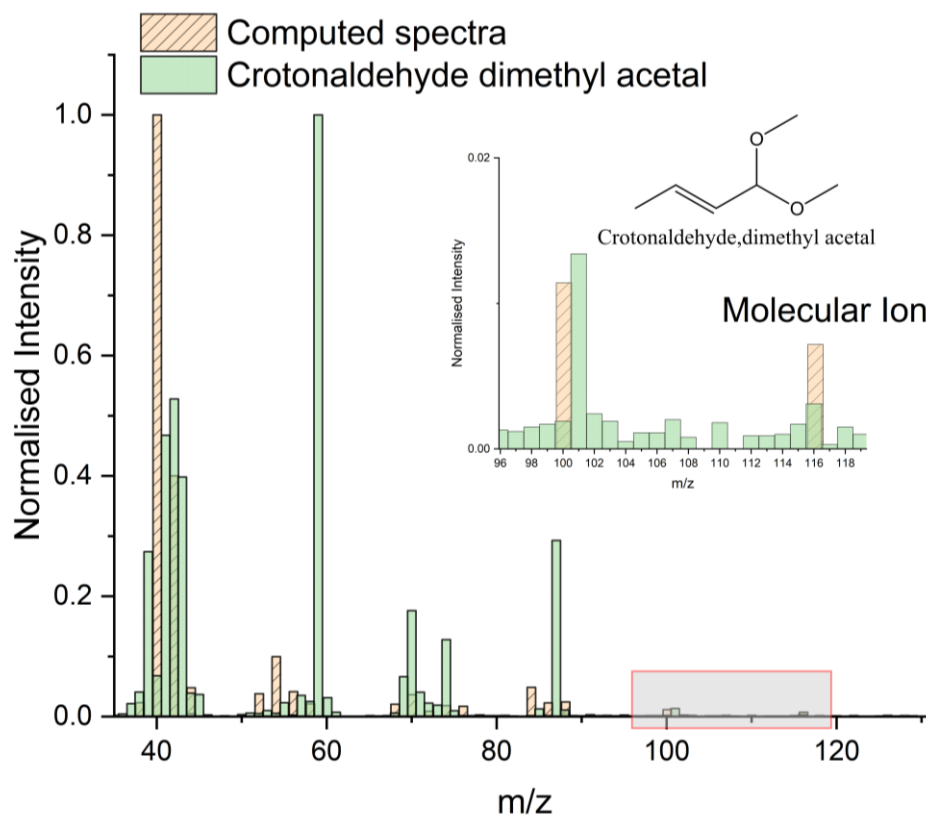


Fig. 7.1.2 Actual and computed [2-4] MS spectra of crotonaldehyde dimethyl acetal.

## 7.2 References

- [1] T. Shen, J. Tang, C. Tang, J. Wu, L. Wang, C. Zhu, H. Ying, Continuous Microflow Synthesis of Fuel Precursors from Platform Molecules Catalyzed by 1,5,7-Triazabicyclo[4.4.0]dec-5-ene, *Org. Process Res. Dev.*, 21 (2017) 890-896.
- [2] F. Allen, R. Greiner, D. Wishart, Competitive fragmentation modeling of ESI-MS/MS spectra for putative metabolite identification, *Metabolomics*, 11 (2015) 98-110.
- [3] F. Allen, A. Pon, R. Greiner, D. Wishart, Computational Prediction of Electron Ionization Mass Spectra to Assist in GC/MS Compound Identification, *Anal. Chem.*, 88 (2016) 7689-7697.
- [4] F. Allen, A. Pon, M. Wilson, R. Greiner, D. Wishart, CFM-ID: a web server for annotation, spectrum prediction and metabolite identification from tandem mass spectra, *Nucleic Acids Res.*, 42 (2014) W94-W99.